Delft University of Technology

Computational micromechanics of time- and cycle-dependent failure in unidirectional composites under off-axis loading

Kovacevic, D.

DOI
10.4233/uuid:18b0b5cc-0572-4cdc-9500-b6710bf6fa63

Publication date
2024

Document Version
Final published version

Citation (APA)
Kovacevic, D. (2024). *Computational micromechanics of time- and cycle-dependent failure in unidirectional composites under off-axis loading*. [Dissertation (TU Delft), Delft University of Technology]. https://doi.org/10.4233/uuid:18b0b5cc-0572-4cdc-9500-b6710bf6fa63

Important note
To cite this publication, please use the final published version (if applicable).
Please check the document version above.

Copyright
Other than for strictly personal use, it is not permitted to download, forward or distribute the text or part of it, without the consent of the author(s) and/or copyright holder(s), unless the work is under an open content license such as Creative Commons.

Takedown policy
Please contact us and provide details if you believe this document breaches copyrights.
We will remove access to the work immediately and investigate your claim.

This work is downloaded from Delft University of Technology.
For technical reasons the number of authors shown on this cover page is limited to a maximum of 10.

COMPUTATIONAL MICROMECHANICS OF TIME- AND CYCLE-DEPENDENT FAILURE IN UNIDIRECTIONAL COMPOSITES UNDER OFF-AXIS LOADING

COMPUTATIONAL MICROMECHANICS OF TIME- AND CYCLE-DEPENDENT FAILURE IN UNIDIRECTIONAL COMPOSITES UNDER OFF-AXIS LOADING

Proefschrift

ter verkrijging van de graad van doctor
aan de Technische Universiteit Delft,
op gezag van de Rector Magnificus prof. dr. ir. T. H. J. J. van der Hagen,
voorzitter van het College voor Promoties,
in het openbaar te verdedigen op maandag 9 december om 12:30 uur

door

Dragan KOVAČEVIĆ

Civiel ingenieur,
Universiteit van Belgrado, Servië,
geboren te Knin, Kroatië.

Dit proefschrift is goedgekeurd door de promotoren.

Samenstelling promotiecommissie:

Rector Magnificus,	voorzitter
Dr. ir. F. P. van der Meer,	Technische Universiteit Delft, promotor
Prof. dr. ir. L. J. Sluys,	Technische Universiteit Delft, promotor
Onafhankelijke leden:	
Prof. dr. P. M. P. R. de Castro Camanho,	University of Porto
Prof. dr. R. Larsson,	Chalmers University of Technology
Prof. dr. ir. L. E. Govaert,	Technische Universiteit Eindhoven
Prof. C. A. Dransfeld,	Technische Universiteit Delft
Dr. B. Chen,	Technische Universiteit Delft
Prof. dr. ir. H. E. J. G. Schlangen,	Technische Universiteit Delft, reservelid

This work falls under the research framework of DPI, P.O. Box 902, 5600 AX Eindhoven, The Netherlands, project Saferide (DPI #811t17).

DPI
Shaping polymer
innovation

Keywords: strain rate, creep, fatigue, viscoplasticity, cohesive damage, thermoplastic composites
Printed by: Ipskamp printing

Copyright © 2024 by D. Kovačević

ISBN 978-94-6384-681-3

An electronic version of this dissertation is available at
`http://repository.tudelft.nl/`.

CONTENTS

SUMMARY

Structures made of fiber-reinforced polymer (FRP) composites are usually considered lightweight. On account of this feature, polymeric composites find their application in many engineering disciplines, where the expected service lifetime may extend to decades. The advent of thermoplastics has brought about cost-effective processing and the possibility to recycle structural components, among other features. However, the viscous nature of the polymer matrix poses a challenge to the straightforward application of FRP composites in load-bearing situations: the material response is a function of time and temperature. In addition, structural components may be subjected to long-term cyclic loading, that may lead to failure irrespective of the viscous nature of the material constituents. Hence, for an optimal application of (thermoplastic) FRP composites in load-bearing situations, it is necessary to understand, and eventually to predict their long-term performance.

Given the heterogeneous microstructure, two types of failure are encountered in FRP composites: fiber failure and matrix failure. In this thesis, the focus is on matrix-dominated failure under off-axis loading of unidirectional (UD) composites, a process that is often termed transverse matrix cracking. In multidirectional laminates, this failure mode may give rise to delamination that can propagate until catastrophic failure of the laminate is observed. Therefore, properly representing the formation of transverse matrix cracks is necessary when designing damage-tolerant structures.

Material failure is studied at the microscale, under the assumption that failure of a representative volume element (RVE) corresponds to macroscopic crack formation. A thin slice of a three-dimensional RVE is defined in a local coordinate frame aligned with the fiber reinforcement, such that a complex stress state in the material under off-axis loading may be represented in the model. While carbon fibers are modeled as elastic, two nonlinear processes are included in the matrix: viscoplasticity and microcracking. Even though the RVE model may be used for different types of composites, the primary focus is on thermoplastic composites.

Three different loading scenarios are considered: constant strain rate, constant stress and cyclic loading. First, it was necessary to develop a model to impose off-axis loading on the RVE, assuming finite deformations of the RVE as a whole. An arclength model with a strain rate-based constraint equation was developed in order to apply a constant strain rate on the micromodel. After showing that the model is able to represent the nonlinear behavior of UD composites that is rate- and off-axis angle-dependent (in other words orthotropic rate-dependent), the RVE model was supplemented with a cohesive zone model, to simulate failure of the carbon/PEEK composite material under different strain rates and off-axis angles. The model was tested against experimental data obtained in a parallel project.

The same kinematical and stress relations derived in the arclength model can be used to impose a constant stress on the RVE under an off-axis angle, without the need for arclength control. This framework was used to model creep deformation and eventually creep rupture of the material. A cohesive initiation criterion based on a critical energy stored in the matrix was proposed, to broaden the stress range for which creep rupture is possible, compared to quasi-static cohesive initiation that would overly restrict this stress range. The cohesive model was supplemented with a viscous degradation tensor, and creep rupture was studied for different off-axis angles and temperatures.

In further developments the framework was simplified by dropping out viscous degradation from the cohesive model, which was combined with an endurance limit-based cohesive initiation criterion. Making sure that the constitutive models properly respond to cyclic loading, a cyclic variation in the applied stress was considered to study material fatigue failure. To make modeling of a large number of cycles computationally feasible, a two-scale adaptive stepping scheme was proposed and made compatible with the constitutive models. The RVE model is able to distinguish between the plasticity controlled and crack growth controlled failure regimes in cyclic loading and their distinct frequency dependency. As a limit case, the same model also accurately predicts the time to failure in creep loading.

SAMENVATTING

Constructies gemaakt van vezelversterkte kunststof (VVK) composieten worden meestal als lichtgewicht beschouwd. Vanwege deze eigenschap vinden composieten hun toepassing in verschillende technische disciplines, waar de verwachte levensduur tientallen jaren kan zijn. De opkomst van thermoplasten heeft kosteneffectieve verwerking en de mogelijkheid om constructieve componenten te recyclen gebracht. Echter, de viskeuze aard van de polymeermatrix vormt een uitdaging voor de rechtstreekse toepassing van VVK-composieten in dragende situaties: de materiaaleigenschappen zijn afhankelijk van tijd en temperatuur. Bovendien kunnen constructieve componenten worden onderworpen aan langdurige cyclische belasting, wat kan leiden tot falen, ongeacht de viskeuze aard van de materiaalsamenstelling. Daarom is het voor een optimale toepassing van (thermoplastische) VVK-composieten in dragende situaties noodzakelijk om hun langetermijnprestaties te begrijpen en uiteindelijk te kunnen voorspellen.

Gezien de heterogene microstructuur worden in VVK-composieten twee soorten falen waargenomen: vezelfalen en matrixfalen. In dit proefschrift ligt de focus op matrixgedomineerd falen onder *off-axis* belasting van unidirectionele (UD) composieten, of *transverse matrix cracking*. In multidirectionele laminaten kan deze faalmode zich ontwikkelen tot een proces van delaminatie dat kan groeien totdat catastrofaal falen van het laminaat optreedt. Daarom is een correct beschrijving van het ontstaan van matrixscheuren noodzakelijk bij het optimaal ontwerpen van schade-tolerante constructies.

Materiaalfalen wordt in deze studie beschouwd op microschaal, onder de aanname dat falen van een representatief volume-element (RVE) overeenkomt met macroscopische scheurvorming. Een dun drie-dimensionaal RVE wordt gedefinieerd in een lokaal coördinatensysteem uitgelijnd met de vezels, zodat een complexe spanningsstaat in het materiaal onder *off-axis* belasting kan worden weergegeven in het model. Terwijl koolstofvezels als elastisch worden gemodelleerd, worden twee niet-lineaire processen opgenomen in de matrix: viscoplasticiteit en microscheuren. Hoewel het RVE-model kan worden gebruikt voor verschillende soorten composieten, is de studie primair gericht op thermoplastische composieten.

Drie verschillende belastingsscenario's worden beschouwd: constante rek-snelheid, constante spanning en cyclische belasting. Eerst was het noodzakelijk om een model te ontwikkelen om *off-axis* belasting op het RVE op te leggen, waarbij eindige vervormingen van het RVE als geheel werden aangenomen. Een *arclength* model met een op rek-snelheid gebaseerde constraint-vergelijking is ontwikkeld om een constante rek-snelheid op het micromodel toe te passen. Nadat is aangetoond dat het model een niet-lineair gedrag van UD-composieten kan weergeven dat afhankelijk is van de snelheid en de *off-axis* hoek (met andere woorden orthotrope snelheidsafhankelijkheid), is het RVE-model aangevuld met een cohesief model om falen van het koolstof/PEEK-composietmateriaal onder verschillende rek-snelheden en *off-axis* hoeken te simuleren. Het model is getest aan de hand van experimentele gegevens verkregen in een parallell project.

Dezelfde kinematische en spanningsrelaties die in het *arclength* model zijn afgeleid, kunnen worden gebruikt om een constante spanning op het RVE onder een *off-axis* hoek op te leggen, zonder dat *arclength* controle nodig is. Dit raamwerk is gebruikt om kruipvervorming en uiteindelijk kruipbreuk van het materiaal te modelleren. Een initiatiecriterium gebaseerd op een kritische energie in de matrix is voorgesteld om het spanningsbereik waarvoor kruipbreuk mogelijk is, te verbreden, vergeleken met quasi-statische initiatie die dit spanningsbereik te veel zou beperken. Het cohesievemodel is aangevuld met een viskeuze degradatietensor en kruipbreuk is bestudeerd voor verschillende *off-axis* hoeken en temperaturen.

In verdere ontwikkelingen is het raamwerk vereenvoudigd door viskeuze degradatie uit het cohesieve model te schrappen, gecombineerd met een initiatiecriterium gebaseerd op een vermoeiingslimiet. Door ervoor te zorgen dat de constitutieve modellen goed reageren op cyclische belasting, werd een cyclische variatie in de aangelegde spanning overwogen om vermoeiingsfalen van het materiaal te bestuderen. Om het doorrekenen van een groot aantal cycli qua rekentijd haalbaar te maken, is een adaptieve tijdsstapmethode op twee tijdsschalen voorgesteld en gecombineerd met de constitutieve modellen. Het RVE-model kan onderscheid maken tussen de plasticiteitsgecontroleerde en scheurgroei-gecontroleerde faalregimes bij cyclische belasting en hun verschillende frequentieafhankelijkheid. Als limietgeval voorspelt hetzelfde model eveneens nauwkeurig de tijd tot falen bij kruipbelasting.

ACKNOWLEDGEMENTS

The work presented in this thesis is part of the Saferide project funded by the DPI. Therefore, I would like to thank the people from the DPI and the industrial partners for making this project possible. A thank you note goes to Denka Hristova-Bogaerds for coordinating the project. Much of the modeling effort presented here relies on the experimental work done at the University of Twente by our colleagues in the project Prof. Leon Govaert and Bharath Sundararajan, to whom I am grateful for always inspiring discussions and for sharing their insights in the material behavior. I would like to thank my promotor Prof. Bert Sluys for managing the project from the TU Delft side, but also for always being supportive and for creating a flexible and unobtrusive environment for PhD students in the computational mechanics (CM) group.

My thanks go to all the friends and colleagues from the CM group, but also from other parts of the sixth floor and of the CiTG building, that I had a pleasure to work with during my years at the TU. Special thanks to my office colleagues Mehdi, Pieter and Amir, for their friendliness and cooperativeness. A large part of the work in this thesis was built on top of the code developed by my colleague Lu Ke, to whom I am grateful for always being eager to help with the code details.

Thanks to Prof. Mira Petronijević who supported me to explore the field of engineering mechanics, I started the research journey at the University of Belgrade. This journey continued at several other places with an opportunity to meet new people and learn new things. I am grateful to Prof. Yuri Petryna for hosting my stay at the TU Berlin, while still a student in Belgrade. Also, I want to thank Prof. Boris Jeremić for hosting me at the University of California in Davis, where I had a pleasure of attending great lectures on the theory of elasticity by Prof. Mark Rashid. Furthermore, Prof. Rashid was willing to help me in finding a PhD position. In this regard, the help of several other people is greatly appreciated, namely Anina Glumac, Aleksandra Erić, Marko Pavlović and Prof. Rastislav Mandić.

Although the thesis title is followed by a single author, the work presented here is very much due to the efforts and dedication of my promotor and daily supervisor Frans van der Meer. Not only his expertise, but also his conduct with students and colleagues are what make a good work possible. Our weekly meetings and discussions eventually resulted in tackling several interesting problems in mechanics of composites.

Finally, I would like to thank my family for being my support throughout all aspects of life. I am also grateful to my aunt Mira for being there at good and less good moments, although living a long distance apart. At this moment of her battle against a difficult disease, I am sending all the love and support to overcome it.

Dragan

1

INTRODUCTION

Fiber-reinforced polymer (FRP) composites find their application in a wide range of engineering disciplines, where the expected service lifetime may be measured in decades [1]. Owing to their customizable microstructure, FRP composites offer the possibility for a substantial reduction in structural weight compared to metal alternatives, as well as a better corrosion resistance [2]. The emergence of thermoplastic composites opened the space for designing recyclable structures [3], with an improved crack resistance compared to thermoset composites [4]. According to Offringa [5], the cost-effective processing is another reason to use thermoplastics. The opportunity for producing affordable lightweight structures then becomes apparent. However, the inherent time-dependent deformation complicates the straightforward application of polymeric composites in load-bearing situations: *"It is not the question whether failure will occur, but rather on what timescale"* [6]. Furthermore, the long-term behavior of thermoplastic composites is yet to be properly understood. In this regard, a substantial experimental effort was made recently, e.g. [7–9], but a complete characterization of the material is time consuming and expensive [10]. To circumvent this complication, simulation tools come into play as a mean to reduce the number of necessary experiments, help in further understanding the material behavior, and, finally, to design structures of complex geometries.

A computational framework for modeling the nonlinear behavior of solids with evolving discontinuities, based on finite element methodology, is adopted to meet the objective of the thesis: *Develop simulation tools for predicting time- and cycle-dependent failure in unidirectional composites under off-axis loading.* Although the tools can be applied to different types of composites, their development was motivated by the need to understand the time- and cycle-dependent behavior of thermoplastic composites.

1.1. MATRIX FAILURE UNDER OFF-AXIS LOADING

Broadly speaking two types of micromechanical failure modes exist in FRP composites: matrix failure (cracking) and fiber failure [11]. The focus in this thesis is on matrix dominated failure of the material under off-axis loading, such that fibers remain intact during loading. The importance of matrix cracking in composite laminates can be explained with a sketch in Fig. 1.1, where a cross-ply laminate is subjected to uniaxial loading conditions. Progressive failure is started by transverse matrix cracking in off-axis plies. When these cracks reach the interface between two plies, delamination is triggered, yet another form of matrix cracking. Delamination will further propagate until fibers break and catastrophic failure is observed [9]. In this progressive failure process, formation of matrix cracks in off-axis plies is usually the first damage mode to occur in the laminate. Therefore, properly capturing the moment when these cracks form is a precursor to designing damage-tolerant structures.

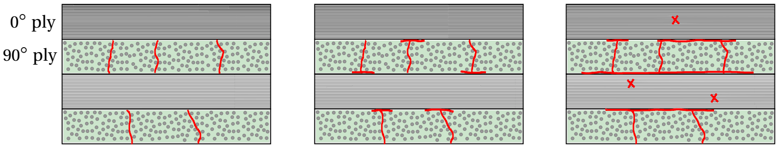

Figure 1.1: Progressive failure of cross-ply laminate; matrix cracking in off-axis plies (left) triggers delamination (middle); delamination propagates until fibers break and catastrophic failure is observed (right)

1.2. REPRESENTATIVE VOLUME ELEMENT

Under the assumption that failure of a representative volume element (RVE) corresponds with macroscopic crack formation, we zoom into the microscale and consider an RVE as a domain to study material failure. The concept of representative volume element is often used in mechanics of heterogeneous materials [12]. The idea behind this approach is to explicitly include material constituents in a (finite element) model. By considering a realistic microstructure, complex material behavior is described with relatively simple constitutive models for the constituents.

Without a proper microscopic insight, understanding or even describing mechanical and physical problems of heterogeneous materials may be excessively difficult. Take, for example, the water diffusion problem in FRP composites, which strongly depends on the material microstructure [13]. Including the experimental observation in a microscale computational framework provides a better insight into all relevant processes and their interaction. With the gained knowledge, formulating a homogeneous constitutive model for the problem at hand becomes an easier task. Another example on the relevance of a realistic microstructure is the effect of viscoplastic deformation in the matrix on composites failure in cyclic loading, a problem dealt with in this thesis. Accurately representing the complex material behavior is not the only advantage of detailed microscale simulations. As it turns out, certain stress states cannot be properly represented by homogeneous constitutive models for composites, when compared with RVE simulations [14].

Several features of composite materials have been investigated through microscale simulations including: stiffness [15], plastic flow [14], strength [16], water diffusion [17] and in-situ effects [18], to name a few. The response of thermoplastic composites under the long-term creep or cyclic loading has not been addressed from this perspective. Also beyond thermoplastic composites, the literature on micromechanical modeling of the long-term response of composites is scarce in general. For example, the creep rupture problem features only one numerical model [19] that uses a unit cell to progressively model the failure process. Govaert et al. [20] proposed a micromechanical model for time-dependent failure of FRP composites under off-axis loading (including creep), that is based on a regular microstructure and a failure criterion in a single integration point of the RVE. As for fatigue, models based on the mean-field homogenization techniques exist [21–23], but those considering more realistic microstructures are rare. The model by Ni et al. [24] considers an example that resembles a composite microstructure loaded in transverse tension in a peridynamics framework. In this paper, crack patterns are discussed for different realizations of the model geometry, together with the number of cycles to failure, but without comparison with experimental data. Two other models with a unit-cell tackle the problem of fatigue in a multiscale framework [25, 26]. In [25], an example of an open-hole laminate under 90° off-axis loading is considered, but without comparison with experimental results. In [26], a multiscale spatio-temporal framework was compared with experiments performed on a quasi-isotropic laminate, in terms of progressive failure events. Rocha et al. [27] introduced an RVE model to represent deformation of a composite material under cyclic loading in transverse tension, together with techniques to accelerate the simulations, but without considering failure.

1.3. KNOWLEDGE GAP

If failure due to molecular degradation is disregarded, two failure regimes can be distinguished in polymeric composites under cyclic loading: plasticity controlled (ductile or low-cycle) and crack growth controlled (brittle or high-cycle) failure regimes [28]. Let us consider experimental data on a unidirectional carbon/PEEK composite system, tested at 90° off-axis angle, different frequencies and the load ratio of 0.1 [9], where the load ratio is defined as:

$$R = \frac{\sigma^{\mathrm{min}}}{\sigma^{\mathrm{max}}} \tag{1.1}$$

σ^{min} and σ^{max} being the minimum and the maximum stress in the experiment, respectively. Depending on the type of plot used to represent fatigue data, the two failure mechanisms show different dependence on the loading frequency. If the applied stress is plotted versus the time to failure

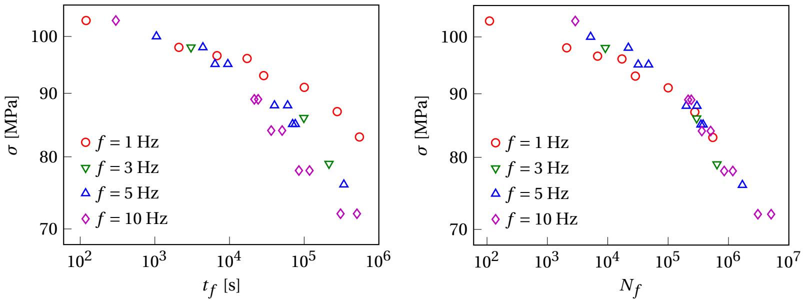

Figure 1.2: Maximum stress applied versus time to failure for carbon/PEEK composite system, tested at 90° off-axis angle, load ratio $R = 0.1$ and different frequencies (left); corresponding number of cycles to failure (right) [9]

in a double logarithmic plot (S-t curve), see Fig. 1.2 (left), the plasticity controlled part is insensitive to the loading frequency and can be approximated with a single line, whereas the crack growth controlled part is frequency-dependent, with the time to failure shortening with an increase in the loading frequency. On the other hand, if the applied stress is plotted versus the cycles to failure in a *loglog* plot (S-N curve), see Fig. 1.2 (right), the plasticity controlled part is frequency-dependent, while the crack growth controlled regime is largely independent of the frequency for $R = 0.1$. It is reported in the literature that frequency dependence of the crack growth controlled failure regime varies with the load ratio. For lower values of R, the response is mostly independent of frequency and can be approximated with a single line in the S-N curve, like in Fig. 1.2 (right). When R increases, the number of cycles to failure in the crack growth controlled regime starts varying significantly with the loading frequency [29]. To further increase the overall complexity, the material response depends on the loading angle and the temperature.

Another important experimental observation is that the two failure regimes show a different trend in the time to failure when switching from static (creep) loading ($R = 1$) to cyclic loading ($R < 1$), e.g. [28]. While for the plasticity controlled failure mechanism the time to failure increases in cyclic loading compared to static loading, the opposite is true for the crack growth controlled failure mechanism, see Fig. 1.3.

As it turns out, there is no computational framework in the literature addressing the described behavior of thermoplastic composites under creep or cyclic loading. Therefore, the *ultimate goal* of this thesis is formulating a computational microscale model capable of simulating long-term time- and cycle-dependent failure of polymeric (thermoplastic) composites.

Additionally, given its relation with creep rupture, strain rate-dependent failure of the material under off-axis loading is another relevant problem deserving attention. In Fig. 1.4, the failure stress of the carbon/PEEK material is plotted versus constant strain rate loading in a *loglog* plot, for two

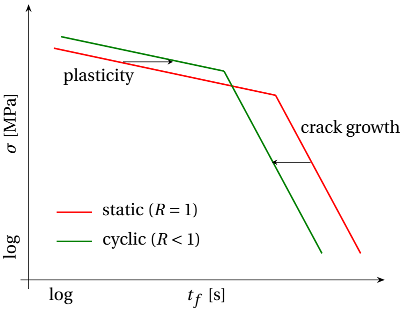

Figure 1.3: Effect of cyclic loading on time to failure for two failure regimes, when compared with static (creep) loading

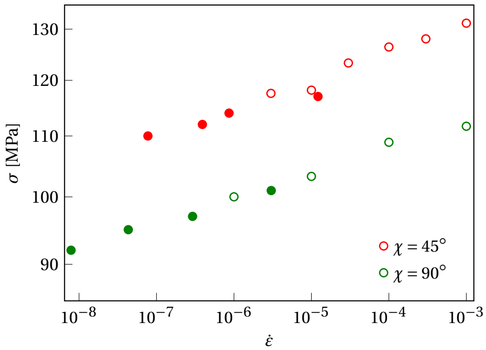

Figure 1.4: Failure stress versus strain rate for two off-axis angles observed experimentally [9]; filled markers represent creep data; empty markers represent constant strain rate data; for creep data, external force was controlled and creep strain rate measured; for strain rate data, stress was measured for the imposed constant strain rate

off-axis angles denoted with χ. In the same plot, the creep stress is plotted versus the minimum creep strain rate observed experimentally for two loading angles [9] (presenting data in a *semilog* plot, with logarithmic scale in the strain rate, would not change the message [30]). It stems from the figure that the failure kinetics are the same for the two loading scenarios (creep and constant strain rate), making it possible to infer one by knowing the other. In other words, the material behavior under the long-term static (creep) loading can be induced from the failure kinetics under constant strain rate loading.

In the literature, the micromodel with a regular microstructure proposed by Govaert et al. [20] estimates the failure state under constant strain rate when the critical plastic strain is reached in an integration point representing the matrix. In this thesis, we propose a micromodel that progressively fails under a constant strain rate.

1.4. COMPUTATIONAL FRAMEWORK

Material failure is simulated on the microscale considering three different loading scenarios: constant strain rate, creep and cyclic loading, see Fig. 1.5. In all cases, unidirectional composite material is subjected to uniaxial loading under an off-axis angle $\chi = 90° - \theta_0$, θ_0 being the initial angle between the global x-axis and the fiber direction.

The micromodel is a thin slice 3D RVE defined in the local frame aligned with the fiber reinforcement, see Figs. 1.5 and 1.6, such that complex stress states under off-axis loading may be represented within the numerical model. Homogenized stresses on the RVE faces in Fig. 1.6, correspond with the stress in the global loading direction, see Fig. 1.5. To mimic the effect of the surrounding material, periodic boundary conditions are imposed on the RVE [14]. With the focus on matrix dominated failure, carbon fibers are represented with a hyperelastic transversely isotropic material model [31].

According to Argon [32], nonlinear processes preceding matrix cracking can be divided in plas-

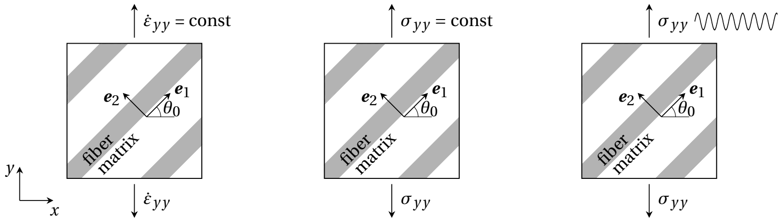

Figure 1.5: Unidirectional composite material subjected to different loading scenarios under off-axis angle $\chi = 90° - \theta_0$

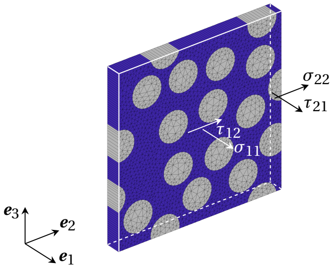

Figure 1.6: 3D RVE model, with periodic boundary conditions, defined in local coordinate frame aligned with reinforcement; homogenized stresses on RVE faces correspond to stress in global loading direction, see Fig. 1.5

ticity (shear yielding) which corresponds to a ductile response of a polymer material, and crazing that causes a brittle response and further develops in a crack growth process. For a proper computational representation of matrix failure, it is desirable to account for both processes in the RVE.

When it comes to plastic deformation in solids, one may think of a constitutive model with a yield surface that evolves under certain loading conditions [33]. A model of that kind has been proposed by Melro et al. [34], and is often used to describe the inelastic response of polymers in composites. An alternative also exists, several models in the literature are based on the Eyring flow theory [35], and the work of Haward and Thackray [36], who proposed that the mechanical response of glassy polymers is governed by two contributions that originate from deforming different parts of the molecular structure. The first one gives rise to the viscous pre-yield and yield response of the material. It is represented with an Eyring-based viscosity function that evolves with the stress applied, eventually leading to the viscoplastic flow of the material. The second component becomes dominant in the post-yield regime which goes up to large strains. This contribution is due to the reorientation of the entangled network and represents the hardening stress. Models following this idea have been formulated in different research groups [37–39]. As one of these models, the Eindhoven Glassy Polymer (EGP) model is used in this thesis to represent deformation of the matrix under different loading and temperature conditions [39].

By means of cohesive zone modeling [40], microcracking of the matrix is also included in the RVE. Inter-element cohesive segments are added on the fly [41], when a suitable initiation criterion is satisfied, after which an appropriate cohesive model governs evolution of cohesive microcracks. This nonlinear process certainly relates to crazing in polymers that is also sensitive to the hydrostatic stress [42]. However, in the cohesive initiation criterion we do not consider the effect of hydrostatic stress. Except for Chapter 4, where the initiation criterion is energy-based, a critical combination of traction components on a potential cohesive surface determines the moment of initiation. With the matrix dominated failure in mind, cohesive segments may initiate along finite element edges representing the matrix or the fiber/matrix interface.

Although much of the nonlinearity in the homogenized RVE response comes from viscoplastic deformation of the matrix, the micromodel eventually fails due to evolution of cohesive microcracks through the RVE. This fact is supported with an example in which the RVE is loaded under different off-axis angles at the strain rate $\dot{\varepsilon}_{yy} = 10^{-4}$/s, see Fig. 1.7, where stress-strain curves obtained from the simulations including cohesive microcracks and without them are shown [43]. As observed from the figure, the homogenized response without microcracks shows the tendency of monotonic hardening, making it difficult to determine the failure point. On the other hand, the RVE with evolving cohesive zones eventually enters the softening phase with a clear post-peak response, whose onset is taken as the failure point in the considered examples.

Adding cohesive segments to the RVE is not the only way to drive the RVE towards the failure state. Smeared modeling of microcracking is also possible, that is based on principles of continuum damage mechanics [44]. This approach would require regularization of the degradation process inside a bulk constitutive model, e.g. [45, 46]. Phase-field modeling is another option to

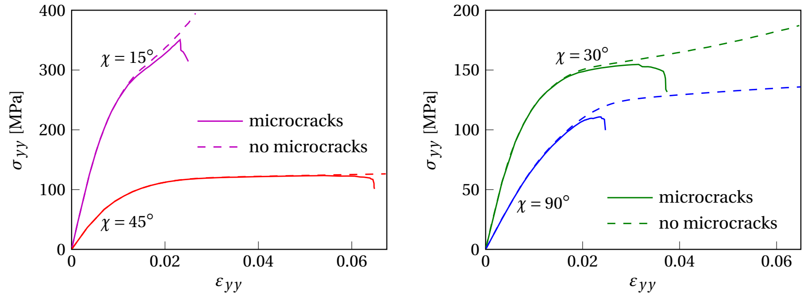

Figure 1.7: Stress-strain curves at $\dot{\varepsilon}_{yy} = 10^{-4}$/s, obtained from the model with and without cohesive microcracks; onset of softening taken as failure point in simulations [43]; examples without cohesive microcracks display monotonic hardening

account for relevant degradation processes in the matrix in a regularized way [47].

Another route to define failure of the RVE, without including any additional process beside plasticity in the matrix, is also possible. For example, one can define a critical combination of homogenized stress measures like the hydrostatic stress and the Von Mises stress and declare it as the failure state. In that scenario, the simulation would still be able to run past the declared failure state, which would be defined at some point along the dashed lines in Fig. 1.7.

1.5. THESIS OUTLINE

Before trying to simulate failure of the material under certain loading scenario, it was necessary to formulate a model to impose off-axis loading on the RVE, assuming finite homogenized deformations of the micromodel. In *Chapter 2*, a strain rate-based arclength model is presented to impose a constant (true) strain rate on the RVE, that allows for reorientation of the microstructure in the loading process.

In *Chapter 3*, failure of the material under constant strain rate is studied, where the RVE model from Chapter 2 is supplemented with a cohesive zone model. Special care is dedicated to derive kinematical and stress relations for the cohesive model in 3D, accounting for geometric nonlinearity as well [48]. A direct application of a quasi-static cohesive model leads to an inaccurate prediction of failure, indicating that some aspect of the cohesive model (maximum traction, fracture energy) needs to be rate-dependent. Since making the fracture energy rate-dependent did not lead to sufficiently good results, an approach where the maximum traction depends on the local rate of deformation was followed. An alternative, where both the fracture energy and the maximum traction are rate-dependent, is also possible, but was not investigated in the thesis. The model results are compared with experimental data on carbon/PEEK thermoplastic composites tested at different strain rates and off-axis angles.

In *Chapter 4*, a model to simulate creep rupture of the material under off-axis loading is presented. Referring to the statement about polymeric materials: *"It is not the question whether failure will occur, but rather on what timescale"*[6], the question of a proper cohesive initiation criterion arises. It is clear that working with the quasi-static strength would preclude a large range of stresses from possible creep rupture. Therefore, a more general initiation criterion is introduced in Chapter 4, that is energy-based: a cohesive segment initiates when the total free energy in the bulk material reaches a critical value. However, to reach a reasonable agreement with experimental results, an auxiliary condition checking for a certain ratio between the free energy components was necessary. A quasi-static cohesive model is supplemented with a viscous degradation tensor to achieve decay of the stress on a cohesive surface in creep loading. The addition of another failure mechanism in the cohesive zone was necessary to achieve failure within the timescale that was experimentally observed.

In *Chapter 5*, the model developed in the previous chapter is adjusted to account for cyclic variation of the applied stress, and failure due to off-axis fatigue loading is studied. To properly account for viscous deformation in the matrix under cyclic loading, a two-scale EGP model is formulated and combined with a two-scale time stepping scheme, proposed to efficiently traverse the loading signal. Dávila's fatigue cohesive model [49] is used for microcracking of the matrix, together with an endurance limit-based cohesive initiation criterion [50]. The model addresses frequency dependence of the plasticity controlled and crack growth controlled failure mechanisms, and is tested against experimental observations. As a limit case when $R = 1$, the model accurately predicts the time to failure in creep loading.

Finally, *Chapter 6* includes concluding remarks and future perspectives.

Since Chapters 2-5 represent already published (or submitted) journal papers, the reader will notice the repetition of some content.

REFERENCES

[1] Brinson HF. Matrix dominated time dependent failure predictions in polymer matrix composites. *Compos Struct*, 47 (1-4), 1999, pp. 445–456. DOI: `10.1016/S0263-8223(00)00075-1`.

[2] Alderliesten R. *Introduction to aerospace structures and materials*. Delft University of Technology, 2018.

[3] Teltschik J et al. Review on recycling of carbon fibre reinforced thermoplastics with a focus on polyetheretherketone. *Composites A*, 2024, p. 108236. DOI: `10.1016/j.compositesa.2024.108236`.

[4] Danzi F et al. Longitudinal failure mechanisms and crack resistance curves of unidirectional thermoplastic composites. *Eng Fract Mech*, 282, 2023, p. 109147. DOI: `10.1016/j.engfracmech.2023.109147`.

[5] Offringa AR. Thermoplastic composites—rapid processing applications. *Composites A*, 27 (4), 1996, pp. 329–336. DOI: `10.1016/1359-835X(95)00048-7`.

[6] Kanters M. Prediction of long-term performance of load-bearing thermoplastics. PhD thesis. Eindhoven, The Netherlands: Technische Universiteit Eindhoven, 2015.

[7] Pastukhov L. Long-term performance of fibre-reinforced thermoplastics. PhD thesis. Eindhoven, The Netherlands: Technische Universiteit Eindhoven, 2019.

[8] Erartsin O. Matrix dominated, time-dependent failure of continuous fiber-reinforced thermoplastic composites. PhD thesis. Enschede, The Netherlands: University of Twente, 2020. DOI: `10.3990/1.9789036549929`.

[9] Sundararajan BK. Matrix dominated failure in continuous carbon fibre reinforced poly(ether ether ketone). PhD thesis. Enschede, The Netherlands: University of Twente, 2024. DOI: `10.3990/1.9789036560405`.

[10] Dávila CG. From S-N to the Paris law with a new mixed-mode cohesive fatigue model for delamination in composites. *Theor Appl Fract Mech*, 106, 2020, p. 102499. DOI: `10.1016/j.tafmec.2020.102499`.

[11] Wisnom MR, Hallett SR. The role of delamination in strength, failure mechanism and hole size effect in open hole tensile tests on quasi-isotropic laminates. *Composites A*, 40 (4), 2009, pp. 335–342. DOI: `10.1016/j.compositesa.2008.12.013`.

[12] Gitman IM, Askes H, Sluys LJ. Representative volume: Existence and size determination. *Eng Fract Mech*, 74 (16), 2007, pp. 2518–2534. DOI: `10.1016/j.engfracmech.2006.12.021`.

[13] Rocha I et al. Combined experimental/numerical investigation of directional moisture diffusion in glass/epoxy composites. *Compos Sci Technol*, 151, 2017, pp. 16–24. DOI: `10.1016/j.compscitech.2017.08.002`.

[14] Van der Meer FP. Micromechanical validation of a mesomodel for plasticity in composites. *Eur J Mech A Solids*, 60, 2016, pp. 58–69. DOI: `10.1016/j.euromechsol.2016.06.008`.

[15] Melro AR, Camanho PP, Pinho ST. Influence of geometrical parameters on the elastic response of unidirectional composite materials. *Compos Struct*, 94 (11), 2012, pp. 3223–3231. DOI: `10.1016/j.compstruct.2012.05.004`.

[16] Totry E, González C, LLorca J. Failure locus of fiber-reinforced composites under transverse compression and out-of-plane shear. *Compos Sci Technol*, 68 (3), 2008, pp. 829–839. DOI: `10.1016/j.compscitech.2007.08.023`.

[17] Rocha IBCM, Van der Meer FP, Nijssen RPL, Sluys LJ. A multiscale and multiphysics numerical framework for modelling of hygrothermal ageing in laminated composites. *Int J Numer Methods Eng*, 112 (4), 2017, pp. 360–379. DOI: `10.1002/nme.5542`.

[18] Arteiro A et al. Micro-mechanical analysis of the in situ effect in polymer composite laminates. *Compos Struct*, 116, 2014, pp. 827–840. DOI: `10.1016/j.compstruct.2014.06.014`.

[19] Gal E, Fish J. Anisotropic micromechanical creep damage model for composite materials: a reduced-order approach. *Int J Mult Comp Eng*, 6 (2), 2008, pp. 113–121. DOI: `10.1615/IntJMultCompEng.v6.i2.10`.

[20] Govaert LE et al. A micromechanical approach to time-dependent failure in off-axis loaded polymer composites. *Composites A*, 32 (12), 2001, pp. 1697–1711. DOI: `10.1016/S1359-835X(01)00028-8`.

[21] Reifsnider KL, Gao Z. A micromechanics model for composites under fatigue loading. *Int J Fatigue*, 13 (2), 1991, pp. 149–156. DOI: `10.1016/0142-1123(91)90007-L`.

[22] Hessman PA, Welschinger F, Hornberger K, Böhlke T. A micromechanical cyclic damage model for high cycle fatigue failure of short fiber reinforced composites. *Composites B*, 264, 2023, p. 110855. DOI: `10.1016/j.compositesb.2023.110855`.

[23] Mohammadi B et al. Damage-entropy model for fatigue life evaluation of off-axis unidirectional composites. *Compos Struct*, 270, 2021, p. 114100. DOI: `10.1016/j.compstruct.2021.114100`.

[24] Ni T, Zaccariotto M, Galvanetto U. A peridynamic approach to simulating fatigue crack propagation in composite materials. *Proc R Soc A*, 381 (2240), 2023, p. 20210217. DOI: `10.1098/rsta.2021.0217`.

[25] Fish J, Yu Q. Computational mechanics of fatigue and life predictions for composite materials and structures. *Comput Methods Appl Mech Eng*, 191 (43), 2002, pp. 4827–4849. DOI: `10.1016/S0045-7825(02)00401-2`.

[26] Crouch R, Oskay C, Clay S. Multiple spatio-temporal scale modeling of composites subjected to cyclic loading. *Comput Mech*, 51 (1), 2013, pp. 93–107. DOI: `10.1007/s00466-012-0707-9`.

[27] Rocha IBCM, Van der Meer FP, Sluys LJ. Efficient micromechanical analysis of fiber-reinforced composites subjected to cyclic loading through time homogenization and reduced-order modeling. *Comput Methods Appl Mech Eng*, 345, 2019, pp. 644–670. DOI: `10.1016/j.cma.2018.11.014`.

[28] Kanters MJW, Kurokawa T, Govaert LE. Competition between plasticity-controlled and crack-growth controlled failure in static and cyclic fatigue of thermoplastic polymer systems. *Polym Test*, 50, 2016, pp. 101–110. DOI: `10.1016/j.polymertesting.2016.01.008`.

[29] Kanters MJW, Engels TAP, Van Erp TB, Govaert LE. Predicting long-term crack growth dominated static fatigue based on short-term cyclic testing. *Int J Fatigue*, 112, 2018, pp. 318–327. DOI: `10.1016/j.ijfatigue.2018.03.011`.

[30] Govaert LE, Van der Vegt AK, Van Drongelen M. *Polymers: From Structure to Properties*. Delft: Delft Academic Press, 2019.

[31] Bonet J, Burton AJ. A simple orthotropic, transversely isotropic hyperelastic constitutive equation for large strain computations. *Comput Methods Appl Mech Eng*, 162 (1), 1998, pp. 151–164. DOI: `10.1016/S0045-7825(97)00339-3`.

[32] Argon AS. *The physics of deformation and fracture of polymers*. Cambridge University Press, 2013.

[33] Ibrahimbegovic A. *Nonlinear solid mechanics: theoretical formulations and finite element solution methods*. Vol. 160. Springer Science & Business Media, 2009.

[34] Melro AR, Camanho PP, Andrade Pires FM, Pinho ST. Micromechanical analysis of polymer composites reinforced by unidirectional fibres: Part I – Constitutive modelling. *Int J Solids Struct*, 50 (11), 2013, pp. 1897–1905. DOI: `10.1016/j.ijsolstr.2013.02.009`.

[35] Eyring H. Viscosity, plasticity, and diffusion as examples of absolute reaction rates. *J Chem Phys*, 4 (4), 1936, pp. 283–291. DOI: `10.1063/1.1749836`.

[36] Haward RN, Thackray G. The use of a mathematical model to describe isothermal stress-strain curves in glassy thermoplastics. *Proc R Soc A*, 302 (1471), 1968, pp. 453–472. DOI: `10.1098/rspa.1968.0029`.

[37] Boyce MC, Parks DM, Argon AS. Large inelastic deformation of glassy polymers. part I: rate dependent constitutive model. *Mech Mater*, 7 (1), 1988, pp. 15–33. DOI: `10.1016/0167-6636(88)90003-8`.

[38] Buckley CP, Jones DC. Glass-rubber constitutive model for amorphous polymers near the glass transition. *Polymer*, 36 (17), 1995, pp. 3301–3312. DOI: `10.1016/0032-3861(95)99429-X`.

[39] Van Breemen LCA, Klompen ETJ, Govaert LE, Meijer HEH. Extending the EGP constitutive model for polymer glasses to multiple relaxation times. *J Mech Phys Solids*, 59 (10), 2011, pp. 2191–2207. DOI: `10.1016/j.jmps.2011.05.001`.

[40] Ortiz M, Pandolfi A. Finite-deformation irreversible cohesive elements for three-dimensional crack-propagation analysis. *Int J Numer Methods Eng*, 44 (9), 1999, pp. 1267–1282. DOI: `10.1002/(SICI)1097-0207(19990330)44:9<1267::AID-NME486>3.0.CO;2-7`.

[41] Camacho GT, Ortiz M. Computational modelling of impact damage in brittle materials. *Int J Solids Struct*, 33 (20), 1996, pp. 2899–2938. DOI: `10.1016/0020-7683(95)00255-3`.

[42] Tijssens MGA, van der Giessen E, Sluys LJ. Modeling of crazing using a cohesive surface methodology. *Mech Mater*, 32 (1), 2000, pp. 19–35. DOI: `10.1016/S0167-6636(99)00044-7`.

[43] Kovačević D, Sundararajan BK, Van der Meer FP. Microscale modeling of rate-dependent failure in thermoplastic composites under off-axis loading. *Eng Fract Mech*, 276, 2022, p. 108884. DOI: `10.1016/j.engfracmech.2022.108884`.

[44] Krajcinovic D. Damage mechanics. *Mech Mater*, 8 (2), 1989, pp. 117–197. DOI: `10.1016/0167-6636(89)90011-2`.

[45] Bažant ZP, Oh BH. Crack band theory for fracture of concrete. *Mat Constr*, 16 (3), 1983, pp. 155–177. DOI: `10.1007/BF02486267`.

[46] Peerlings RHJ, De Borst R, Brekelmans WaM, Geers MGD. Gradient-enhanced damage modelling of concrete fracture. *Mech Cohesive-frict Mater*, 3 (4), 1998, pp. 323–342. DOI: `10.1002/(SICI)1099-1484(1998100)3:4<323::AID-CFM51>3.0.CO;2-Z`.

[47] Macías J et al. Micro-mechanical analysis of composite materials using Phase-Field models of brittle fracture. *Eur J Mech A Solids*, 102, 2023, p. 105069. DOI: `10.1016/j.euromechsol.2023.105069`.

[48] Reinoso J, Paggi M. A consistent interface element formulation for geometrical and material nonlinearities. *Comput Mech*, 54 (6), 2014, pp. 1569–1581. DOI: `10.1007/s00466-014-1077-2`.

[49] Dávila CG, Camanho PP, Rose CA. Failure Criteria for FRP Laminates. *J Compos Mater*, 39 (4), 2005, pp. 323–345. DOI: `10.1177/0021998305046452`.

[50] Hofman P, Van der Meer FP, Sluys LJ. A numerical framework for simulating progressive failure in composite laminates under high-cycle fatigue loading. *Eng Fract Mech*, 295, 2024, p. 109786. DOI: `10.1016/j.engfracmech.2023.109786`.

2

STRAIN RATE-BASED ARCLENGTH MODEL

2.1. INTRODUCTION

Continuous fiber reinforced composites are used in many load-carrying applications where structural reliability is of great importance. The ability to accurately predict the mechanical response of the material for different loading scenarios is essential in the optimal process of design and maintenance of those structures. In last decades the concept of the Representative Volume Element (RVE) has been used frequently to study the mechanics of heterogeneous materials on a scale of observation finer than the macroscopic scale. Several features of composite materials have been investigated through such microscale simulations. Melro et al. [2] analyzed elastic properties of composites that differ from the properties of the individual constituents. Van der Meer [3] compared the behavior of a homogenized orthotropic plasticity model for fiber reinforced composites with that of an RVE with plastic matrix and elastic fibers. Totry et al. [4] calculated the strength of a composite lamina for different loading scenarios. In [5] Rocha et al. studied hygrothermal ageing in laminated composites in a multiscale FE^2 framework. The in-situ effect in polymer composite laminates has been investigated by Arteiro et al. [6]. Naya et al. [7] included environmental conditions, such as temperature and humidity, in predicting stiffness and strength properties of one ply. In a multiscale approach, Govaert et al. [8] modeled the rate-dependent off-axis strength of unidirectional (UD) laminates.

Even though many features of UD composites can be studied on two-dimensional (2D) RVE, modeling of stress states that arise in off-axis testing requires formulation in 3D space because of the presence of stress in fiber direction and longitudinal shear stress. The aim of this work is to develop a micromechanical framework that accommodates geometric and material nonlinear analysis of UD composites exposed to uniaxial loading at a predefined strain rate, with an arbitrary orientation of the reinforcement with respect to the loading direction, i.e., different off-axis angles. The framework is designed for the RVE of a thin slice of fiber reinforced composite material that is oriented perpendicular to the direction of the reinforcement. By using a thin slice, excessive computational costs that would be associated with a full 3D RVE with geometric representation of the off-axis fibers are avoided. The challenge addressed in this work is to satisfy the requirement that the deformation and stress state of the RVE, in its local coordinate frame, are equivalent to the state of the lamina in the global coordinate system of the off-axis experiment. The exact solution to this problem demands control over the update in nodal displacements of the RVE, which determines the strain rate in the global frame of reference. Also, it requires control over the external load level on the RVE, which is related to the uniaxial stress state in the global frame. Because of the requirement to simultaneously control both the displacements and the load level in the analysis, an arclength control formulation is pursued.

Arclength control methods stem from the work of Wempner [9] and Riks [10]. In order to solve the problem of snap-back or snap-through behavior that may arise in a structural analysis, Riks added an auxiliary equation with a path following constraint to the existing set of equations. This framework is versatile in the sense that an arbitrary constraint can be defined. Initially the constraint equation was mostly based on a proper geometrical combination of norms of the nodal displacements and load increment. It was realized by De Borst [11] that the constraint equation which includes all nodal degrees of freedom cannot be successfully applied to strain-softening problems, but that specific degrees of freedom can be selected to control the crack opening displacement. A more general solution that does not require a priori information on where the localization will

---

Apart from minor text adjustments, this chapter was reproduced from [1].

take place, introduced by Gutiérrez [12], is a constraint based on the global energy release rate in the framework of a geometrically linear continuum damage model, which was foundation for the class of dissipation based arclength models. This idea was later extended by Verhoosel et al. [13] to account for geometrically linear plasticity and geometrically nonlinear damage. Van der Meer et al. [14] extended the constraint equation to account also for the presence of thermal strains in the dissipation process. A common element among all mentioned arclength formulations is that they work with a fixed unit load vector and a predefined constraint equation. For off-axis loading at constant strain rate on an RVE, such unit force vector and constraint can also be defined, depending on the mapping between local and global coordinates. In geometric nonlinear context which is relevant for shear loading of polymer composites, however, this mapping will change as a consequence of deformations.

In this study a strain rate-based arclength model is proposed. The constraint equation is constructed such that the deformation pattern of the RVE satisfies that the strain rate in the global loading direction equals a prescribed value. To exactly capture the finite strains, the orientation of the RVE is updated, followed by a change in the unit force vector applied in the arclength method. Closed-form expressions for the unit force components are derived.

In the next section, the formulation for the strain rate-based arclength model is presented, first accounting for geometric nonlinear effects in a general nonlinear framework, and then reduced to a small strain version. After that, the Eindhoven Glassy Polymer (EGP) constitutive law that is used for the bulk (matrix) part of the composite material is introduced. Then a transversely isotropic material model is presented to simulate the response of the reinforcement - in this study carbon fibers. Subsequently the model is validated through examples on the rate-dependent isotropic material (EGP) and the transversely isotropic material. Eventually the off-axis response of a fiber reinforced composite material with thermoplastic matrix is simulated to demonstrate the envisioned use case of the proposed model.

2.2. FORMULATION

2.2.1. PROBLEM STATEMENT

A composite material with unidirectional reinforcement is subjected to a constant strain rate $\dot{\varepsilon}_{yy}$ at uniaxial stress conditions, Fig. 2.1 (left). The uniaxial loading will make the material undergo the deformation shown in Fig. 2.1 (middle). Finite strains are allowed to take place, meaning that the local coordinate frame aligned with the fibers changes orientation from the initial angle θ_0 to a new angle θ_1. Given the angle θ_1, transformation of the stress state from global to local frame of reference results in the Cauchy stress components shown in Fig. 2.1 (right). We aim to simulate this experiment with an RVE that is a 3D slice with random fiber distribution and periodic boundary conditions [3], picked from the composite lamina, where one axis of the RVE is aligned with the reinforcement direction, Fig. 2.2. The implementation of periodic boundary conditions is explained in the Appendix. Unlike a 2D RVE in the plane perpendicular to the fibers, the 3D slice enables representation of the stress state that is encountered in the off-axis loading of composites.

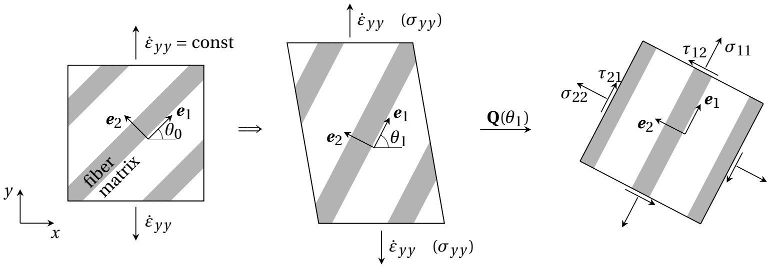

Figure 2.1: Strain rate imposed on unidirectional composite material (left); deformed material due to uniaxial loading (middle); Cauchy stresses in local coordinate system (right)

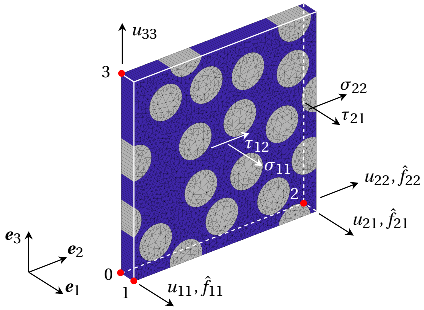

Figure 2.2: RVE with active displacements u_{ij} and applied unit force components $\hat{f}_{ij}$ on master nodes 0, 1, 2, 3

The kinematic relations between microscopic displacements and homogenized strain are calculated numerically, following displacements of the master nodes of the RVE. Displacement components of the master nodes not indicated in Fig. 2.2 are set to zero. Master node 0 is fixed to prevent rigid-body translations. It should be noted that we are not applying a macroscopic strain tensor on the RVE to define Dirichlet boundary conditions, in which case rigid-body rotations would be a priori prevented. Contrary to this, we are imposing forces on the RVE as part of the arclength methodology. Hence, it is necessary to fix three more degrees of freedom to prevent rigid-body rotations. Fixing master node 1 in $\boldsymbol{e}_2$ and $\boldsymbol{e}_3$ directions ensures that the fibers remain oriented in $\boldsymbol{e}_1$ direction. The vector $\boldsymbol{e}_2$ remains perpendicular to $\boldsymbol{e}_1$ and therefore does not necessarily stay parallel to the line between master nodes 0 and 2.

The formulation of the model is derived such that the deformation pattern and stress state of the RVE in the local frame of reference are equivalent to the global state of deformation and stress in the lamina, see Fig. 2.1. With the proposed model it is possible to analyze UD composite systems on the microlevel, accounting for different orientations of the reinforcement and a predefined strain rate, while using the same initial geometry of the RVE. The derived model is valid for both tension and compression. Furthermore, the framework is independent of the material model applied to represent nonlinear processes in the composite constituents. Beside capturing the rate-dependent (visco-plastic) effects in the material, it is also possible to include damage mechanisms in the RVE model. For example, a cohesive surface methodology or a smeared crack model can be applied to represent degradation in the material. However, not all failure mechanisms may be represented by the thin slice RVE. The case of fiber kinking or fiber pull-out would require a longer piece of material to capture longitudinal variations in the fiber deformation and, therefore, cannot be simulated with the proposed model.

In the following, the general nonlinear framework of the model is introduced. Afterwards, the small strain version of the model that is simpler to implement is presented. In the numerical examples, the loss in accuracy when using the small strain version will be assessed.

2.2.2. ARCLENGTH CONTROL METHOD

The discrete equilibrium equation of the RVE, in the absence of cracks and body forces, can be written in Voigt notation as follows:

$$\int_{\Omega} \mathbf{B}^{\mathrm{T}}(\mathbf{a})\boldsymbol{\sigma}(\mathbf{a})\,d\Omega = \int_{\Gamma_t} \mathbf{N}^{\mathrm{T}}\mathbf{t}_{\mathrm{p}}\,d\Gamma \tag{2.1}$$

where $\mathbf{B}$ is the strain - nodal displacement matrix, $\boldsymbol{\sigma}$ is the Cauchy stress, $\mathbf{N}$ is the shape function matrix, $\mathbf{t}_{\mathrm{p}}$ is the prescribed external traction, and $\mathbf{a}$ is the vector of nodal displacements. The left hand side of this equation represents the internal nodal force vector $\mathbf{f}_{\mathrm{int}}$, whereas the right hand side stands for the external force vector $\mathbf{f}_{\mathrm{ext}}$, leading to:

$$\mathbf{f}_{\mathrm{int}}(\mathbf{a}) = \mathbf{f}_{\mathrm{ext}}(\mathbf{a}) \tag{2.2}$$

In the light of the arclength control method, $\mathbf{f}_{\text{ext}}$ is written as the product of the load factor λ and the unit force vector $\hat{\mathbf{f}}$:

$$\mathbf{f}_{\text{ext}}(\mathbf{a}) = \lambda\hat{\mathbf{f}}(\mathbf{a}) \tag{2.3}$$

In the present case, the vector $\hat{\mathbf{f}}$ depends on the deformation state and, therefore, is a function of the nodal displacements. With periodic boundary conditions implemented as linear constraints, the right hand side vector of Eq. (2.1) translates to a force vector with nonzero values on the entries associated with the master nodes as shown in Fig. 2.2.

The system of equations (2.2) consists of N equations and counts $N+1$ unknowns (N nodal displacements plus the load factor λ), rendering the system indeterminate. In order to solve this issue, a path following constraint equation is added, which in the general case has the form:

$$g(\mathbf{a},\lambda,\tau) = 0 \tag{2.4}$$

where τ is an arclength parameter that defines the calculation step size. The combination of Eqs. (2.2)-(2.4) forms the augmented system of equations:

$$\begin{bmatrix} \mathbf{f}_{\text{int}} - \lambda\hat{\mathbf{f}} \\ g \end{bmatrix} = \begin{bmatrix} \mathbf{0} \\ 0 \end{bmatrix} \tag{2.5}$$

This system is solved for the unknown nodal displacements and the load factor λ following the linearized Newton-Raphson procedure:

$$\begin{bmatrix} \mathbf{f}_{\text{int},j} + \frac{\partial \mathbf{f}_{\text{int}}}{\partial \mathbf{a}} d\mathbf{a}_{j+1} - \lambda_j\hat{\mathbf{f}} - d\lambda_{j+1}\hat{\mathbf{f}} \\ g_j + \left(\frac{\partial g}{\partial \mathbf{a}}\right)^{\mathrm{T}} d\mathbf{a}_{j+1} + \left(\frac{\partial g}{\partial \lambda}\right) d\lambda_{j+1} \end{bmatrix} = \begin{bmatrix} \mathbf{0} \\ 0 \end{bmatrix} \tag{2.6}$$

The solution at iteration $j+1$ is obtained by solving:

$$\begin{bmatrix} \mathbf{K} & -\hat{\mathbf{f}} \\ \mathbf{h}^{\mathrm{T}} & s \end{bmatrix} \begin{bmatrix} d\mathbf{a}_{j+1} \\ d\lambda_{j+1} \end{bmatrix} = \begin{bmatrix} \mathbf{r}_j \\ -g_j \end{bmatrix} \tag{2.7}$$

where the tangent stiffness of the system $\mathbf{K}$, vector $\mathbf{h}$, scalar s and the residual force vector $\mathbf{r}_j$ at iteration j are defined as:

$$\mathbf{K} = \frac{\partial \mathbf{f}_{\text{int}}}{\partial \mathbf{a}}, \mathbf{h} = \frac{\partial g}{\partial \mathbf{a}}, s = \frac{\partial g}{\partial \lambda}, \quad \mathbf{r}_j = \lambda_j\hat{\mathbf{f}} - \mathbf{f}_{\text{int},j} \tag{2.8}$$

In this chapter a two-stage solution procedure, first introduced by Ramm [15] and Crisfield [16], and later elaborated by De Borst et al. [17], is used to update the unknown variables. At iteration $j+1$ the partial contributions to the nodal displacements are calculated as:

$$\begin{aligned} d\mathbf{a}^{\mathrm{I}}_{j+1} &= \mathbf{K}^{-1}\hat{\mathbf{f}} \\ d\mathbf{a}^{\mathrm{II}}_{j+1} &= \mathbf{K}^{-1}\mathbf{r}_j \end{aligned} \tag{2.9}$$

Eq. (2.9) is followed by calculating an iterative increment to the load factor:

$$d\lambda_{j+1} = -\frac{g_j + \mathbf{h}^{\mathrm{T}} d\mathbf{a}^{\mathrm{II}}_{j+1}}{s + \mathbf{h}^{\mathrm{T}} d\mathbf{a}^{\mathrm{I}}_{j+1}} \tag{2.10}$$

to finally get the total iterative contribution to the nodal displacements:

$$d\mathbf{a}_{j+1} = d\lambda_{j+1} d\mathbf{a}^{\mathrm{I}}_{j+1} + d\mathbf{a}^{\mathrm{II}}_{j+1} \tag{2.11}$$

In Eq. (2.6) it is assumed that $\partial\hat{\mathbf{f}}/\partial\mathbf{a} = \mathbf{0}$, while in the present case the unit force vector does become a function of the deformation. In order to keep optimal convergence, while avoiding further complications in the formulation, the unit force vector $\hat{\mathbf{f}}$ is only updated at the beginning of the time step, i.e.:

$$\hat{\mathbf{f}}^n = \hat{\mathbf{f}}(\mathbf{a}^{n-1}) \tag{2.12}$$

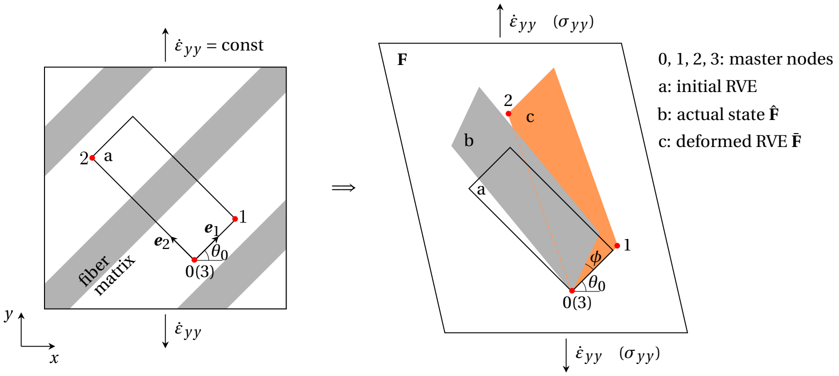

Figure 2.3: RVE picked from composite lamina such that one side is parallel to the reinforcement (left); deformed RVE present in simulation and actual state it is in due to the applied loading (right)

2.2.3. ARCLENGTH CONSTRAINT EQUATION

The constraint equation of the model is derived from a relation between the RVE deformation gradient in the local coordinate system $\bar{\mathbf{F}}$ and the deformation gradient of the UD composite material in the global frame $\mathbf{F}$. To this end, the RVE with periodic boundary conditions, whose initial orientation with respect to the global $x-$axis defines the angle θ_0, is picked from the composite lamina, see Fig. 2.3 (left) for top view and Fig. 2.2 for 3D view. Due to the applied loading, the initial RVE denoted by the shape "a" will deform into the shape "b" defined by the deformation gradient $\hat{\mathbf{F}}$ in the original local frame, Fig. 2.3 (right). The deformation gradient $\hat{\mathbf{F}}$ describes the exact same deformation as the global deformation gradient $\mathbf{F}$. The two are related through a transformation operation as:

$$\hat{\mathbf{F}} = \mathbf{Q}_0\mathbf{F}\mathbf{Q}_0^{\mathrm{T}} \tag{2.13}$$

where the transformation matrix $\mathbf{Q}_0$ reads:

$$\mathbf{Q}_0 = \begin{bmatrix} \cos(\theta_0) & \sin(\theta_0) & 0 \\ -\sin(\theta_0) & \cos(\theta_0) & 0 \\ 0 & 0 & 1 \end{bmatrix} \tag{2.14}$$

A simulation performed on the RVE should resemble this actual deformation state. In the actual state of shape "b" it can be observed that the vector $\boldsymbol{e}_1$ that is tied to the RVE edge 0-1 rotates with an angle ϕ. However, inside the RVE, this rotation is by definition of the boundary conditions not described[1]. In order to relate the homogenized stresses in the RVE simulation to the stress in global frame, the magnitude of the rotation ϕ needs to be determined from the RVE simulation. This is achieved by considering that the RVE present in the simulation is in shape "c", with deformation gradient $\bar{\mathbf{F}}$, see Fig. 2.3 (right). The deformation gradient $\bar{\mathbf{F}}$ is then related to the actual state $\hat{\mathbf{F}}$ by a rigid rotation:

$$\hat{\mathbf{F}} = \mathbf{R}(\phi)\bar{\mathbf{F}} \tag{2.15}$$

where the rotation tensor $\mathbf{R}$ has the following form:

$$\mathbf{R} = \begin{bmatrix} \cos(\phi) & -\sin(\phi) & 0 \\ \sin(\phi) & \cos(\phi) & 0 \\ 0 & 0 & 1 \end{bmatrix} \tag{2.16}$$

---

[1] An assumption that the master node 2 does not move in the local direction 1, while the node 1 moves in the direction 2, would result in different expressions for the RVE kinematics, but the overall simulation results would be the same if a derivation similar to the one outlined here is followed.

With the imposed Dirichlet boundary conditions and active displacements shown in Fig. 2.2, the homogenized deformation gradient of the RVE is:

$$\bar{\mathbf{F}} = \begin{bmatrix} \bar{F}_{11} & \bar{F}_{12} & 0 \\ 0 & \bar{F}_{22} & 0 \\ 0 & 0 & \bar{F}_{33} \end{bmatrix} = \begin{bmatrix} 1+\frac{u_{11}}{l_1^0} & \frac{u_{21}}{l_2^0} & 0 \\ 0 & 1+\frac{u_{22}}{l_2^0} & 0 \\ 0 & 0 & 1+\frac{u_{33}}{l_3^0} \end{bmatrix} \tag{2.17}$$

such that u_{ij} is the displacement on master node i in direction j, whereas l_i^0 is the initial length of the RVE in direction i.

Combining Eqs. (2.15) and (2.13) it is possible to relate $\mathbf{F}$ to $\bar{\mathbf{F}}$ as:

$$\mathbf{F} = \mathbf{Q}_0^{\mathrm{T}} \mathbf{R} \bar{\mathbf{F}} \mathbf{Q}_0 \tag{2.18}$$

Taking the fact that $\mathbf{Q}_0^{\mathrm{T}}\mathbf{R} = \mathbf{Q}_1^{\mathrm{T}}$, Eq. (2.18) can be rewritten as:

$$\mathbf{F} = \mathbf{Q}_1^{\mathrm{T}} \bar{\mathbf{F}} \mathbf{Q}_0 \tag{2.19}$$

Here, the transformation matrix $\mathbf{Q}_1$ depends on the angle $\theta_1 = \theta_0 + \phi$, see Fig. 2.3 (right):

$$\mathbf{Q}_1 = \begin{bmatrix} \cos(\theta_1) & \sin(\theta_1) & 0 \\ -\sin(\theta_1) & \cos(\theta_1) & 0 \\ 0 & 0 & 1 \end{bmatrix} \tag{2.20}$$

The angle ϕ marks the change in orientation of the RVE with respect to the global frame of reference from the angle θ_0 to the angle θ_1. This change in the orientation stems from the finite deformation that the RVE undergoes, and is present also for an isotropic material: if we consider from the tensile specimen a slice of material initially aligned with an angle θ_0 unequal to 0° or 90°, the orientation of this slice will change as the material deforms, see Fig. 2.4. The shear deformation of an orthotropic material under uniaxial loading further contributes to this reorientation. In order to compute ϕ from $\bar{\mathbf{F}}$ we make use of the knowledge on the deformation gradient $\mathbf{F}$, which has $F_{yx} = 0$. We assume that the experimental boundary conditions are such that rotation of the specimen edges on which the stress is applied is prevented, while relative transverse translation of these edges is free. The specimen then deforms into the shape of the outermost parallelogram shown in Fig. 2.3. With loading in y-direction, this implies that the gradient of u_y in x-direction is

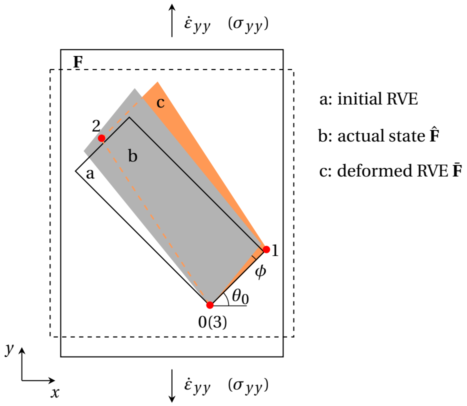

Figure 2.4: Deformed RVE present in simulation and actual state it is in due to the applied loading on isotropic material

equal to zero, while the gradient of u_x in y-direction can take a nonzero value. Therefore, $F_{yx} = 0$ and **F** has the following form:

$$\mathbf{F} = \begin{bmatrix} F_{xx} & F_{xy} & 0 \\ 0 & F_{yy} & 0 \\ 0 & 0 & F_{zz} \end{bmatrix} \tag{2.21}$$

An expression for the angle ϕ is determined by equating the F_{yx} component of the global deformation gradient **F** from Eq. (2.18) to zero. This condition leads to the following expression for ϕ:

$$\phi = \arctan\left(\frac{-\bar{F}_{11} c_0 s_0 + \bar{F}_{12} s_0^2 + \bar{F}_{22} c_0 s_0}{\bar{F}_{11} c_0^2 - \bar{F}_{12} c_0 s_0 + \bar{F}_{22} s_0^2}\right) \tag{2.22}$$

where s_0 and c_0 denote $\sin(\theta_0)$ and $\cos(\theta_0)$.

In order to derive the strain rate based constraint equation, the F_{yy} component of the lamina deformation gradient **F** is picked from Eq. (2.19), and equated to the corresponding value imposed from the input:

$$g = 0: \quad \underbrace{\bar{F}_{11} s_0 s_1 + \bar{F}_{22} c_0 c_1 + \bar{F}_{12} c_0 s_1}_{F_{yy}\text{ calculated from RVE}} - \underbrace{\exp(\varepsilon_{yy}^{n-1} + \dot{\varepsilon}_{yy}\Delta t)}_{F_{yy}\text{ imposed from input}} = 0 \tag{2.23}$$

where s_1 and c_1 stand for $\sin(\theta_1)$ and $\cos(\theta_1)$, ε_{yy}^{n-1} is the total strain in the loading direction from last converged time step, $\dot{\varepsilon}_{yy}$ is the strain rate imposed in the analysis, and Δt is the time increment. The F_{yy} term imposed from the input derives from the true-strain definition in the loading direction:

$$\varepsilon_{yy} = \ln\left(\frac{l_y^0 + u_{yy}}{l_y^0}\right) = \ln(F_{yy}) \tag{2.24}$$

in which l_y^0 is the initial length of the lamina in the loading direction, and u_{yy} is the displacement in the same direction. The true strain in the loading direction at the current time step is numerically represented as:

$$\varepsilon_{yy}^n = \varepsilon_{yy}^{n-1} + \dot{\varepsilon}_{yy}\Delta t \tag{2.25}$$

which after substitution in Eq. (2.24) yields:

$$F_{yy}^n = \exp(\varepsilon_{yy}^{n-1} + \dot{\varepsilon}_{yy}\Delta t) \tag{2.26}$$

The term $\dot{\varepsilon}_{yy}\Delta t$ plays the role of the arclength parameter in Eq. (2.4) and ensures that the deformation pattern of the RVE corresponds to the global strain rate imposed in the analysis.

By replacing the $\bar{F}_{ij}$ components in Eq. (2.23) with corresponding expressions from Eq. (2.17), the constraint equation $g = 0$ is expressed in terms of nodal displacements:

$$\left(1 + \frac{u_{11}}{l_1^0}\right) s_0 s_1 + \left(1 + \frac{u_{22}}{l_2^0}\right) c_0 c_1 + \frac{u_{21}}{l_2^0} c_0 s_1 - \exp(\varepsilon_{yy}^{n-1} + \dot{\varepsilon}_{yy}\Delta t) = 0 \tag{2.27}$$

It is obvious that the equation does not depend on the load factor λ. Therefore:

$$s = \frac{\partial g}{\partial \lambda} = 0 \tag{2.28}$$

An assumption is introduced that the angle ϕ is calculated given the deformation state from last converged time step. With this assumption, it is true within each time step that:

$$\frac{\partial \cos(\theta_1)}{\partial \mathbf{a}} = \frac{\partial \sin(\theta_1)}{\partial \mathbf{a}} = \mathbf{0} \tag{2.29}$$

which simplifies the linearization of the constraint equation with respect to the displacements of the master nodes, such that:

$$\mathbf{h}^{\mathrm{T}} = \left(\frac{\partial g}{\partial \mathbf{a}}\right)^{\mathrm{T}} = [\underbrace{0 \quad 0 \quad 0}_{\text{node 0}} \quad \underbrace{s_0 s_1 / l_1^0 \quad 0 \quad 0}_{\text{node 1}} \quad \underbrace{c_0 s_1 / l_2^0 \quad c_0 c_1 / l_2^0 \quad 0}_{\text{node 2}} \quad \underbrace{0 \quad 0 \quad 0}_{\text{node 3}}] \tag{2.30}$$

2.2.4. UNIT FORCE VECTOR

Another essential ingredient of every arclength control method is the unit force vector $\hat{\mathbf{f}}$. It is applied at nodes where the external force level needs to be controlled. In the context of a uniaxial test, $\hat{\mathbf{f}}$ should correspond to unit applied stress. Since the model aims at capturing finite strains in the material, the relative magnitude of the forces defined on the master nodes and the homogenized applied stress cannot be set on the initial configuration of the RVE, in the sense of small strain theory. The geometrically nonlinear effect on the unit force vector is twofold. Firstly, the change in the initial geometry of the RVE from the shape "a" to the shape "c", see Fig. 2.3, asks for an update in $\hat{\mathbf{f}}$. Secondly, the actual change in orientation of the RVE for the angle ϕ introduces another geometric effect to the unit force vector. With this in mind it becomes apparent that $\hat{\mathbf{f}}$ depends on the deformation state of the RVE, and is a function of the nodal displacements.

The unit force vector is applied on the RVE such that the corresponding stress state is equivalent to the global stress state of the material, see Fig 5.1. The components of this vector are derived considering the formula for internal nodal forces [18], for a single hexahedral finite element with the size and orientation of the initial RVE domain in the local coordinate system:

$$\bar{\mathbf{f}}_{\text{int}} = \int_{\Omega_0} \bar{\mathbf{B}}_0^{\mathrm{T}} \bar{\mathbf{F}}^{-1} \bar{\boldsymbol{\sigma}} \bar{J} d\Omega_0 \tag{2.31}$$

where $\bar{\mathbf{B}}_0$ is the strain - nodal displacement matrix defined for trilinear shape functions defined over the whole RVE domain, while $\bar{J}$ is the determinant of the RVE deformation gradient $\bar{\mathbf{F}}$ [2]. The Cauchy stress tensor $\bar{\boldsymbol{\sigma}}$ comes from the transformation of the global stress state to the local frame, see Fig. 2.1:

$$\bar{\boldsymbol{\sigma}} = \mathbf{Q}_1 \boldsymbol{\sigma} \mathbf{Q}_1^{\mathrm{T}} = \sigma_{yy} \begin{bmatrix} s_1^2 & c_1 s_1 & 0 \\ c_1 s_1 & c_1^2 & 0 \\ 0 & 0 & 0 \end{bmatrix} = \begin{bmatrix} \sigma_{11} & \tau_{12} & 0 \\ \tau_{21} & \sigma_{22} & 0 \\ 0 & 0 & 0 \end{bmatrix} \tag{2.32}$$

For the problem at hand, the load factor λ is identical to the magnitude of the stress component in the global loading direction:

$$\lambda \equiv \sigma_{yy} \tag{2.33}$$

The stress state of Eq. (2.32) and the imposed Dirichlet boundary conditions imply that three components of the unit force vector acting on the RVE are nonzero, see Fig. 2.2. Expressions for these components follow from evaluating Eq. (2.31):

$$\begin{aligned} \hat{f}_{11} &= A_1^0 \bar{J} \left(\frac{s_1^2}{\bar{F}_{11}} - c_1 s_1 \frac{\bar{F}_{12}}{\bar{F}_{11} \bar{F}_{22}} \right) \\ \hat{f}_{21} &= A_2^0 \bar{J} \frac{c_1 s_1}{\bar{F}_{22}} \\ \hat{f}_{22} &= A_2^0 \bar{J} \frac{c_1^2}{\bar{F}_{22}} \end{aligned} \tag{2.34}$$

Here $\hat{f}_{ij}$ is the unit force component on master node i in direction j, whereas A_i^0 represents an initial surface (side of the RVE) on which a corresponding stress component is acting. From Eq. (2.34) it is clear that $\hat{\mathbf{f}}$ depends on the deformation state of the RVE through its deformation gradient components, but also on a proper transformation that relies on the change in the RVE orientation through the angle ϕ, as needed for c_1 and s_1.

2.2.5. IMPLEMENTATION

Time discretization in Eq. (2.27) is exact and so far all equations are derived in the current configuration. The angles ϕ and hence θ_1 are a function of the current displacements. For a fully implicit formulation, ϕ would need to be updated every iteration, rendering the linearization of Eq. (2.6)

---

[2] The relevant quantities here are written in tensor notation, making $\bar{\mathbf{f}}_{\text{int}}$ matrix of the size Nnodes × 3, such that each row represents three components of the force vector at one node

Table 2.1: Algorithm of the strain-rate based arclength model for time step n

```
1) set step size $\Delta t$; set $j = 0$, $\Delta \mathbf{a}_0 = 0$
2) given $\bar{\mathbf{F}}^{n-1}$, compute $\phi$ from Eq. (2.22); set $\theta_1 = \theta_0 + \phi$
3) update the unit force vector $\hat{\mathbf{f}}$, Eq. (2.34)
4) compute the tangent stiffness matrix of the system $\mathbf{K}_j$
5) set prescribed displacements
6) compute $d\mathbf{a}^{\mathrm{I}}_{j+1}$ and $d\mathbf{a}^{\mathrm{II}}_{j+1}$, Eq. (2.9)
7) compute $d\lambda_{j+1}$, Eq. (2.10)
8) compute $\Delta \mathbf{a}_{j+1} = \Delta \mathbf{a}_j + d\lambda_{j+1} d\mathbf{a}^{\mathrm{I}}_{j+1} + d\mathbf{a}^{\mathrm{II}}_{j+1}$
9) given $\Delta \mathbf{a}_{j+1}$, compute $\Delta \bar{\mathbf{F}}_{i,j+1}$ for every integration point
10) compute deformation gradient $\bar{\mathbf{F}}_{i,j+1} = \Delta \bar{\mathbf{F}}_{i,j+1} \cdot \bar{\mathbf{F}}^{n-1}_i$ for every integration point
11) given $\bar{\mathbf{F}}_{i,j+1}$, compute $\boldsymbol{\sigma}_{i,j+1}$ for every integration point
12) compute the internal force vector $\mathbf{f}_{\mathrm{int},j+1}$
13) check convergence, Eq. (2.5); if converged go to the next time step, otherwise go to 4)
```

inexact. To keep optimal convergence without the need to extend the arclength solution algorithm with additional linearization terms, the angle ϕ is only updated between time steps and in every time step the c_1, s_1 and $\bar{\mathbf{F}}$ in Eqs. (2.23) and (2.34) are based on the converged deformation from the previous time step.

The algorithmic details of the model, adjusted for the present case from [17], are summarized in Table 2.1. It is important to note that in these steps $\bar{\mathbf{F}}_i$ represents the deformation gradient at integration point i of the RVE, and is not to be confused with the deformation gradient $\mathbf{F}$ of the lamina as a whole, and the homogenized deformation gradient $\bar{\mathbf{F}}$ of the RVE as a whole.

2.2.6. SMALL STRAIN VERSION

The elaborated formulation does not impose any restriction on the kinematics relations and is considered as the general nonlinear framework. However, in many applications of practical interest structural components made of composites remain in the small strain regime, even in a failure event. Therefore it is relevant to show equations applicable in the range of small deformations which allow for a more straightforward implementation.

A first simplification comes from the fact that the angle ϕ remains close to zero in the case of a small strain deformation process. Correspondingly, the constraint equation (2.27) reduces to a new form:

$$\left(1 + \frac{u_{11}}{l_1^0}\right) s_0^2 + \left(1 + \frac{u_{22}}{l_2^0}\right) c_0^2 + \frac{u_{21}}{l_2^0} c_0 s_0 - \exp(\varepsilon_{yy}^{n-1} + \dot{\varepsilon}_{yy}\Delta t) = 0 \tag{2.35}$$

in which the transformation completely depends on the initial angle θ_0, see Fig. 2.3, through $\sin(\theta_0)$ and $\cos(\theta_0)$ terms.

Another simplification concerns the unit force vector, which in the event of small deformations will be the same in every time step:

$$\begin{aligned} \hat{f}_{11} &= A_1^0 s_0^2 \\ \hat{f}_{21} &= A_2^0 c_0 s_0 \\ \hat{f}_{22} &= A_2^0 c_0^2 \end{aligned} \tag{2.36}$$

Compared to Eq. (2.34) the terms in Eq. (2.36) do not depend on the components of the RVE deformation gradient $\bar{\mathbf{F}}$, which means that the right hand side of Eq. (2.1) is calculated on the initial configuration, in the small strain sense. Furthermore, the transformation is conducted with the constant angle θ_0.

These two simplifications mean that geometric nonlinear effects are neglected in the constraint equation and the unit force vector, and throughout the simulation the RVE is taken to be in the shape "a", see Fig. 2.3.

2.3. THE EINDHOVEN GLASSY POLYMER CONSTITUTIVE MODEL

In this section, the governing equations of the Eindhoven Glassy Polymer (EGP) model, that is used to describe the matrix behavior in the composite material are summarized. The EGP model will also be used in a standalone manner in a single element test, to test the performance of the arclength model.

The EGP is an isotropic, elasto-viscoplastic, 3D constitutive law. It is based on the Eyring flow theory [19], in the sense that an Eyring-based viscosity exponentially reduces with applied stress, also reducing the material relaxation time. Consequently, the plastic flow at yield is regarded as a stress-induced melting, and there is no need for an explicit yield surface.

Description of the formulation starts from the deformation gradient of a material point. Let that material point be integration point i whose deformation gradient is denoted with $\mathbf{F}_i$[3]. It is decomposed in the elastic and the plastic part [20]:

$$\mathbf{F}_i = \mathbf{F}_{i\mathrm{e}} \cdot \mathbf{F}_{i\mathrm{p}} \tag{2.37}$$

The plastic deformation preserves volume, so that the volumetric change is purely elastic:

$$J_i = \det(\mathbf{F}_i) = \det(\mathbf{F}_{i\mathrm{e}}) \tag{2.38}$$

An additive decomposition of the Cauchy stress is assumed:

$$\boldsymbol{\sigma} = \boldsymbol{\sigma}_\mathrm{h} + \boldsymbol{\sigma}_\mathrm{r} + \boldsymbol{\sigma}_\mathrm{s} \tag{2.39}$$

where $\boldsymbol{\sigma}_\mathrm{h}$ is the hydrostatic component, $\boldsymbol{\sigma}_\mathrm{r}$ is the hardening stress, and $\boldsymbol{\sigma}_\mathrm{s}$ is the driving stress contribution. The hydrostatic stress depends on the bulk modulus κ and the change in volume J_i:

$$\boldsymbol{\sigma}_\mathrm{h} = \kappa(J_i - 1)\mathbf{I} \tag{2.40}$$

where $\mathbf{I}$ is the second-order unit tensor. The hardening stress, explained as a rubber elastic response due to orienting of the entangled network, emerges as:

$$\boldsymbol{\sigma}_\mathrm{r} = G_\mathrm{r}\tilde{\mathbf{B}}^\mathrm{d} \tag{2.41}$$

in which G_r is the strain hardening modulus, and $\tilde{\mathbf{B}}^\mathrm{d}$ is the deviatoric part of the isochoric left Cauchy-Green deformation tensor:

$$\tilde{\mathbf{B}}^\mathrm{d} = \left(\tilde{\mathbf{F}}_i \cdot \tilde{\mathbf{F}}_i^\mathrm{T}\right)^\mathrm{d} = J_i^{-2/3}\left(\mathbf{F}_i \cdot \mathbf{F}_i^\mathrm{T}\right)^\mathrm{d} \tag{2.42}$$

The driving stress in the EGP model, ascribed to intermolecular interactions of the polymer, may also account for thermorheologically complex behavior [21]. The deformation kinetics are then governed by multiple molecular processes, here denoted for two different ones as α and β:

$$\boldsymbol{\sigma}_\mathrm{s} = \boldsymbol{\sigma}_\alpha + \boldsymbol{\sigma}_\beta \tag{2.43}$$

In addition, every relaxation process may be represented by a spectrum of viscosities (or relaxation times) and corresponding shear moduli [22]. This feature is achieved by a number of Maxwell elements connected in parallel:

$$\begin{aligned}\boldsymbol{\sigma}_\mathrm{s} &= \sum_{k=1}^{n} \boldsymbol{\sigma}_{\alpha,k} + \sum_{l=1}^{m} \boldsymbol{\sigma}_{\beta,l} \\ &= \sum_{k=1}^{n} G_{\alpha,k}\tilde{\mathbf{B}}^\mathrm{d}_{\mathrm{e}\alpha,k} + \sum_{l=1}^{m} G_{\beta,l}\tilde{\mathbf{B}}^\mathrm{d}_{\mathrm{e}\beta,l}\end{aligned} \tag{2.44}$$

---

[3] $\mathbf{F}_i$ is the same as $\bar{\mathbf{F}}_i$ in Table 2.1, but for the sake of simplified notation the bar sign is omitted in this and the subsequent section

In this equation, $G_{x,j}$ stands for the shear modulus of Maxwell element j belonging to process x, where x is either α or β. $\tilde{\mathbf{B}}^{\mathrm{d}}_{\mathrm{e}x,j}$ is the elastic part of the isochoric, deviatoric left Cauchy-Green deformation tensor, that describes the deformation process in the spring of j-th Maxwell element of the relaxation process x. Because of the time- and history-dependence of a polymer material, the elastic deformation measure is calculated by integrating the evolution equation of $\tilde{\mathbf{B}}_{\mathrm{e}x,j}$:

$$\dot{\tilde{\mathbf{B}}}_{\mathrm{e}x,j} = \left(\tilde{\mathbf{L}} - \mathbf{D}_{\mathrm{p}x,j}\right) \cdot \tilde{\mathbf{B}}_{\mathrm{e}x,j} + \tilde{\mathbf{B}}_{\mathrm{e}x,j} \cdot \left(\tilde{\mathbf{L}}^{\mathrm{T}} - \mathbf{D}_{\mathrm{p}x,j}\right) \tag{2.45}$$

where $\tilde{\mathbf{L}}$ is the isochoric velocity gradient. To solve the evolution equation for $\tilde{\mathbf{B}}_{\mathrm{e}x,j}$, a constitutive relation is introduced for the plastic part of the rate of deformation tensor:

$$\mathbf{D}_{\mathrm{p}x,j} = \frac{\boldsymbol{\sigma}_{x,j}}{2\eta_{x,j}(\bar{\tau}_x, p, S_x)} \tag{2.46}$$

$\mathbf{D}_{\mathrm{p}x,j}$ is given in the form of a non-Newtonian flow rule, such that the viscosity is a function of the equivalent stress, which is an Eyring-based feature. Additionally the viscosity depends on two other parameters, the hydrostatic pressure $p = -\mathrm{tr}(\boldsymbol{\sigma})/3$, and the thermodynamic state parameter S_x[4]:

$$\eta_{x,j} = \eta_{0x,j} \frac{\bar{\tau}_x/\tau_{0x}}{\sinh(\bar{\tau}_x/\tau_{0x})} \exp\left(\frac{\mu_x p}{\tau_{0x}}\right) \exp(S_x) \tag{2.47}$$

Here, $\eta_{x,j}$ is the viscosity in the dashpot of Maxwell element j as part of relaxation process x, $\eta_{0x,j}$ is the corresponding initial viscosity, τ_{0x} is the characteristic shear stress, while μ_x represents the pressure-dependency parameter. The equivalent stress is computed according to:

$$\bar{\tau}_x = \sqrt{\frac{1}{2}\boldsymbol{\sigma}_x : \boldsymbol{\sigma}_x} \tag{2.48}$$

The state parameter S_x takes into account the thermodynamical history of the polymer. In the EGP model, it is a product of two competing mechanisms: the aging parameter $S_{\mathrm{a}x}$, and the softening function $R_{\gamma x}(\bar{\gamma}_{\mathrm{p}})$.

$$S_x(\bar{\gamma}_{\mathrm{p}}) = S_{\mathrm{a}x} R_{\gamma x}(\bar{\gamma}_{\mathrm{p}}) \tag{2.49}$$

where $\bar{\gamma}_{\mathrm{p}}$ is the equivalent plastic strain. The state parameter initially has the value $S_{\mathrm{a}x}$ which causes an increase in the yield stress due to aging effects. On the other side, the softening function tends to reverse this process and bring it to mechanically rejuvenated reference state. $R_{\gamma x}(\bar{\gamma}_{\mathrm{p}})$ varies from 1 at the onset of yielding, to 0 at fully rejuvenated state, implying that in the same range, the state parameter S_x varies from $S_{\mathrm{a}x}$ to 0. The softening function, included in the EGP model by Klompen et al. [23], is represented as a modified Carreau-Yasuda function:

$$R_{\gamma x}(\bar{\gamma}_{\mathrm{p}}) = \left\{ \frac{1 + [r_{0x} \exp(\bar{\gamma}_{\mathrm{p}})]^{r_{1x}}}{1 + r_{0x}^{r_{1x}}} \right\}^{\frac{r_{2x}-1}{r_{1x}}} \tag{2.50}$$

Fitting parameters r_{0x}, r_{1x}, r_{2x} are usually taken the same for both relaxation processes. The equivalent plastic strain is calculated by numerically integrating the rate of equivalent plastic strain:

$$\dot{\bar{\gamma}}_{\mathrm{p}} = \frac{\bar{\tau}_{\alpha,1}}{\eta_{\alpha,1}}, \quad \bar{\tau}_{\alpha,1} = \sqrt{\frac{1}{2}\boldsymbol{\sigma}_{\alpha,1} : \boldsymbol{\sigma}_{\alpha,1}} \tag{2.51}$$

It is assumed that accumulation of the equivalent plastic strain is driven by the evolution of the mode with the highest initial viscosity. Usually this is the viscosity of the first Maxwell element of the α process $\eta_{\alpha,1}$.

Input data for the EGP model as used in this chapter are listed in Tables 2.2 and 2.3. The data correspond to polyether ether ketone (PEEK) material. Only the relaxation process α is considered.

---

[4] There are versions of the EGP model where the viscosity depends on additional parameters, see e.g. [20]

Table 2.2: Material parameters of the EGP model

κ [MPa]	G_r [MPa]	$\tau_{0\alpha}$ [MPa]	μ_α	$S_{\mathrm{a}\alpha}$	$r_{0\alpha}$	$r_{1\alpha}$	$r_{2\alpha}$
5475	14.2	1.386	0.08	3	0.95	1	-5

Table 2.3: Relaxation spectrum of the EGP model

x,j	$G_{x,j}$ [MPa]	$\eta_{0x,j}$ [MPa·s]
$\alpha,1$	721.05	$7.5900{\cdot}10^{21}$
$\alpha,2$	275.88	$4.2510{\cdot}10^{20}$
$\alpha,3$	31.77	$1.2852{\cdot}10^{19}$
$\alpha,4$	60.19	$9.2160{\cdot}10^{18}$
$\alpha,5$	49.95	$2.9562{\cdot}10^{18}$
$\alpha,6$	43.47	$9.9600{\cdot}10^{17}$
$\alpha,7$	31.35	$2.7600{\cdot}10^{17}$
$\alpha,8$	29.26	$9.9360{\cdot}10^{16}$
$\alpha,9$	34.90	$4.5990{\cdot}10^{16}$
$\alpha,10$	57.89	$1.1358{\cdot}10^{16}$
$\alpha,11$	53.30	$4.3782{\cdot}10^{14}$
$\alpha,12$	41.80	$1.4370{\cdot}10^{13}$
$\alpha,13$	39.08	$5.6358{\cdot}10^{11}$
$\alpha,14$	3.20	$1.9254{\cdot}10^{10}$
$\alpha,15$	36.58	$9.1980{\cdot}10^{8}$
$\alpha,16$	2.36	$2.4804{\cdot}10^{7}$
β,-	-	-

2.4. TRANSVERSELY ISOTROPIC CONSTITUTIVE MODEL

In this study carbon fibers are considered as reinforcement, where the carbon fibers themselves have transversely isotropic elastic properties. The constitutive law selected to model the carbon fibers is the hyperelastic, transversely isotropic material model developed by Bonet and Burton [24]. The constitutive law derives from the strain energy density function, that is split in an isotropic and a transversely isotropic component:

$$\Psi(\mathbf{C}) = \Psi_{\mathrm{iso}}(\mathbf{C}) + \Psi_{\mathrm{tri}}(\mathbf{C}) \tag{2.52}$$

The strain energy function refers to any material point in the initial configuration. Let a material point represent an integration point i whose deformation gradient is denoted with $\mathbf{F}_i$. The right Cauchy-Green deformation tensor reads:

$$\mathbf{C} = \mathbf{F}_i^{\mathrm{T}}\mathbf{F}_i \tag{2.53}$$

The isotropic strain energy function used in this chapter is a neo-Hookean potential of the form presented in, e.g., [18]:

$$\Psi_{\mathrm{iso}} = \frac{\mu}{2}(I_1 - 3) - \mu \ln(J_i) + \frac{\lambda}{2}\left[\ln(J_i)\right]^2 \tag{2.54}$$

where I_1 is the trace of $\mathbf{C}$, J_i is the determinant of $\mathbf{F}_i$, λ and μ are material constants. The corresponding strain energy function in the reference paper [24] assumes $(J_i - 1)^2$ instead of $[\ln(J_i)]^2$ in Eq. (2.54). The transversely isotropic potential is constructed as:

$$\Psi_{\mathrm{tri}} = \left[\alpha + \beta(I_1 - 3) + \gamma(I_4 - 1)\right](I_4 - 1) - \frac{1}{2}\alpha(I_5 - 1) \tag{2.55}$$

Here α, β and γ denote material constants, whereas the pseudo invariants I_4 and I_5 are defined as:

$$\begin{aligned} I_4 &= \boldsymbol{A}\cdot\mathbf{C}\boldsymbol{A} \\ I_5 &= \boldsymbol{A}\cdot\mathbf{C}^2\boldsymbol{A} \end{aligned} \tag{2.56}$$

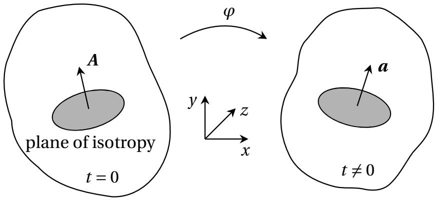

Figure 2.5: Preferential stiffness direction $\boldsymbol{A}$ of the transversely isotropic material model maps to vector $\boldsymbol{a}$ upon deformation process

so that the vector $\boldsymbol{A}$ signifies the preferential stiffness direction of the material in the initial configuration, Fig. 2.5. Upon deformation $\boldsymbol{A}$ maps to vector $\boldsymbol{a}$, the preferential stiffness direction in the current configuration:

$$\boldsymbol{a} = \mathbf{F}_i \boldsymbol{A} \tag{2.57}$$

Knowing the strain energy density function, the second Piola-Kirchhoff stress emerges as:

$$\mathbf{S} = 2\frac{\partial \Psi}{\partial \mathbf{C}} \tag{2.58}$$

This stress measure can be pushed forward to obtain expressions for the Cauchy stress contributions:

$$\boldsymbol{\sigma}_{\text{iso}} = \frac{\mu}{J_i}(\mathbf{B}-\mathbf{I}) + \frac{\lambda}{J_i}\ln(J_i)\mathbf{I} \tag{2.59}$$

and:

$$\boldsymbol{\sigma}_{\text{tri}} = J_i^{-1}\{2\beta(I_4-1)\mathbf{B} + 2[\alpha+\beta(I_1-3)+2\gamma(I_4-1)]\boldsymbol{a}\otimes\boldsymbol{a} - \alpha(\mathbf{B}\boldsymbol{a}\otimes\boldsymbol{a}+\boldsymbol{a}\otimes\mathbf{B}\boldsymbol{a})\} \tag{2.60}$$

with the pseudo invariant $I_4 = \boldsymbol{a}\cdot\boldsymbol{a}$. In Eqs. (2.59) and (2.60) $\mathbf{B}$ represents the left Cauchy-Green deformation tensor.

The constants in the expressions for the strain energy potentials and stress tensors in this chapter are slightly modified from that in the reference paper [24]. Here it is assumed that the Poisson ratio in the plane of isotropy, marked by ν_{23}, is different from the Poisson ratio, ν_{12}, for the planes orthogonal to the isotropic plane. This assumption leads to the following expressions for the constants:

$$\begin{aligned}
n &= \frac{E_1}{E_2}\\
m &= 1-\nu_{23}-2n\nu_{12}^2\\
\lambda &= \frac{E_2(\nu_{23}+n\nu_{12}^2)}{m(1+\nu_{23})}\\
\mu &= \frac{E_2}{2(1+\nu_{23})}\\
\alpha &= \mu - G_{12}\\
\beta &= \frac{E_2(\nu_{12}+\nu_{23}\nu_{12}-\nu_{23}-n\nu_{12}^2)}{4m(1+\nu_{23})}\\
\gamma &= \frac{E_1(1-\nu_{23})}{8m} - \frac{\lambda+2\mu}{8} + \frac{\alpha}{2} - \beta
\end{aligned} \tag{2.61}$$

where E_1 is the Young's modulus in preferential stiffness direction, E_2 and ν_{23} define behavior of the material in the plane of isotropy, while the shear stiffness G_{12} and Poisson's ratio ν_{12} define the behavior in planes perpendicular to the plane of isotropy. In the case of $\nu_{12} = \nu_{23}$ the expressions in Eq. (2.61) reduce to those in [24]. The material parameters utilized in this study are listed in Table 2.4.

Table 2.4: Material parameters of the transversely isotropic constitutive law

E_1 [GPa]	E_2 [GPa]	G_{12} [GPa]	ν_{12}	ν_{23}
125	15	45	0.05	0.3

2.5. EXAMPLES

The strain rate-based arclength model has been tested on several examples, in order to prove the validity of the formulation. The aim is to check whether the model properly accounts for different orientation of the load relative to the orientation of the reinforcement, i.e., different off-axis angles, captures finite strains exactly, and reproduces the rate dependency of the material. Where appropriate, the distinction is made between results obtained by applying the small strain version of the model and the general nonlinear framework. In the following, the angle χ denotes an initial off-axis angle between load direction and fiber direction, which from Fig. 2.3 reads as:

$$\chi = 90^\circ - \theta_0 \tag{2.62}$$

The stress-strain curves show the corresponding values in the global loading direction, see Fig. 2.1. Those related to the arclength model have been generated making use of the fact that σ_{yy} is equal to the load factor λ of the arclength model, while for every time step ε_{yy} is updated with Eq. (2.25).

The first example is a homogeneous RVE with an isotropic constitutive law, see Fig. 2.4. For the isotropic material model, no matter what is the considered off-axis angle, the stress-strain response must be the same. The RVE with the EGP material model is subjected to constant strain rate $\dot{\varepsilon}_{yy} = 10^{-4}$/s, and several different off-axis angles are considered, covering the range from 0° to 90°. With the computational efficiency in mind, the analysis has been done on a single hexahedral finite element. Still, in the homogeneous RVE, one can expect to find the same results, for any number of finite elements in the mesh. Fig. 2.6 (left) shows results in case the small strain version of the arclength model with Eqs. (2.35) and (2.36) is used. Here the unit force vector is not updated for the previous deformation in the RVE and also there is no change in the orientation of the RVE for the angle ϕ. These simplifications lead to a large error when compared with the true stress-strain curve in moderate strain regime.

If in an intermediate formulation an update is made in $\hat{\mathbf{f}}$ for the deformation state of the RVE (shape "c" in Fig. 2.3), but there is no update in the orientation ($\phi = 0$), more accurate results are obtained, Fig. 2.6 (right). For this isotropic material, the angle ϕ only becomes important around the strain level of 0.3, after which the response drifts away from the reference curve. This deviation is especially noticeable for the off-axis angles of 30°, 45° and 60°, when the shear stresses acting on the RVE increase. For 0° and 90°, there is no need to evaluate the angle ϕ because the edges of the micromodel do not rotate. Finally, if the model is updated according to the finite deformation framework including update of the angle ϕ, i.e. with Eqs. (2.27) and (2.34), it exactly matches the true stress-strain curve for all considered angles χ, Fig. 2.7.

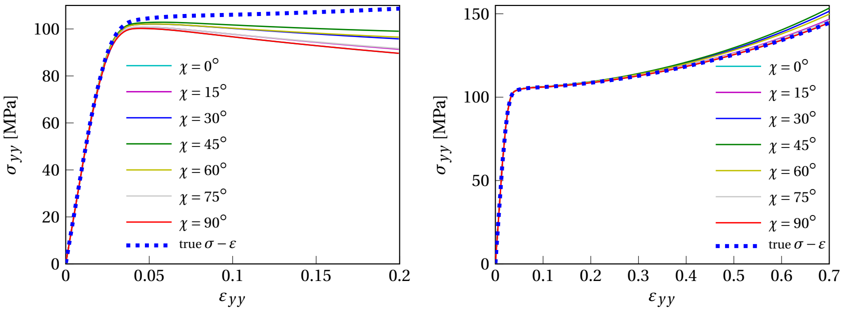

Figure 2.6: The EGP response for $\dot{\varepsilon}_{yy} = 10^{-4}$/s with the small strain version (left); with the nonlinear version with $\phi = 0$ (right)

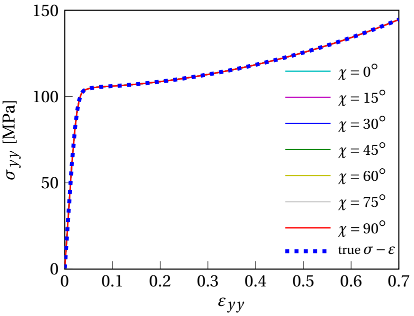

Figure 2.7: The EGP response for $\dot{\varepsilon}_{yy} = 10^{-4}$/s with the general nonlinear framework

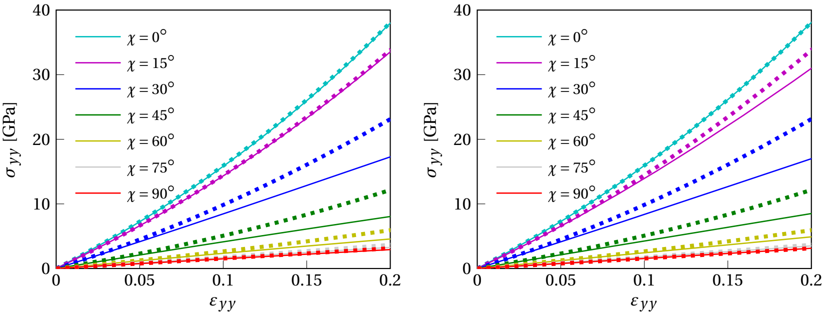

Figure 2.8: Response of the transversely isotropic material for $\dot{\varepsilon}_{yy} = 10^{-4}$/s with the small strain version (left); with the nonlinear version with $\phi = 0$ (right); solid lines - the arclength model, dotted lines - reference

The next example focuses on a homogeneous RVE with the hyperelastic transversely isotropic constitutive law [24]. Results obtained with the strain rate-based arclength model are compared with reference results. For off-axis loading of a homogeneous orthotropic material, a straightforward approach is available in which the load direction remains aligned with the global computational domain, while the preferential stiffness direction (i.e. the vector $\boldsymbol{A}$ in Fig. 2.5) is varied. Accordingly, reference results are generated from analysis of a simple cube, in which the vector $\boldsymbol{A}$ is varied with respect to the fixed loading direction. In the arclength model, this preferential stiffness direction always coincides with the local unit vector $\boldsymbol{e}_1$, see Fig. 2.2, while the orientation of the applied stress is varied. Again, three situations are examined, considering the strain rate $\dot{\varepsilon}_{yy} = 10^{-4}$/s. First, the small strain version of the arclength model produces inaccurate results when compared with the reference case, Fig. 2.8 (left). This inaccuracy is most pronounced for the off-axis angles of 30° and 45°. Contrary to the isotropic EGP model, an update in $\hat{\mathbf{f}}$ for the past deformation process, but without a proper change in the orientation, does not lead to significant improvement of the results, Fig. 2.8 (right). The off-axis angles of 0° and 90° are indeed exactly reproduced, since $\phi = 0$ in these cases, but the response for the other angles is markedly incorrect. Finally, the adequately updated arclength model precisely matches the reference case, Fig. 2.9. From the same figure it is visible that the arclength model has not fully traced the equilibrium path of the reference case for $\chi = 15°$. The reason being a numerical instability in the Newton-Raphson iteration scheme. For all off-axis angles and all strain levels for which data were obtained, the results are in exact agreement with the reference results, even for very large strain values.

The following example deals with the rate-dependent aspects of the arclength model. The EGP is used as the material of the RVE, the off-axis angle is 45°, and three different strain rates are considered (since the material is isotropic, any other angle has the same relevance, except for 0° and 90° where some of the terms in the formulation remain 0). The simulations have been done

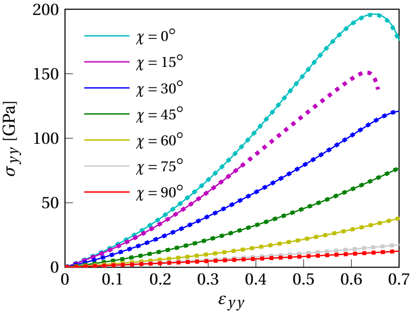

Figure 2.9: Response of the transversely isotropic material for $\dot{\varepsilon}_{yy} = 10^{-4}$ /s with the general nonlinear framework; solid lines - the arclength model, dotted lines - reference

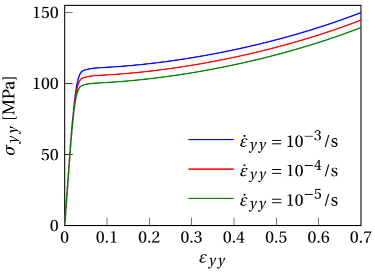

Figure 2.10: The arclength model with the EGP material under different strain rates

only with the general nonlinear framework. From Fig. 2.10 the conclusion arises that the arclength model is able to reproduce the rate dependency of the material.

For completeness, rate dependency is also checked for the transversely isotropic material at two different off-axis angles. For this material there should be no influence of loading rate on the stress-strain response. In Fig. 2.11, the stress strain curves obtained with three different loading rates in the general nonlinear framework are plotted. It can be observed that for both angles a unique rate-independent response is obtained. These results confirm that the rate dependence found with the EGP material completely stems from the constitutive model.

It has been stated in the formulation part that some quantities of the model depend on the deformation state from the last converged time step. Namely, the unit force vector $\hat{\mathbf{f}}$ and the the angle ϕ for time step n are determined from $\bar{\mathbf{F}}^{n-1}$. This choice leads to an error with respect to a fully implicit formulation, where the unit force vector and the constraint equation would be updated every iteration. This error will vanish upon reducing the time step size Δt. Therefore, it is impor-

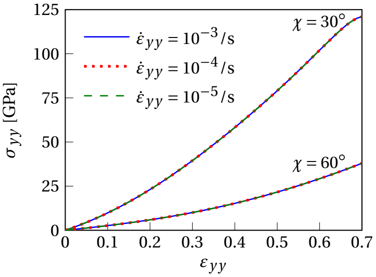

Figure 2.11: The arclength model with the transversely isotropic material under different strain rates

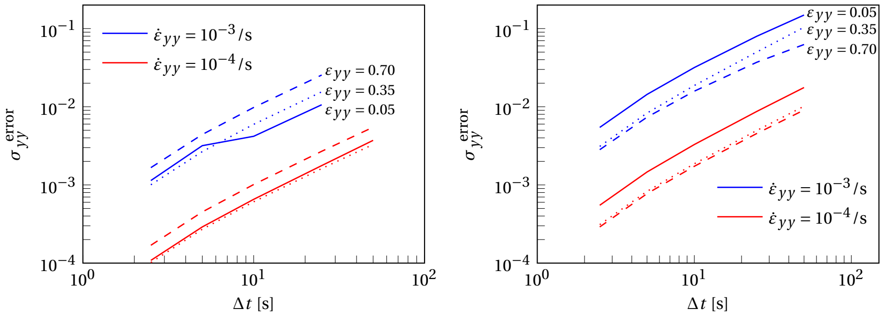

Figure 2.12: Error in σ_{yy} for different time step sizes at different strain levels, measured relative to the case $\Delta t = 1$ s, for the EGP (left) and the transversely isotropic material (right)

tant to check how the calculation step size Δt influences the accuracy of the output. An error is measured in the stress σ_{yy}, relative to the reference stress measured for $\Delta t = 1$s. For this purpose Δt of: 2.5, 5, 10, 25 and 50 seconds has been chosen such that:

$$\sigma_{yy}^{\text{error}} = \left| \frac{\sigma_{yy}^{\text{ref}}(\Delta t = 1\text{s}) - \sigma_{yy}(\Delta t)}{\sigma_{yy}^{\text{ref}}(\Delta t = 1\text{s})} \right| \tag{2.63}$$

The error has been measured at strain levels of: 0.05, 0.35 and 0.7. The initial off-axis angle is 45°, since in this case the shear stresses acting on the RVE reach a maximum value, and the change in orientation is largest. Fig. 2.12 (left) illustrates the error in a double logarithmic plot for the arclength model with the EGP material. The trend is such that the error increases with an increase in Δt. An increase in the strain rate applied also increases the error, which is due to the fact that, at the same Δt, a higher strain rate means larger strain increments. In the case of $\dot{\varepsilon}_{yy} = 10^{-3}$/s, it has not been possible to include a simulation with $\Delta t = 50$s due to convergence problems. Common to both strain rates is that the largest error is observed at the strain level of 0.7, and does not surpass 3%.

Fig. 2.12 (right) shows the error for the transversely isotropic material. Here as well, the increase in the strain rate enlarges the error, but this time it can exceed 10%. A conclusion drawn from the graphs is that at a strain rate of 10^{-3}/s, a time step size of $\Delta t < 5$ s will keep the relative error below 1%. At higher strain rates not considered in this study, it would be necessary to reduce Δt to a lower value.

The concluding example in this study is an RVE for an actual fiber reinforced composite material composed of thermoplastic polymer matrix (PEEK) and carbon fibers. The EGP material model represents the matrix part, whereas the transversely isotropic constitutive law with preferential stiffness direction parallel to the fiber axis is used for carbon fibers. The RVE is exposed to three different strain rates, while considering two different orientations of the reinforcement with respect to the loading direction: $\chi = 30°$ and $\chi = 60°$. Results of the small strain version are compared with the stress-strain curves generated by applying the general nonlinear framework in Fig. 2.13. Both sets of results confirm that the strain rate-based arclength model can be used to simulate the response of UD composite systems on the microlevel, accounting for off-axis loading and an arbitrary strain rate. Whereas the difference between the small strain and the finite strain version of the model is negligible for $\chi = 60°$, it increases for lower off-axis angles. The reason for this change in the difference is that in the range of low off-axis angles, a small variation in this angle significantly changes the axial stress component in the stiff carbon fibers. This variation in the off-axis angle is zero in the case of the small strain version model, and the hardening effect due to the change in orientation is not captured.

The contour plots of Fig. 2.14 show the distribution of the three stress components in the local frame of the RVE analyzed with the general nonlinear framework. While σ_{22} and τ_{21} components

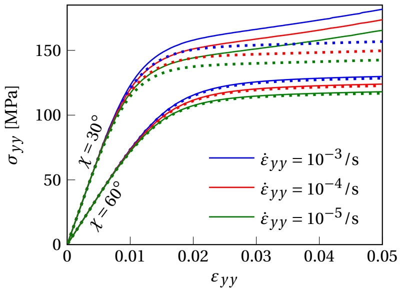

Figure 2.13: The arclength model applied on thermoplastic composite RVE, considering different strain rates and orientation of the fibers with respect to load direction; solid lines - general nonlinear framework, dotted lines - small strain version of the model

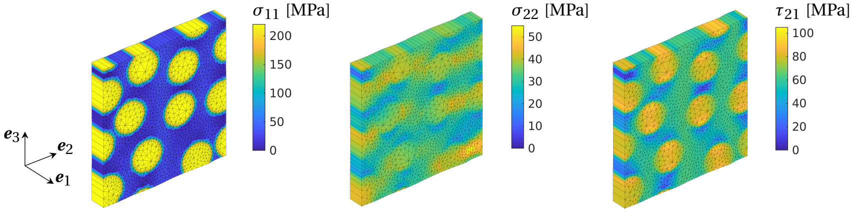

Figure 2.14: Stress distribution in local coordinate system of the RVE, for $\chi = 30°$ and $\dot{\varepsilon}_{yy} = 10^{-4}$/s, at $\varepsilon_{yy} = 0.025$; finite element mesh is generated with Gmsh [25]

are distributed between the matrix and fibers, the σ_{11} component is almost exclusively taken by the fibers.

2.6. CONCLUSION

In this chapter a strain rate-based arclength model that enables geometric and material nonlinear analysis of unidirectional composite systems at the microlevel is introduced. The same RVE can be used to simulate response of a UD composite material subjected to an arbitrary strain rate, with an arbitrary orientation of the reinforcement relative to the loading direction. The constraint equation of the model ensures that the deformation pattern of the RVE corresponds to the strain rate in the global loading direction, imposed in the analysis. Moreover, in order to ensure that the local stress state remains consistent with global uniaxial stress even when the RVE deforms and rotates, the unit force vector of the arclength model is updated as a function of the deformation state. A simplification is made that the change in orientation of the RVE and the unit force vector depend on the converged deformation state from the last time step. The numerical analysis has shown that the error induced by this explicit approach can be kept below 1% by properly choosing the size of the time increment. Several examples have been considered in order to show that the model accounts for different off-axis angles, captures finite strains exactly, and resolves the rate dependency of the material. The intended usage of the method has been demonstrated with the simulation of the rate-dependent response of fiber-reinforced thermoplastic composite material resulting in homogenized stress-strain curves and microscopic stress distributions.

A small strain version of the model has been derived from the general nonlinear framework. In the case of the composite RVE, it has been shown that this version of the model gives results that differ significantly from those obtained with the general nonlinear framework, particularly for lower off-axis angles. For the homogeneous transversely isotropic material this difference is most pronounced for off-axis angles in the range 30°-45°.

The arclength model has been derived without any assumptions on the constitutive behavior. Therefore the framework can also be used to investigate the failure of composite materials under off-axis loading when softening behavior and/or cohesive cracking is included in the micromodel formulation.

2.7. DATA AVAILABILITY

Data presented in this chapter are available at the 4TU.ResearchData repository through https://doi.org/10.4121/17166974.v1

2.8. APPENDIX

The periodicity in the RVE geometry enables application of periodic boundary conditions. Linear constraints are imposed between corresponding degrees of freedom on opposite faces of the RVE. For this purpose, four master nodes are defined at corners of the RVE, see Fig. 2.2. Let x_i represent coordinates in local coordinate frame, where $i = 1, 2, 3$. The relative displacement between matching nodes on opposite sides of the RVE is equal to the difference in displacement between corresponding master nodes:

$$\begin{aligned}
\mathbf{u}(l_1^0, x_2, x_3) &= \mathbf{u}(0, x_2, x_3) + \mathbf{u}(l_1^0, 0, 0) - \mathbf{u}(0,0,0) \\
\mathbf{u}(x_1, l_2^0, x_3) &= \mathbf{u}(x_1, 0, x_3) + \mathbf{u}(0, l_2^0, 0) - \mathbf{u}(0,0,0) \\
\mathbf{u}(x_1, x_2, l_3^0) &= \mathbf{u}(x_1, x_2, 0) + \mathbf{u}(0, 0, l_3^0) - \mathbf{u}(0,0,0)
\end{aligned} \tag{2.64}$$

where l_i^0 is the initial length of the RVE in direction i, $\mathbf{u}(l_1^0, 0, 0)$, $\mathbf{u}(0, l_2^0, 0)$ and $\mathbf{u}(0, 0, l_3^0)$ are displacements on master nodes 1, 2 and 3, respectively, whereas $\mathbf{u}(0,0,0)$ represent displacements on master node 0. Any added displacement constraint is automatically substituted in all existing displacement constraints, such that a single degree of freedom cannot be a slave and a master node simultaneously. As part of the arclength control method, a unit force vector is specified on the master nodes, see Fig. 2.2. The magnitude of every unit force component, multiplied with the load factor λ of the arclength method, is distributed among the nodes belonging to the RVE face on which the force component is acting when the constraints are applied.

REFERENCES

[1] Kovačević D, Van der Meer FP. Strain-rate based arclength model for nonlinear microscale analysis of unidirectional composites under off-axis loading. *Int J Solids Struct*, 250, 2022, p. 111697. DOI: `10.1016/j.ijsolstr.2022.111697`.

[2] Melro AR, Camanho PP, Pinho ST. Influence of geometrical parameters on the elastic response of unidirectional composite materials. *Compos Struct*, 94 (11), 2012, pp. 3223–3231. DOI: `10.1016/j.compstruct.2012.05.004`.

[3] Van der Meer FP. Micromechanical validation of a mesomodel for plasticity in composites. *Eur J Mech A Solids*, 60, 2016, pp. 58–69. DOI: `10.1016/j.euromechsol.2016.06.008`.

[4] Totry E, González C, LLorca J. Failure locus of fiber-reinforced composites under transverse compression and out-of-plane shear. *Compos Sci Technol*, 68 (3), 2008, pp. 829–839. DOI: `10.1016/j.compscitech.2007.08.023`.

[5] Rocha IBCM, Van der Meer FP, Nijssen RPL, Sluys LJ. A multiscale and multiphysics numerical framework for modelling of hygrothermal ageing in laminated composites. *Int J Numer Methods Eng*, 112 (4), 2017, pp. 360–379. DOI: `10.1002/nme.5542`.

[6] Arteiro A et al. Micro-mechanical analysis of the in situ effect in polymer composite laminates. *Compos Struct*, 116, 2014, pp. 827–840. DOI: `10.1016/j.compstruct.2014.06.014`.

[7] Naya F et al. Computational micromechanics of the transverse and shear behavior of unidirectional fiber reinforced polymers including environmental effects. *Composites A*, 92, 2017, pp. 146–157. DOI: `10.1016/j.compositesa.2016.06.018`.

[8] Govaert LE et al. A micromechanical approach to time-dependent failure in off-axis loaded polymer composites. *Composites A*, 32 (12), 2001, pp. 1697–1711. DOI: `10.1016/S1359-835X(01)00028-8`.

[9] Wempner GA. Discrete approximations related to nonlinear theories of solids. *Int J Solids Struct*, 7 (11), 1971, pp. 1581–1599. DOI: `10.1016/0020-7683(71)90038-2`.

[10] Riks E. The Application of Newton's Method to the Problem of Elastic Stability. *J Appl Mech*, 39 (4), 1972, pp. 1060–1065. DOI: `10.1115/1.3422829`.

[11] De Borst R. Computation of post-bifurcation and post-failure behavior of strain-softening solids. *Comput Struct*, 25 (2), 1987, pp. 211–224. DOI: `10.1016/0045-7949(87)90144-1`.

[12] Gutiérrez MA. Energy release control for numerical simulations of failure in quasi-brittle solids. *Commun Numer Methods Eng*, 20 (1), 2004, pp. 19–29. DOI: `10.1002/cnm.649`.

[13] Verhoosel CV, Remmers JJC, Gutiérrez MA. A dissipation-based arc-length method for robust simulation of brittle and ductile failure. *Int J Numer Methods Eng*, 77 (9), 2009, pp. 1290–1321. DOI: `10.1002/nme.2447`.

[14] Van der Meer FP, Oliver C, Sluys LJ. Computational analysis of progressive failure in a notched laminate including shear nonlinearity and fiber failure. *Compos Sci Technol*, 70 (4), 2010, pp. 692–700. DOI: `10.1016/j.compscitech.2010.01.003`.

[15] Ramm E. Strategies for Tracing the Nonlinear Response Near Limit Points. In: W Wunderlich, E Stein, KJ Bathe, eds. *Nonlinear Finite Element Analysis in Structural Mechanics.* Berlin, Heidelberg: Springer, 1981, pp. 63–89. DOI: `10.1007/978-3-642-81589-8_5`.

[16] Crisfield MA. Accelerated solution techniques and concrete cracking. *Comput Methods Appl Mech Eng*, 33 (1), 1982, pp. 585–607. DOI: `10.1016/0045-7825(82)90124-4`.

[17] De Borst R, Crisfield MA, Remmers JJC, Verhoosel CV. *Nonlinear finite element analysis of solids and structures.* John Wiley & Sons, 2012.

[18] Belytschko T, Liu WK, Moran B, Elkhodary K. *Nonlinear finite elements for continua and structures.* John Wiley & Sons, 2014.

[19] Eyring H. Viscosity, plasticity, and diffusion as examples of absolute reaction rates. *J Chem Phys*, 4 (4), 1936, pp. 283–291. DOI: `10.1063/1.1749836`.

[20] Senden DJA, Krop S, Van Dommelen JAW, Govaert LE. Rate- and temperature-dependent strain hardening of polycarbonate. *J Polym Sci B: Polym Phys*, 50 (24), 2012, pp. 1680–1693. DOI: `10.1002/polb.23165`.

[21] Klompen E, Govaert L. Nonlinear Viscoelastic Behaviour of Thermorheologically Complex Materials. *Mech Time Depend Mater*, 3 (1), 1999, pp. 49–69. DOI: `10.1023/A:1009853024441`.

[22] Van Breemen LCA, Klompen ETJ, Govaert LE, Meijer HEH. Extending the EGP constitutive model for polymer glasses to multiple relaxation times. *J Mech Phys Solids*, 59 (10), 2011, pp. 2191–2207. DOI: `10.1016/j.jmps.2011.05.001`.

[23] Klompen ETJ, Engels TAP, Govaert LE, Meijer HEH. Modeling of the postyield response of glassy polymers: Influence of thermomechanical history. *Macromolecules*, 38 (16), 2005, pp. 6997–7008. DOI: `10.1021/ma050498v`.

[24] Bonet J, Burton AJ. A simple orthotropic, transversely isotropic hyperelastic constitutive equation for large strain computations. *Comput Methods Appl Mech Eng*, 162 (1), 1998, pp. 151–164. DOI: `10.1016/S0045-7825(97)00339-3`.

[25] Geuzaine C, Remacle JF. Gmsh: A 3-D finite element mesh generator with built-in pre- and post-processing facilities. *Int J Numer Methods Eng*, 79 (11), 2009, pp. 1309–1331. DOI: `10.1002/nme.2579`.

3

FAILURE UNDER CONSTANT STRAIN RATE

3.1. INTRODUCTION

Continuous fiber reinforced polymer (FRP) composites are used in many load-carrying applications that require high performance, especially in the transportation industry. They offer the possibility for a substantial reduction in weight of structural components and better resistance to corrosion compared to metallic alternatives [2]. In addition, thermoplastic composites provide an opportunity for welding, and also recycling by melting the material. However, the melting process limits the viscosity of the material such that thermoplastics are not immediately suitable for large structures, when the resin cannot be pushed through the whole component even applying high pressures [2]. Furthermore, the viscous nature of the polymer matrix and the inherent heterogeneous structure of FRP composites make prediction of the material behavior under the time-dependent loading conditions a rather difficult task.

Historically, different scales of observation have been utilized in modeling the mechanical response of composites. Many studies to predict failure of the material have been conducted on the ply level or mesoscale where the polymer matrix and carbon fibers are represented in a homogenized way, making this approach computationally efficient. Classical mesoscale failure theories that account for interaction between different homogenized stress components in a ply are those by Azzi and Tsai [3] that led to definition of the Tsai-Hill failure criterion, and by Tsai and Wu [4], which are frequently used to this date. Hashin and Rotem [5] realized the necessity to distinguish between fiber and matrix failure that gave rise to failure-mode-based criteria. Following this idea new theories have been proposed including that by Puck and Schürmann [6] and Dávila et al. [7]. Camanho et al. [8] introduced a three-dimensional (3D) invariant-based failure criteria where the preferred material directions are accounted for by means of structural tensors.

Once defined, mesoscale failure criteria can be readily used in laminate analysis of different composite systems. However, one general issue with mesoscale formulations is the difficulty to explicitly include additional physical influences such as strain-rate effects in a failure criterion.

On the other hand, micromechanical modeling offers more information about the material structure and, therefore, a more suitable environment to develop physics-based models, although this advantage comes along with higher computational cost. Regarding material failure, by means of microscale simulations the ply level failure criteria may be checked and refined or new theories can be proposed. In this way, Sun et al. [9] derived failure envelopes from Representative Volume Element (RVE) simulations along with a comparison with classical mesoscale failure theories. Totry et al. [10] compared micromechanical failure prediction with experiments on a carbon/polyetheretherketone (C/PEEK) system subjected to transverse compression and longitudinal shear [11]. Vaughan and McCarthy [12] introduced a micromechanical model to study fracture under transverse shear and normal loading. Sharma et al. [13] showed that an RVE model calibrated at uniaxial loading cases is able to predict biaxial failure of a lamina. An image-based RVE from an actual microstructure was developed by Bhuiyan et al. [14] to examine the effect of geometrical features such as the distribution and morphology of fibers on the biaxial transverse strength. A new rate- and temperature-dependent material model for polymers was proposed by Bai et al. [15], and applied to analysis of kink band formation under longitudinal compression of a composite material. In a multiscale reduced order modeling approach Gao et al. [16] incorporated the RVE microstructure in predicting failure of a 10° off-axis composite laminate. The rate- and temperature-dependent failure under transverse tension of unidirectional (UD) composites was studied by Sato et al. [17] and compared with the three-point bending experiments.

Apart from minor text adjustments, this chapter was reproduced from [1].

The majority of the micromechanical modeling does not account for an arbitrary off-axis loading of the composite material. Exceptions among the mentioned papers are the work of Bai et al. [15] and Gao et al. [16], but they do not consider different strain-rates in the failure process. Govaert et al. [18] do account for rate-dependent failure under an arbitrary off-axis loading, but on a regular distribution of fibers inside the matrix and with a failure criterion based on a local equivalent shear strain in a single point in the micromodel.

In this chapter we develop a 3D micromechanical framework for modeling off-axis failure in UD composites subjected to a prescribed strain-rate. The model is defined in the finite deformation framework, accounting for viscoplasticity in the matrix, as well as for microcracking by means of a cohesive zone (CZ) model. The geometrically nonlinear formulation for the cohesive zones is based on the work of Reinoso and Paggi [19], which is generalized to 3D. Cohesive segments are added on the fly [20], when a microcrack initiation criterion is satisfied. A new initiation criterion is proposed based on the local stress and the local rate of deformation in the polymer matrix. A constant global strain-rate is imposed on the RVE following kinematic relations introduced in [21], that are in accordance with the finite deformation requirement of the model.

The model behavior is compared with experimental results on a UD C/PEEK composite system, exposed to a range of strain-rates at different off-axis angles and room temperature conditions. The nearly homogeneous stress states in these tests allows for direct comparison between the experimental response and results obtained from single scale micromechanical simulations up to failure.

The developed framework is envisioned to contribute to better understanding of the long-term behavior of thermoplastic composites. In the first place, the model estimates failure of the material under rate-dependent off-axis loading. Potentially the RVE can also be used in multiscale simulations to take the place of mesoscale constitutive models.

The layout of the chapter is as follows: the experimental benchmark is introduced in the next section. Then the requirements of a microscale analysis are defined, followed by the homogenized kinematics description of the RVE. After that, the variational formulation of the equilibrium equation is presented, with special attention for the linearization of the cohesive contribution to the internal force vector. The explanation of constitutive models used to represent the polymer matrix and the carbon fibers follows. Subsequently a mixed-mode damage cohesive law is introduced, together with the microcrack initiation criterion. Next, the simulation results are compared with the experiment and the chapter ends with some concluding remarks.

3.2. EXPERIMENTAL BENCHMARK

The micromechanical modeling of the rate-dependent failure is compared with experiments on UD C/PEEK composite material. Carbon fiber reinforced UD tapes with PEEK matrix, specifically made for the experimental part of the project, were provided by Solvay. The tapes were 103 mm wide with a nominal thickness of 0.25 mm. Previous work suggested that using commercial UD tapes with a higher fiber volume ratio leads to high variation in experimental results [22]. Hence, to have better repeatability in data, tapes with the fiber volume ratio $V_f = 0.4$ with more matrix than in commercial UD tapes were prepared. The quoted V_f of 0.4 was also verified by microscopy and measuring the fiber weight after burning off the resin in consolidated laminates. UD composite laminates were prepared from these tapes using the Pinette P.E.I press at the ThermoPlastic composites Research Centre (TPRC) in a two stage process.

UD plies of 390 × 390 mm dimensions were prepared from the prepreg tapes and were stacked in $[0]_{4s}$ layup. They were then placed between 1 mm thick stainless steel caul sheets, coated with Marbocote 227CEE release agent, in a picture frame. The plies were first heated to 385°C (beyond the melting temperature of PEEK) at a rate of 5°C/min under 2 bar pressure. The consolidation process was then carried out for 20 minutes under a pressure of 20 bar. Finally, the consolidated laminate was cooled down to room temperature at a uniform cooling rate of 5°C/min.

The consolidated laminates were cut into 4 smaller laminates of 190 × 190 mm dimension. They were then heated using an IR oven to 400°C in 2 minutes and flat formed between 2 flat steel

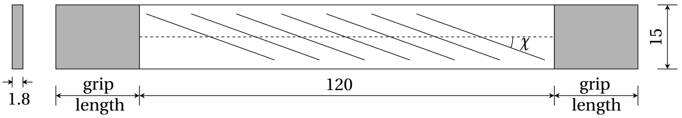

Figure 3.1: Schematic representation of test coupons used for uniaxial tension experiments; all dimensions are in mm

plates maintained at 175°C, in order to isothermally crystallize the PEEK matrix. The flat formed laminates were then manually cut to rectangular tensile test coupons using a diamond saw. Water was used as a coolant to prevent any heating during the cutting process. The test coupons have a gauge length of 120 mm, width of 15 mm and thickness of 1.8 mm, as shown in Fig. 3.1, with grip length of either 20 mm or 25 mm depending on the clamp type. Sandpaper tabs were used to avoid failure in the clamping region. χ is the angle between the fibers and loading direction, which is often referred to as the off-axis angle.

A Zwick Z100 universal tensile tester equipped with a 50 kN load cell was used to perform the experiments. Constant strain-rate experiments on off-axis UD test coupons were performed at room temperature using constant crosshead speeds corresponding to strain-rates ranging between 10^{-6}/s and 10^{-3}/s. A clip-on extensometer with a gauge length of 25 mm was used to record the stress-strain relationship for some specimens. Specifically, the extensometer was used for all the experiments performed on 90° loaded samples, whereas at other loading angles it was used only at the strain-rate of 10^{-4}/s. The exception is $\chi = 15°$ in which case the extensometer was never used. A set of the broken specimens is shown in Fig. 3.2, indicating a matrix-dominated failure mechanism with a straight crack parallel to the fibers for all off-axis angles. We acknowledge that the rectangular shape of specimens in combination with the gripping effect will cause global inhomogeneity in the deformation for off-axis angles other than 90°. This effect could be monitored using Digital Image Correlation (DIC) [23], but that was not part of this study. An alternative approach to alleviate the potential inhomogeneity in the specimen response would be the application of the oblique end tabs [24].

3.3. MICROMECHANICAL FRAMEWORK

The RVE model aims at simulating failure of UD composite material under a constant strain-rate as depicted in Fig. 3.3, such that failure of the micromodel corresponds to the macroscopic crack formation. The micromodel is defined in the local coordinate system aligned with the fibers, providing that one side is parallel to the reinforcement. This allows for representing three-dimensional stress states in a micromodel of only a thin slice of the material. There is no restriction on the strain magnitude in the material, meaning that the local coordinate frame may change orientation from the angle $\theta_0 = 90° - \chi$ to a new angle θ_1, see Fig. 3.3. The state of the micromodel must be equivalent to the deformation and stress state of the material shown in Fig. 3.3. This means that in a homogenized sense the stresses acting on the RVE, see Fig. 3.4 (left), must be equal to the

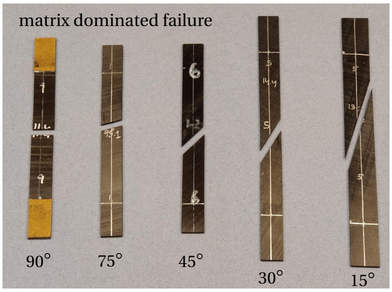

Figure 3.2: Fractured UD composite laminates for different off-axis angles

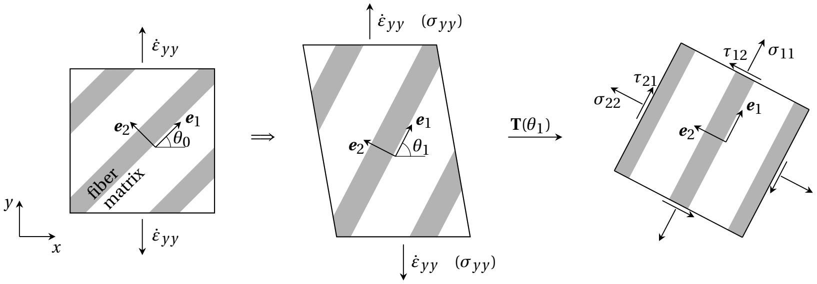

Figure 3.3: Constant strain-rate applied on unidirectional composite material (left); finite deformation of the material (middle); Cauchy stress components in local coordinate system (right)

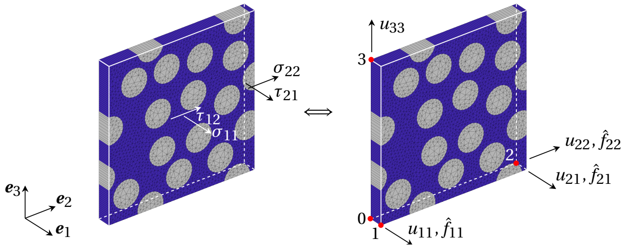

Figure 3.4: Homogenized stress state of the RVE (left); active displacements and applied unit force components on master nodes of the RVE (right)

Cauchy stresses in Fig. 3.3 (right), and the deformation pattern of the RVE should correspond to the strain-rate applied in the global y-direction. In order to satisfy these requirements, a dedicated strain-rate based arclength formulation was derived [21]. The detailed derivation of the model is presented in [21], while here only the main equations are summarized.

3.3.1. HOMOGENIZED KINEMATICS

An RVE with periodic boundary conditions is considered [25]. Kinematic relations are calculated from displacements on the master nodes of the RVE. The active master node displacements are shown in Fig. 3.4(right), accompanied by the unit force components of the arclength model. Master node displacements not indicated in the figure are fully restrained. With such defined boundary conditions, the homogenized deformation gradient of the RVE is:

$$\bar{\mathbf{F}} = \begin{bmatrix} \bar{F}_{11} & \bar{F}_{12} & 0 \\ 0 & \bar{F}_{22} & 0 \\ 0 & 0 & \bar{F}_{33} \end{bmatrix} = \begin{bmatrix} 1+\frac{u_{11}}{l_1^0} & \frac{u_{21}}{l_2^0} & 0 \\ 0 & 1+\frac{u_{22}}{l_2^0} & 0 \\ 0 & 0 & 1+\frac{u_{33}}{l_3^0} \end{bmatrix} \tag{3.1}$$

where u_{ij} is the displacement on master node i in direction j and l_i^0 is the initial length of the RVE in direction i. The constraint equation of the arclength control method enforces that the RVE deforms according to the strain-rate prescribed in the analysis:

$$\left(1+\frac{u_{11}}{l_1^0}\right) s_0 s_1 + \left(1+\frac{u_{22}}{l_2^0}\right) c_0 c_1 + \frac{u_{21}}{l_2^0} c_0 s_1 - \exp(\varepsilon_{yy}^{n-1} + \dot{\varepsilon}_{yy}\Delta t) = 0 \tag{3.2}$$

In this equation s_i and c_i stand for $\sin(\theta_i)$ and $\cos(\theta_i)$ respectively, where i is either 0 or 1. The new angle θ_1, see Fig. 3.3, is calculated as $\theta_1 = \theta_0 + \phi$, in which the angle ϕ represents the change in orientation of the RVE due to the finite deformation and is defined as:

$$\phi = \arctan\left(\frac{-\bar{F}_{11}c_0 s_0 + \bar{F}_{12}s_0^2 + \bar{F}_{22}c_0 s_0}{\bar{F}_{11}c_0^2 - \bar{F}_{12}c_0 s_0 + \bar{F}_{22}s_0^2}\right) \tag{3.3}$$

In order to maintain a uniaxial stress state in the material at finite strains, the unit force vector of the arclength method is updated accordingly:

$$\begin{aligned}
\hat{f}_{11} &= A_1^0 \bar{J}\left(\frac{s_1^2}{\bar{F}_{11}} - c_1 s_1 \frac{\bar{F}_{12}}{\bar{F}_{11}\bar{F}_{22}}\right)\\
\hat{f}_{21} &= A_2^0 \bar{J}\frac{c_1 s_1}{\bar{F}_{22}}\\
\hat{f}_{22} &= A_2^0 \bar{J}\frac{c_1^2}{\bar{F}_{22}}
\end{aligned} \tag{3.4}$$

Here, A_i^0 is the initial surface of the RVE on which a corresponding stress component is acting, and $\bar{J}$ is the determinant of the RVE homogenized deformation gradient, Eq. (3.1). When multiplied with the load factor λ of the arclength method, the unit force components produce the desired homogenized stress state in the RVE, see Fig. 3.4. For this problem, the load factor is the same as the applied stress in the global loading direction, i.e., $\lambda = \sigma_{yy}$. Eventually, the simulation is performed on the RVE as depicted in Fig. 3.4(right), following the analysis steps as explained in [21].

3.3.2. VARIATIONAL FORMULATION

In this section the equilibrium equation between the internal and external force vector of a cracked body in the finite deformation framework is derived. The presence of cracks in the body is accounted for by means of a cohesive surface methodology. Special attention is dedicated to accurately represent geometric nonlinear effects of the cohesive zone. This problem has been treated in the literature in different contexts. Wells et al. [26] derived necessary equations in the XFEM framework to model delamination in laminated composites. Zhi et al. [27] tackled the problem of matrix cracking and delamination in composites and included the CZ geometric nonlinearity in the floating node method. In this chapter the CZ geometric nonlinearity is based on the idea introduced by Ortiz and Pandolfi [28], and further elaborated for 2D problems by Reinoso and Paggi [19]. We extend the work of Reinoso and Paggi [19] to 3D.

The virtual work of a cracked body, neglecting the body forces, can be written in the reference configuration as:

$$\int_{\Omega_0} (\nabla_{\mathbf{X}}\delta\mathbf{u}) : \mathbf{P}\, d\Omega_0 + \int_{\Gamma_{c0}} \delta[\![\mathbf{u}]\!] \cdot \mathbf{t}_0\, d\Gamma_0 = \int_{\Gamma_{u0}} \delta\mathbf{u} \cdot \mathbf{t}_{p0}\, d\Gamma_0 \tag{3.5}$$

where $\delta\mathbf{u}$ is the virtual displacement, $\mathbf{P}$ is the first Piola-Kirchhoff stress, $\mathbf{t}_0$ is the nominal traction acting on a cohesive surface, $\delta[\![\mathbf{u}]\!]$ is the virtual displacement jump of the cohesive zone, and $\mathbf{t}_{p0}$ is the nominal traction prescribed on the boundary of the body. $\nabla_{\mathbf{X}}$ represents the gradient operator with respect to the initial coordinates $\mathbf{X}$. In order to derive the equilibrium equation between the internal end external forces in the current configuration, Eq. (3.5) is pushed forward. First, $\mathbf{P}$ is written as the product of the deformation gradient $\mathbf{F}$ and the second Piola-Kirchhoff stress $\mathbf{S}$:

$$\int_{\Omega_0} (\nabla_{\mathbf{X}}\delta\mathbf{u}) : (\mathbf{F}\mathbf{S})\, d\Omega_0 + \int_{\Gamma_{c0}} \delta[\![\mathbf{u}]\!] \cdot (\mathbf{F}\mathbf{S}\mathbf{n}_0)\, d\Gamma_0 = \int_{\Gamma_{u0}} \delta\mathbf{u} \cdot \mathbf{t}_{p0}\, d\Gamma_0 \tag{3.6}$$

in which the nominal traction on the cohesive surface is replaced with $\mathbf{t}_0 = \mathbf{P}\mathbf{n}_0 = \mathbf{F}\mathbf{S}\mathbf{n}_0$, $\mathbf{n}_0$ being the vector normal to the cohesive surface in the initial configuration. The following relations from

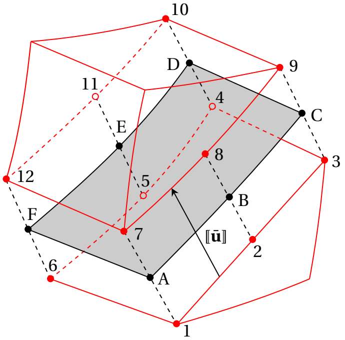

Figure 3.5: Wedge-shaped bulk finite elements in decohesion process defined by displacement jump $[\![\bar{\mathbf{u}}]\!]$; cohesive segment represented as mid-surface between the two bulk elements

e.g. [26] are considered:

$$\begin{aligned}\nabla_{\mathbf{X}}\delta\mathbf{u} &= (\nabla_{\mathbf{x}}\delta\mathbf{u})\mathbf{F}\\ \mathbf{n}_0 &= \frac{1}{\det(\mathbf{F})}\mathbf{F}^{\mathrm{T}}\mathbf{n}\frac{d\Gamma}{d\Gamma_0}\\ d\Omega_0 &= \frac{1}{\det(\mathbf{F})}d\Omega\end{aligned}\tag{3.7}$$

where $\nabla_{\mathbf{x}}$ is the gradient operator with respect to the deformed coordinates $\mathbf{x}$, and $\mathbf{n}$ is the normal vector in the current configuration. After substituting Eq. (3.7) in Eq. (3.6) and recognizing the relation between the Cauchy stress $\boldsymbol{\sigma}$ and $\mathbf{S}$ of the form:

$$\boldsymbol{\sigma} = \frac{1}{\det(\mathbf{F})}\mathbf{F}\mathbf{S}\mathbf{F}^{\mathrm{T}}\tag{3.8}$$

the virtual work of the system in the current configuration emerges as:

$$\int_{\Omega}(\nabla_{\mathbf{x}}\delta\mathbf{u}):\boldsymbol{\sigma}\,d\Omega + \int_{\Gamma_{\mathrm{c}}}\delta[\![\mathbf{u}]\!]\cdot(\boldsymbol{\sigma}\mathbf{n})\,d\Gamma = \int_{\Gamma_{\mathrm{u}}}\delta\mathbf{u}\cdot\mathbf{t}_{\mathrm{p}}\,d\Gamma\tag{3.9}$$

The further derivation is expressed in Voigt notation, and the current traction on the cohesive surface $\mathbf{t} = \boldsymbol{\sigma}\mathbf{n}$, such that:

$$\int_{\Omega}(\nabla_{\mathbf{x}}\delta\mathbf{u})^{\mathrm{T}}\boldsymbol{\sigma}\,d\Omega + \int_{\Gamma_{\mathrm{c}}}\delta[\![\mathbf{u}]\!]^{\mathrm{T}}\mathbf{t}\,d\Gamma = \int_{\Gamma_{\mathrm{u}}}\delta\mathbf{u}^{\mathrm{T}}\mathbf{t}_{\mathrm{p}}\,d\Gamma\tag{3.10}$$

The displacement field is discretized by means of the following relation:

$$\mathbf{u} = \mathbf{N}\mathbf{a}\tag{3.11}$$

where $\mathbf{N}$ is the shape function matrix, and $\mathbf{a}$ is the vector of nodal displacements. Similarly, the displacement jump is defined as:

$$[\![\mathbf{u}]\!] = \tilde{\mathbf{N}}\mathbf{a} = \begin{bmatrix}\mathbf{N}_{\mathrm{cz}} & -\mathbf{N}_{\mathrm{cz}}\end{bmatrix}\begin{bmatrix}\mathbf{a}_{\mathrm{top}}\\ \mathbf{a}_{\mathrm{bottom}}\end{bmatrix}\tag{3.12}$$

where $\mathbf{N}_{\mathrm{cz}}$ is the shape function matrix defined over the cohesive surface, while the vector of nodal displacements is partitioned in the part corresponding to the top and bottom bulk finite elements of the cohesive zone, see Fig. 3.5. Upon transformation of the displacement jump from global to local frame of reference by means of the transformation matrix $\mathbf{Q}$, the displacement jump in local frame is written as:

$$[\![\bar{\mathbf{u}}]\!] = \mathbf{Q}\tilde{\mathbf{N}}\mathbf{a}\tag{3.13}$$

Replacing Eqs. (3.11) and (3.12) in Eq. (3.10) in terms of their virtual counterparts, and expressing the cohesive zone contribution by means of the quantities defined in local frame, the discretized weak equilibrium equation in the current configuration becomes:

$$\int_{\Omega}[\nabla_{\mathbf{x}}\delta(\mathbf{N}\mathbf{a})]^{\mathrm{T}}\boldsymbol{\sigma}\,d\Omega+\int_{\Gamma_{\mathrm{c}}}\delta(\mathbf{Q}\tilde{\mathbf{N}}\mathbf{a})^{\mathrm{T}}\bar{\mathbf{t}}\,d\Gamma=\int_{\Gamma_{\mathrm{u}}}\delta(\mathbf{N}\mathbf{a})^{\mathrm{T}}\mathbf{t}_{\mathrm{p}}\,d\Gamma \tag{3.14}$$

where $\bar{\mathbf{t}}$ is the current cohesive traction in local coordinate system. Taking the first variation of Eq. (3.14) with respect to virtual nodal displacements yields the following expression:

$$\delta\mathbf{a}^{\mathrm{T}}\int_{\Omega}(\nabla_{\mathbf{x}}\mathbf{N})^{\mathrm{T}}\boldsymbol{\sigma}\,d\Omega+\delta\mathbf{a}^{\mathrm{T}}\int_{\Gamma_{\mathrm{c}}}\left(\mathbf{Q}\tilde{\mathbf{N}}+\frac{\partial\mathbf{Q}}{\partial\mathbf{a}}\tilde{\mathbf{N}}\mathbf{a}\right)^{\mathrm{T}}\bar{\mathbf{t}}\,d\Gamma=\delta\mathbf{a}^{\mathrm{T}}\int_{\Gamma_{\mathrm{u}}}\mathbf{N}^{\mathrm{T}}\mathbf{t}_{\mathrm{p}}\,d\Gamma \tag{3.15}$$

which holds for any kinematically admissible variation in the nodal displacements $\delta\mathbf{a}$. Therefore:

$$\int_{\Omega}(\nabla_{\mathbf{x}}\mathbf{N})^{\mathrm{T}}\boldsymbol{\sigma}\,d\Omega+\int_{\Gamma_{\mathrm{c}}}\left(\mathbf{Q}\tilde{\mathbf{N}}+\frac{\partial\mathbf{Q}}{\partial\mathbf{a}}\tilde{\mathbf{N}}\mathbf{a}\right)^{\mathrm{T}}\bar{\mathbf{t}}\,d\Gamma=\int_{\Gamma_{\mathrm{u}}}\mathbf{N}^{\mathrm{T}}\mathbf{t}_{\mathrm{p}}\,d\Gamma \tag{3.16}$$

This equation represents the equilibrium between the internal and external forces:

$$\mathbf{f}_{\mathrm{bulk}}^{\mathrm{int}}+\mathbf{f}_{\mathrm{cz}}^{\mathrm{int}}=\mathbf{f}^{\mathrm{ext}} \tag{3.17}$$

where the internal force vector consists of two parts. The bulk part is:

$$\mathbf{f}_{\mathrm{bulk}}^{\mathrm{int}}=\int_{\Omega}(\nabla_{\mathbf{x}}\mathbf{N})^{\mathrm{T}}\boldsymbol{\sigma}\,d\Omega=\int_{\Omega}\mathbf{B}^{\mathrm{T}}\boldsymbol{\sigma}\,d\Omega \tag{3.18}$$

in which $\mathbf{B}$ is the strain - nodal displacement matrix. The CZ part is:

$$\mathbf{f}_{\mathrm{cz}}^{\mathrm{int}}=\int_{\Gamma_{\mathrm{c}}}\left(\mathbf{Q}\tilde{\mathbf{N}}+\frac{\partial\mathbf{Q}}{\partial\mathbf{a}}\tilde{\mathbf{N}}\mathbf{a}\right)^{\mathrm{T}}\bar{\mathbf{t}}\,d\Gamma \tag{3.19}$$

Compared to the small displacement theory that would only account for the material contribution, Eq. (3.19) also features the geometric contribution to the internal force vector. This geometric contribution emerges as a consequence of the change in the transformation matrix with nodal displacements.

3.3.3. LINEARIZATION

The computational framework for the RVE model is based on the updated Lagrangian formulation [29]. Accordingly, the linearization can be done in the initial reference configuration, where the volume (or the cohesive surface) does not depend on the displacement field. Subsequently, in every iteration the current configuration is taken as the reference for the linearization, while all quantities are computed with respect to the current coordinates. Hence, although the integration domain for the internal force is changing from one iteration to the next, linearization does not require an additional term that accounts for this change.

The linearization of the bulk internal force vector leads to the following expressions for the global tangent stiffness matrix [29]:

$$\mathbf{K}_{\mathrm{bulk}}=\frac{\partial\mathbf{f}_{\mathrm{bulk}}^{\mathrm{int}}}{\partial\mathbf{a}}=\mathbf{K}_{\mathrm{bulk}}^{\mathrm{mat}}+\mathbf{K}_{\mathrm{bulk}}^{\mathrm{geo}} \tag{3.20}$$

where the material contribution to the tangent stiffness is:

$$\mathbf{K}_{\mathrm{bulk}}^{\mathrm{mat}}=\int_{\Omega}\mathbf{B}^{\mathrm{T}}\mathbf{C}\mathbf{B}\,d\Omega \tag{3.21}$$

with $\mathbf{C}$ being the bulk constitutive matrix in the deformed configuration. The geometric contribution to the tangent stiffness relating degrees of freedom of nodes I and J is:

$$\mathbf{K}_{\mathrm{bulk},IJ}^{\mathrm{geo}}=\mathbf{I}\int_{\Omega}\mathbf{B}_{I}^{\mathrm{T}}\boldsymbol{\sigma}\mathbf{B}_{J}\,d\Omega \tag{3.22}$$

where the quantity inside the integral is a scalar and **I** is the unit matrix.

The linearization of the CZ internal force vector is more involved and treated here in more detail. The CZ tangent stiffness matrix includes the material and the geometric part:

$$\mathbf{K}_{\mathrm{cz}} = \frac{\partial \mathbf{f}_{\mathrm{cz}}^{\mathrm{int}}}{\partial \mathbf{a}} = \mathbf{K}_{\mathrm{cz}}^{\mathrm{mat}} + \mathbf{K}_{\mathrm{cz}}^{\mathrm{geo}} \tag{3.23}$$

The material part is defined as:

$$\mathbf{K}_{\mathrm{cz}}^{\mathrm{mat}} = \int_{\Gamma} \left(\mathbf{Q}\tilde{\mathbf{N}}\right)^{\mathrm{T}} \bar{\mathbf{T}}\mathbf{Q}\tilde{\mathbf{N}}\, d\Gamma \tag{3.24}$$

where $\bar{\mathbf{T}}$ is the material tangent stiffness operator that provides mapping between the displacement jump and the traction vector in the local frame. In the linearization process the second derivative of the transformation matrix with respect to nodal displacements is neglected. Therefore, the geometric part of the tangent stiffness comprises four terms:

$$\mathbf{K}_{\mathrm{cz}}^{\mathrm{geo}} = \mathbf{K}_{\mathrm{g1}} + \mathbf{K}_{\mathrm{g2}} + \mathbf{K}_{\mathrm{g3}} + \mathbf{K}_{\mathrm{g4}} \tag{3.25}$$

$$\begin{aligned}
\mathbf{K}_{\mathrm{g1}} &= 2\int_{\Gamma} \left(\frac{\partial \mathbf{Q}}{\partial \mathbf{a}}\tilde{\mathbf{N}}\right)^{\mathrm{T}} \bar{\mathbf{t}}\, d\Gamma \\
\mathbf{K}_{\mathrm{g2}} &= \int_{\Gamma} \left(\frac{\partial \mathbf{Q}}{\partial \mathbf{a}}\tilde{\mathbf{N}}\mathbf{a}\right)^{\mathrm{T}} \bar{\mathbf{T}}\frac{\partial \mathbf{Q}}{\partial \mathbf{a}}\tilde{\mathbf{N}}\mathbf{a}\, d\Gamma \\
\mathbf{K}_{\mathrm{g3}} &= \int_{\Gamma} \left(\mathbf{Q}\tilde{\mathbf{N}}\right)^{\mathrm{T}} \bar{\mathbf{T}}\frac{\partial \mathbf{Q}}{\partial \mathbf{a}}\tilde{\mathbf{N}}\mathbf{a}\, d\Gamma \\
\mathbf{K}_{\mathrm{g4}} &= \int_{\Gamma} \left(\frac{\partial \mathbf{Q}}{\partial \mathbf{a}}\tilde{\mathbf{N}}\mathbf{a}\right)^{\mathrm{T}} \bar{\mathbf{T}}\mathbf{Q}\tilde{\mathbf{N}}\, d\Gamma
\end{aligned} \tag{3.26}$$

To account for the CZ geometric contribution in both the internal force vector and the tangent stiffness matrix, it is necessary to compute the 3D array $\partial\mathbf{Q}/\partial\mathbf{a}$. For this computation, we need to express every component of **Q** in terms of nodal displacements. The transformation matrix derives from the orthonormal basis **n**, **s**, **t**, that is associated with any point of the cohesive surface, see Fig. 3.6, such that:

$$\mathbf{Q} = \begin{bmatrix} n_x & n_y & n_z \\ s_x & s_y & s_z \\ t_x & t_y & t_z \end{bmatrix} \tag{3.27}$$

Computationally, the cohesive surface is represented as a mid-surface between two adjacent bulk finite elements, involved in the decohesion process. Since the bulk elements are wedge-shaped with 12 nodes, in order to ensure the compatibility in the discretization, the cohesive element is also a 12-node element, connecting two 6-node quadrilateral faces, see Fig. 3.5. The position

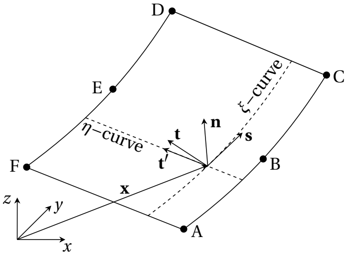

Figure 3.6: **n**, **s**, **t** orthonormal vector triad derived from unit vectors **s** and **t**′ in direction of parametric curves ξ and η, respectively

vector **x** of any node of the mid-surface in the current configuration points to the half-distance between two corresponding bulk nodes:

$$\begin{aligned} \mathbf{x}_\mathrm{A} &= \frac{1}{2}(\mathbf{x}_1+\mathbf{x}_7), & \mathbf{x}_\mathrm{D} &= \frac{1}{2}(\mathbf{x}_4+\mathbf{x}_{10}) \\ \mathbf{x}_\mathrm{B} &= \frac{1}{2}(\mathbf{x}_2+\mathbf{x}_8), & \mathbf{x}_\mathrm{E} &= \frac{1}{2}(\mathbf{x}_5+\mathbf{x}_{11}) \\ \mathbf{x}_\mathrm{C} &= \frac{1}{2}(\mathbf{x}_3+\mathbf{x}_9), & \mathbf{x}_\mathrm{F} &= \frac{1}{2}(\mathbf{x}_6+\mathbf{x}_{12}) \end{aligned} \tag{3.28}$$

The utilized 6-node quadrilateral shape that parametrizes the mid-surface features the isoparametric formulation, such that the shape functions are defined in the parent ξ-η coordinate system as follows:

$$\begin{aligned} N_\mathrm{A} &= \frac{1}{4}(1-\eta)(\xi^2-\xi), & N_\mathrm{D} &= \frac{1}{4}(1+\eta)(\xi^2+\xi) \\ N_\mathrm{B} &= \frac{1}{2}(1-\eta)(1-\xi^2), & N_\mathrm{E} &= \frac{1}{2}(1+\eta)(1-\xi^2) \\ N_\mathrm{C} &= \frac{1}{4}(1-\eta)(\xi^2+\xi), & N_\mathrm{F} &= \frac{1}{4}(1+\eta)(\xi^2-\xi) \end{aligned} \tag{3.29}$$

Following the principles of the isoparametric formulation, the position vector of any point of the cohesive surface, see Fig. 3.6, emerges as:

$$\mathbf{x} = N_\mathrm{A}\mathbf{x}_\mathrm{A} + \cdots + N_\mathrm{F}\mathbf{x}_\mathrm{F} \tag{3.30}$$

Given the position vector in Eq. (3.30), it is possible to define the unit vectors associated with the parametrized directions ξ and η in the current configuration, see Fig. 3.6:

$$\mathbf{s} = \frac{\partial\mathbf{x}/\partial\xi}{\|\partial\mathbf{x}/\partial\xi\|} = \frac{\tilde{\mathbf{s}}}{\|\tilde{\mathbf{s}}\|} \tag{3.31}$$

$$\mathbf{t}' = \frac{\partial\mathbf{x}/\partial\eta}{\|\partial\mathbf{x}/\partial\eta\|} = \frac{\tilde{\mathbf{t}}'}{\|\tilde{\mathbf{t}}'\|} \tag{3.32}$$

With the unit vectors **s** and $\mathbf{t}'$, the unit vector normal to the cohesive surface is calculated as:

$$\mathbf{n} = \mathbf{s}\times\mathbf{t}' = \begin{bmatrix} s_y t'_z - s_z t'_y \\ s_z t'_x - s_x t'_z \\ s_x t'_y - s_y t'_x \end{bmatrix} \tag{3.33}$$

In the general deformation process the cohesive surface can be distorted such that the unit vectors **s** and $\mathbf{t}'$ are not perpendicular. In order to form the orthonormal basis, vectors **n** and **s** are employed to calculate the vector **t**, see Fig. 3.6:

$$\mathbf{t} = \mathbf{n}\times\mathbf{s} = \begin{bmatrix} n_y s_z - n_z s_y \\ n_z s_x - n_x s_z \\ n_x s_y - n_y s_x \end{bmatrix} \tag{3.34}$$

In order to compute $\partial\mathbf{Q}/\partial\mathbf{a}$, it is necessary to find the derivative of every component of the transformation matrix, Eq. (3.27), with respect to nodal displacements:

$$\frac{\partial\mathbf{Q}}{\partial\mathbf{a}} = \begin{bmatrix} n_{x,\mathbf{a}} & n_{y,\mathbf{a}} & n_{z,\mathbf{a}} \\ s_{x,\mathbf{a}} & s_{y,\mathbf{a}} & s_{z,\mathbf{a}} \\ t_{x,\mathbf{a}} & t_{y,\mathbf{a}} & t_{z,\mathbf{a}} \end{bmatrix}_{3\times3\times36(\mathrm{ndof})} \tag{3.35}$$

A derivation of these derivatives is shown in the Appendix.

3.4. CONSTITUTIVE MODELS

In this section the viscoplastic constitutive model used for the matrix is described. Then, the material model for carbon fibers is briefly outlined, and finally the cohesive law to represent microcracking in the matrix is introduced.

3.4.1. THE EINDHOVEN GLASSY POLYMER CONSTITUTIVE MODEL

In order to include viscous and plasticity effects in the polymer matrix we choose the Eindhoven Glassy Polymer (EGP) model. Unlike many material models used to represent inelastic behavior of engineering materials, the EGP does not feature a yield surface. Instead it follows the Eyring flow theory [30] to describe the deformation kinetics of polymer materials. In the EGP an Eyring-based viscosity function reduces as a consequence of the stress applied on the material, such that the plastic flow at yield is regarded as the stress induced melting [31]. In this chapter, only equations needed to define the model parameters are shown, whereas an in depth derivation can be found in, e.g., [31, 32].

The EGP is an isotropic, elasto-viscoplastic material model that accounts for the finite strains in polymer material. The model builds upon the multiplicative decomposition of the deformation gradient into the elastic and the plastic part:

$$\mathbf{F} = \mathbf{F}_\mathrm{e} \cdot \mathbf{F}_\mathrm{p} \tag{3.36}$$

The change in volume is purely elastic, such that:

$$J = \det(\mathbf{F}) = \det(\mathbf{F}_\mathrm{e}) \tag{3.37}$$

The Cauchy stress is additively decomposed in three components:

$$\boldsymbol{\sigma} = \boldsymbol{\sigma}_\mathrm{h} + \boldsymbol{\sigma}_\mathrm{r} + \boldsymbol{\sigma}_\mathrm{s} \tag{3.38}$$

Here $\boldsymbol{\sigma}_\mathrm{h}$ is the hydrostatic stress, $\boldsymbol{\sigma}_\mathrm{r}$ the hardening stress, and $\boldsymbol{\sigma}_\mathrm{s}$ is the driving stress. The hydrostatic stress depends on the bulk modulus κ:

$$\boldsymbol{\sigma}_\mathrm{h} = \kappa(J-1)\mathbf{I} \tag{3.39}$$

where $\mathbf{I}$ is the second order unit tensor. The hardening stress is defined as [31]:

$$\boldsymbol{\sigma}_\mathrm{r} = G_\mathrm{r}\tilde{\mathbf{B}}^\mathrm{d} \tag{3.40}$$

in which G_r is the hardening modulus and $\tilde{\mathbf{B}}^\mathrm{d}$ is the isochoric, deviatoric, left Cauchy-Green deformation tensor:

$$\tilde{\mathbf{B}}^\mathrm{d} = \left(\tilde{\mathbf{F}} \cdot \tilde{\mathbf{F}}^\mathrm{T}\right)^\mathrm{d} = J^{-2/3}\left(\mathbf{F} \cdot \mathbf{F}^\mathrm{T}\right)^\mathrm{d} \tag{3.41}$$

The driving stress introduces viscoplasticity in the model. This stress component allows for thermorheologically complex behavior of the material, meaning that more than one relaxation process may govern the material response [33]. In the case of two relaxation processes, α and β, the driving stress reads:

$$\boldsymbol{\sigma}_\mathrm{s} = \boldsymbol{\sigma}_\alpha + \boldsymbol{\sigma}_\beta \tag{3.42}$$

However, in this chapter only α process is considered, such that $\boldsymbol{\sigma}_\mathrm{s} = \boldsymbol{\sigma}_\alpha$. The α relaxation process is represented by a Maxwell model with shear modulus on the elastic spring and viscosity on the dashpot. In order to improve the accuracy in the pre-yield regime Van Bremen et al. [31] considered a spectrum of relaxation times. This way, the α process consists of a number of Maxwell elements connected in parallel, with different shear moduli and viscosities, see Fig. 3.7. Let $G_{\alpha,j}$ be the shear modulus of j-th Maxwell element of the process α, and $\tilde{\mathbf{B}}^\mathrm{d}_{\mathrm{e}\alpha,j}$ be the elastic part of the isochoric, deviatoric left Cauchy-Green deformation tensor describing the deformation on spring of Maxwell element j. Then the driving stress is:

$$\boldsymbol{\sigma}_\mathrm{s} = \sum_{j=1}^{q} \boldsymbol{\sigma}_{\alpha,j} = \sum_{j=1}^{q} G_{\alpha,j}\tilde{\mathbf{B}}^\mathrm{d}_{\mathrm{e}\alpha,j} \tag{3.43}$$

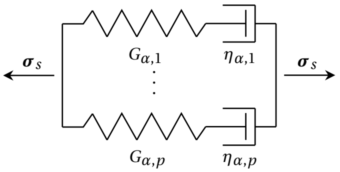

Figure 3.7: Mechanical analog for a single process (α), multi-mode driving stress in the EGP model

with q the number of modes for the process α. In order to calculate $\tilde{\mathbf{B}}^{\mathrm{d}}_{\mathrm{e}\alpha,j}$ in Eq. (3.43), it is necessary to solve for $\tilde{\mathbf{B}}_{\mathrm{e}\alpha,j}$ by integrating the corresponding rate equation:

$$\dot{\tilde{\mathbf{B}}}_{\mathrm{e}\alpha,j} = \left(\tilde{\mathbf{L}} - \mathbf{D}_{\mathrm{p}\alpha,j}\right) \cdot \tilde{\mathbf{B}}_{\mathrm{e}\alpha,j} + \tilde{\mathbf{B}}_{\mathrm{e}\alpha,j} \cdot \left(\tilde{\mathbf{L}}^{\mathrm{T}} - \mathbf{D}_{\mathrm{p}\alpha,j}\right) \tag{3.44}$$

where $\tilde{\mathbf{L}}$ is the isochoric velocity gradient. At this point it is necessary to define a constitutive relation for the plastic part of the rate of deformation tensor in Eq. (3.44), which is introduced in the form of a non-Newtonian flow rule:

$$\mathbf{D}_{\mathrm{p}\alpha,j} = \frac{\boldsymbol{\sigma}_{\alpha,j}}{2\eta_{\alpha,j}(\bar{\tau}_{\alpha}, p, S_{\alpha})} \tag{3.45}$$

$\eta_{\alpha,j}$ is the viscosity of Maxwell element j. It depends on the equivalent stress $\bar{\tau}_{\alpha}$, the hydrostatic pressure $p = -\mathrm{tr}(\boldsymbol{\sigma})/3$, and the thermodynamic state parameter S_{α}:

$$\eta_{\alpha,j} = \eta_{0\alpha,j} \frac{\bar{\tau}_{\alpha}/\tau_{0\alpha}}{\sinh(\bar{\tau}_{\alpha}/\tau_{0\alpha})} \exp\left(\frac{\mu_{\alpha} p}{\tau_{0\alpha}}\right) \exp(S_{\alpha}) \tag{3.46}$$

where $\eta_{0\alpha,j}$ is the corresponding initial viscosity, $\tau_{0\alpha}$ is the characteristic shear stress, and μ_{α} is the pressure dependency parameter. The equivalent stress has the following form:

$$\bar{\tau}_{\alpha} = \sqrt{\frac{1}{2}\boldsymbol{\sigma}_{\alpha} : \boldsymbol{\sigma}_{\alpha}} \tag{3.47}$$

The state parameter S_{α} represents the thermodynamical history of the material as a function of the equivalent plastic strain $\bar{\gamma}_{\mathrm{p}}$:

$$S_{\alpha}(\bar{\gamma}_{\mathrm{p}}) = S_{\mathrm{a}\alpha} R_{\gamma\alpha}(\bar{\gamma}_{\mathrm{p}}) \tag{3.48}$$

It accounts for two interacting mechanisms: the physical aging $S_{\mathrm{a}\alpha}$ and mechanical rejuvenation modeled by the softening function $R_{\gamma\alpha}(\bar{\gamma}_{\mathrm{p}})$. While the aging process increases the yield stress of the material, the presence of mechanical load tends to reverse this process and bring it to the (mechanically) rejuvenated state. The softening function in the EGP model is a modified Carreau-Yasuda function [34]:

$$R_{\gamma\alpha}(\bar{\gamma}_{\mathrm{p}}) = \left\{ \frac{1 + [r_{0\alpha} \exp(\bar{\gamma}_{\mathrm{p}})]^{r_{1\alpha}}}{1 + r_{0\alpha}^{r_{1\alpha}}} \right\}^{\frac{r_{2\alpha}-1}{r_{1\alpha}}} \tag{3.49}$$

The equivalent plastic strain $\bar{\gamma}_{\mathrm{p}}$ in Eq. (3.49) is calculated by integrating the evolution law:

$$\dot{\bar{\gamma}}_{\mathrm{p}} = \frac{\bar{\tau}_{\alpha,1}}{\eta_{\alpha,1}}, \quad \bar{\tau}_{\alpha,1} = \sqrt{\frac{1}{2}\boldsymbol{\sigma}_{\alpha,1} : \boldsymbol{\sigma}_{\alpha,1}} \tag{3.50}$$

which depends on the equivalent stress and the viscosity of a mode with the highest initial viscosity, that is mode 1. The relaxation spectrum for the process α is presented in Table 3.1. The other material model parameters are specified in Table 3.2. The starting point to determine parameters in Tables 3.1 and 3.2 was the data set describing the behavior of PEEK obtained according to [31]. However, the corresponding relaxation spectrum led to inaccurate behavior of the composite RVE when compared with the experimental results. A reason for this inaccuracy might be a different

Table 3.1: Relaxation spectrum of the EGP model

j	$G_{\alpha,j}$ [MPa]	$\eta_{0\alpha,j}$ [MPa·s]	j	$G_{\alpha,j}$ [MPa]	$\eta_{0\alpha,j}$ [MPa·s]
1	1045.52	$7.590 \cdot 10^{21}$	9	50.61	$9.198 \cdot 10^{10}$
2	400.03	$8.502 \cdot 10^{16}$	10	83.94	$2.272 \cdot 10^{10}$
3	46.06	$2.570 \cdot 10^{14}$	11	77.28	$8.756 \cdot 10^{8}$
4	87.28	$1.843 \cdot 10^{13}$	12	60.61	$2.874 \cdot 10^{7}$
5	72.43	$5.912 \cdot 10^{12}$	13	56.67	$1.127 \cdot 10^{6}$
6	63.03	$1.992 \cdot 10^{12}$	14	4.64	$3.851 \cdot 10^{4}$
7	45.46	$5.520 \cdot 10^{11}$	15	53.03	$1.840 \cdot 10^{3}$
8	42.43	$1.987 \cdot 10^{11}$	16	3.42	$4.961 \cdot 10^{1}$

Table 3.2: Material parameters of the EGP model

κ [MPa]	G_r [MPa]	$\tau_{0\alpha}$ [MPa]	μ_α	$S_{a\alpha}$	$r_{0\alpha}$	$r_{1\alpha}$	$r_{2\alpha}$
2600	14.2	1.386	0.08	3	0.95	1	-5

crystallinity of neat polymer and the polymer matrix in the composite. Therefore, the original relaxation spectrum was modified as follows: the highest viscosity was calibrated to achieve the stress level corresponding to the plateau of the $\chi = 45°$ experiment at $\dot{\varepsilon}_{yy} = 10^{-4}/\mathrm{s}$; the rest of the spectrum was shifted such that the nonlinear part prior to the plateau of the $\chi = 45°$ experiment is properly captured, resulting in the data shown in Table 3.1.

3.4.2. TRANSVERSELY ISOTROPIC MATERIAL MODEL FOR CARBON FIBERS

No failure is assumed to take place in the carbon fibers, therefore the reinforcement behaves elastically in the RVE. The material model chosen to describe the behavior of the fibers is the hyperelastic transversely isotropic constitutive model formulated by Bonet and Burton [35]. In this chapter only the part of formulation related to the stress calculation is shown. The Cauchy stress is decomposed in an isotropic and a transversely isotropic stress contribution:

$$\boldsymbol{\sigma} = \boldsymbol{\sigma}_{\mathrm{iso}} + \boldsymbol{\sigma}_{\mathrm{tri}} \tag{3.51}$$

The isotropic stress tensor reads:

$$\boldsymbol{\sigma}_{\mathrm{iso}} = \frac{\mu}{J}(\mathbf{B} - \mathbf{I}) + \frac{\bar{\lambda}}{J}\ln(J)\mathbf{I} \tag{3.52}$$

This stress component slightly differs from the original paper [35] and is the same as in [21]. The transversely isotropic contribution is defined as:

$$\boldsymbol{\sigma}_{\mathrm{tri}} = J^{-1}\{2\beta(I_4 - 1)\mathbf{B} + 2[\alpha + \beta(I_1 - 3) + 2\gamma(I_4 - 1)]\boldsymbol{a} \otimes \boldsymbol{a} - \alpha(\mathbf{B}\boldsymbol{a} \otimes \boldsymbol{a} + \boldsymbol{a} \otimes \mathbf{B}\boldsymbol{a})\} \tag{3.53}$$

In Eqs. (3.52) and (3.53), $\mathbf{B}$ is the left Cauchy-Green deformation tensor, J is the determinant of the deformation gradient $\mathbf{F}$, and $\mathbf{I}$ is the second order unit tensor. The vector $\boldsymbol{a}$ is the preferential stiffness direction of the material in the deformed configuration, obtained as $\boldsymbol{a} = \mathbf{F}\boldsymbol{A}$, where $\boldsymbol{A}$ is the preferential stiffness direction in the initial configuration. The invariants I_1 and I_4 are defined as:

$$\begin{aligned} I_1 &= \mathrm{tr}(\mathbf{B}) \\ I_4 &= \boldsymbol{a} \cdot \boldsymbol{a} \end{aligned} \tag{3.54}$$

Table 3.3: Material parameters of the transversely isotropic constitutive model

E_1 [GPa]	E_2 [GPa]	G_{12} [GPa]	ν_{12}	ν_{23}
125	15	45	0.05	0.3

The other material parameters in Eqs. (3.52) and (3.53): $\bar{\lambda}$, μ, α, β, γ are adopted according to [21]:

$$\begin{aligned}
n &= \frac{E_1}{E_2}\\
m &= 1-\nu_{23}-2n\nu_{12}^2\\
\bar{\lambda} &= \frac{E_2(\nu_{23}+n\nu_{12}^2)}{m(1+\nu_{23})}\\
\mu &= \frac{E_2}{2(1+\nu_{23})}\\
\alpha &= \mu - G_{12}\\
\beta &= \frac{E_2(\nu_{12}+\nu_{23}\nu_{12}-\nu_{23}-n\nu_{12}^2)}{4m(1+\nu_{23})}\\
\gamma &= \frac{E_1(1-\nu_{23})}{8m}-\frac{\bar{\lambda}+2\mu}{8}+\frac{\alpha}{2}-\beta
\end{aligned} \tag{3.55}$$

Here, E_1 is the Young's modulus in the preferential stiffness direction, G_{12} and ν_{12} are the shear modulus and Poisson's ratio in the planes perpendicular to the plane of isotropy, E_2 and ν_{23} are the elastic constants in the transverse plane. Values of these parameters are listed in Table 3.3. Note that G_{12} has a higher value than usually reported in the literature, e.g. [36]. This value is calibrated to provide a good match in the initial slope between the experiments and the RVE simulation.

3.4.3. COHESIVE LAW

Microcracking in the matrix is represented by means of a cohesive surface methodology. Cohesive segments along element edges are added on the fly [20] whenever a microcrack initiation criterion is satisfied. As introduced in Section 3.3.2, the traction is acting on a cohesive surface as a function of the displacement jump, see Fig. 3.5. The relation between the traction and the displacement jump is provided by a mixed-mode damage cohesive law elaborated by Liu et al. [37]. The governing equations of the cohesive model are summarized here with the extension to 3D. Since cohesive elements are inserted on the fly, the cohesive traction should have a non-zero value at zero opening, see Fig. 3.8 (left), where the normal component of the traction is plotted against the normal component of the displacement jump. The area under the graph is the fracture energy of the material G_c. Direct application of this kind of cohesive law under mixed-mode conditions would lead

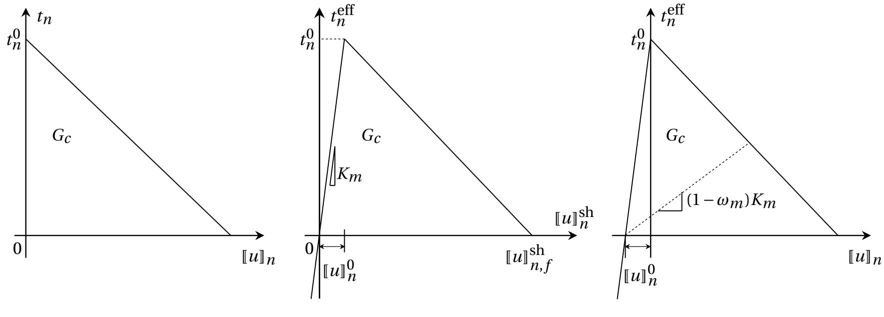

Figure 3.8: Mode I representation of the shifted mixed-mode damage cohesive law

to a singularity [38]. To avoid working with an infinite initial stiffness, the cohesive law is evaluated by shifting the displacement jump $\llbracket \bar{\mathbf{u}} \rrbracket$ for a value depending on the magnitude of the jump at crack initiation as proposed by Hille et al. [39], see Fig. 3.8 (middle):

$$\llbracket \bar{\mathbf{u}} \rrbracket^{\mathrm{sh}} = \llbracket \bar{\mathbf{u}} \rrbracket + \llbracket \bar{\mathbf{u}} \rrbracket^{0} \tag{3.56}$$

The shift $\llbracket \bar{\mathbf{u}} \rrbracket^{0}$ is defined as:

$$\llbracket \bar{\mathbf{u}} \rrbracket^{0} = \frac{\bar{\mathbf{t}}^{0}}{K_m} \tag{3.57}$$

where $\bar{\mathbf{t}}^{0}$ is the traction on the cohesive surface in the local frame at the instant of microcrack initiation, and $K_m = 10^6$ N/mm^3 is the initial dummy stiffness. In simulating rate-dependent failure, we assume that the magnitude of $\bar{\mathbf{t}}^{0}$ may depend on the local rate of deformation. The evolution of the traction with changing displacement jump is governed by the cohesive law through:

$$\bar{\mathbf{t}} = (\mathbf{I} - \Omega) K_m \llbracket \bar{\mathbf{u}} \rrbracket^{\mathrm{sh}} = (\mathbf{I} - \Omega) \bar{\mathbf{t}}^{\mathrm{eff}} \tag{3.58}$$

where $\mathbf{I}$ is the unit tensor and $\bar{\mathbf{t}}^{\mathrm{eff}}$ is the effective traction on the cohesive surface. The decohesion process is driven by the damage variable ω_m used to construct the damage tensor Ω:

$$\Omega_{ij} = \omega_m \delta_{ij} \left(1 + \delta_{i1} \frac{\langle -t_n^{\mathrm{eff}} \rangle}{t_n^{\mathrm{eff}}} \right) \tag{3.59}$$

Essentially, only the diagonal terms of Ω are nonzero. The diagonal terms are equal to ω_m, except in the case of compression when the diagonal term corresponding with normal opening and traction vanishes. The evolution of the scalar damage variable ω_m is irreversible:

$$\omega_m = \max_{\tau \le t} \begin{cases} 0, & \Delta \le \Delta_0 \\ \frac{\Delta_f}{\Delta} \left(\frac{\Delta - \Delta_0}{\Delta_f - \Delta_0} \right), & \Delta_0 < \Delta < \Delta_f \\ 1, & \Delta > \Delta_f \end{cases} \tag{3.60}$$

where Δ is the shifted equivalent displacement jump:

$$\Delta = \left[(\langle \llbracket u \rrbracket_n^{\mathrm{sh}} \rangle)^2 + (\llbracket u \rrbracket_s^{\mathrm{sh}})^2 + (\llbracket u \rrbracket_t^{\mathrm{sh}})^2 \right]^{1/2} \tag{3.61}$$

In Eq. (3.60) Δ_0 is the equivalent displacement jump at the onset of failure:

$$\Delta_0 = \frac{t_{\mathrm{eq}}^{0}}{K_m} \tag{3.62}$$

where t_{eq}^{0} is the corresponding equivalent traction on the cohesive surface:

$$t_{\mathrm{eq}}^{0} = \left[(t_n^0)^2 + (t_s^0)^2 + (t_t^0)^2 \right]^{1/2} \tag{3.63}$$

The degradation process is completed when the equivalent shifted displacement jump reaches a critical value Δ_f defined as:

$$\Delta_f = \frac{2 G_c}{t_{\mathrm{eq}}^{0}} \tag{3.64}$$

The unloading of the cohesive law is secant, with the slope depending on the current state of damage at an integration point, see Fig. 3.8 (right). In the space of finite elements, the complete unloading happens when two neighboring bulk finite elements overlap for the value Δ_0, which is the consequence of the introduced shift when evaluating the cohesive law. Moreover, due to this shift, the actual energy dissipation during decohesion will be smaller than G_c. However, both the overlapping upon unloading and the reduction in effective energy dissipation vanish when K_m approaches infinity.

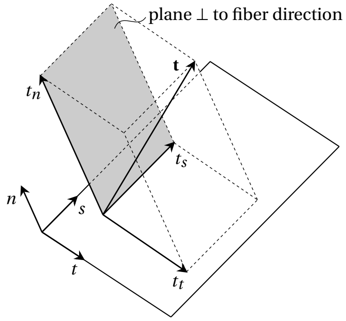

Figure 3.9: Traction acting on a potential cohesive surface with corresponding stress components

3.4.4. MICROCRACK INITIATION CRITERION

Before the cohesive law activates, a proper microcrack initiation criterion must be satisfied. In order to have quantitative comparison with the experiment, we propose an initiation criterion that is rate-dependent. First, at every time step the traction is computed on a potential cohesive surface, see Fig. 3.9, that is on any surface between finite elements of the matrix part or interface between the carbon fibers and the matrix. The traction is then decomposed in the components perpendicular and parallel to the fiber direction:

$$\begin{aligned} t_\perp &= \left(t_n^2 + t_s^2\right)^{1/2} \\ t_\parallel &= t_t \end{aligned} \tag{3.65}$$

The reason for this stress decomposition is the fact that for the off-axis angle of 90° the fracture process is completely governed by $t_\perp$, whereas $t_\parallel = 0$. On the other hand, for the lower off-axis angles, e.g. $\chi = 15°$, the stress component parallel with the fibers becomes more dominant and mostly drives the microcracking process. With these two stress components a power law initiation criterion is proposed in the following form:

$$\left(\frac{t_\perp}{f_\perp}\right)^m + \left(\frac{t_\parallel}{f_\parallel}\right)^n < 1 \tag{3.66}$$

where m and n are the constants, while $f_\perp$ and $f_\parallel$ are the strength parameters in the corresponding directions. An alternative approach, in which the stress vector is decomposed in the component normal to the cohesive surface t_n and shear component $t_{\text{sh}} = \left(t_s^2 + t_t^2\right)^{1/2}$ is also possible. This would lead to different calibration of the cohesive law, i.e., different initiation stress and fracture energies. Due to the possible misalignment of the cohesive surface normal and maximum principal stress, the t_s component is not necessarily equal to zero for a mode I fracture process.

In this study $n = 2$ was chosen to ensure the symmetry of the initiation criterion with respect to the shear stress $t_\parallel$, while $m = 3$ was calibrated to achieve a good estimate for the strain at failure for $\chi = 45°$ and a reasonably good estimate for $\chi = 30°$ off-axis angle. The change in coefficient m has much lower effect on the strain at failure for $\chi = 15°$, as compared for 30° and 45° loading angles. Further, the strain-rate $\dot{\varepsilon}_{yy} = 10^{-4}$/s is applied on the RVE with the fiber volume ratio $V_f = 0.4$. The calibrated strength values are: $f_\perp = 130$ MPa and $f_\parallel = 60$ MPa for matrix cracks and $f_\perp = 130$ MPa and $f_\parallel^{\text{if}} = 75$ MPa for fiber/matrix interface cracks. The simulation results for different off-axis angles are plotted in Fig. 3.10 and compared with the experiment. The onset of softening in the RVE response corresponds with macroscopic failure, and that point is used to make comparison with the experimental stress and strain at failure. The model qualitatively and quantitatively corresponds well with the experiment for the angles ranging from 30° to 90°, while for the angle of 15° there is an offset. In this case the simulation does match the observed stress at failure, but the strain at failure differs significantly. To achieve a similar level of accuracy for the

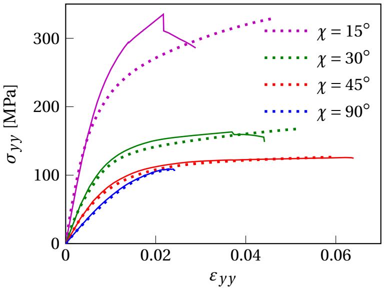

Figure 3.10: Simulation results (solid) compared with experiment (dotted) at $\dot{\varepsilon}_{yy} = 10^{-4}$/s; one initiation envelope assumed for every point in matrix, and one initiation envelope assumed at matrix/fiber interface

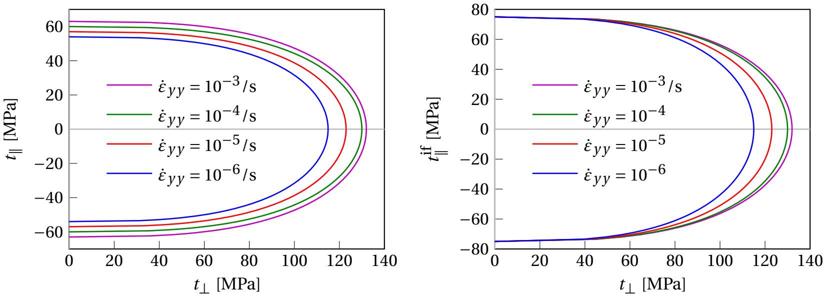

Figure 3.11: Microcrack initiation envelopes for matrix (left) and matrix/fiber interface (right) for different strain-rates, according to Eq. 3.66

strain-rates other than $\dot{\varepsilon}_{yy} = 10^{-4}$/s it proves necessary to change the strength parameters $f_\perp$ and $f_\parallel$. The initiation envelopes corresponding to different global strain-rates are shown in Fig. 3.11, for matrix and matrix/fiber interface, where the matrix/fiber interface strength $f_\parallel^{\mathrm{if}} = 75$ MPa is kept constant.

This state of the initiation criteria is similar to the idea presented by Sato et al. [17]. They employ a unique initiation envelope according to the Christensen failure theory [40] for every global (macroscopic) strain-rate acting on the RVE. Accordingly, every point of the RVE has the same initiation envelope, irrespective of the possibly different local deformation rate. In this chapter, we propose a microscopic initiation criterion based on the stress and the local rate of deformation state at any point of the RVE. To characterize the deformation rate, the rate of deformation tensor **D** is used, which is defined as the symmetric part of the velocity gradient **L**:

$$\mathbf{D} = \frac{1}{2}(\mathbf{L} + \mathbf{L}^{\mathrm{T}}) = \frac{1}{2}(\dot{\mathbf{F}}\mathbf{F}^{-1} + \mathbf{F}^{-\mathrm{T}}\dot{\mathbf{F}}^{\mathrm{T}}) \tag{3.67}$$

The reason for this choice is twofold. First, **D** is the work-conjugate to the Cauchy stress. Second, it is objective under a rigid-body rotation and follows the same transformation rule as the Cauchy stress [41], i.e.:

$$\bar{\mathbf{D}} = \mathbf{Q}\mathbf{D}\mathbf{Q}^{\mathrm{T}} \tag{3.68}$$

Therefore, together with the traction components on the potential cohesive surface, the corresponding rate of deformation components are also computed:

$$\begin{aligned} D_\perp &= \left(D_{nn}^2 + D_{ns}^2\right)^{1/2} \\ D_\parallel &= D_{nt} \end{aligned} \tag{3.69}$$

The RVE analyses have been repeated with the feature that every time an initiation criterion from Fig. 3.11 is met, the rate of deformation components are stored. Results are plotted in Fig. 3.12. It

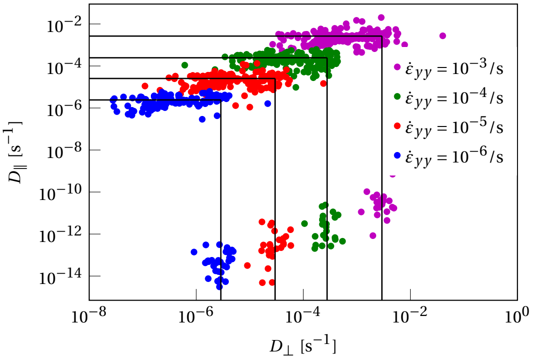

Figure 3.12: Rate of deformation components computed when microcrack initiation criterion from Fig. 3.11 is satisfied for different strain-rates

can be seen that the components $D_\perp$ and $D_\parallel$ form separate clouds of points in the rate of deformation space for every considered global strain-rate. This distinction in the local rate of deformation enables constructing different regions, such that the boundary of a region is parametrized with the $\dot{\varepsilon}_{yy}$ that defines a corresponding initiation envelope in Fig. 3.11. Each boundary is determined with a $D_\perp$ and a $D_\parallel$ component, which are listed in Table 3.4 together with the $\dot{\varepsilon}_{yy}$ parameter. The vertical lines in Fig. 3.12 represent the average value of the $D_\perp$ component calculated for $\chi = 90°$. The horizontal lines in the same figure correspond to the average value of the $D_\parallel$ component obtained from the simulations with off-axis angles of 15°, 30° and 45°. These angles are considered because the power law initiation parameters in Eq. (3.66) are calibrated from the corresponding off-axis experiments. In Fig. 3.12 there are also points from $\chi = 60°$ and $\chi = 75°$ simulations which oscillate around the corresponding horizontal lines, but are not included in defining the average values, although accounting for these points as well would not drastically change the outcome.

As already stated, the $\dot{\varepsilon}_{yy}$ parametrizes the curves in Fig. 3.11, which are calculated from Eq. (3.66). The strength parameters adopted to construct these curves for different values of the $\dot{\varepsilon}_{yy}$ are also listed in Table 3.4. The strategy to compute the local initiation envelope for any potential cohesive surface is as follows:

1. compute components $D_\perp$ and $D_\parallel$ at a point of possible microcrack initiation
2. given $D_\perp$ and $D_\parallel$ find the equivalent loading rate $\dot{\varepsilon}_{yy}^{\max}$ from Table 3.4, linearly interpolating between the corresponding rate of deformation components; $\dot{\varepsilon}_{yy}^{(1)} = f(D_\perp)$, $\dot{\varepsilon}_{yy}^{(2)} = f(D_\parallel)$, $\dot{\varepsilon}_{yy}^{\max} = \max(\dot{\varepsilon}_{yy}^{(1)}, \dot{\varepsilon}_{yy}^{(2)})$
3. given $\dot{\varepsilon}_{yy}^{\max}$, compute $f_\perp$ and $f_\parallel$ from Table 3.4, linearly interpolating between the corresponding strength parameters; note that $f_\parallel^{\text{if}}$ always equals 75 MPa
4. given $f_\perp$ and $f_\parallel$, construct the initiation envelope using Eq. (3.66)

Table 3.4: The rate of deformation components defining boundaries in Fig. 3.12 and the strength values defining initiation envelopes in Fig. 3.11 corresponding to parameter $\dot{\varepsilon}_{yy}$

$\dot{\varepsilon}_{yy}$ [s^{-1}]	$D_\perp$ [s^{-1}]	$D_\parallel$ [s^{-1}]	$f_\perp$ [MPa]	$f_\parallel$ [MPa]
10^{-6}	$2.88 \cdot 10^{-6}$	$2.42 \cdot 10^{-6}$	115	54
10^{-5}	$2.97 \cdot 10^{-5}$	$2.54 \cdot 10^{-5}$	123	57
10^{-4}	$2.78 \cdot 10^{-4}$	$2.46 \cdot 10^{-4}$	130	60
10^{-3}	$2.94 \cdot 10^{-3}$	$2.65 \cdot 10^{-3}$	132	63

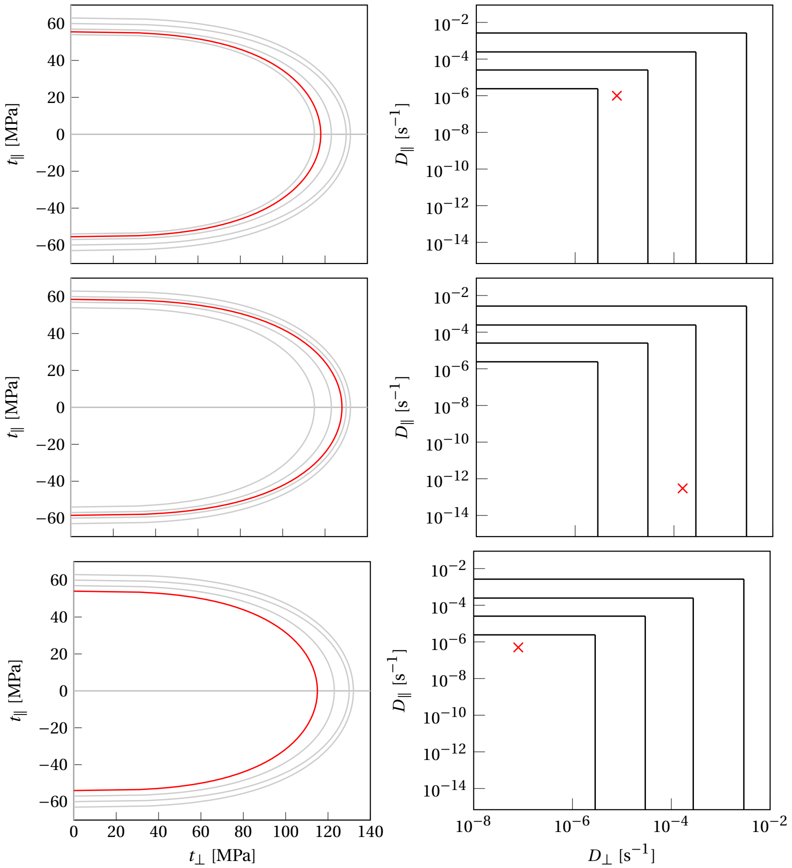

Figure 3.13: Strategy to construct microcrack initiation envelope by interpolating between two neighboring parametric curves (left), depending on the local rate of deformation state (right)

This strategy is illustrated in Fig. 3.13, where for a given point in the rate of deformation space the corresponding initiation envelope represents a proper interpolation between two adjacent parametric curves. If the point is outside the defined regions, the envelope is the closest parametric curve.

As part of this procedure we need to evaluate the rate of deformation tensor at the integration point level, Eq. (3.67). In the updated Lagrangian formulation followed in this thesis, the deformation gradient from the previous time step $\mathbf{F}^{n-1}$ and the current time step $\mathbf{F}^{n}$ are available at every integration point. Therefore the time derivative of $\mathbf{F}$ in Eq. (3.67) can be approximated:

$$\dot{\mathbf{F}} = \lim_{\Delta t \to 0} \frac{\Delta \mathbf{F}}{\Delta t} \approx \frac{\Delta \mathbf{F}}{\Delta t} = \frac{\mathbf{F}^{n} - \mathbf{F}^{n-1}}{\Delta t} \tag{3.70}$$

$\Delta\mathbf{F}$ in this equation should not be confused with an increment in the deformation gradient $d\mathbf{F}$ used to update the deformation gradient $\mathbf{F}^{n} = d\mathbf{F}{\cdot}\mathbf{F}^{n-1}$. In the case no additional deformation is present $\Delta\mathbf{F}$ is a zero tensor, while $d\mathbf{F}$ is a unit tensor.

Beside an initiation stress, the cohesive law also requires the fracture energy G_c as an input. The fracture mode changes with different off-axis angles, and the fracture mode likely influences the effective energy dissipation. To account for this effect, the G_c provided to the cohesive law interpolates between a lower bound value G_{Ic} calibrated for $\chi = 90°$, and an upper bound value G_{IIc} determined for $\chi = 15°$ at the strain-rate $\dot{\varepsilon}_{yy} = 10^{-4}$/s, see Fig. 3.14. The local value of G_c

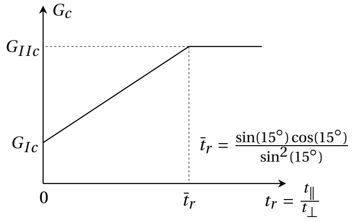

Figure 3.14: Cohesive law fracture energy as function of local stress ratio at the moment of microcrack initiation

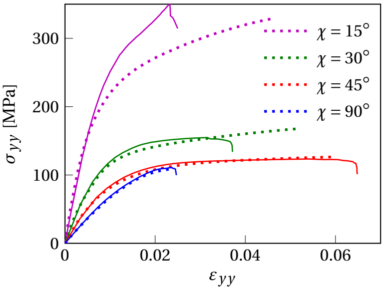

Figure 3.15: Simulation (solid) versus experiment (dotted) for $\dot{\varepsilon}_{yy} = 10^{-4}$/s and different off-axis angles

is determined when the cohesive segment is inserted and depends on the ratio $t_\parallel / t_\perp$ at initiation, which represents for these micromechanical simulations a sufficient insight in the mode, or degree of mode mixity of the fracture process. The quantity $\bar{t}_r$ in Fig. 3.14 is the initial ratio between the homogenized shear stress τ_{21} and normal stress σ_{22} acting on a plane parallel with the fiber direction when $\chi = 15°$, see Fig 3.4. In this chapter the following values are adopted: $G_{Ic} = 0.03$ N/mm, $G_{IIc} = 0.095$ N/mm, for all strain-rates and for matrix cracks and fiber/matrix interfacial cracks alike.

3.5. RESULTS AND DISCUSSION

In this section the performance of the RVE model is examined through comparison with the experimental benchmark. The stress σ_{yy} in the global loading direction, see Fig. 3.3, is plotted against the strain component ε_{yy}. The goal of this exercise is to illustrate capabilities of the model, without detailed statistical analysis on the size of the RVE. Therefore, the micromodel counting in total 9 fibers (3 × 3) of the diameter $D_f = 5$ μm is considered. A single set of parameters describing the rate and the stress dependent initiation as outlined in the previous section is considered in every simulation. As for the experiments, in the cases when the extensometer was not used to measure the exact strain, an empirically determined coefficient of 0.8 multiplies the experimental strain to cancel the compliance effect.

The RVE model has been subjected to the strain-rate of $\dot{\varepsilon}_{yy} = 10^{-4}$/s under different off-axis angles. In Fig. 3.15 the simulation results are plotted against the experimental measurements. It can be seen from the figure that the results obtained with the rate-dependent initiation criterion are similar to those obtained earlier with fixed initiation criterion calibrated for this strain-rate only (cf. Fig. 3.10). For $\chi = 15°$, there is an offset in the response, as already observed in Section 3.4.4. In this case the measurement has been performed without the extensometer which may have affected the accuracy of the strain measurements. Another reason for this discrepancy might be in different boundary conditions in the experiment and the model. The change in orientation of the RVE shows the tendency of the fibers to align with the loading direction and reduce the initial off-axis angle. In the experiment, however, clamps of the testing machine introduce constraining effect, such that rotation of the fibers is reduced close to the boundaries. This fact implies a mis-

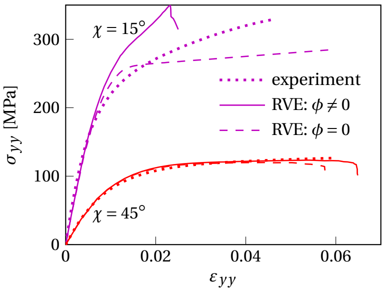

Figure 3.16: Experiment compared with simulation results when the model accounts for changes in orientation ($\phi \neq 0$) and when orientation is fixed ($\phi = 0$), for two different off-axis angles

match between the stress state in the experiment and the model. The simulation results with the fixed RVE orientation is plotted in Fig. 3.16 together with the experiment and the model response for the changing orientation for $\chi = 15°$ and $\chi = 45°$. These results confirm that a small variation in the off-axis angle significantly changes the response for small off-axis angles, like $\chi = 15°$, whereas for the angle of 45° this variation has less impact on the outcome. Consequently, the effect of mismatch between the stress state of the experiment and the model increases for smaller off-axis angles. From Fig. 3.16 it may be hypothesized that the actual response of the specimen for $\chi = 15°$ lies between the case when the RVE freely changes orientation, and the case when this change is restrained. A full multiscale analysis similar to that performed by Gao et al. [16], with separate RVEs linked to individual macroscopic integration points accounting for macroscopic variations in the deformation, possibly provides a better match with the experiment. It may be noted that if macroscopic variations are indeed significant, the experimental results should not be interpreted as direct stress-strain measurements of the composite material. To what extent such variations are present could be checked with DIC, although that has not been done in this study.

Next, the strain-rate $\dot{\varepsilon}_{yy} = 10^{-3}$/s is considered. The simulation outcome is plotted in Fig. 3.17 and compared with available experiments. There is a good correspondence with the experimental observation for the angles of 45° and 90°, while for $\chi = 30°$ the simulation fails prematurely, resulting in a lower stress at failure.

In the next example $\dot{\varepsilon}_{yy} = 10^{-5}$/s is applied on the RVE. Comparison with the experiment is depicted in Fig. 3.18 (left). The similar conclusion as for the case $\dot{\varepsilon}_{yy} = 10^{-4}$/s holds here as well. For $\chi = 45°$, the simulation ends up with a response more ductile than experimentally observed, but the stress at failure is still very close to the testing one.

Results for the strain-rate of 10^{-6}/s and two different off-axis angles $\chi = 15°$ and $\chi = 90°$ are shown in Fig. 3.18 (right). While there is a good match for 90° off-axis angle, again there is an offset for $\chi = 15°$.

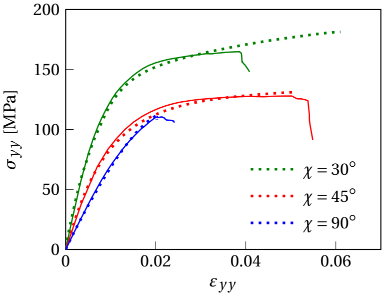

Figure 3.17: Simulation (solid) versus experiment (dotted) for $\dot{\varepsilon}_{yy} = 10^{-3}$/s and different off-axis angles

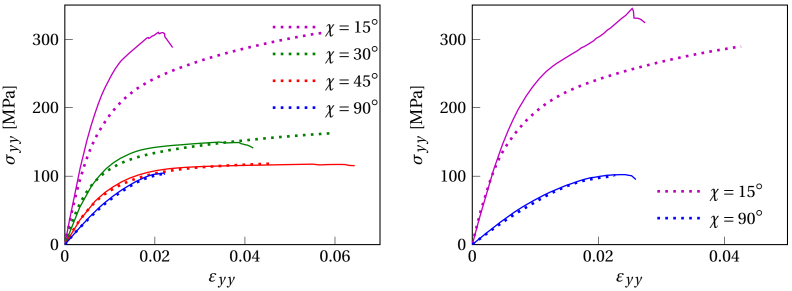

Figure 3.18: Simulation (solid) versus experiment (dotted) for $\dot{\varepsilon}_{yy} = 10^{-5}$/s (left), $\dot{\varepsilon}_{yy} = 10^{-6}$/s (right), and different off-axis angles

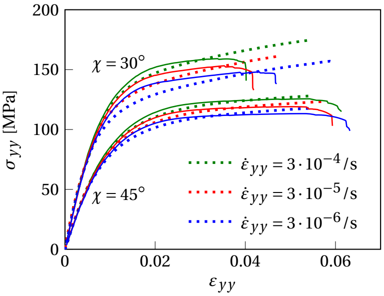

Figure 3.19: Simulation (solid) versus experiment (dotted) for range of strain-rates and two different off-axis angles

In the following, three different strain-rates of: $3 \cdot 10^{-4}$/s, $3 \cdot 10^{-5}$/s and $3 \cdot 10^{-6}$/s are imposed on the RVE under two different off axis angles: 30° and 45°. The simulation outcome is plotted in Fig. 3.19, accompanied by the experimental results. The strain-rates considered here have not been included in the construction of the parametric curves in Fig. 3.11. A good agreement between the model and the experiment is obtained for $\chi = 45°$, whereas under $\chi = 30°$ a larger difference is present with a lower stress at failure than in the experiments, similar to what was observed for the other considered strain-rates. This aspect can be improved by increasing the strength $f_{\parallel}$ in Eq. (3.66), but that action would result in an even larger offset for $\chi = 15°$.

In Fig. 3.20 the computationally determined stress at failure is plotted against the corresponding strain-rate in a semilog plot, and comparison is made with the experiment. It is clear that the model matches well with the experimental observations for the angles 45° and 90°. As the off-axis angle decreases the absolute difference between the model and the observation increases. We as-

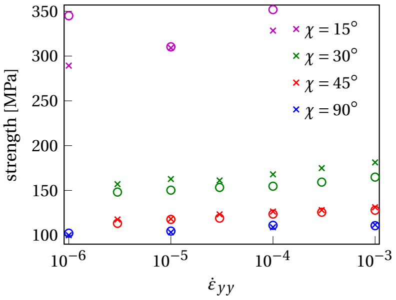

Figure 3.20: Material strength determined numerically (o) and experimentally (x) under different off-axis angles

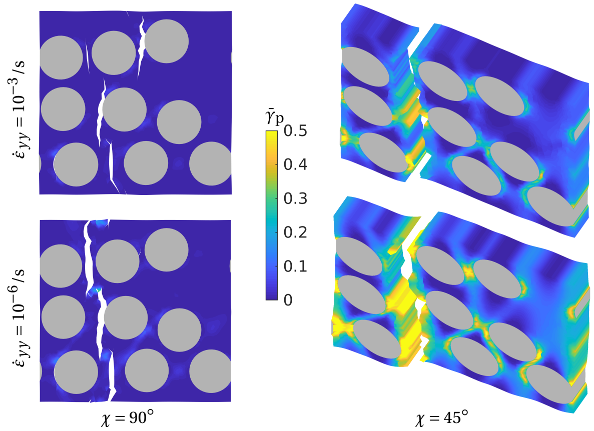

Figure 3.21: Distribution of equivalent plastic strain in fracturing RVE for two different strain-rates and off-axis angles

sume that the biggest part of this difference is due to an inconsistent stress state in the experiment and the micromodel, whose effect increases for lower off-axis angles.

The fracturing RVE is visualized in Fig. 3.21 for two different strain-rates: $\dot{\varepsilon}_{yy} = 10^{-3}$/s, $\dot{\varepsilon}_{yy} = 10^{-6}$/s, and two different off-axis angles: $\chi = 45°$ and $\chi = 90°$. The contour plots indicate the distribution of the equivalent plastic strain in the polymer matrix. There is more equivalent plastic strain accumulated for $\chi = 45°$ compared to $\chi = 90°$, in line with the observation that the 45° response is much more ductile than the 90° response, see e.g. Fig. 3.17. Comparing the strain-rates considered, there is more equivalent plastic strain for the lower strain-rate of 10^{-6}/s for both off-axis angles.

The nonlinear response of the RVE is a competition of viscoplasticity and microcracking. To shed light on the contribution of the each source of nonlinearity, the RVE response without microcracking is plotted together with the RVE response when microcracking is included, and the comparison is made with the experiments for different off-axis angles and $\dot{\varepsilon}_{yy} = 10^{-4}$/s, see Fig. 3.22. As can be observed from the figure, initially the nonlinear response is not affected by microcracking and therefore is dominated by viscoplasticity. However, without microcracking the RVE response is monotonically hardening, which does not provide an opportunity to define the failure point. Therefore, the presence of cohesive microcracks in the model is necessary to observe softening and define the material strength.

For all loading angles, the actual fracture plane forms in the post peak, i.e., in the softening regime. This process is depicted for $\chi = 45°$ and $\dot{\varepsilon}_{yy} = 10^{-4}$/s in Fig. 3.23, where four different

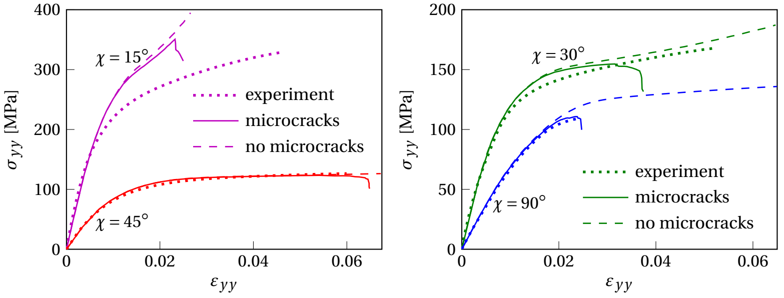

Figure 3.22: Simulation with microcracking and without microcracking compared with experiments for different off-axis angles and the strain-rate of 10^{-4}/s

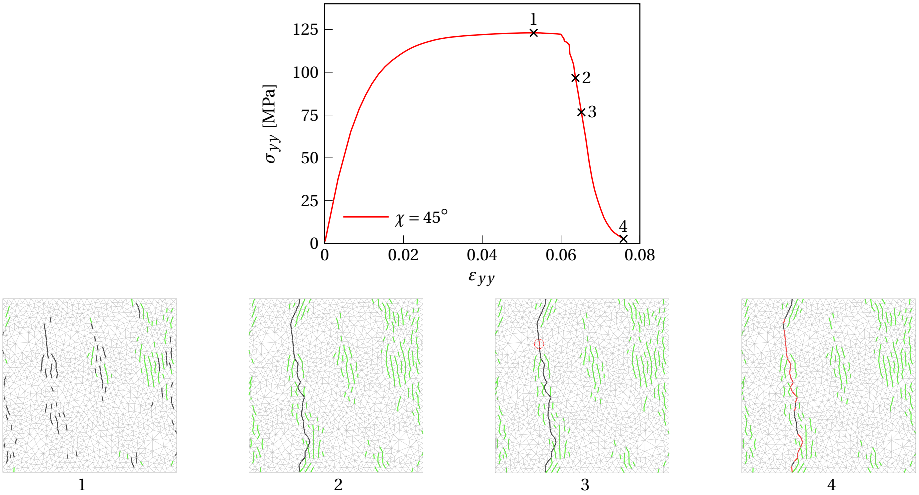

Figure 3.23: Evolution of microcracking process after the material strength is reached (snapshot 1); gray color indicates uncracked element boundaries, green color stand for unloading cohesive segments, black color indicates damaging but not completely broken cohesive segments, red color represents formed microcrack with zero cohesive traction

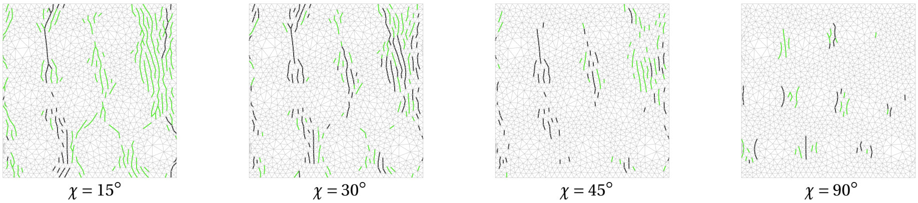

Figure 3.24: Density of initiated microcracks when material strength is reached for different off-axis angles and $\dot{\varepsilon}_{yy} = 10^{-4}$/s; color scheme is the same as in Fig. 3.23

states of the fracturing RVE corresponding to different points of the stress-strain curve are shown. After the material strength is reached (snapshot 1), the cohesive microcracks coalesce and deformation localizes in the fracture plane (snapshot 2), along which an actual microcrack is formed when the cohesive traction is reduced to zero locally (snapshot 3). This microcrack further propagates as more cohesive elements reach a fully damaged state along the initiated fracture plane (snapshot 4).

From Fig. 3.23 it is concluded that no actual microcracks with zero cohesive traction exist in the RVE when the maximum homogenized stress is reached. This fact holds true for other off-axis angles as well, and is depicted in Fig. 3.24, where snapshots captured at the moment of reaching the peak point in the RVE stress-strain curve are shown. The absence of cohesive segments with zero traction when the peak point is reached implies that the fracture process zone up to the failure point is larger than the RVE. Further, it is observed that the density of cohesive microcracks decreases with an increase in the off-axis angle.

The ability of the model to account for changes in the material composition is illustrated next. The strain-rate $\dot{\varepsilon}_{yy} = 10^{-4}$/s is applied on the RVE under several off-axis angles, considering the fiber volume ratio of 0.4, 0.5 and 0.6. The obtained results are shown in Fig. 3.25. As expected, an increase in the fiber volume ratio increases the initial stiffness of the model. Furthermore, an increase in V_f leads to a decrease in the strain at failure, implying more brittle behavior of the composite material. As for the ultimate strength, or the stress at failure, no clear trend is observed. In most of the cases, the strength increases for increasing V_f, but for $\chi = 15°$ the lowest strength is

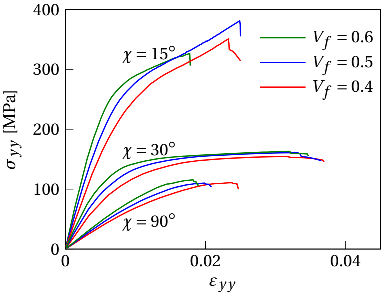

Figure 3.25: Micromodel response for several fiber volume ratios, under different off-axis angles

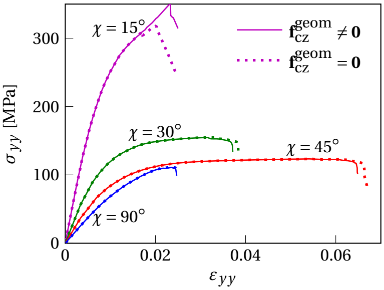

Figure 3.26: Comparison of RVE response when cohesive zone geometric nonlinear effect is accounted for, and when this effect is neglected

obtained with $V_f = 0.6$.

Quite often the modeling of failure processes in engineering materials by means of a cohesive zone model neglects the related geometric nonlinear effect. In this chapter we have used a finite deformation framework that allows for geometric nonlinearity in the cohesive zones as well, see Eq. (3.19). To check the effect of this on the RVE response, results as shown before that include the geometric contribution are plotted together with simulation results for which this contribution is neglected. The results are shown in Fig. 3.26, for $\dot{\varepsilon}_{yy} = 10^{-4}$/s and a range of off-axis angles. For the off-axis angles 30°-90° there is a small effect of the geometric nonlinear part, reflected in different strain at failure, whereas the stress at failure remains almost the same. For $\chi = 15°$ the geometric nonlinear effect is more obvious. In this case, carbon fibers bear most of the loading and a small variation in the stress and displacement field caused by the geometric nonlinear part results in obviously different stress at failure.

It should be noted that, even if the geometric contribution to the force vector was neglected, in the process of linearization there would still be a geometric contribution to the global tangent stiffness matrix. Specifically, $\mathbf{K}_{g1}$ without the factor of 2, and $\mathbf{K}_{g3}$ in Eq. (3.26) would be nonzero.

3.6. CONCLUSION

In this chapter a 3D microscale model to simulate rate-dependent failure in unidirectional composites under off-axis loading is introduced. A prescribed macroscopic strain-rate is applied on the RVE by means of an arclength control method. The RVE model is constructed in local coordinate frame aligned with the reinforcement that may have an arbitrary orientation with respect to the global loading direction. The micromodel is defined in the finite deformation framework, and accounts for two different nonlinear processes in the polymer matrix: viscous plasticity and microcracking. The plastic deformation is represented with the Eindhoven Glassy Polymer material model, whereas a cohesive zone model represents the microcracking process. Cohesive segments are added on the fly, whenever a microcrack initiation criterion is satisfied. A new initiation criterion based on the local stress as well as the local rate of deformation state in the matrix is introduced. The fracture energy of the cohesive law depends on the mode of fracture, but is not changing for different strain-rates in the model. The presence of cohesive microcracks in the model is necessary to reach the material strength and trigger the softening response.

The ability of the RVE model to predict failure of the material is illustrated through comparison with experiments on thermoplastic UD C/PEEK composite laminates for different strain-rates and off-axis angles, at room temperature conditions. A good match is obtained for the off-axis angles 45°-90°, whereas the discrepancy between the simulation and the observation increases for the off-axis angle of 30°, and especially for 15°. A large influence of rotations of the fibers on the averaged stress-strain response is identified for the smaller off-axis angles. This observation supports the proposed explanation for the mismatch between model and test: that boundary conditions in the experiment introduce macroscopic variations in the deformation, which are not accounted for in the microscale simulations. The contour plots of the fractured RVE indicate that more equivalent plastic strain accumulates for lower strain-rates, implying the more brittle failure of the material at higher strain-rates. It has been shown that the geometric nonlinearity of the cohesive zone model has negligible impact on failure stress of C/PEEK composite system, except for $\chi = 15°$.

3.7. DATA AVAILABILITY

Data presented in this chapter are available at the 4TU.ResearchData repository through `https://doi.org/10.4121/20065976.v1`

3.8. APPENDIX

To find derivatives $\partial\mathbf{Q}/\partial\mathbf{a}$ we express the transformation matrix components, Eq. (3.27), in terms of the initial nodal coordinates X, Y, Z and corresponding nodal displacements. Given the isoparametric mapping this is initially possible for the vectors $\mathbf{s}$ and $\mathbf{t}'$. Combining Eqs. (3.28)-(3.31) the x-component of the vector $\mathbf{s}$ is:

$$\begin{aligned} s_x = \frac{\tilde{s}_x}{\|\tilde{\mathbf{s}}\|} = \frac{1}{2}[&N_{\mathrm{A},\xi}(X_1 + u_{x1} + X_7 + u_{x7}) + N_{\mathrm{D},\xi}(X_4 + u_{x4} + X_{10} + u_{x10}) \\ &+N_{\mathrm{B},\xi}(X_2 + u_{x2} + X_8 + u_{x8}) + N_{\mathrm{E},\xi}(X_5 + u_{x5} + X_{11} + u_{x11}) \\ &+N_{\mathrm{C},\xi}(X_3 + u_{x3} + X_9 + u_{x9}) + N_{\mathrm{F},\xi}(X_6 + u_{x6} + X_{12} + u_{x12})]/\|\tilde{\mathbf{s}}\| \end{aligned} \tag{3.71}$$

Components s_y and s_z can be obtained in a similar way, replacing X respectively with Y and Z initial nodal coordinates, and also replacing u_{xi} with nodal displacements associated with y- and z-direction. In Eq. (3.71) the shape function gradients in ξ-direction are defined as:

$$\begin{aligned} N_{\mathrm{A},\xi} &= \frac{1}{4}(1-\eta)(2\xi-1), & N_{\mathrm{D},\xi} &= \frac{1}{4}(1+\eta)(2\xi+1) \\ N_{\mathrm{B},\xi} &= -(1-\eta)\xi, & N_{\mathrm{E},\xi} &= -(1+\eta)\xi \\ N_{\mathrm{C},\xi} &= \frac{1}{4}(1-\eta)(2\xi+1), & N_{\mathrm{F},\xi} &= \frac{1}{4}(1+\eta)(2\xi-1) \end{aligned} \tag{3.72}$$

Following the same approach but combining Eqs. (3.28)-(3.30) with Eq. (3.32), it is possible to derive expressions for the components of the vector $\mathbf{t}'$. The x-component of this vector is:

$$\begin{aligned} t'_x = \frac{\tilde{t}'_x}{\|\tilde{\mathbf{t}}'\|} = \frac{1}{2}[&N_{\mathrm{A},\eta}(X_1 + u_{x1} + X_7 + u_{x7}) + N_{\mathrm{D},\eta}(X_4 + u_{x4} + X_{10} + u_{x10}) \\ &+N_{\mathrm{B},\eta}(X_2 + u_{x2} + X_8 + u_{x8}) + N_{\mathrm{E},\eta}(X_5 + u_{x5} + X_{11} + u_{x11}) \\ &+N_{\mathrm{C},\eta}(X_3 + u_{x3} + X_9 + u_{x9}) + N_{\mathrm{F},\eta}(X_6 + u_{x6} + X_{12} + u_{x12})]/\|\tilde{\mathbf{t}}'\| \end{aligned} \tag{3.73}$$

where the shape function gradients in η-direction are as follows:

$$\begin{aligned} N_{\mathrm{A},\eta} &= -\frac{1}{4}(\xi^2-\xi), & N_{\mathrm{D},\eta} &= \frac{1}{4}(\xi^2+\xi) \\ N_{\mathrm{B},\eta} &= -\frac{1}{2}(1-\xi^2), & N_{\mathrm{E},\eta} &= \frac{1}{2}(1-\xi^2) \\ N_{\mathrm{C},\eta} &= -\frac{1}{4}(\xi^2+\xi), & N_{\mathrm{F},\eta} &= \frac{1}{4}(\xi^2-\xi) \end{aligned} \tag{3.74}$$

From Eq. (3.71) it is possible to find the derivative of the s_x component with respect to the nodal displacements:

$$s_{x,\mathbf{a}} = \frac{\partial}{\partial \mathbf{a}}\left(\frac{\tilde{s}_x}{\|\tilde{\mathbf{s}}\|}\right) = \frac{\tilde{s}_{x,\mathbf{a}}\|\tilde{\mathbf{s}}\| - \tilde{s}_x\|\tilde{\mathbf{s}}\|_{,\mathbf{a}}}{\|\tilde{\mathbf{s}}\|^2} \tag{3.75}$$

in which the derivative of the norm $\|\tilde{\mathbf{s}}\|$ is defined as:

$$\|\tilde{\mathbf{s}}\|_{,\mathbf{a}} = \frac{\tilde{s}_x\tilde{s}_{x,\mathbf{a}} + \tilde{s}_y\tilde{s}_{y,\mathbf{a}} + \tilde{s}_z\tilde{s}_{z,\mathbf{a}}}{\|\tilde{\mathbf{s}}\|} \tag{3.76}$$

Differentiation of the numerator in Eq. (3.71) with respect to the vector **a** yields the following expression:

$$\begin{aligned} \tilde{s}_{x,\mathbf{a}} = \frac{1}{2}[&N_{\mathrm{A},\xi} \quad 0 \quad 0 \quad N_{\mathrm{B},\xi} \quad 0 \quad 0 \quad N_{\mathrm{C},\xi} \quad 0 \quad 0 \ldots \\ &N_{\mathrm{D},\xi} \quad 0 \quad 0 \quad N_{\mathrm{E},\xi} \quad 0 \quad 0 \quad N_{\mathrm{F},\xi} \quad 0 \quad 0 \quad \text{repeat}]_{1\times 36(\mathrm{ndof})} \end{aligned} \tag{3.77}$$

which can be substituted in Eqs. (3.75) and (3.76). The vectors $\tilde{s}_{y,\mathbf{a}}$ and $\tilde{s}_{z,\mathbf{a}}$ from Eq. (3.76) are determined in a similar way as $\tilde{s}_{x,\mathbf{a}}$. After determining the vectors $\tilde{s}_{x,\mathbf{a}}$, $\tilde{s}_{y,\mathbf{a}}$ and $\tilde{s}_{z,\mathbf{a}}$ it is possible to calculate $s_{x,\mathbf{a}}$ with Eq. (3.75), as well as the vectors $s_{y,\mathbf{a}}$ and $s_{z,\mathbf{a}}$ with similar expressions.

For completeness, similar equations are shown for the derivative of $\mathbf{t}'$ vector x-component:

$$t'_{x,\mathbf{a}} = \frac{\partial}{\partial \mathbf{a}}\left(\frac{\tilde{t}'_x}{\|\tilde{\mathbf{t}}'\|}\right) = \frac{\tilde{t}'_{x,\mathbf{a}}\|\tilde{\mathbf{t}}'\| - \tilde{t}'_x\|\tilde{\mathbf{t}}'\|_{,\mathbf{a}}}{\|\tilde{\mathbf{t}}'\|^2} \tag{3.78}$$

$$\|\tilde{\mathbf{t}}'\|_{,\mathbf{a}} = \frac{\tilde{t}'_x\tilde{t}'_{x,\mathbf{a}} + \tilde{t}'_y\tilde{t}'_{y,\mathbf{a}} + \tilde{t}'_z\tilde{t}'_{z,\mathbf{a}}}{\|\tilde{\mathbf{t}}'\|} \tag{3.79}$$

$$\begin{aligned} \tilde{t}'_{x,\mathbf{a}} = \frac{1}{2}[&N_{\mathrm{A},\eta} \quad 0 \quad 0 \quad N_{\mathrm{B},\eta} \quad 0 \quad 0 \quad N_{\mathrm{C},\eta} \quad 0 \quad 0 \ldots \\ &N_{\mathrm{D},\eta} \quad 0 \quad 0 \quad N_{\mathrm{E},\eta} \quad 0 \quad 0 \quad N_{\mathrm{F},\eta} \quad 0 \quad 0 \quad \text{repeat}]_{1\times 36(\mathrm{ndof})} \end{aligned} \tag{3.80}$$

Now that the vectors $s_{i,\mathbf{a}}$ and $t'_{i,\mathbf{a}}$ are fully defined, where $i = x, y, z$, they can be used to define the change in the unit normal vector with nodal displacements. Differentiating Eq. (3.33) with respect to **a** leads to:

$$\frac{\partial \mathbf{n}}{\partial \mathbf{a}} = \begin{bmatrix} n_{x,\mathbf{a}} \\ n_{y,\mathbf{a}} \\ n_{z,\mathbf{a}} \end{bmatrix} = \begin{bmatrix} s_{y,\mathbf{a}}t'_z + s_y t'_{z,\mathbf{a}} - s_{z,\mathbf{a}}t'_y - s_z t'_{y,\mathbf{a}} \\ s_{z,\mathbf{a}}t'_x + s_z t'_{x,\mathbf{a}} - s_{x,\mathbf{a}}t'_z - s_x t'_{z,\mathbf{a}} \\ s_{x,\mathbf{a}}t'_y + s_x t'_{y,\mathbf{a}} - s_{y,\mathbf{a}}t'_x - s_y t'_{x,\mathbf{a}} \end{bmatrix} \tag{3.81}$$

Applying the same differentiation procedure in Eq. (3.34) yields:

$$\frac{\partial \mathbf{t}}{\partial \mathbf{a}} = \begin{bmatrix} t_{x,\mathbf{a}} \\ t_{y,\mathbf{a}} \\ t_{z,\mathbf{a}} \end{bmatrix} = \begin{bmatrix} n_{y,\mathbf{a}}s_z + n_y s_{z,\mathbf{a}} - n_{z,\mathbf{a}}s_y - n_z s_{y,\mathbf{a}} \\ n_{z,\mathbf{a}}s_x + n_z s_{x,\mathbf{a}} - n_{x,\mathbf{a}}s_z - n_x s_{z,\mathbf{a}} \\ n_{x,\mathbf{a}}s_y + n_x s_{y,\mathbf{a}} - n_{y,\mathbf{a}}s_x - n_y s_{x,\mathbf{a}} \end{bmatrix} \tag{3.82}$$

Eqs. (3.81) and (3.82), together with the vectors $s_{i,\mathbf{a}}$ are finally used in Eq. (3.35) to construct $\partial\mathbf{Q}/\partial\mathbf{a}$.

REFERENCES

[1] Kovačević D, Sundararajan BK, Van der Meer FP. Microscale modeling of rate-dependent failure in thermoplastic composites under off-axis loading. *Eng Fract Mech*, 276, 2022, p. 108884. DOI: `10.1016/j.engfracmech.2022.108884`.

[2] Alderliesten R. *Introduction to aerospace structures and materials*. Delft University of Technology, 2018.

[3] Azzi VD, Tsai SW. Anisotropic strength of composites. *Exp Mech*, 5 (9), 1965, pp. 283–288. DOI: `10.1007/BF02326292`.

[4] Tsai SW, Wu EM. A general theory of strength for anisotropic materials. *J Compos Mater*, 5 (1), 1971, pp. 58–80. DOI: `10.1177/002199837100500106`.

[5] Hashin Z, Rotem A. A fatigue failure criterion for fiber reinforced materials. *J Compos Mater*, 7 (4), 1973, pp. 448–464. DOI: `10.1177/002199837300700404`.

[6] Puck A, Schürmann H. Failure analysis of FRP laminates by means of physically based phenomenological models. *Compos Sci Technol*, 62 (12), 2002, pp. 1633–1662. DOI: `10.1016/S0266-3538(01)00208-1`.

[7] Dávila CG, Camanho PP, Rose CA. Failure Criteria for FRP Laminates. *J Compos Mater*, 39 (4), 2005, pp. 323–345. DOI: `10.1177/0021998305046452`.

[8] Camanho PP et al. Three-dimensional invariant-based failure criteria for fibre-reinforced composites. *Int J Solids Struct*, 55, 2015, pp. 92–107. DOI: `10.1016/j.ijsolstr.2014.03.038`.

[9] Sun Q et al. Failure criteria of unidirectional carbon fiber reinforced polymer composites informed by a computational micromechanics model. *Compos Sci Technol*, 172, 2019, pp. 81–95. DOI: `10.1016/j.compscitech.2019.01.012`.

[10] Totry E, González C, LLorca J. Prediction of the failure locus of C/PEEK composites under transverse compression and longitudinal shear through computational micromechanics. *Compos Sci Technol*, 68 (15), 2008, pp. 3128–3136. DOI: `10.1016/j.compscitech.2008.07.011`.

[11] Vogler T, Kyriakides S. Inelastic behavior of an AS4/PEEK composite under combined transverse compression and shear. Part I: experiments. *Int J Plast*, 15 (8), 1999, pp. 783–806. DOI: `10.1016/S0749-6419(99)00011-X`.

[12] Vaughan T, McCarthy C. A micromechanical study on the effect of intra-ply properties on transverse shear fracture in fibre reinforced composites. *Composites A*, 42 (9), 2011, pp. 1217–1228. DOI: `10.1016/j.compositesa.2011.05.004`.

[13] Sharma A, Daggumati S, Gupta A, Van Paepegem W. On the prediction of the bi-axial failure envelope of a UD CFRP composite lamina using computational micromechanics: Effect of microscale parameters on macroscale stress–strain behavior. *Compos Struct*, 251, 2020, p. 112605. DOI: `10.1016/j.compstruct.2020.112605`.

[14] Bhuiyan FH, Sanei SHR, Fertig RS. Predicting variability in transverse effective elastic moduli and failure initiation strengths in UD composite microstructures due to randomness in fiber location and morphology. *Compos Struct*, 237, 2020, p. 111887. DOI: `10.1016/j.compstruct.2020.111887`.

[15] Bai X et al. High-fidelity micro-scale modeling of the thermo-visco-plastic behavior of carbon fiber polymer matrix composites. *Compos Struct*, 134, 2015, pp. 132–141. DOI: `10.1016/j.compstruct.2015.08.047`.

[16] Gao J et al. Predictive multiscale modeling for Unidirectional Carbon Fiber Reinforced Polymers. *Compos Sci Technol*, 186, 2020, p. 107922. DOI: `10.1016/j.compscitech.2019.107922`.

[17] Sato M et al. Numerical simulation for strain rate and temperature dependence of transverse tensile failure of unidirectional carbon fiber-reinforced plastics. *J Compos Mater*, 53 (28-30), 2019, pp. 4305–4312. DOI: `10.1177/0021998319857111`.

[18] Govaert LE et al. A micromechanical approach to time-dependent failure in off-axis loaded polymer composites. *Composites A*, 32 (12), 2001, pp. 1697–1711. DOI: `10.1016/S1359-835X(01)00028-8`.

[19] Reinoso J, Paggi M. A consistent interface element formulation for geometrical and material nonlinearities. *Comput Mech*, 54 (6), 2014, pp. 1569–1581. DOI: `10.1007/s00466-014-1077-2`.

[20] Camacho GT, Ortiz M. Computational modelling of impact damage in brittle materials. *Int J Solids Struct*, 33 (20), 1996, pp. 2899–2938. DOI: `10.1016/0020-7683(95)00255-3`.

[21] Kovačević D, Van der Meer FP. Strain-rate based arclength model for nonlinear microscale analysis of unidirectional composites under off-axis loading. *Int J Solids Struct*, 250, 2022, p. 111697. DOI: `10.1016/j.ijsolstr.2022.111697`.

[22] Erartsin O, Van Drongelen M, Govaert LE. Identification of plasticity-controlled creep and fatigue failure mechanisms in transversely loaded unidirectional thermoplastic composites. *J Compos Mater*, 55 (14), 2021, pp. 1947–1965. DOI: `10.1177/0021998320964252`.

[23] Koerber H, Xavier J, Camanho PP. High strain rate characterisation of unidirectional carbon-epoxy IM7-8552 in transverse compression and in-plane shear using digital image correlation. *Mech Mater*, 42 (11), 2010, pp. 1004–1019. DOI: `10.1016/j.mechmat.2010.09.003`.

[24] Sun CT, Chung I. An oblique end-tab design for testing off-axis composite specimens. *Composites*, 24 (8), 1993, pp. 619–623. DOI: `10.1016/0010-4361(93)90124-Q`.

[25] Van der Meer FP. Micromechanical validation of a mesomodel for plasticity in composites. *Eur J Mech A Solids*, 60, 2016, pp. 58–69. DOI: `10.1016/j.euromechsol.2016.06.008`.

[26] Wells GN, de Borst R, Sluys LJ. A consistent geometrically non-linear approach for delamination. *Int J Numer Meth Engng*, 54 (9), 2002, pp. 1333–1355. DOI: `10.1002/nme.462`.

[27] Zhi J, Chen BY, Tay TE. Geometrically nonlinear analysis of matrix cracking and delamination in composites with floating node method. *Comput Mech*, 63 (2), 2019, pp. 201–217. DOI: `10.1007/s00466-018-1591-8`.

[28] Ortiz M, Pandolfi A. Finite-deformation irreversible cohesive elements for three-dimensional crack-propagation analysis. *Int J Numer Methods Eng*, 44 (9), 1999, pp. 1267–1282. DOI: `10.1002/(SICI)1097-0207(19990330)44:9<1267::AID-NME486>3.0.CO;2-7`.

[29] Belytschko T, Liu WK, Moran B, Elkhodary K. *Nonlinear finite elements for continua and structures.* John Wiley & Sons, 2014.

[30] Eyring H. Viscosity, plasticity, and diffusion as examples of absolute reaction rates. *J Chem Phys*, 4 (4), 1936, pp. 283–291. DOI: `10.1063/1.1749836`.

[31] Van Breemen LCA, Klompen ETJ, Govaert LE, Meijer HEH. Extending the EGP constitutive model for polymer glasses to multiple relaxation times. *J Mech Phys Solids*, 59 (10), 2011, pp. 2191–2207. DOI: `10.1016/j.jmps.2011.05.001`.

[32] Tervoort TA, Smit RJM, Brekelmans WAM, Govaert LE. A constitutive equation for the elasto-viscoplastic deformation of glassy polymers. *Mech Time Depend Mater*, 1 (3), 1997, pp. 269–291. DOI: `10.1023/A:1009720708029`.

[33] Klompen E, Govaert L. Nonlinear Viscoelastic Behaviour of Thermorheologically Complex Materials. *Mech Time Depend Mater*, 3 (1), 1999, pp. 49–69. DOI: `10.1023/A:1009853024441`.

[34] Klompen ETJ, Engels TAP, Govaert LE, Meijer HEH. Modeling of the postyield response of glassy polymers: Influence of thermomechanical history. *Macromolecules*, 38 (16), 2005, pp. 6997–7008. DOI: `10.1021/ma050498v`.

[35] Bonet J, Burton AJ. A simple orthotropic, transversely isotropic hyperelastic constitutive equation for large strain computations. *Comput Methods Appl Mech Eng*, 162 (1), 1998, pp. 151–164. DOI: `10.1016/S0045-7825(97)00339-3`.

[36] Miyagawa H et al. Transverse elastic modulus of carbon fibers measured by Raman spectroscopy. *Mater Sci Eng A*, 412 (1), 2005, pp. 88–92. DOI: `10.1016/j.msea.2005.08.037`.

[37] Liu Y, van der Meer FP, Sluys LJ, Ke L. Modeling of dynamic mode I crack growth in glass fiber-reinforced polymer composites: fracture energy and failure mechanism. *Eng Fract Mech*, 243, 2021, p. 107522. DOI: `10.1016/j.engfracmech.2020.107522`.

[38] Van der Meer FP, Sluys LJ. A phantom node formulation with mixed mode cohesive law for splitting in laminates. *Int J Fract*, 158 (2), 2009, p. 107. DOI: `10.1007/s10704-009-9344-5`.

[39] Hille TS, Suiker ASJ, Turteltaub S. Microcrack nucleation in thermal barrier coating systems. *Eng Fract Mech*, 76 (6), 2009, pp. 813–825. DOI: `10.1016/j.engfracmech.2008.12.010`.

[40] Christensen RM. *The theory of materials failure*. Oxford University Press, 2013.

[41] Bonet J, Wood RD. *Nonlinear continuum mechanics for finite element analysis*. Cambridge university press, 1997.

4

FAILURE UNDER CONSTANT STRESS

4.1. INTRODUCTION

Structural parts made of fiber reinforced polymer (FRP) composites usually require operational time that spans from several years to several decades [2]. Therefore, the long-term structural integrity of these components is of utmost importance. A challenge to this requirement is the inherent time dependent mechanical response of the composites which has its roots in the viscous nature of the polymer matrix. When exposed to a constant stress level FRP composites will undergo creep deformation, whose magnitude further depends on the off-axis loading angle, temperature, moisture, etc.

Many models that describe deformation kinetics of polymers are based on the Eyring thermally activated flow theory [3]. Kanters et al. [4] represented a constant plastic strain-rate in thermoplastic polymers and composites and applied a creep rupture criterion based on a critical value of the plastic strain accumulated in the material. The similar idea was followed by Erartsin et al. [5] and extended to off-axis failure of unidirectional (UD) glass/iPP composite systems. Also based on the Eyring flow theory, Spathis and Kontou [6] proposed an equation for the creep strain-rate, and assumed the creep rupture time as the moment when the creep strain-rate reaches a minimum value. Raghavan and Meshii [7] developed a creep rupture model for composites, in which the creep strain is modeled by the thermal activation theory, and the creep rupture happens when the stored elastic energy in the material attains a critical value. As an alternative to the Eyring flow theory, the single integral approach developed by Schapery [8] has often been used to represent the creep behavior in polymers. Lou and Schapery [9] showed that this theory can also represent the creep response of composites for different stress levels and off-axis angles. All models for the composite material mentioned so far aim to describe the homogenized response in (semi-)analytical form. Although this approach is computationally efficient, complete characterization of the homogenized orthotropic material is challenging, giving rise to complex formulations and extensive experimental identification procedures.

On the other side, computationally more expensive microscale models explicitly account for the heterogeneous microstructure of the composite material. In this context a numerical implementation of the Schapery's model for polymers was done by Haj-Ali and Muliana [10], and later used in the Aboudi four-cell micromodel [11] to represent the creep response of different FRP composites under off-axis loading [12], but no creep rupture was predicted. Jafaripour and Taheri-Behrooz [13] also applied the Schapery's integral to model creep behavior in a UD composite representative volume element (RVE). However, the RVE model is not suitable for every fiber orientation and does not predict creep rupture. In order to represent degradation of the composite constituents on the microlevel, Gal and Fish [14] applied an isotropic continuum creep damage model [15, 16], followed by the upscaling of the unit cell response in structural analyses of composite components. In a multiscale model aimed at predicting the time-dependent response of UD composites Govaert et al. [17] also addressed creep failure due to off-axis loading. The model assumes a regular distribution of fibers in the RVE, and a failure criterion based on the critical plastic strain at one point in the RVE.

Despite the vast amount of literature dealing with the micromechanical modeling of FRP composites, only a small part concerns the creep behavior and to our knowledge only the model by Gal and Fish [14] describes progressive creep rupture of the material. Recently, we have developed a micromechanical model to impose a constant strain-rate on the RVE under an off-axis angle [18], assuming finite deformations in the material locally and in the homogenized sense. The

---

Apart from minor text adjustments, this chapter is reproduced from [1].

model was supplemented with a cohesive surface methodology to simulate rate-dependent failure in thermoplastic composites [19]. In this study the microscale numerical model is modified to apply a constant stress on the RVE and analyze off-axis creep rupture in unidirectional composites. The Eindhoven Glassy Polymer (EGP) material model is used to represent the creep behavior in the polymer matrix. In order to simulate the rupture process, a modified version of the Reiner-Weissenberg material failure theory [20] is proposed. Specifically, when the Helmholtz free energy of the EGP model locally reaches a critical value, a cohesive segment is inserted in the RVE. The necessity to use a time-dependent cohesive law to model decohesion due to creep loading is illustrated. Global failure of the material coincides with the homogenized creep strain-rate of the RVE reaching a minimum value. Simulation results obtained for different off-axis angles, temperatures and stress levels are compared with experimental observations on a UD carbon / polyetheretherketone (PEEK) composite system.

The chapter is organized as follows: the experimental benchmark for comparing the model predictions is introduced in the next section. Then the micromechanical framework is outlined, with emphasis on the changes with respect to earlier work [18, 19]. In the subsequent section the constitutive models for the composite constituents are explained. Afterward, the results obtained by the model are compared with experiments.

4.2. EXPERIMENTAL BENCHMARK

Carbon fiber reinforced UD tapes with PEEK matrix were provided by Solvay. Previous research efforts by Erartsin et al. [21] on commercial UD tapes with the fiber volume fraction V_f of 0.6, showed a large scatter in the experimental data. Hence, in the experimental part of the project, tapes with more matrix ($V_f = 0.4$) than commercial tapes were preferred to ensure good repeatability of data. The tensile test coupons were prepared according to the procedure outlined in [19]. The coupons had a thickness of 1.8 mm and a width of 15 mm. A gauge length of 100 mm was used for 90° and 45° loaded samples. For smaller loading angles of 30° and 15°, a longer gauge length of 120 mm was used to contain the failure within the gauge section. A tab length of 25 mm was utilized to carry out the experiments. However, while carrying out experiments at higher temperature, smaller clamps that could fit inside the temperature chamber were used, with a reduced tab length of 20 mm.

Creep experiments under uniaxial tension at room temperature were performed using a Zwick Z100 universal tensile tester equipped with a 50 kN load cell. Zwick Z05 tester equipped with a smaller 5 kN load cell was used for higher temperature experiments, also utilizing temperature chambers with digital controls to ensure precise control of temperature, see Fig. 4.1 (right). A constant force was applied on the specimen, from which the engineering (eng.) stress was computed. The reported creep strains are a direct translation of the crosshead displacement, and measure the engineering strain. A schematic representation of the testing specimen is shown in Fig. 4.1 (left), where χ is the initial angle between the fibers and loading direction, often referred to as the off-axis angle. It is defined as $\chi = 90° - \theta_0$, where θ_0 is the initial angle between the global x-axis and the fibers, see Fig. 4.2.

4.3. MICROMECHANICAL FRAMEWORK

4.3.1. HOMOGENIZED KINEMATICS AND EXTERNAL FORCE VECTOR

In this section, the equations needed to impose a constant Cauchy stress on the RVE under an off-axis angle and compute the logarithmic strain in the global loading direction are presented. To facilitate the comparison with experimental results, the adjustment to impose a constant engineering stress on the RVE and calculate the engineering strain is introduced afterward.

In the case at hand unidirectional composite material is exposed to a constant stress, i.e., to creep loading conditions, see Fig. 4.2 (left). Beside the extensional deformation, this uniaxial loading will deform the orthotropic material also in shear, see Fig. 4.2 (middle). Due to the viscous nature of the polymer matrix, deformation in the material will keep increasing. Furthermore, accounting for finite strains in the material the local coordinate frame aligned with the reinforcement

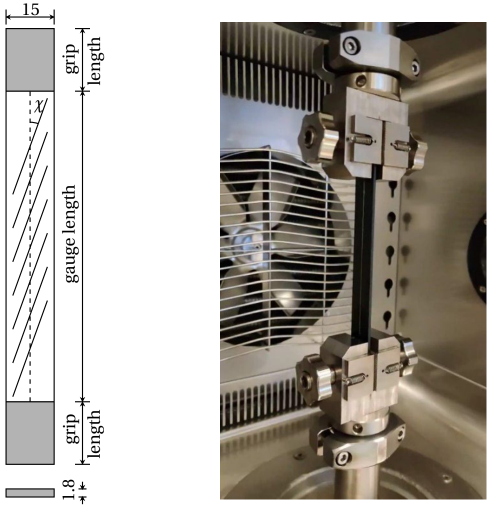

Figure 4.1: Schematic representation of testing specimen (left), where χ is the initial off-axis angle; creep testing of UD carbon/PEEK composite system at higher temperature in a temperature chamber (right); dimensions in mm

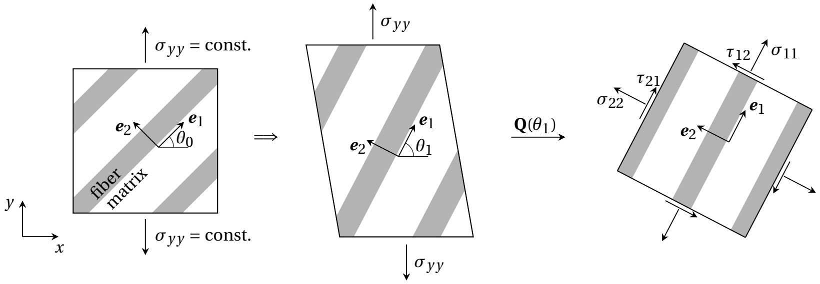

Figure 4.2: Constant stress applied on unidirectional composite material (left); deformed material due to uniaxial loading (middle); Cauchy stresses in local coordinate system (right)

may change orientation from the angle θ_0 to a new angle θ_1. Given the angle θ_1 the stress state can be transformed to the local coordinate frame, resulting in the Cauchy stress components shown in Fig. 4.2 (right). We aim to simulate this deformation process on the microscale, by means of an RVE model of a thin slice of material perpendicular to the fibers. Therefore, the homogenized stress components acting on the RVE, see Fig. 4.3 (left), must be equal to the stress components in Fig. 4.2 (right). This condition implies that the RVE, which is defined in the local coordinate system aligned with the fibers, must account for the change in orientation during the deformation process from the angle θ_0 to the angle θ_1. To satisfy this requirement, proper kinematic relations and the external force vector components acting on the micromodel need to be derived for a thin slice RVE. Defining an off-axis uniaxial stress state in an RVE while accounting for a possible update in its orientation can be achieved with the arclength formulation proposed in [18]. This formulation was originally designed for constant strain-rate simulations, where the deformation in load direction is known for every time step while the magnitude of the stress is not. By contrast, for creep simulations, the stress magnitude is given and the corresponding deformation unknown, which asks for a small modification of the formulation. We consider an RVE with periodic boundary conditions [22], that also enforce the periodicity in microcracking [23]. Homogenized kinematic relations are defined following displacement components of master nodes of the RVE. Active displacements of the master nodes are shown in Fig. 4.3 (right), accompanied with non-zero force components.

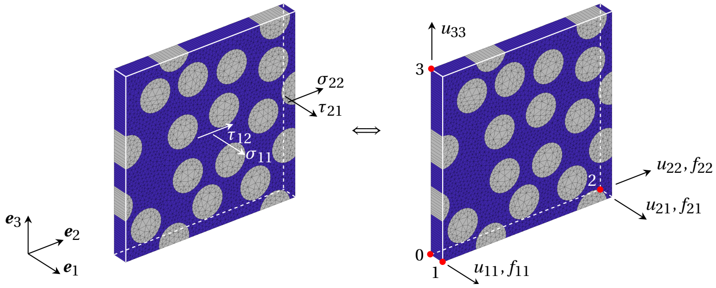

Figure 4.3: Homogenized stress components on RVE faces (left) as result of force components applied on RVE master nodes (right); non-zero displacement components of four RVE master nodes also indicated in the right figure

Master node displacements not indicated in the figure are set to zero. The detailed discussion of this choice of boundary conditions is presented in [18].

To derive expressions for the external force components, first we need to introduce the homogenized deformation gradient of the RVE, $\bar{\mathbf{F}}$. With the Dirichlet boundary conditions as defined in Fig. 4.3 (right), the homogenized deformation gradient is:

$$\bar{\mathbf{F}} = \begin{bmatrix} \bar{F}_{11} & \bar{F}_{12} & 0 \\ 0 & \bar{F}_{22} & 0 \\ 0 & 0 & \bar{F}_{33} \end{bmatrix} = \begin{bmatrix} 1 + \frac{u_{11}}{l_1^0} & \frac{u_{21}}{l_2^0} & 0 \\ 0 & 1 + \frac{u_{22}}{l_2^0} & 0 \\ 0 & 0 & 1 + \frac{u_{33}}{l_3^0} \end{bmatrix} \tag{4.1}$$

where u_{ij} is displacement of master node i in direction j, and l_i^0 is the initial length of the RVE in direction i. Components of the external force vector are derived considering the equilibrium between the homogenized internal and external force vector: $\bar{\mathbf{f}}^{\text{int}} = \bar{\mathbf{f}}^{\text{ext}}$. Without loss of generality we assume that the whole RVE domain is represented with a single trilinear hexahedral finite element. Following Belytchko et al. [24] the homogenized internal force vector can be expressed as:

$$\bar{\mathbf{f}}^{\text{int}} = \int_{\Omega_0} \bar{\mathbf{B}}_0^{\mathrm{T}} \bar{\mathbf{F}}^{-1} \bar{\boldsymbol{\sigma}} \bar{J} d\Omega_0 \tag{4.2}$$

in which $\bar{\mathbf{B}}_0$ is the strain - nodal displacement matrix defined over the reference configuration, $\bar{J}$ is the determinant of $\bar{\mathbf{F}}$, while $\bar{\boldsymbol{\sigma}}$ represents the homogenized Cauchy stress acting on the material in the local frame. After evaluating the integral in Eq. (4.2), the expressions for the corresponding external force vector components acting on the master nodes yield:

$$\begin{aligned} f_{11} &= \sigma_{yy} A_1^0 \bar{J} \left(\frac{s_1^2}{\bar{F}_{11}} - c_1 s_1 \frac{\bar{F}_{12}}{\bar{F}_{11} \bar{F}_{22}} \right) \\ f_{21} &= \sigma_{yy} A_2^0 \bar{J} \frac{c_1 s_1}{\bar{F}_{22}} \\ f_{22} &= \sigma_{yy} A_2^0 \bar{J} \frac{c_1^2}{\bar{F}_{22}} \end{aligned} \tag{4.3}$$

Here f_{ij} is force component acting on master node i in direction j, A_i^0 is the initial surface of the RVE on which a corresponding stress component is acting, while s_i and c_i denote $\sin(\theta_i)$ and $\cos(\theta_i)$ respectively, with i being either 0 or 1. The angle θ_1 is computed as: $\theta_1 = \theta_0 + \phi$, where the angle ϕ represents the change in orientation of the RVE in the deformation process. Following [18], it can be expressed as:

$$\phi = \arctan\left(\frac{-\bar{F}_{11} c_0 s_0 + \bar{F}_{12} s_0^2 + \bar{F}_{22} c_0 s_0}{\bar{F}_{11} c_0^2 - \bar{F}_{12} c_0 s_0 + \bar{F}_{22} s_0^2} \right) \tag{4.4}$$

The expressions for the force components, Eq. (4.3), are very similar to the unit force components of the strain-rate based arclength model [18], differing only for the presence of the creep stress σ_{yy}. When periodic boundary conditions are applied, every force component in Eq. (4.3) is distributed over the nodes belonging to the side of the RVE on which the force component is acting. This way, the external force vector $\mathbf{f}^{\text{ext}}$ applied on the RVE is fully defined. This vector has to be in equilibrium with the internal force vector, i.e., $\mathbf{f}^{\text{ext}} = \mathbf{f}^{\text{int}}$. In the presence of cracks, and the absence of body forces, the internal force vector is defined as presented in [19].

Since we are dealing with the creep problem, it is pertinent to plot the strain in the material versus time. For this purpose an expression for the homogenized strain component ε_{yy} corresponding to the creep stress in the global loading direction needs to be derived. To find this expression, a relation between the RVE homogenized deformation gradient and the deformation gradient $\mathbf{F}$ of the material in the global frame is needed. Due to the analogy between an off-axis creep stress and an off-axis strain-rate loading, we can follow the transformation rules and kinematic relations derived in [18] for an off-axis strain-rate acting on the material. Accordingly:

$$\mathbf{F} = \mathbf{Q}_1^{\mathrm{T}} \bar{\mathbf{F}} \mathbf{Q}_0 \tag{4.5}$$

In this equation $\mathbf{Q}_0$ is the transformation matrix that depends on the angle θ_0:

$$\mathbf{Q}_0 = \begin{bmatrix} \cos(\theta_0) & \sin(\theta_0) & 0 \\ -\sin(\theta_0) & \cos(\theta_0) & 0 \\ 0 & 0 & 1 \end{bmatrix} \tag{4.6}$$

The transformation matrix $\mathbf{Q}_1$ has the same form, although it depends on the angle θ_1. Given Eq. (4.5), the homogenized strain in the loading direction can be written as:

$$\varepsilon_{yy} = \ln(F_{yy}) \tag{4.7}$$

where F_{yy} is the component of $\mathbf{F}$ in the global loading direction.

Eqs. (4.3) and (4.7), impose the homogenized Cauchy (true) stress on the RVE and measure the homogenized logarithmic (true) strain, respectively. However, the experimental results are reported in the form of engineering strain as the result of a constant force imposed on the specimen. The consequence of applying the constant force and relying on the engineering stress, is that the actual stress on the material changes with deformation. In that regard, the Cauchy stress σ_{yy} in Eq. (4.3) is computed from the engineering stress σ_{yy}^{eng}:

$$\sigma_{yy} = \frac{\sigma_{yy}^{\text{eng}}}{F_{xx} F_{zz}} \tag{4.8}$$

where F_{xx} and F_{zz} are components of the homogenized deformation gradient in the global frame, Eq. (4.5). Finally, the engineering strain in the global loading direction is extracted from the model as follows:

$$\varepsilon_{yy}^{\text{eng}} = F_{yy} - 1 \tag{4.9}$$

4.3.2. IMPLEMENTATION

The computational framework for the model presented herein is based on the updated Lagrangian formulation [24], an approach suitable for modeling finite deformations. The equations introduced so far assume no discretization in time. However, in the spirit of a force controlled analysis an incremental-iterative procedure is applied, with a finite time increment Δt in every simulation step. In order to match the experiment in terms of the time needed to reach a constant load level, the engineering stress-rate $\dot{\sigma}_{yy}^{\text{eng}}$ is considered, such that at time step n the engineering stress in Eq. (4.8) is computed as follows:

$$\sigma_{yy,n}^{\text{eng}} = \min\left(\sigma_{yy,n-1}^{\text{eng}} + \dot{\sigma}_{yy}^{\text{eng}} \Delta t, \sigma_{yy}^{\text{const}}\right) \tag{4.10}$$

Table 4.1: Algorithm of the microscale creep model for time step n

```
1) set step size $\Delta t$
2) given $\bar{\mathbf{F}}^{n-1}$, compute $\phi$ from Eq.(4.4); set $\theta_1 = \theta_0 + \phi$
3) update $\mathbf{f}^{\text{ext}}$ using Eqs. (4.3) and (4.10), for eng. stress-strain use Eq. (4.8) in Eq. (4.3)
4) follow the algorithm outlined in [25]
5) if commit, compute $\varepsilon_{yy}$ combining Eqs. (4.5) and (4.7),
   for eng. strain, compute $\varepsilon_{yy}^{\text{eng}}$ combining Eqs. (4.5) and (4.9)
```

where $\sigma_{yy}^{\text{const}}$ is the constant (engineering) stress. If the simulation considers a constant Cauchy stress, then the superscript "eng" is dropped from Eq. (4.10) and $\sigma_{yy,n}$ is directly applied in Eq. (4.3) without correcting the stress for the previous deformation, as done in Eq. (4.8) for the engineering stress. The algorithm for one time step of the analysis is presented in Table 4.1. The core part of the implementation with adaptive stepping and insertion of cohesive cracks on the fly coincides with the algorithm introduced by Van der Meer and Sluys [25]. It should be noted that the external force vector is computed knowing the homogenized deformation gradient from the last converged time step $\bar{\mathbf{F}}^{n-1}$, and no update in the $\mathbf{f}^{\text{ext}}$ is made during iterations within the current time step.

4.4. CONSTITUTIVE MODELS

In this section the constitutive models representing the behavior of the composite constituents are outlined. The description of the EGP model for the polymer matrix is followed by explaining a transversely isotropic material model for carbon fibers. The creep rupture process is simulated with interelement cohesive surfaces that are inserted during the simulation. For the creep simulations, a new cohesive zone (CZ) initiation criterion is proposed as well as a time-dependent cohesive law.

4.4.1. THE EINDHOVEN GLASSY POLYMER CONSTITUTIVE MODEL

To represent the behavior of the polymer matrix we choose the EGP material model. The EGP is a 3D elasto-viscoplastic model without a yield surface. Instead, it is based on the Eyring flow theory [3], in the sense that the viscosity reduces with the stress applied on the material [26], leading to the flow of the polymer. In this regard, the yield point is perceived as the stress induced melting [27].

The model formulation builds upon the multiplicative decomposition of the deformation gradient in the elastic and the plastic part:

$$\mathbf{F}_i = \mathbf{F}_{i\text{e}} \cdot \mathbf{F}_{i\text{p}} \tag{4.11}$$

To make the distinction from the homogenized deformation gradient of the RVE in the global frame, Eq. (4.5), the subscript i is used to indicate the deformation gradient at integration point i inside the RVE. It is assumed that the plastic part of deformation is volume preserving, such that:

$$J_i = \det(\mathbf{F}_i) = \det(\mathbf{F}_{i\text{e}}) \tag{4.12}$$

The derivation of the Cauchy stress follows from principles of continuum thermodynamics as described by Khaleghi et al. [28], but without damage. Following the Clausius-Duhem inequality, the internal dissipation for an isothermal process can be written as:

$$\mathscr{D}_{\text{int}} = \boldsymbol{\sigma} : \mathbf{L} - \frac{1}{J_i}\dot{\psi} \geq 0 \tag{4.13}$$

where $\boldsymbol{\sigma}$ is the Cauchy stress, $\mathbf{L}$ is the velocity gradient, and ψ is the Helmholtz free energy. The free energy is decomposed in the hydrostatic part ψ_{h}, the hardening part ψ_{r}, and the driving part ψ_{d}. The definition of the hydrostatic free energy is the same as in [28]:

$$\psi_{\text{h}} = \frac{\kappa}{2}(J_i - 1)^2 \tag{4.14}$$

in which κ is the bulk modulus. The hardening part of the free energy is different than in [28] and is defined such that the derived stress component corresponds to the neo-Hookean model [27]. Accordingly:

$$\psi_\mathrm{r} = \frac{G_\mathrm{r}}{2}\left[\mathrm{tr}\left(\tilde{\mathbf{B}}\right) - 3\right] \tag{4.15}$$

where G_r is the hardening modulus, and $\tilde{\mathbf{B}}$ is the isochoric left Cauchy-Green deformation tensor:

$$\tilde{\mathbf{B}} = J_i^{-2/3}\left(\mathbf{F}_i \cdot \mathbf{F}_i^\mathrm{T}\right) \tag{4.16}$$

The driving component allows for thermorheologically complex response of the model, meaning that multiple relaxation processes may govern the material response. In this study, we consider two relaxation processes, α and β. In addition, each relaxation process may be represented by a number of Maxwell elements connected in parallel, with the mechanical analog of the stress tensor corresponding to the driving free energy shown in Fig. 4.4. Therefore, the driving free energy is defined as:

$$\psi_\mathrm{d} = \frac{1}{2}\sum_{k=1}^{p} G_{\alpha,k}\left[\mathrm{tr}\left(\tilde{\mathbf{B}}_{\mathrm{e}\alpha,k}\right) - 3\right] + \frac{1}{2}\sum_{l=1}^{q} G_{\beta,l}\left[\mathrm{tr}\left(\tilde{\mathbf{B}}_{\mathrm{e}\beta,l}\right) - 3\right] \tag{4.17}$$

In this equation, p and q are the number of modes respectively for process α and β, $G_{x,j}$ is the shear modulus of Maxwell element j belonging to relaxation process x, where x is either α or β, and j is either k or l, $\tilde{\mathbf{B}}_{\mathrm{e}x,j}$ is the isochoric elastic left Cauchy-Green deformation tensor of the same Maxwell element.

Given the definition of the free energy, the corresponding stress tensors can be defined. Following the Coleman-Noll formalism [29] and the procedure outlined in [28] the stress tensors corresponding to the free energy components emerge as:

$$\begin{aligned}
\boldsymbol{\sigma}_\mathrm{h} &= \kappa(J_i - 1)\mathbf{I} \\
\boldsymbol{\sigma}_\mathrm{r} &= \frac{1}{J_i} G_\mathrm{r}\tilde{\mathbf{B}}^\mathrm{d} \\
\boldsymbol{\sigma}_\mathrm{d} &= \sum_{k=1}^{p}\boldsymbol{\sigma}_{\alpha,k} + \sum_{l=1}^{q}\boldsymbol{\sigma}_{\beta,l} \\
&= \frac{1}{J_i}\sum_{k=1}^{p} G_{\alpha,k}\tilde{\mathbf{B}}^\mathrm{d}_{\mathrm{e}\alpha,k} + \frac{1}{J_i}\sum_{l=1}^{q} G_{\beta,l}\tilde{\mathbf{B}}^\mathrm{d}_{\mathrm{e}\beta,l}
\end{aligned} \tag{4.18}$$

where $\mathbf{I}$ is the second-order unit tensor, and the total Cauchy stress is the summation of three stress tensors, the hydrostatic stress $\boldsymbol{\sigma}_\mathrm{h}$, the hardening stress $\boldsymbol{\sigma}_\mathrm{r}$, and the driving stress $\boldsymbol{\sigma}_\mathrm{d}$: $\boldsymbol{\sigma} = \boldsymbol{\sigma}_\mathrm{h} + \boldsymbol{\sigma}_\mathrm{r} + \boldsymbol{\sigma}_\mathrm{d}$.

In order to determine $\tilde{\mathbf{B}}^\mathrm{d}_{\mathrm{e}x,j}$ in Eq. (4.18) it is necessary to integrate the rate equation of $\tilde{\mathbf{B}}_{\mathrm{e}x,j}$:

$$\dot{\tilde{\mathbf{B}}}_{\mathrm{e}x,j} = \left(\tilde{\mathbf{L}} - \mathbf{D}_{\mathrm{p}x,j}\right)\cdot\tilde{\mathbf{B}}_{\mathrm{e}x,j} + \tilde{\mathbf{B}}_{\mathrm{e}x,j}\cdot\left(\tilde{\mathbf{L}}^\mathrm{T} - \mathbf{D}_{\mathrm{p}x,j}\right) \tag{4.19}$$

Here, $\mathbf{D}_{\mathrm{p}x,j}$ is the plastic part of the rate of deformation tensor of Maxwell element j as part of relaxation process x, which is defined by introducing a constitutive relation of the form [30]:

$$\mathbf{D}_{\mathrm{p}x,j} = \frac{\boldsymbol{\sigma}_{x,j}}{2\eta_{x,j}(\bar{\tau}_x, p, S_x, T)} \tag{4.20}$$

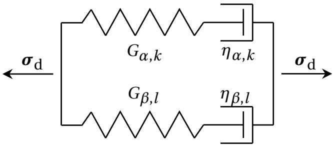

Figure 4.4: Mechanical analog for multi-process, multi-mode driving stress in the EGP model

Table 4.2: EGP model parameters

κ [MPa]	G_r [MPa]	V_α [nm^3]	V_β [nm^3]
2600	25	3.518	3.518
ΔH_α [kJ/mol]	ΔH_β [kJ/mol]	$\mu_\alpha = \mu_\beta$	$S_\alpha = S_\beta$
375.87	325.28	0.08	0

Table 4.3: Relaxation spectrum of the EGP model

x, j	$G_{x,j}$ [MPa]	$\eta_{0x,j}$ [MPa·s]
$\alpha, 1$	521.96	$1.992 \cdot 10^{26}$
$\beta, 1$	455.96	$4.965 \cdot 10^{22}$
$\beta, 2$	385.58	$5.518 \cdot 10^{21}$
$\beta, 3$	312.50	$6.761 \cdot 10^{20}$
$\beta, 4$	238.85	$2.108 \cdot 10^{19}$
$\beta, 5$	166.87	$1.591 \cdot 10^{15}$
$\beta, 6$	98.51	$2.571 \cdot 10^{12}$
$\beta, 7$	35.14	$7.086 \cdot 10^{9}$

where $\eta_{x,j}$ is the viscosity in the dashpot of Maxwell element j and relaxation process x. It is a function of the equivalent stress $\bar{\tau}_x$, the hydrostatic stress $p = -\mathrm{tr}(\boldsymbol{\sigma})/3$, the state parameter S_x and the absolute temperature T:

$$\eta_{x,j} = \eta_{0x,j} \frac{\bar{\tau}_x/\tau_{0x}}{\sinh(\bar{\tau}_x/\tau_{0x})} \exp\left(\frac{\mu_x p}{\tau_{0x}}\right) \exp(S_x) \exp\left[\frac{\Delta H_x}{R}\left(\frac{1}{T} - \frac{1}{T_\mathrm{ref}}\right)\right] \tag{4.21}$$

In this equation $\eta_{0x,j}$ is the initial viscosity, τ_{0x} is the characteristic shear stress, μ_x is the pressure dependency parameter, ΔH_x is the activation enthalpy, R is the gas constant, and $T_\mathrm{ref} = 298.15$ K is the reference absolute temperature. The equivalent stress is defined as:

$$\bar{\tau}_x = \sqrt{\frac{1}{2}\boldsymbol{\sigma}_x : \boldsymbol{\sigma}_x} \tag{4.22}$$

with $\boldsymbol{\sigma}_x = \sum \boldsymbol{\sigma}_{x,j}$, whereas the definition of the characteristic shear stress is:

$$\bar{\tau}_{0x} = \frac{k_\mathrm{B} T}{V_x} \tag{4.23}$$

in which k_B is the Boltzmann constant, and V_x is the activation volume.

The state parameter S_x takes into account the thermodynamical history of the material, which in turn depends on its processing history. In the EGP model it is represented as a product of the aging parameter $S_{\mathrm{a}x}$ and the softening function $R_{\gamma x}$, i.e., $S_x = S_{\mathrm{a}x} R_{\gamma x}$. Since the influence of processing on the mechanical properties is not addressed in this study, the aging parameter is set to zero. Furthermore, the experimental results considered in this study show no flattening of the creep curves, which, if present, would indicate progressive aging.

The EGP model parameters are shown in Table 4.2, while the relaxation spectrum is listed in Table 4.3. As claimed in [19], a different cristallinity of PEEK in the composite material and that of neat PEEK may imply a different mechanical behavior of the polymer matrix. Hence, the calibration of the EGP parameters was done directly on the creep experiments of UD tapes. Because the extensometer was not used in the experiments, the relaxation spectrum implicitly takes into account the compliance effect of the machine grips, see Fig. 4.1. More accurate measurements of the strain response would result in re-calibration of the EGP and the cohesive law parameters.

The equivalent plastic strain $\bar{\gamma}_\mathrm{p}$ in the EGP model is computed by integrating the evolution law:

$$\dot{\bar{\gamma}}_\mathrm{p} = \frac{\bar{\tau}_{\alpha,1}}{\eta_{\alpha,1}}, \quad \bar{\tau}_{\alpha,1} = \sqrt{\frac{1}{2}\boldsymbol{\sigma}_{\alpha,1} : \boldsymbol{\sigma}_{\alpha,1}} \tag{4.24}$$

where $\bar{\tau}_{\alpha,1}$ is the equivalent stress associated with the mode of highest viscosity $\eta_{\alpha,1}$.

4.4.2. TRANSVERSELY ISOTROPIC CONSTITUTIVE MODEL FOR CARBON FIBERS

With the assumption that failure processes take place only in the polymer matrix, carbon fibers are modeled with a hyperelastic transversely isotropic material model [31], with a small modification as presented in [18]. In the model, the Cauchy stress is decomposed in two parts:

$$\boldsymbol{\sigma} = \boldsymbol{\sigma}_{\text{iso}} + \boldsymbol{\sigma}_{\text{tri}} \tag{4.25}$$

where the neo-Hookean model [24] describes the isotropic stress tensor:

$$\boldsymbol{\sigma}_{\text{iso}} = \frac{\mu}{J_i}(\mathbf{B} - \mathbf{I}) + \frac{\lambda}{J_i}\ln(J_i)\mathbf{I} \tag{4.26}$$

while the transversely isotropic part of the stress tensor is derived as:

$$\boldsymbol{\sigma}_{\text{tri}} = J_i^{-1}\{2\beta(I_4 - 1)\mathbf{B} + 2[\alpha + \beta(I_1 - 3) + 2\gamma(I_4 - 1)]\boldsymbol{a} \otimes \boldsymbol{a} - \alpha(\mathbf{B}\boldsymbol{a} \otimes \boldsymbol{a} + \boldsymbol{a} \otimes \mathbf{B}\boldsymbol{a})\} \tag{4.27}$$

In Eqs. (4.26) and (4.27) J_i is the determinant of the deformation gradient at an integration point, $\mathbf{B}$ is the left Cauchy-Green deformation tensor, $\mathbf{I}$ is the second-order unit tensor, $\boldsymbol{a}$ is the vector defining the material preferential stiffness direction in the deformed configuration. The invariants I_1 and I_4 are defined as:

$$\begin{aligned} I_1 &= \text{tr}(\mathbf{B}) \\ I_4 &= \boldsymbol{a} \cdot \boldsymbol{a} \end{aligned} \tag{4.28}$$

The other model parameters assume the form as presented in [18]:

$$\begin{aligned} n &= \frac{E_1}{E_2} \\ m &= 1 - \nu_{23} - 2n\nu_{12}^2 \\ \lambda &= \frac{E_2(\nu_{23} + n\nu_{12}^2)}{m(1+\nu_{23})} \\ \mu &= \frac{E_2}{2(1+\nu_{23})} \\ \alpha &= \mu - G_{12} \\ \beta &= \frac{E_2(\nu_{12} + \nu_{23}\nu_{12} - \nu_{23} - n\nu_{12}^2)}{4m(1+\nu_{23})} \\ \gamma &= \frac{E_1(1-\nu_{23})}{8m} - \frac{\lambda + 2\mu}{8} + \frac{\alpha}{2} - \beta \end{aligned} \tag{4.29}$$

The five elastic constants of the material model are shown in Table 4.4, where E_1 is the Young's modulus in the preferential stiffness direction. It was determined from quasi-static experiments on UD tapes under 0° off-axis angle. E_2 and ν_{23} are the Young's modulus and the Poisson's ratio defining the model behavior in the plane of isotropy, adopted according to [32]. G_{12} and ν_{12} are the shear modulus and the Poisson's ratio in the plane perpendicular to the isotropic plane. The former is determined in the process of fitting the experimental creep response of the composite material for 45° loading angle, while the latter is adopted according to [18], which ensures the computational stability of the hyperelastic constitutive model.

Table 4.4: Elastic constants of the transversely isotropic constitutive model

E_1 [GPa]	E_2 [GPa]	G_{12} [GPa]	ν_{12}	ν_{23}
125	15	5	0.05	0.3

4.4.3. MICROCRACK INITIATION

The EGP model can capture creep deformation but it does not predict creep rupture in the material. According to Fig. 4.4, as creep deformation proceeds, there is stress relaxation in the Maxwell elements, which is picked up by the elastic hardening and hydrostatic stress components. In the limit of complete stress redistribution the creep deformation would reach a constant value without failure taking place.

In order to simulate the creep rupture mechanism in the RVE the cohesive zone modeling is applied. When a suitable initiation criterion is satisfied, a cohesive segment is inserted between two bulk finite elements on the fly [33]. A stress-based initiation criterion seems not suitable for capturing creep rupture because the microscale stresses might remain less than a prescribed critical value, while rupture may still occur if the creep load is kept long enough, making it difficult to actually define the critical stress. Therefore, we also account for the deformation component by proposing an initiation criterion that is energy-based. According to the Reiner-Weissenberg theory [20], material fails when the deviatoric part of the stored energy attains a critical value. In a slightly modified form this theory was followed by Brüller [34] to model failure in thermoplastic polymers, and by Hiel et al. [35] to model failure of polymer composites. Instead of the deviatoric part, as stated by Brinson [2], the total stored energy may be a better indicator of failure in composites. Following this idea, we propose that a cohesive microcrack initiates when the total free energy reaches a critical value. In order to define the critical value ψ_{cr}, it is pertinent to plot the evolution of the free energy and its components for different loading angles, without adding cohesive segments in the micromodel. For several points in the RVE that exceed the eventually determined critical energy this evolution is shown in Fig. 4.5, for two loading angles, 90° and 45°, and two stress levels, 95 MPa and 112 MPa, respectively. Vertical and horizontal gray lines show the time instance on which the constant stress level is reached and the eventual calibrated value for the critical energy value, respectively. The total free energy evolves differently for the two loading angles, resulting in much lower energy values for $\chi = 90°$. Much of the difference is due to the significantly different change in the hardening part of the free energy, which for $\chi = 45°$ attains a high value. The homogenized strain evolution corresponding to these two loading cases is shown in Fig. 4.23 in Appendix A.

The chosen value for the critical energy is $\psi_{\mathrm{cr}} = 2.74\ \mathrm{N/mm^2}$. This value needs to be low enough to have progressive failure in $\chi = 90°$ simulations, but high enough to avoid premature failure in $\chi = 45°$ simulations. The balancing between these two requirements is due to the large difference in the stored energy for the two loading angles. The critical value intersects the total energy already in the phase of increasing loading ($t < 10$ s) for the 45° loading angle. In this phase the driving energy part reaches a maximum after which relaxation takes place and this energy part reduces, for some points even to a negative value, see Fig 4.5(right). What causes the unexpected

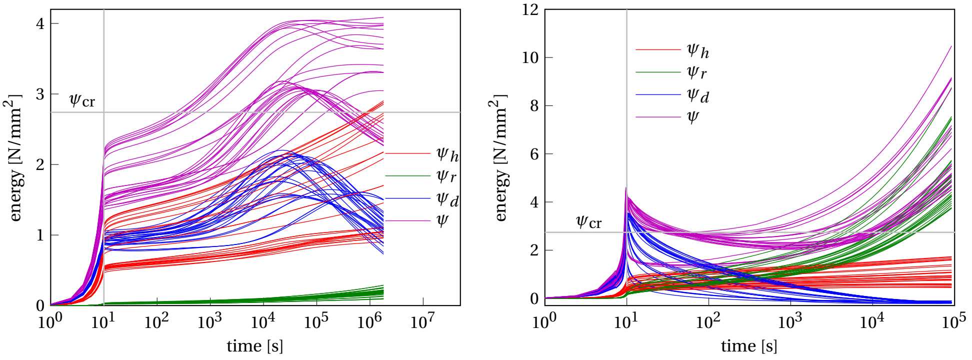

Figure 4.5: Evolution of the Helmholtz free energy and its components in the EGP model for $\chi = 90°$ and $\sigma_{yy}^{\mathrm{eng}} = 95$ MPa (left), $\chi = 45°$ and $\sigma_{yy}^{\mathrm{eng}} = 112$ MPa (right); $T = 25°$C

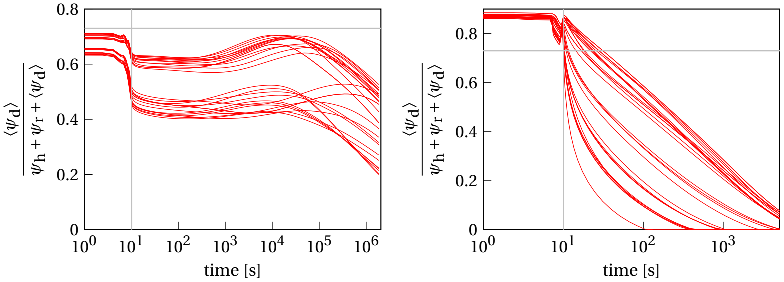

Figure 4.6: Ratio of driving free energy component and the total free energy for $\chi = 90°$ and $\sigma_{yy}^{\mathrm{eng}} = 95$ MPa (left), $\chi = 45°$ and $\sigma_{yy}^{\mathrm{eng}} = 112$ MPa (right); $T = 25°$C; horizontal gray line at 0.73 defines the energy ratio above which microcrack initiation is not allowed

negative energy deserves special attention in future investigations, but is outside the scope of this thesis. When computing the total free energy, which remains positive in a deformed state, the possible negative values of the driving energy are precluded by performing the Macaulay operation: $\langle\psi_{\mathrm{d}}\rangle = \max(0, \psi_{\mathrm{d}})$. Since this energy component corresponds with the Maxwell viscous element, we intend to enable the relaxation process in the early loading phase. Therefore, an auxiliary condition is added, whose role is to prevent early microcrack initiation and enable relaxation in the 45° loading case. The auxiliary condition states that the driving energy part must be less than a prescribed fraction of the total free energy for initiation to happen:

$$\frac{\langle\psi_{\mathrm{d}}\rangle}{\psi_{\mathrm{h}}+\psi_{\mathrm{r}}+\langle\psi_{\mathrm{d}}\rangle} < 0.73 \tag{4.30}$$

How the energy ratio in Eq. (4.30) changes with time for the off-axis angles of 90° and 45° is shown in Fig. 4.6, where the data correspond to the same points as in Fig. 4.5. For the 90° loading angle the reported results show no intersection between the energy ratio and the auxiliary condition. On the other hand, for the 45° loading angle the value of 0.73 crosses the energy ratio close to the end of increasing loading phase, practically preventing the microcrack initiation in the early loading phase.

With the energy-based initiation criterion, it is possible to have cohesive segments along every edge of the bulk finite element. Since this situation may lead to computational instability, initiation is allowed along maximum two edges of the 12-node wedge-shaped finite element, while the remaining edge must remain intact. Another consequence of the energy-based initiation criterion for interelement cohesive segments is that the orientation of the cohesive zone may be any orientation defined by the edges of the bulk finite element. To prevent initiation along a physically less favorable direction, a cohesive segment cannot initiate if the angle between the projection of the maximum principal stress direction in the xy-plane of the RVE (the plane perpendicular to fiber direction) and the potential cohesive surface normal is larger than 60°.

4.4.4. TIME-DEPENDENT COHESIVE ZONE MODEL

After initiation takes place, a cohesive zone model controls the process of decohesion. A CZ model used as the base model in this work is the shifted mixed-mode damage cohesive law elaborated by Liu et al. [36], and extended to 3D in [19]. Mode I representation of this CZ model is shown in Fig. 4.7, where the normal traction component is plotted versus the normal component of the displacement jump. The area below the diagram is defined as the fracture energy G_c. When cohesive segment is inserted in the RVE the traction on the cohesive surface is non-zero, while the displacement jump is zero. In a mixed-mode loading scenario this combination would lead to the singularity problem [25], therefore the cohesive law is evaluated with a shifted displacement jump:

$$[\![\bar{\mathbf{u}}]\!]^{\mathrm{sh}} = [\![\bar{\mathbf{u}}]\!] + [\![\bar{\mathbf{u}}]\!]^{0} \tag{4.31}$$

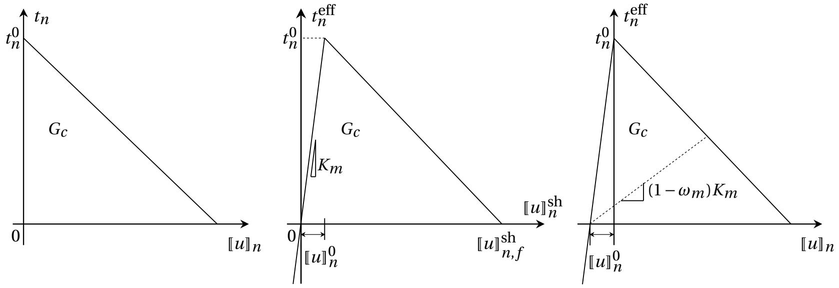

Figure 4.7: Mode I representation of the shifted mixed-mode damage cohesive law

where $\llbracket \bar{\mathbf{u}} \rrbracket^0$ is the displacement shift:

$$\llbracket \bar{\mathbf{u}} \rrbracket^0 = \frac{\bar{\mathbf{t}}^0}{K_m} \tag{4.32}$$

Here, $\bar{\mathbf{t}}^0$ is the traction vector at the moment of CZ initiation, and K_m is the dummy stiffness. The constitutive law for the traction is given by the following relation:

$$\bar{\mathbf{t}} = (\mathbf{I}-\Omega)K_m \llbracket \bar{\mathbf{u}} \rrbracket^{\mathrm{sh}} = (\mathbf{I}-\Omega)\bar{\mathbf{t}}^{\mathrm{eff}} \tag{4.33}$$

In this equation $\bar{\mathbf{t}}^{\mathrm{eff}}$ is the effective traction on the cohesive surface, $\mathbf{I}$ is the second-order unit tensor, and Ω is the damage tensor accounting for stiffness recovery in normal direction under compression:

$$\Omega_{ij} = \omega_m \delta_{ij}\left(1+\delta_{i1}\frac{\langle -t_n^{\mathrm{eff}}\rangle}{t_n^{\mathrm{eff}}}\right) \tag{4.34}$$

The Ω depends on the damage variable ω_m which is a non-decreasing function of time defined as:

$$\omega_m = \max_{\tau\le t}\begin{cases} 0, & \Delta \le \Delta_0 \\ \frac{\Delta_f}{\Delta}\left(\frac{\Delta-\Delta_0}{\Delta_f-\Delta_0}\right), & \Delta_0 < \Delta < \Delta_f \\ 1, & \Delta > \Delta_f \end{cases} \tag{4.35}$$

where Δ is the equivalent shifted displacement jump:

$$\Delta = \left[(\langle \llbracket u \rrbracket_n^{\mathrm{sh}} \rangle)^2 + (\llbracket u \rrbracket_s^{\mathrm{sh}})^2 + (\llbracket u \rrbracket_t^{\mathrm{sh}})^2\right]^{1/2} \tag{4.36}$$

with the subscripts n, s and t representing normal and two shear orthonormal directions respectively. In Eq. (4.35) Δ_0 is the equivalent displacement jump at the instant of initiation:

$$\Delta_0 = \frac{t_{\mathrm{eq}}^0}{K_m} \tag{4.37}$$

which depends on the equivalent traction t_{eq}^0 at the same moment:

$$t_{\mathrm{eq}}^0 = \left[(t_n^0)^2 + (t_s^0)^2 + (t_t^0)^2\right]^{1/2} \tag{4.38}$$

The decohesion process is completed when the equivalent shifted displacement jump attains a failure value Δ_f:

$$\Delta_f = \frac{2G_c}{t_{\mathrm{eq}}^0} \tag{4.39}$$

The fracture energy G_c provided to the model interpolates between a lower bound value G_{Ic} and an upper bound value G_{IIc} as a function of the local stress ratio at the moment of CZ initiation

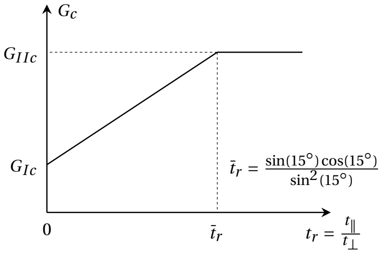

Figure 4.8: Cohesive law fracture energy depending on local stress ratio when cohesive segment is initiated

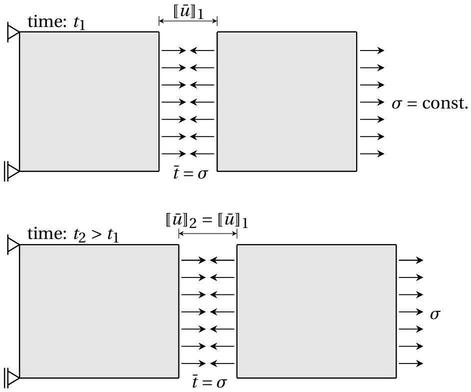

Figure 4.9: Displacement jump and traction of a cohesive zone governed by time-independent constitutive model during creep loading of polymer material not changing at different time instants

[19], see Fig. 4.8. In this figure $t_\perp$ is the stress component on the cohesive surface perpendicular to the fiber direction when the cohesive segment initiates, while $t_\parallel$ is the stress component parallel with the fiber direction.

This CZ model is time-independent, and in a creep rupture scenario the traction vector on the cohesive surface may not change at all as the time progresses. This fact is explained with a simple example illustrated in Fig. 4.9. A polymer material is loaded in tension with a constant stress. As the consequence of the creep stress a cohesive segment is inserted in the polymer material when a suitable initiation criterion is satisfied. Due to the equilibrium condition the stress transmitted through the CZ from the right piece of the material to the left piece is equal to the creep stress applied. Given the viscous material, the deformation will keep increasing, but for the same amount for the left and the right part, keeping the displacement jump unchanged from the previous time instants. Being purely a function of the displacement jump, the cohesive law would keep the constant stress in this deformation process, and rupture would never occur. This fact holds true for any CZ model whose traction vector is defined only in terms of the displacement jump.

The time-independent cohesive law remains ineffective also in the context of a more complex RVE geometry. Some decohesion due to stress redistribution is possible, but any changes in traction are very slow resulting in the material time-to-failure being much longer than experimentally observed[1]. Due to this reason a modification is proposed to the base cohesive law, such that the traction on the cohesive surface also depends on time through the viscous degradation tensor $\mathbf{D}_v$:

$$\bar{\mathbf{t}} = (\mathbf{I} - \Omega)\mathbf{D}_v K_m [\![\bar{\mathbf{u}}]\!]^{\mathrm{sh}} \tag{4.40}$$

---

[1] This statement is actually true when the time needed to initiate cohesive segments is on the same order as the material time to failure, and the number of initiated cohesive segments in the model is small. As shown in Chapter 5, with the presence of many cohesive cracks from early on in the simulation, it is possible to achieve creep rupture within the experimental timescale.

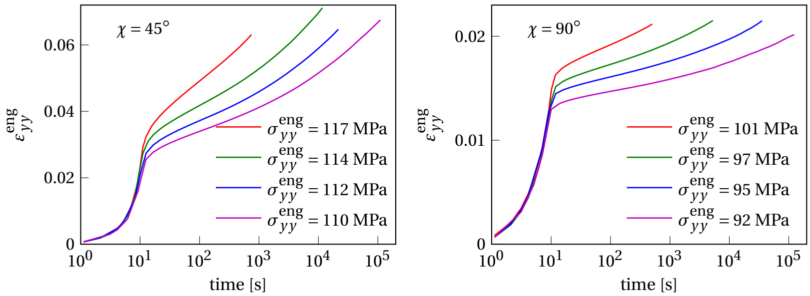

Figure 4.10: Experimentally measured engineering strain versus time due to constant engineering stress for two loading angles; constant load level is reached after 10 s; failure of specimen coincides with termination of the strain curves

To define components of the tensor $\mathbf{D}_v$, the viscous degradation variable D_v at time step n is defined as a non-increasing function:

$$D_v^n = D_v^{n-1} \exp(-\Delta t / \tau_\text{r}) \tag{4.41}$$

where Δt is the time increment, and τ_r is the relaxation time which depends on the normal component of the traction vector through the following relation:

$$\tau_\text{r} = \tau_{\text{r}0} \frac{t_n / (D_v t_0)}{\sinh[t_n / (D_v t_0)]} \tag{4.42}$$

In this equation $\tau_{\text{r}0}(T)$ is the initial relaxation time that depends on the temperature, while $t_0(T)$ is the traction-like variable also dependent on the temperature. This constitutive relation for the relaxation time is chosen on the basis of experimentally observed rupture time, see Fig. 4.10, which indicates that a small change in the applied stress causes a significant change in the rupture time. The shift function:
$[t_n/(D_v t_0)]/\sinh[t_n/(D_v t_0)]$ has a similar counterpart in the viscosity definition of the EGP model, Eq. (4.21), and its role is to shift the initial relaxation time given an adequate stress measure. In this regard, the time-dependent component of the cohesive law can be perceived as an Eyring-based. It should be noted that τ_r moves towards the initial value $\tau_{\text{r}0}$ as t_n decreases. Finally, inclusion of D_v in Eq. (4.42) prevents the evolution in the relaxation time from drastically slowing down the rupture event, after the minimum creep strain-rate is observed.

It can be shown that for constant τ_r the discrete evolution law in Eq. (4.41) is equivalent to the following continuous rate equation:

$$\dot{D}_v = -\frac{D_v}{\tau_\text{r}} \tag{4.43}$$

Under the assumption that τ_r is changing more slowly than D_v, Eq. (4.41) provides a more accurate time-integration of this rate equation than the direct Euler forward approach.

The viscous degradation tensor has three non-zero components corresponding with the orthogonal directions defining the orientation of the cohesive surface:

$$\mathbf{D}_v = \begin{bmatrix} D_n & & \\ & D_s & \\ & & D_t \end{bmatrix} \tag{4.44}$$

With the scalar D_v defined in Eq. (4.41), the components of the tensor $\mathbf{D}_v$ assume the following form: $D_s = D_t = D_v$, whereas the component D_n restores the initial stiffness in the normal direction, in the case of compression:

$$D_n = \begin{cases} D_v, & t_n \geq 0 \\ 1, & t_n < 0 \end{cases} \tag{4.45}$$

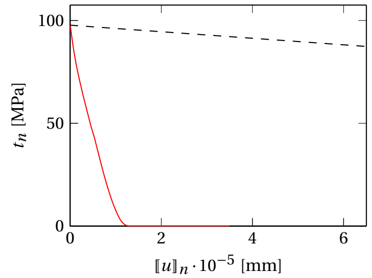

Figure 4.11: Red line representing one possible trajectory of the normal traction component as function of the displacement jump; actual fracture energy of time-dependent cohesive law is reduced due to viscous degradation; dashed line represents quasi-static cohesive law

Table 4.5: Model parameters of time-dependent cohesive law

K_m [N/mm^3]	G_{Ic} [N/mm]	G_{IIc} [N/mm]	$\tau_{r0}(25°\text{C})$ [s]	$t_0(25°\text{C})$ [N/mm^2]
10^7	0.03	0.095	10^9	4.6

The initial value of D_v is equal to 1, and evolves towards 0 with time. To simplify the linearization and implementation of the cohesive law, the normal traction component and the viscous degradation variable from the previous converged time step are used in Eq. (4.42).

The time-dependent components of the cohesive law trigger a decrease in the traction due to creep loading and subsequently a change in the displacement jump. One possible trajectory of the normal traction component plotted against the normal jump component is depicted in Fig. 4.11. As a consequence of the stress relaxation, the actual fracture energy is lower than G_c defined for the time-independent cohesive law. The parameters used to run simulations with the described time-dependent cohesive law are listed in Table 4.5.

4.5. RESULTS AND DISCUSSION

In this section several examples are considered to illustrate the model performance. Since the main purpose of the chapter is to formulate the framework and indicate necessary components to model creep deformation and rupture, only one RVE was considered in the study, with 9 (3 × 3) fibers in total and the fiber diameter of 5 μm.

The first example aims at showing the inability to model creep rupture with the time-independent cohesive zone model, i.e., without the viscous degradation introduced in Eq. (4.40). In Fig. 4.12 the homogenized strain-rate is plotted versus time for two off-axis angles, 45° and 90°, and several stress levels. The strain-rate at the current time step is computed as: $\dot{\varepsilon}^n_{yy} = (\varepsilon^n_{yy} - \varepsilon^{n-1}_{yy})/\Delta t$, where ε^n_{yy} is obtained from Eq. (4.7) or Eq. (4.9). Unless otherwise stated, the creep stress is reached at

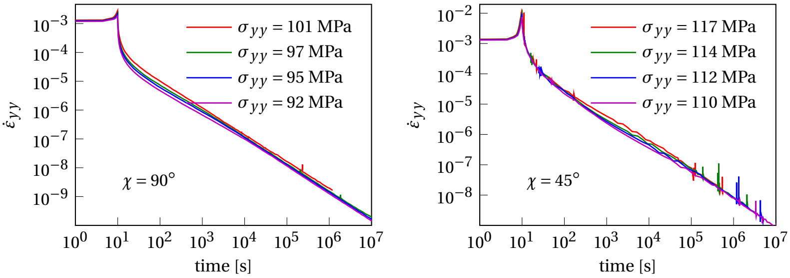

Figure 4.12: Homogenized strain-rate versus time for $T = 25°\text{C}$, different off-axis angles and stress levels, with time-independent cohesive law governing decohesion process

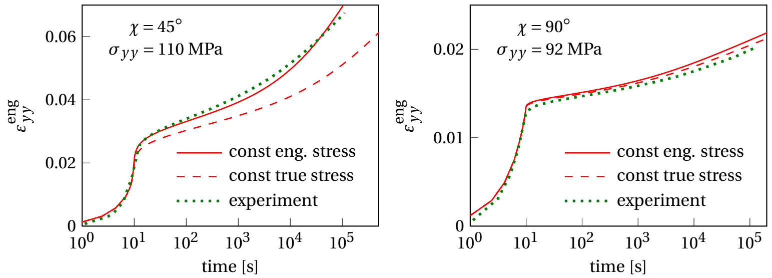

Figure 4.13: Comparison of experimental results with simulations assuming constant engineering stress and constant true stress on the material, for two off-axis angles and $T = 25°$C

$t = 10$ s. After the increasing loading phase is completed, the strain-rate corresponding to the creep stress is gradually decreasing. When the initiation criterion is satisfied cohesive segments are inserted in the RVE, causing a disturbance in the displacement field, which is reflected in oscillations of the homogenized strain-rate. Apart from these brief oscillations, the strain-rate is monotonically decreasing and comparison with experiments in terms of the rupture time cannot be made.

Next, the difference when considering a constant engineering stress and a constant true stress in the analysis is illustrated in Fig. 4.13. Without inserting cohesive segments in the RVE, the engineering strain is computed for two loading angles, and comparison is also made with experimental data. For the homogenized strain of approximately 0.03 and higher, the difference in the outcome for the two stress measures becomes significant. A constant engineering stress in tension implies an increase in the actual stress on the material, see Eq. (4.8), leading to higher strains as opposed to the case of a constant true stress applied. Because the experimental results are reported in terms of the engineering strain as the result of a constant engineering stress, the following simulation results consider engineering stress and strain measures.

The ability of the time-dependent cohesive law to trigger a global increase in the homogenized creep strain-rate is shown in Fig. 4.14(right), where the strain-rate evolution corresponding to $\chi = 90°$, $T = 25°$C and different stress levels is plotted. The minimum point in the strain-rate curve is taken as the point of rupture and used to define the material time-to-failure. Comparison of the homogenized strain plotted against time with experimental results is shown in Fig. 4.14(left), where the rupture points obtained from the strain-rate plot are also indicated. The model predicts reasonably well the creep strain response, whereas the accuracy in predicting the rupture time decreases with a decrease in the creep stress. The largest difference is for the stress $\sigma_{yy} = 92$ MPa. It is important to notice that in all considered cases the experimentally observed failure mechanism is brittle, with the lack of tertiary creep and without large macroscopic deformation. For plotting the strain-rate curves in Fig. 4.14 and the subsequent figures for $T = 25°$C, median filtering is

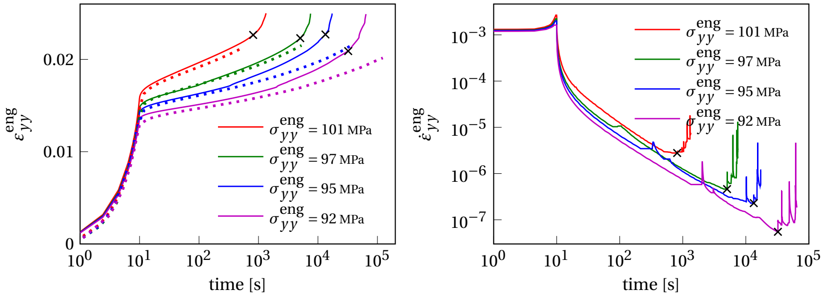

Figure 4.14: Evolution of homogenized strain for $\chi = 90°$ and $T = 25°$C (left); evolution of homogenized strain-rate (right); solid lines: model response, markers: model creep rupture points, dotted lines: experiment

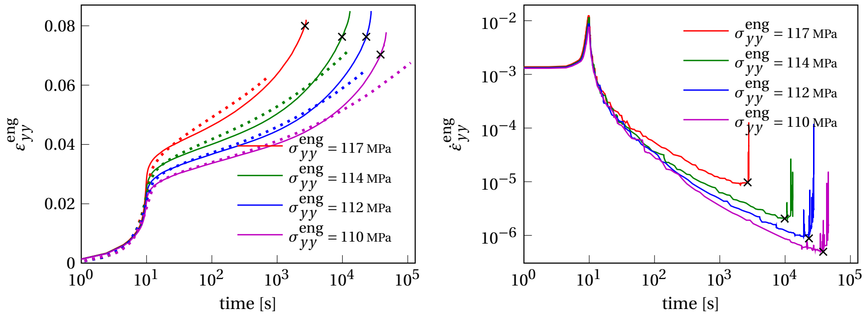

Figure 4.15: Evolution of homogenized strain for $\chi = 45°$ and $T = 25°$C (left); change in homogenized strain-rate with time (right); solid lines: model response, markers: model creep rupture points, dotted lines: experiment

performed on the data, see e.g. [37]. This is because the oscillations become substantial around the minimum point, making it difficult to clearly mark the rupture point. Comparison of the filtered curves with the unfiltered ones is shown in Fig. 4.24 in Appendix B.

In the next example the off-axis angle of 45° is considered, with the temperature $T = 25°$C and different stress levels. In Fig. 4.15 the homogenized strain and the homogenized strain-rate are plotted versus time. Similarly to the previous example, the creep strain response is reasonably well reproduced by the model as well as the general trend of a rupture time that decreases with increasing stress. The difference in the predicted rupture time relative to the experiment is pronounced for the stress level of 110 MPa and 117 MPa.

The possibility to model the creep response at an elevated temperature is presented next. First, all the parameters are kept the same as in the previous cases, including the initial relaxation time τ_{r0} and the traction-like variable t_0 in Eq. (4.42) The evolution of the homogenized strain and strain-rate are shown in Fig. 4.16, for $\chi = 90°$, $T = 90°$C and different stress levels. The creep strain is captured reasonably well, except for $\sigma_{yy} = 72$ MPa. According to the experimental observation there is a significant change in the response when increasing the creep stress from 71 MPa to 72 MPa. This change is not captured by the model. Correspondingly, the model overestimates the time-to-failure that is experimentally observed (a minimum in strain-rate is not observed in the considered time range, see Fig. 4.16). On the other hand, if different values are assigned to τ_{r0} and t_0 at the higher temperature, better results are obtained. Accordingly, we consider a case with $\tau_{r0}(90°\text{C}) = 10^3$ s and $t_0(90°\text{C}) = 10.5$ N/mm^2, see Fig. 4.17, where the homogenized strain and strain-rate are plotted versus time. The newly obtained results lead to a better match with the experiment in terms of the rupture time, even though a difference remains present, particularly for a creep stress of 72 MPa.

Although the homogenized strain and strain-rate curves are plotted in the previous graphs, the

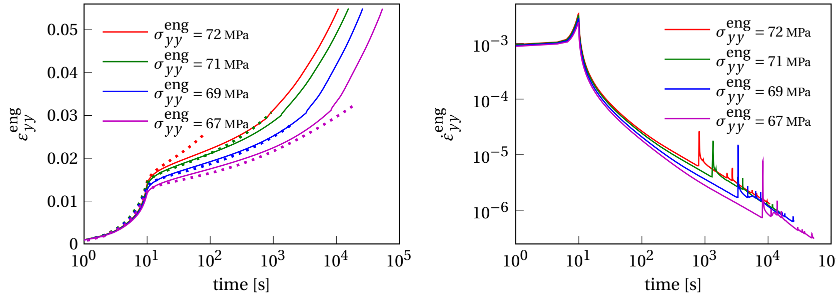

Figure 4.16: Creep response at elevated temperature with all parameters the same as before; homogenized strain versus time for $\chi = 90°$ and $T = 90°$C (left); evolution of homogenized strain-rate (right); solid lines: model response, dotted lines: experiment

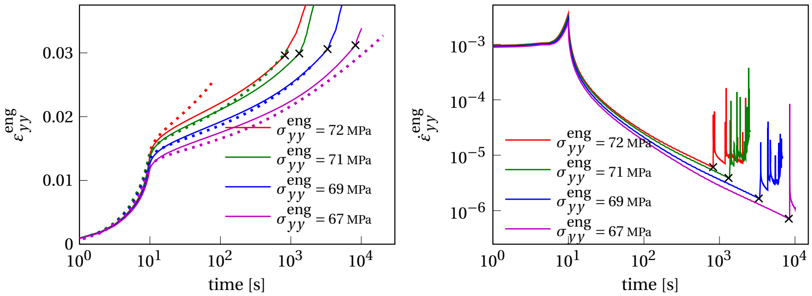

Figure 4.17: Creep response at elevated temperature with updated parameters for the time-dependent part of the cohesive model: $\tau_{\text{r}0}(90°\text{C}) = 10^3$ s, and $t_0(90°\text{C}) = 10.5$ N/mm^2; evolution of homogenized strain for $\chi = 90°$, $T = 90°$C (left); homogenized strain-rate versus time (right); solid lines: model response, markers: model creep rupture points, dotted lines: experiment

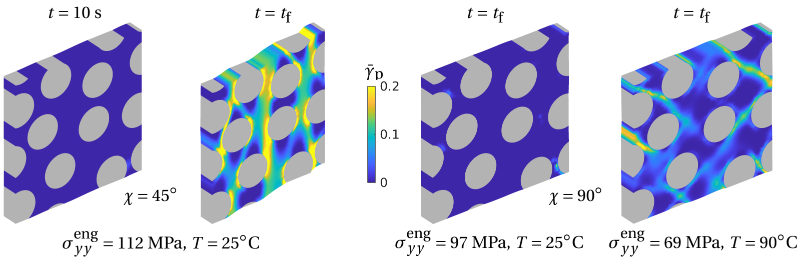

Figure 4.18: Distribution of equivalent plastic strain in RVE at the end of increasing loading phase $t = 10$ s, and when failure is observed $t = t_\text{f}$ for different off-axis angles, stress levels and temperatures

numerical framework also provides for the microstructural distribution of stress, strain and history variables. As an example, the distribution of the equivalent plastic strain is shown in Fig. 4.18 for different off-axis angles, temperatures and stress levels, at the moment of failure $t = t_\text{f}$ and at the time when the constant stress level is reached, $t = 10$ s, for one of the cases. As can be observed from the figure, after $t = 10$ s there is practically no visible plastic strain in the model. The situation has changed at the moment of rupture, with significant plastic strain predicted in the polymer matrix throughout the RVE domain. Notably, the case of $\chi = 90°$ and $T = 25°$C features much less plastic strain than the other depicted cases, which is due to the higher viscosity compared to the $T = 90°$C case, see Eq. (4.21), and the lower deviatoric deformation compared to the $\chi = 45°$ case.

Beside the equivalent plastic strain, it is interesting to show initiated cohesive zones when the minimum creep strain-rate is reached, that defines the rupture time and is followed by a sudden change in the homogenized strain. In Fig. 4.19 cohesive segments in the RVE at $t = t_f$ are shown for two loading angles and two temperature conditions. The number of initiated cohesive segments varies with the loading angle and temperature. For $T = 90°$C this number is rather limited, indicating that a small zone of degrading material triggers a sudden change in the creep strain and leads to rupture. The effect of cohesive segments on the evolution of homogenized strain is illustrated in Fig. 4.20, for the same loading cases considered in the previous figure. Again it is observed that localization of deformation in the present framework cannot be achieved without a cohesive zone model.

The microscale model accounts for finite strains in the material, which implies the change in orientation of the RVE with respect to the loading direction, see Fig. 4.2. It was already shown that this rotation of the RVE has an important effect on the material strength for a constant strain-rate loading scenario [19]. The effect of this rotation on the creep response is illustrated next. In Fig. 4.21 the RVE response, without including the rupture process, is plotted for when the rotation is allowed ($\phi \neq 0$) as well as for when the rotation is restrained ($\phi = 0$) in comparison with the exper-

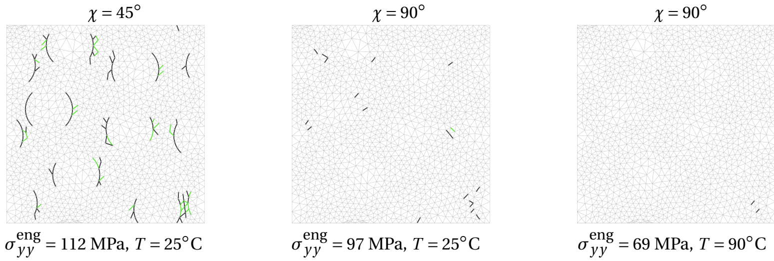

Figure 4.19: Black lines representing degrading cohesive elements at the moment of minimum creep strain-rate in the RVE, which coincides with defined rupture time; green lines indicate unloading cohesive segments, whereas gray lines represent finite element mesh

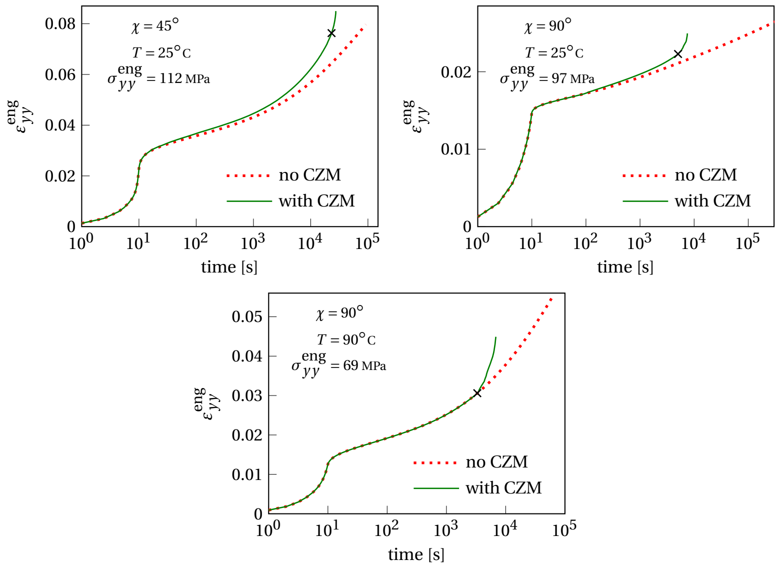

Figure 4.20: Evolution of homogenized strain without cohesive zone model (CZM), and with cohesive zone model in the RVE, for different loading angles and temperature conditions; x marks predicted rupture time

iment. This is done for three loading angles: 15°, 30° and 45°. The change in orientation implies an alignment of the stiff fibers with the loading direction and the change in the actual off-axis angle, which reduces the material compliance. The rotation of the microstructure has a drastic effect on the creep response for lower off-axis angles: 15° and 30°. For these loading angles the fibers carry most of the loading, and a small variation in the off-axis angle leads to a significant increase in the material stiffness, with a corresponding decrease of the creep deformation rate. Given the experimental setup which does not allow for completely free shear deformation as assumed in the rotating RVE simulation (cf. Fig. 4.2), it may be expected that the experimental response is a combination of the two limit cases considered here: one in which material points align with the loading direction and the other in which orientation of material points is fixed. This hypothesis may be checked by a multiscale analysis, in which different integration points represented by individual RVEs would undergo different deformation depending on their position in the specimen. The stiffening effect due to the reorientation of the microstructure is present for $\chi = 45°$ as well, although to a lesser extent. It is because of this reason that the creep rupture time was compared with the experiments for $\chi = 45°$, and also $\chi = 90°$ for which there is no rotation of the microstructure during the loading process.

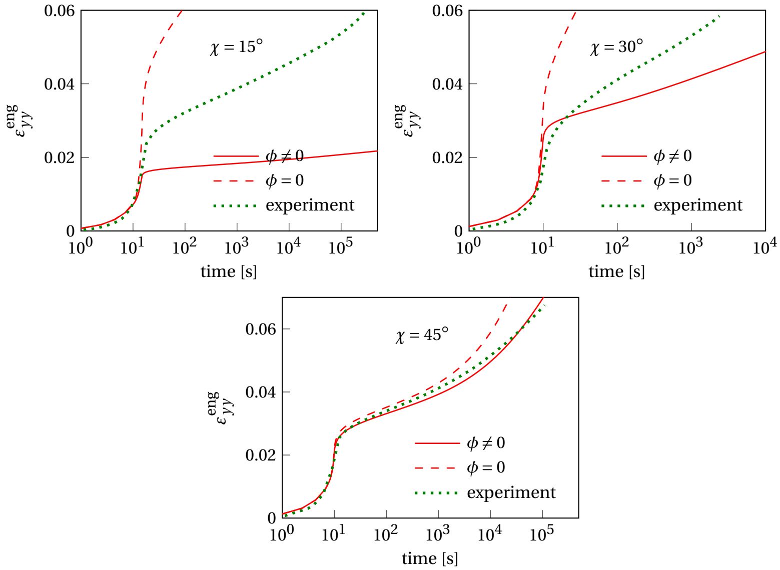

Figure 4.21: Creep response of rotating RVE ($\phi \neq 0$) and non-rotating RVE ($\phi = 0$) compared with experiments for $T = 25°$C and three off-axis angles: 15° (290 MPa), 30° (154 MPa) and 45° (110 MPa); creep stress for $\chi = 15°$ reached at $t = 15$ s

A recommendation stemming from the previous discussion is that numerical models aiming to simulate the mechanical behavior of orthotropic materials should account for the potential reorientation of the microstructure in the course of deformation. Quite often semi-analytical models to predict the creep behavior of composites under off-axis loading assume an equation which, among other parameters, depends on an off-axis angle. In the prediction, this angle is assumed a constant. Raghavan and Meshii [38] have proposed one such model to predict creep response of UD composites. For the off-axis angle of 30° and 60° they report more compliant results than experimentally obtained. Beside the explanation provided therein, an additional reason for this discrepancy might be a change in the actual off-axis angle during the process of creep deformation.

Bauwens-Crowet et al. [39] noticed a relation between the response of glassy polymers when tested under constant strain-rate and creep loading conditions. Namely, when plotted in a semi-log plot, yield stresses versus the corresponding constant strain-rates and creep stresses versus the corresponding minimum creep strain-rates lie on a single straight line (the same statement holds for a *loglog* plot). Erartsin et al. [5] confirmed the similar relation for UD glass/iPP composites for different off-axis angles, only instead of the yield stress, the failure stress of the composite material is paired with the strain-rate. Fig. 4.22 shows the plot for the material system investigated here, with creep results (filled markers) from this chapter together with constant strain-rate results from [19] (empty markers). Results from $\chi = 45°$ and $\chi = 90°$ are shown in red and green respectively, triangles are used for experimental measurements and circles for simulation results. As observed from the figure, the experimental creep data indeed follow the trend established by the constant strain-rate data. On the other hand, the trend is less followed by the creep data as predicted by the model, resulting in a lower stress dependency of the minimum creep strain-rate. The comparison of the numerical model presented in this chapter with the model from [19] is made, even though notable differences exist between the two. The cohesive zone model used in [19] does not feature the viscous degradation term and assumes a different initiation criterion. Furthermore, the relaxation spectra of the EGP model are different. For the constant strain-rate simulations, a relaxation spectrum was calibrated on stress-strain curves obtained from extensometer measurements. Finally, the stress values computed in [19] are the Cauchy stress values, as opposed to constant engineering stress considered in creep simulations.

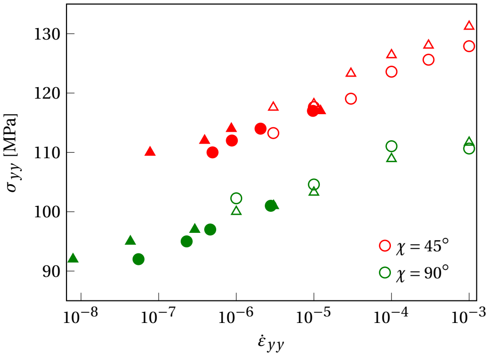

Figure 4.22: Material failure stress versus corresponding strain-rate, obtained from the model (circles) and from the experiment (triangles); empty markers represent data for constant strain-rate loading case [19], filled markers represent creep data

A unified numerical framework to model progressive failure of a UD composite material under off-axis creep, constant strain-rate and eventually under general time-dependent loading has not yet been achieved, but the formulations provided in this chapter and the preceding one on constant strain-rate tests together introduce essential ingredients for this purpose.

4.6. CONCLUSION

In this chapter a micromechanical model has been developed to simulate creep rupture in UD composites subjected to off-axis loading. The main ingredients of the model are a state of the art rate-dependent plasticity model, a recently developed formulation for off-axis loading on RVEs and a new time-dependent cohesive formulation. Creep deformation in the polymer matrix of the RVE is represented by the viscosity-dependent Eindhoven Glassy Polymer material model. The creep rupture process, which terminates creep deformation, is triggered by inserting cohesive segments along the finite element edges when an initiation criterion is satisfied. For this matter, an energy-based criterion depending on the critical Helmholtz free energy stored in the polymer matrix is proposed. After the CZ initiates, the necessity to apply a time-dependent cohesive law to further drive the decohesion process in creep loading is illustrated. The composite material eventually fails when the homogenized creep strain-rate of the RVE reaches a minimum value, which defines the creep rupture time.

The model is compared with experiments on UD thermoplastic carbon/PEEK composite system tested at different stress levels, temperatures and loading angles. The accuracy in predicting creep deformation is satisfactory, but a discrepancy is observed in the rupture time. Three new parameters are introduced to describe creep rupture, the critical energy ψ_{cr} for initiation, the traction-like variable t_0 and the initial relaxation time of the cohesive law $\tau_{\mathrm{r}0}$. Of these, the last two needed to be made temperature-dependent to get a reasonable agreement with experimentally observed creep rupture times. Kinematical relations allow for finite strains and, correspondingly, the change in orientation of the RVE during the loading process. This reorientation affects the creep response, reducing the material compliance especially for lower off-axis angles.

4.7. DATA AVAILABILITY

Data presented in this chapter are available at the 4TU.ResearchData repository through `https://doi.org/10.4121/21835773.v1`

4.8. APPENDIX A

Homogenized strain curves for two loading cases ($\chi = 45°$ and $\chi = 90°$), without inserting cohesive segments are shown in Fig. 4.23. The evolution of the creep deformation corresponds with the free energy evolution shown in Fig. 4.5.

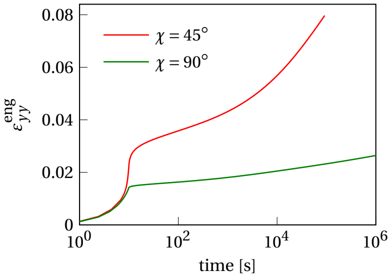

Figure 4.23: Homogenized strain evolution without initiated cohesive zones for two loading cases: 45° (112 MPa) and 90° (95 MPa); creep stress reached at $t = 10$ s

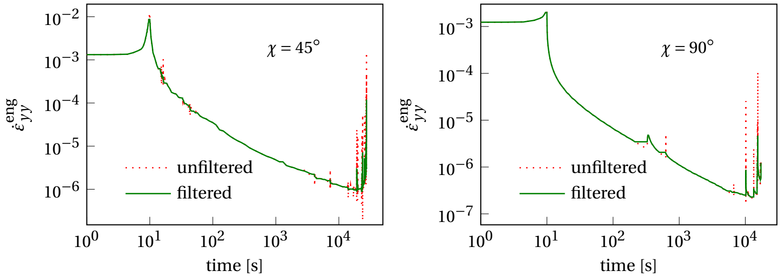

Figure 4.24: Unfiltered versus (median) filtered homogenized strain-rate curves for $\chi = 45°$ and $\sigma_{yy}^{\text{eng}} = 112$ MPa (left), and $\chi = 90°$ and $\sigma_{yy}^{\text{eng}} = 95$ MPa (right)

4.9. APPENDIX B

The unfiltered strain-rate curves are compared with the filtered ones for RVE simulations with included cohesive segments and for two loading angles in Fig. 4.24.

REFERENCES

[1] Kovačević D, Sundararajan BK, Van Der Meer FP. Micromechanical model for off-axis creep rupture in unidirectional composites undergoing finite strains. *Composites A*, 176, 2024, p. 107860. DOI: `10.1016/j.compositesa.2023.107860`.

[2] Brinson HF. Matrix dominated time dependent failure predictions in polymer matrix composites. *Compos Struct*, 47 (1-4), 1999, pp. 445–456. DOI: `10.1016/S0263-8223(00)00075-1`.

[3] Eyring H. Viscosity, plasticity, and diffusion as examples of absolute reaction rates. *J Chem Phys*, 4 (4), 1936, pp. 283–291. DOI: `10.1063/1.1749836`.

[4] Kanters MJW, Kurokawa T, Govaert LE. Competition between plasticity-controlled and crack-growth controlled failure in static and cyclic fatigue of thermoplastic polymer systems. *Polym Test*, 50, 2016, pp. 101–110. DOI: `10.1016/j.polymertesting.2016.01.008`.

[5] Erartsin O, Amiri-Rad A, Van Drongelen M, Govaert LE. Time-dependent failure of off-axis loaded unidirectional glass/iPP composites. *J Appl Polym Sci*, 139 (23), 2022, p. 52293. DOI: `10.1002/app.52293`.

[6] Spathis G, Kontou E. Creep failure time prediction of polymers and polymer composites. *Compos Sci Technol*, 72 (9), 2012, pp. 959–964. DOI: `10.1016/j.compscitech.2012.03.018`.

[7] Raghavan J, Meshii M. Prediction of creep rupture of unidirectional carbon fiber reinforced polymer composite. *Mater Sci Eng A*, 197 (2), 1995, pp. 237–249. DOI: `10.1016/0921-5093(94)09730-5`.

[8] Schapery RA. On the characterization of nonlinear viscoelastic materials. *Polym Eng Sci*, 9 (4), 1969, pp. 295–310. DOI: `10.1002/pen.760090410`.

[9] Lou Y, Schapery R. Viscoelastic characterization of a nonlinear fiber-reinforced plastic. *J Compos Mater*, 5 (2), 1971, pp. 208–234. DOI: `10.1177/002199837100500206`.

[10] Haj-Ali RM, Muliana AH. Numerical finite element formulation of the Schapery non-linear viscoelastic material model. *Int J Numer Methods Eng*, 59 (1), 2004, pp. 25–45. DOI: `10.1002/nme.861`.

[11] Aboudi J. Micromechanical characterization of the non-linear viscoelastic behavior of resin matrix composites. *Compos Sci Technol*, 38 (4), 1990, pp. 371–386. DOI: `10.1016/0266-3538(90)90022-W`.

[12] Haj-Ali RM, Muliana AH. A multi-scale constitutive formulation for the nonlinear viscoelastic analysis of laminated composite materials and structures. *Int J Solids Struct*, 41 (13), 2004, pp. 3461–3490. DOI: `10.1016/j.ijsolstr.2004.02.008`.

[13] Jafaripour M, Taheri-Behrooz F. Creep behavior modeling of polymeric composites using Schapery model based on micro-macromechanical approaches. *Eur J Mech A Solids*, 81, 2020, p. 103963. DOI: `10.1016/j.euromechsol.2020.103963`.

[14] Gal E, Fish J. Anisotropic micromechanical creep damage model for composite materials: a reduced-order approach. *Int J Mult Comp Eng*, 6 (2), 2008, pp. 113–121. DOI: `10.1615/IntJMultCompEng.v6.i2.10`.

[15] Rabotnov YN. Creep rupture. In: M Hetényi, WG Vincenti, eds. *Applied Mechanics*. International Union of Theoretical and Applied Mechanics. Berlin, Heidelberg: Springer, 1969, pp. 342–349. DOI: `10.1007/978-3-642-85640-2_26`.

[16] Leckie FA, Hayhurst DR, Baker JF. Creep rupture of structures. *Proc R Soc A*, 340 (1622), 1974, pp. 323–347. DOI: `10.1098/rspa.1974.0155`.

[17] Govaert LE et al. A micromechanical approach to time-dependent failure in off-axis loaded polymer composites. *Composites A*, 32 (12), 2001, pp. 1697–1711. DOI: `10.1016/S1359-835X(01)00028-8`.

[18] Kovačević D, Van der Meer FP. Strain-rate based arclength model for nonlinear microscale analysis of unidirectional composites under off-axis loading. *Int J Solids Struct*, 250, 2022, p. 111697. DOI: `10.1016/j.ijsolstr.2022.111697`.

[19] Kovačević D, Sundararajan BK, Van der Meer FP. Microscale modeling of rate-dependent failure in thermoplastic composites under off-axis loading. *Eng Fract Mech*, 276, 2022, p. 108884. DOI: `10.1016/j.engfracmech.2022.108884`.

[20] Reiner M, Weissenberg K. A thermodynamic theory of the strength of the materials. *Rheol Leaf*, 10, 1939, pp. 12–20.

[21] Erartsin O, Van Drongelen M, Govaert LE. Identification of plasticity-controlled creep and fatigue failure mechanisms in transversely loaded unidirectional thermoplastic composites. *J Compos Mater*, 55 (14), 2021, pp. 1947–1965. DOI: `10.1177/0021998320964252`.

[22] Van der Meer FP. Micromechanical validation of a mesomodel for plasticity in composites. *Eur J Mech A Solids*, 60, 2016, pp. 58–69. DOI: `10.1016/j.euromechsol.2016.06.008`.

[23] Ke L, Van der Meer FP. A computational homogenization framework with enhanced localization criterion for macroscopic cohesive failure in heterogeneous materials. *J Theor Comp App Mech*, 2022. DOI: `10.46298/jtcam.7707`.

[24] Belytschko T, Liu WK, Moran B, Elkhodary K. *Nonlinear finite elements for continua and structures.* John Wiley & Sons, 2014.

[25] Van der Meer FP, Sluys LJ. A phantom node formulation with mixed mode cohesive law for splitting in laminates. *Int J Fract*, 158 (2), 2009, p. 107. DOI: `10.1007/s10704-009-9344-5`.

[26] Tervoort TA, Smit RJM, Brekelmans WAM, Govaert LE. A constitutive equation for the elasto-viscoplastic deformation of glassy polymers. *Mech Time Depend Mater*, 1 (3), 1997, pp. 269–291. DOI: `10.1023/A:1009720708029`.

[27] Van Breemen LCA, Klompen ETJ, Govaert LE, Meijer HEH. Extending the EGP constitutive model for polymer glasses to multiple relaxation times. *J Mech Phys Solids*, 59 (10), 2011, pp. 2191–2207. DOI: `10.1016/j.jmps.2011.05.001`.

[28] Khaleghi H, Amiri-Rad A, Mashayekhi M. A thermodynamically consistent continuum damage model for time-dependent failure of thermoplastic polymers. *Int J Plast*, 154, 2022, p. 103278. DOI: `10.1016/j.ijplas.2022.103278`.

[29] Coleman BD, Noll W. The thermodynamics of elastic materials with heat conduction and viscosity. *Arch Rational Mech Anal*, 13 (1), 1963, pp. 167–178. DOI: `10.1007/BF01262690`.

[30] Senden DJA, Krop S, Van Dommelen JAW, Govaert LE. Rate- and temperature-dependent strain hardening of polycarbonate. *J Polym Sci B: Polym Phys*, 50 (24), 2012, pp. 1680–1693. DOI: `10.1002/polb.23165`.

[31] Bonet J, Burton AJ. A simple orthotropic, transversely isotropic hyperelastic constitutive equation for large strain computations. *Comput Methods Appl Mech Eng*, 162 (1), 1998, pp. 151–164. DOI: `10.1016/S0045-7825(97)00339-3`.

[32] Miyagawa H et al. Transverse elastic modulus of carbon fibers measured by Raman spectroscopy. *Mater Sci Eng A*, 412 (1), 2005, pp. 88–92. DOI: `10.1016/j.msea.2005.08.037`.

[33] Camacho GT, Ortiz M. Computational modelling of impact damage in brittle materials. *Int J Solids Struct*, 33 (20), 1996, pp. 2899–2938. DOI: `10.1016/0020-7683(95)00255-3`.

[34] Brüller OS. Energy-related failure criteria of thermoplastics: Energy-Related Failure Criteria of Thermoplastics. *Polym Eng Sci*, 21 (3), 1981, pp. 145–150. DOI: `10.1002/pen.760210306`.

[35] Hiel CC, Brinson HF, Cardon AH. The nonlinear viscoelastic response of resin matrix composites. In: IH Marshall, ed. *Composite Structures 2*. Dordrecht: Springer Netherlands, 1983, pp. 271–281. DOI: `10.1007/978-94-009-6640-6_20`.

[36] Liu Y, van der Meer FP, Sluys LJ, Ke L. Modeling of dynamic mode I crack growth in glass fiber-reinforced polymer composites: fracture energy and failure mechanism. *Eng Fract Mech*, 243, 2021, p. 107522. DOI: `10.1016/j.engfracmech.2020.107522`.

[37] Pratt WK. *Digital image processing: PIKS Scientific inside.* Vol. 4. Wiley Online Library, 2007.

[38] Raghavan J, Meshii M. Creep of polymer composites. *Compos Sci Technol*, 57 (12), 1998, pp. 1673–1688. DOI: `10.1016/S0266-3538(97)00104-8`.

[39] Bauwens-Crowet C, Ots J, Bauwens J. The strain-rate and temperature dependence of yield of polycarbonate in tension, tensile creep and impact tests. *J Mater Sci*, 9 (7), 1974, pp. 1197–1201. DOI: `10.1007/BF00552841`.

5

UNIFIED MODEL FOR CREEP AND FATIGUE

5.1. INTRODUCTION

The problem of fatigue in composites sparks research effort in experimental characterization as well as in computational modeling. Experiments represent the starting point to understand the thermo-mechanical behavior of the material under different loading conditions. However, experimental campaigns for characterizing composites under fatigue loading are expensive and time consuming [2]. In that regard, modeling offers the possibility to reduce the number of required experiments, but also to better understand the mechanisms underlying the fatigue failure process.

Usually two failure regimes are observed in composites under long-term loading. These two failure regimes are sometimes called plasticity controlled failure, for ductile failure, creep rupture or low-cycle fatigue, and crack growth controlled failure for brittle fracture or high-cycle fatigue [3]. When fatigue results are plotted in the form of S-t curves (maximum applied stress versus time to failure in a double logarithmic plot), the plasticity controlled regime is insensitive to the loading frequency, i.e., the material response can be approximated with a single line for different frequencies [4]. On the other hand, the time to failure in the crack growth controlled regime shows dependence on the loading frequency and shifts towards shorter timescales with increasing frequency. Alternatively, and more commonly in the composites literature, fatigue results can be reported in the form of S-N curves (maximum applied stress versus number of cycles to failure in a *loglog* plot). In this representation, the plasticity controlled mechanism is frequency-dependent, while the crack growth controlled fatigue behavior is often regarded as frequency-independent. However, frequency dependency of the crack growth mechanism was reported for glass fiber-reinforced polyphenylene-ether (PPE)/polystyrene (PS) blend by Kanters et al. [4], depending on the load ratio R:

$$R = \frac{\sigma^{\text{min}}}{\sigma^{\text{max}}} \tag{5.1}$$

where σ^{min} and σ^{max} stand for the minimum and the maximum stress in the experiment, respectively. For lower values of the load ratio, the number of cycles to failure is largely independent of frequency [4], and can be approximated with a single line. However, as the load ratio increases, the measured number of cycles to failure in the crack growth regime varies with frequency [4].

The literature on micromechanical modeling of composites is rich, where representative volume elements (RVEs) with a random fiber distribution have been used to model different features of the material: stiffness [5], plastic flow [6], strength [7], water diffusion [8], in-situ effects [9], etc. However, the number of numerical models dealing with the long-term time-dependent behavior of the material, including fatigue, is limited. The majority of microscale models for fatigue are based on the mean-field homogenization techniques [10–12], which are computationally efficient but miss the actual geometry of the material microstructure. In a multiscale approach, a unit cell was used by Fish and Yu [13], and Crouch et al. [14] to simulate the fatigue response of structural components. A model developed by Ni et al. [15] takes into account the more detailed geometry of composites in a bond-based peridynamics framework. Although dimensionally not the microscale, an example presented in that paper closely resembles the composites microstructure loaded in transverse tension. Rocha et al. [16] also introduced a micromechanical model for high-cycle fatigue under transverse loading together with techniques to speed-up the simulations. To the best of our knowledge, there is no computational model in the literature able to reproduce the observed frequency dependency of the S-N (or S-t) curve, for both plasticity controlled and

---

Apart from minor text adjustments and the lack of appendix, this chapter is reproduced from [1].

crack growth controlled regimes. We aim to develop a model that can capture these dependencies, believing that such ability indicates that the model describes the relevant physics for time- and cycle-dependent failure of thermoplastic composites. Here, we tackle this issue by introducing a microscale spatial and two-scale temporal framework to predict failure of unidirectional (UD) composites under cyclic loading.

To impose an off-axis stress on the RVE, kinematical and stress relations inherit the form from our previously published RVE model for creep rupture [17]. Two important requirements are set for numerical models describing the long-term behavior under cyclic loading. Firstly, the loading strategy must ensure computational feasibility, where tracing the loading path in detail is too demanding, and secondly, the material models must be formulated such that deformation of the constituents under the simplified loading strategy matches the deformation obtained for the actual loading scheme. Accordingly, we propose an adaptive two-scale time stepping scheme with time homogenization including the macro time steps where viscoplasticity evolves in the polymer matrix, and micro time steps where the material response is elastic, but the stress evolution over the cycle is recorded. The polymer response under cyclic loading is represented with the Eindhoven Glassy Polymer (EGP) material model [18] for which a two-scale temporal version is formulated. The state variables of the two-scale EGP model are updated at macro time steps using an effective time increment, based on information collected at micro time steps. Carbon fibers are modeled with a hyperelastic transversely isotropic constitutive model [19]. Microcracking of the matrix due to cyclic loading is accounted for by means of Dávila's cycle-dependent cohesive model [2], with the fatigue damage function as presented in [20]. Cohesive segments are added on the fly [21], when a suitable initiation criterion is satisfied [22], for which we introduce a small modification in this study. The cohesive model is able to represent the kink point in S-N curve distinguishing between the low- and high-cycle failure mechanisms, but not the frequency dependency of each failure mechanism. Its formulation is built on the notion that for a given stress, the number of cycles governs failure, and includes no frequency or time dependence. The timescale, and correspondingly the observed frequency dependency, is introduced in the model through the viscous response of the matrix represented with the (two-scale) EGP model. To make the cohesive zone model compatible with the two-scale EGP model, cohesive initiation and damage evolution are blocked at micro time steps. The RVE model results are compared with available experimental S-N (or S-t) curves of UD carbon/PEEK thermoplastic composite material, tested at different load ratios, frequencies and loading angles [23].

The content of the chapter includes the following topics: homogenized kinematical and stress relations to impose an off-axis stress on the RVE; description of the bulk material models including the formulation of the two-scale EGP model; review of the cohesive zone model (CZM); introduction of the adaptive time stepping strategy; evaluation of the model performance in comparison with experimental results and conclusions.

5.2. OFF-AXIS LOADING: HOMOGENIZED KINEMATICS AND STRESS

Uniaxial cyclic loading is applied on a unidirectional composite material under an off-axis angle, see Fig. 5.1 (left), where the initial off-axis angle χ is defined as: $\chi = 90° - \theta_0$, θ_0 being the initial angle between the global x-direction and the local e_1-direction. In this setting, the orthotropic material deforms in extension as well as in shear, see Fig 5.1 (middle). Allowing for finite strains in the material, the local coordinate frame aligned with the reinforcement may change orientation from the angle θ_0 to a new angle θ_1. In this deformed configuration, the stress state can be transformed from the global coordinate system to the local frame, to obtain the Cauchy stress components shown in Fig. 5.1 (right). The goal is to simulate this deformation process on the microscale by means of a thin slice 3D RVE, aligned with the local frame. The homogenized deformation and stress state of the RVE must be the same as that in Fig. 5.1. Correspondingly, the homogenized Cauchy stress components acting on the RVE faces are shown in Fig. 5.2 (left). This stress state is imposed on the RVE with periodic boundary conditions through the force vector components applied on the four master nodes of the RVE, see Fig. 5.2 (right). In the same figure, along with the

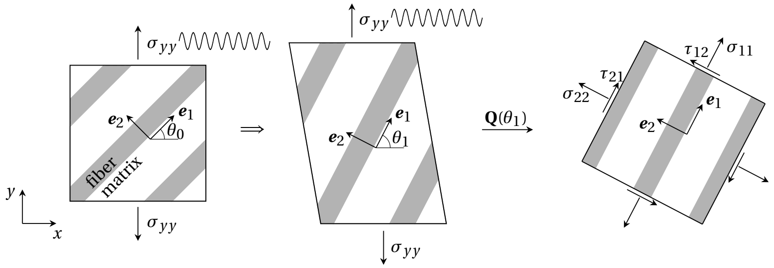

Figure 5.1: Cyclic stress applied on unidirectional composite material under off-axis angle (left); deformed material (middle); Cauchy stress components on the material in local frame (right)

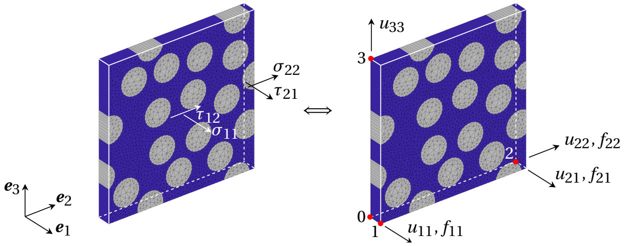

Figure 5.2: Homogenized Cauchy stresses on RVE faces (left) as a result of the force vector components applied on the master nodes (right); nonzero displacements of master nodes also indicated in the right figure

force vector components, the corresponding nonzero displacements of the master nodes are also indicated. A detailed discussion on this choice of boundary conditions is part of [24] and Chapter 2. The boundary conditions enforce periodicity in the deformation process [6], also allowing for microcracking [25].

Equations needed to impose an off-axis loading on the RVE assuming finite deformations were introduced in [24]. A small adjustment to impose an off-axis creep stress, including a constant engineering stress, was presented in [17]. Exactly the same framework is used here, with the adjustment that the applied stress σ_{yy} cyclically changes its magnitude. Relevant equations are repeated here, without detailed explanation. Expressions for the nonzero force vector components on the master nodes read:

$$\begin{aligned} f_{11} &= \sigma_{yy} A_1^0 \bar{J} \left(\frac{s_1^2}{\bar{F}_{11}} - c_1 s_1 \frac{\bar{F}_{12}}{\bar{F}_{11}\bar{F}_{22}} \right) \\ f_{21} &= \sigma_{yy} A_2^0 \bar{J} \frac{c_1 s_1}{\bar{F}_{22}} \\ f_{22} &= \sigma_{yy} A_2^0 \bar{J} \frac{c_1^2}{\bar{F}_{22}} \end{aligned} \tag{5.2}$$

where A_i^0 is the initial surface on which the corresponding stress component is acting, $\bar{J}$ is the determinant of the RVE homogenized deformation gradient in local frame $\bar{\mathbf{F}}$, s_1 and c_1 are $\sin(\theta_1)$ and $\cos(\theta_1)$ respectively, while $\bar{F}_{ij}$ are components of $\bar{\mathbf{F}}$:

$$\bar{\mathbf{F}} = \begin{bmatrix} \bar{F}_{11} & \bar{F}_{12} & 0 \\ 0 & \bar{F}_{22} & 0 \\ 0 & 0 & \bar{F}_{33} \end{bmatrix} = \begin{bmatrix} 1+\frac{u_{11}}{l_1^0} & \frac{u_{21}}{l_2^0} & 0 \\ 0 & 1+\frac{u_{22}}{l_2^0} & 0 \\ 0 & 0 & 1+\frac{u_{33}}{l_3^0} \end{bmatrix} \tag{5.3}$$

Here, u_{ij} is the displacement of master node i in direction j, whereas l_i^0 is the initial length of the RVE in direction i. $\bar{\mathbf{F}}$ can be related to the homogenized deformation gradient in global frame $\mathbf{F}$

through the following relation:

$$\mathbf{F} = \mathbf{Q}_1^{\mathrm{T}} \bar{\mathbf{F}} \mathbf{Q}_0 \tag{5.4}$$

where $\mathbf{Q}_0$ is the transformation matrix:

$$\mathbf{Q}_0 = \begin{bmatrix} \cos(\theta_0) & \sin(\theta_0) & 0 \\ -\sin(\theta_0) & \cos(\theta_0) & 0 \\ 0 & 0 & 1 \end{bmatrix} \tag{5.5}$$

The transformation matrix $\mathbf{Q}_1$ shares the same form with $\mathbf{Q}_0$, but depends on the angle θ_1. This angle is computed as: $\theta_1 = \theta_0 + \phi$, where the angle ϕ measures reorientation of the RVE in the deformation process. The procedure to compute the angle ϕ is detailed in [24] and Chapter 2.

By knowing **F**, different strain measures in the global loading direction can be computed. For example, the true (logarithmic) strain reads:

$$\varepsilon_{yy} = \ln(F_{yy}) \tag{5.6}$$

where F_{yy} is a component of **F**. Alternatively, the engineering strain can be computed as:

$$\varepsilon_{yy}^{\text{eng}} = F_{yy} - 1 \tag{5.7}$$

If a constant engineering stress is considered in the analysis, the actual stress σ_{yy} in Eq. (5.2) is obtained by correcting the engineering stress for the previous deformation:

$$\sigma_{yy} = \frac{\sigma_{yy}^{\text{eng}}}{F_{xx} F_{zz}} \tag{5.8}$$

where F_{xx} and F_{zz} are components of **F**.

The expression for the internal force vector in the presence of cohesive microcracks and the absence of body forces is adopted according to [26].

5.3. CONSTITUTIVE MODELS

5.3.1. EINDHOVEN GLASSY POLYMER CONSTITUTIVE MODEL

To represent the behavior of the polymer matrix under cyclic loading we formulate a two-scale temporal version of the EGP material model. The governing equations of the EGP model are briefly reviewed, in order to set the stage for the two-scale version of the model.

Different from many material models dealing with plasticity, the EGP does not define a yield surface. Instead it features a viscosity function, which changes with the stress applied on the material [27], such that the yielding is considered as the stress-induced melting [18]. Several assumptions are introduced in the EGP formulation, starting with the multiplicative decomposition of the deformation gradient into elastic and plastic parts:

$$\boldsymbol{F} = \boldsymbol{F}_{\mathrm{e}} \cdot \boldsymbol{F}_{\mathrm{p}} \tag{5.9}$$

In this equation the *italic* font is used to distinguish the deformation gradient at the integration point level, from the homogenized deformation gradient of the RVE, Eq. (5.4). The plastic deformation is assumed volume preserving, i.e.:

$$J = \det(\boldsymbol{F}) = \det(\boldsymbol{F}_{\mathrm{e}}) \tag{5.10}$$

Yet another assumption says that the Cauchy stress is additively decomposed in three stress tensors:

$$\boldsymbol{\sigma} = \boldsymbol{\sigma}_{\mathrm{h}} + \boldsymbol{\sigma}_{\mathrm{r}} + \boldsymbol{\sigma}_{\mathrm{d}} \tag{5.11}$$

where $\boldsymbol{\sigma}_{\mathrm{h}}$ is the hydrostatic, $\boldsymbol{\sigma}_{\mathrm{r}}$ the hardening, and $\boldsymbol{\sigma}_{\mathrm{d}}$ the driving stress tensor. The hydrostatic stress tensor is defined as:

$$\boldsymbol{\sigma}_{\mathrm{h}} = \kappa(J-1)\mathbf{I} \tag{5.12}$$

in which κ is the bulk modulus and $\mathbf{I}$ is the second-order unit tensor. The hardening stress tensor $\boldsymbol{\sigma}_{\mathrm{r}}$ has the following form:

$$\boldsymbol{\sigma}_{\mathrm{r}} = \frac{1}{J} G_{\mathrm{r}} \tilde{\mathbf{B}}^{\mathrm{d}} \tag{5.13}$$

Here, G_{r} is the hardening modulus, whereas $\tilde{\mathbf{B}}^{\mathrm{d}}$ is the deviatoric part of the isochoric left Cauchy-Green deformation tensor defined as:

$$\tilde{\mathbf{B}} = J^{-2/3}\left(\boldsymbol{F}\cdot\boldsymbol{F}^{\mathrm{T}}\right) \tag{5.14}$$

The mechanical analog for the driving stress of the EGP is shown in Fig. 5.3. This part of the total stress tensor admits multiple relaxation processes in the model, representing the thermorheologically complex behavior of the material [28]. Each process may be modeled with multiple modes, that is with multiple Maxwell elements connected in parallel. Assuming two relaxation processes α and β, the definition of the driving stress tensor $\boldsymbol{\sigma}_{\mathrm{d}}$ reads [29]:

$$\begin{aligned}\boldsymbol{\sigma}_{\mathrm{d}} &= \sum_{k=1}^{p} \boldsymbol{\sigma}_{\alpha,k} + \sum_{l=1}^{q} \boldsymbol{\sigma}_{\beta,l} \\ &= \frac{1}{J}\sum_{k=1}^{p} G_{\alpha,k}\tilde{\mathbf{B}}^{\mathrm{d}}_{\mathrm{e}\alpha,k} + \frac{1}{J}\sum_{l=1}^{q} G_{\beta,l}\tilde{\mathbf{B}}^{\mathrm{d}}_{\mathrm{e}\beta,l}\end{aligned} \tag{5.15}$$

Here, $G_{x,j}$ is the shear modulus of Maxwell element j from process x, where x is either α or β and j is either k or l; $\tilde{\mathbf{B}}^{\mathrm{d}}_{\mathrm{e}x,j}$ is the deviatoric part of the isochoric elastic left Cauchy-Green deformation tensor in Maxwell element j belonging to process x; p and q represent the total number of α and β modes, respectively. To compute $\tilde{\mathbf{B}}^{\mathrm{d}}_{\mathrm{e}x,j}$ it is necessary to integrate the rate equation:

$$\dot{\tilde{\mathbf{B}}}_{\mathrm{e}x,j} = \left(\tilde{\mathbf{L}} - \mathbf{D}_{\mathrm{p}x,j}\right)\cdot\tilde{\mathbf{B}}_{\mathrm{e}x,j} + \tilde{\mathbf{B}}_{\mathrm{e}x,j}\cdot\left(\tilde{\mathbf{L}}^{\mathrm{T}} - \mathbf{D}_{\mathrm{p}x,j}\right) \tag{5.16}$$

where $\tilde{\mathbf{L}}$ is the isochoric velocity gradient and $\mathbf{D}_{\mathrm{p}x,j}$ is the plastic part of the rate of deformation tensor belonging to process x and Maxwell element j. This tensor is defined by introducing a constitutive relation of the following form:

$$\mathbf{D}_{\mathrm{p}x,j} = \frac{\boldsymbol{\sigma}_{x,j}}{2\eta_{x,j}(\bar{\tau}_x, p, S_x, T)} \tag{5.17}$$

where $\eta_{x,j}$ is the viscosity of the corresponding Maxwell element. In the context of the EGP model, the viscosity function motivated by the Eyring flow theory [30] depends on the equivalent stress $\bar{\tau}_x$, the hydrostatic stress $p = -\kappa(J-1)$, the state parameter S_x and the absolute temperature T:

$$\eta_{x,j} = \eta_{0x,j}\frac{\bar{\tau}_x/\tau_{0x}}{\sinh(\bar{\tau}_x/\tau_{0x})}\exp\left(\frac{\mu_x p}{\tau_{0x}}\right)\exp(S_x)\exp\left[\frac{\Delta H_x}{R}\left(\frac{1}{T}-\frac{1}{T_{\mathrm{ref}}}\right)\right] \tag{5.18}$$

In this equation $\eta_{0x,j}$ is the initial viscosity of the corresponding Maxwell element, τ_{0x} the characteristic shear stress, μ_x the pressure dependency parameter, ΔH_x the activation enthalpy, R the gas constant, and $T_{\mathrm{ref}} = 298.15$ K is the reference absolute temperature. The equivalent stress reads:

$$\bar{\tau}_x = \sqrt{\frac{1}{2}\boldsymbol{\sigma}_x : \boldsymbol{\sigma}_x} \tag{5.19}$$

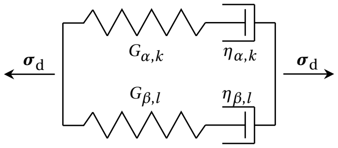

Figure 5.3: Mechanical analog for driving stress of the EGP model; multiple Maxwell elements connected in parallel can also distinguish between two different relaxation processes: α and β

where $\boldsymbol{\sigma}_x = \sum \boldsymbol{\sigma}_{x,j}$. The characteristic shear stress reads:

$$\bar{\tau}_{0x} = \frac{k_{\mathrm{B}} T}{V_x} \tag{5.20}$$

in which k_{B} is the Boltzmann constant, and V_x is the activation volume.

The state parameter S_x takes into account the thermodynamic history of the material, and is defined as a product of the ageing parameter $S_{\mathrm{a}x}$ and the softening function $R_{\gamma x}$ [31]. However, following earlier work on creep rupture [17], the ageing parameter is set to zero.

In the EGP model, the equivalent plastic strain $\bar{\gamma}_{\mathrm{p}}$ is obtained by integrating the corresponding rate equation:

$$\dot{\bar{\gamma}}_{\mathrm{p}} = \frac{\bar{\tau}_{\alpha,1}}{\eta_{\alpha,1}} \equiv C, \quad \bar{\tau}_{\alpha,1} = \sqrt{\frac{1}{2}\boldsymbol{\sigma}_{\alpha,1} : \boldsymbol{\sigma}_{\alpha,1}} \tag{5.21}$$

where $\bar{\tau}_{\alpha,1}$ is the equivalent stress of the mode with the highest viscosity $\eta_{\alpha,1}$. For the sake of time homogenization procedure, this ratio is also denoted by C.

Since the time derivative of the isochoric elastic left Cauchy-Green deformation tensor, Eq. (5.16), is not an objective tensor, the formulation for the driving stress is cast into a form relying on the plastic right Cauchy-Green deformation tensor $\mathbf{C}_{\mathrm{p}}$ that is invariant. A relation between this tensor and the tensor $\tilde{\mathbf{B}}_{\mathrm{e}}$ can be derived. In the context of the Updated Lagrangian formulation, this relation in the modal form reads:

$$\mathbf{C}_{\mathrm{p}x,j} = \Delta\tilde{\boldsymbol{F}}^{\mathrm{T}}\tilde{\mathbf{B}}_{\mathrm{e}x,j}^{-1}\Delta\tilde{\boldsymbol{F}} \tag{5.22}$$

where $\Delta\tilde{\boldsymbol{F}}$ is the incremental isochoric deformation gradient. Once $\mathbf{C}_{\mathrm{p}x,j}$ at current time step is computed, Eq. (5.22) can be used to express $\tilde{\mathbf{B}}_{\mathrm{e}x,j}$ that is further used in the driving stress update, Eq. (5.15). To this end, the rate equation for $\mathbf{C}_{\mathrm{p}x,j}$ is considered:

$$\dot{\mathbf{C}}_{\mathrm{p}x,j} = \frac{G_{x,j}}{\eta_{x,j}}\left(\Delta\tilde{\mathbf{C}} - \frac{1}{3}\mathrm{tr}\left(\bar{\tilde{\mathbf{B}}}_{\mathrm{e}x,j}\right)\mathbf{C}_{\mathrm{p}x,j}\right) \tag{5.23}$$

Because the right Cauchy-Green deformation tensor and its derivatives are invariant, while the left Cauchy-Green deformation tensor is objective, the rotation neutralized version of $\tilde{\mathbf{B}}_{\mathrm{e}x,j}$ is considered in the previous equation, which is defined as:

$$\bar{\tilde{\mathbf{B}}}_{\mathrm{e}x,j} = \Delta\mathbf{R}^{\mathrm{T}}\tilde{\mathbf{B}}_{\mathrm{e}x,j}\Delta\mathbf{R} \tag{5.24}$$

Assuming that $\mathrm{tr}(\bar{\tilde{\mathbf{B}}}_{\mathrm{e}x,j})/3 \approx 1$ in Eq. (5.23), the expression for $\mathbf{C}_{\mathrm{p}x,j}$ at current time step n can be derived as:

$$\mathbf{C}^{n}_{\mathrm{p}x,j} = (1-\lambda^{n}_{x,j})\Delta\tilde{\mathbf{C}}^{n} + \lambda^{n}_{x,j}\mathbf{C}^{n-1}_{\mathrm{p}x,j} \tag{5.25}$$

where the plasticity parameter $\lambda^{n}_{x,j}$ measures the amount of plastic deformation in the time step and emerges as:

$$\lambda^{n}_{x,j} = \frac{1}{1+\Gamma^{n}_{x,j}\Delta t} \tag{5.26}$$

where $\Gamma^{n}_{x,j} = G_{x,j}/\eta^{n}_{x,j}$ is the ratio between the modal shear modulus and viscosity, and Δt is the time increment. When $\lambda^{n}_{x,j} = 1$ the deformation increment is purely elastic; when $\lambda^{n}_{x,j} = 0$ the increment is completely plastic. The modal plasticity parameters depend on the viscosity through $\Gamma^{n}_{x,j}$, which in turn depends on the equivalent stress that defines the equivalent plastic strain rate, Eq. (5.21). With this in mind, a coupled system of equations is iteratively solved, whereby the plasticity parameters are computed together with the equivalent plastic strain, assuming the backward Euler integration scheme:

$$\begin{gathered} \lambda^{n}_{x,j}\left(1+\Gamma^{n}_{x,j}\Delta t\right) = 1 \\ \bar{\gamma}^{n}_{\mathrm{p}} - \dot{\bar{\gamma}}^{n}_{\mathrm{p}}\Delta t = \bar{\gamma}^{n-1}_{\mathrm{p}} \end{gathered} \tag{5.27}$$

Values of the model parameters used in this work are listed in Table 5.1, followed by the relaxation spectrum in Table 5.2. All these EGP model inputs are the same as in [17].

Table 5.1: EGP model parameters

κ [MPa]	G_r [MPa]	V_α [nm^3]	V_β [nm^3]
2600	25	3.518	3.518
ΔH_α [kJ/mol]	ΔH_β [kJ/mol]	$\mu_\alpha = \mu_\beta$	$S_\alpha = S_\beta$
375.87	325.28	0.08	0

Table 5.2: Relaxation spectrum of the EGP model

x, j	$G_{x,j}$ [MPa]	$\eta_{0x,j}$ [MPa·s]
$\alpha, 1$	521.96	$1.992\cdot10^{26}$
$\beta, 1$	455.96	$4.965\cdot10^{22}$
$\beta, 2$	385.58	$5.518\cdot10^{21}$
$\beta, 3$	312.50	$6.761\cdot10^{20}$
$\beta, 4$	238.85	$2.108\cdot10^{19}$
$\beta, 5$	166.87	$1.591\cdot10^{15}$
$\beta, 6$	98.51	$2.571\cdot10^{12}$
$\beta, 7$	35.14	$7.086\cdot10^{9}$

5.3.2. TWO-SCALE EINDHOVEN GLASSY POLYMER CONSTITUTIVE MODEL

In this section, a two-scale version of the EGP model is developed to efficiently take into account the high-cycle loading scenario. Following the concept of time homogenization (TH), see e.g. [16, 32–34], the model distinguishes between two timescales: micro timescale (t_μ) and macro timescale (t_M). In that regard, the physical time t is represented as a combination of the slowly varying time coordinate t_M and the rapidly varying time coordinate t_μ:

$$t = t_M + T t_\mu \tag{5.28}$$

where T is the load period and $t_\mu \in [0, 1]$. With this decomposition in mind, any field variable ζ can be expressed as a function of the initial position $\mathbf{X}$ and two time coordinates: $\zeta(\mathbf{X}, t_M, t_\mu)$. Since the whole consideration concerns an integration point initially located at $\mathbf{X}$, the position coordinate is dropped from further equations. The total derivative of ζ with respect to the physical time then reads:

$$\dot{\zeta} = \frac{\partial \zeta}{\partial t_M} + \frac{1}{T}\frac{\partial \zeta}{\partial t_\mu} \tag{5.29}$$

The field variable ζ can be asymptotically expanded in a series:

$$\zeta(t_M, t_\mu) = \sum_{i=0}^{\infty} T^i \zeta_i(t_M, t_\mu) \tag{5.30}$$

where $\zeta_i(t_M, t_\mu)$ is almost periodic in t_μ due to the evolving viscosity in the EGP model, and its relative contribution to ζ decays as the power i increases.

If a field quantity, e.g. the equivalent plastic strain rate in Eq. (5.21), admits a gradient at a point, its first-order asymptotic expansion can be written as the following [34]:

$$C = C_0 + T DC(\bar{\tau}_0, \eta_0) \cdot (\bar{\tau}_1, \eta_1) + O(T^2) \tag{5.31}$$

where O is the Landau notation for higher-order terms, $DC(\bar{\tau}_0, \eta_0) \cdot (\bar{\tau}_1, \eta_1)$ is the inner product of the gradient of C with respect to $\bar{\tau}_0$ and η_0 with the corresponding quantities of the order 1 ($\bar{\tau}_1$, η_1). The subscripts here should not be confused with different modes of the EGP model: they represent quantities of different order associated with the mode of highest viscosity. Applying the asymptotic expansion on $\bar{\gamma}_\mathrm{p}$ and performing the total time differentiation, Eqs. (5.30) and (5.29), yields an expression for the equivalent plastic strain rate:

$$\dot{\bar{\gamma}}_\mathrm{p} = \frac{\partial \bar{\gamma}_\mathrm{p0}}{\partial t_M} + \frac{1}{T}\frac{\partial \bar{\gamma}_\mathrm{p0}}{\partial t_\mu} + T\frac{\partial \bar{\gamma}_\mathrm{p1}}{\partial t_M} + \frac{\partial \bar{\gamma}_\mathrm{p1}}{\partial t_\mu} + T\frac{\partial \bar{\gamma}_\mathrm{p2}}{\partial t_\mu} + O(T^2) \tag{5.32}$$

If we now group the terms of the same order of T in Eqs. (5.31) and (5.32) the following relations are obtained (up to order 0):

$$\begin{aligned} \left(T^{-1}\right):& \frac{\partial \bar{\gamma}_{\mathrm{p}0}}{\partial t_\mu} = 0 \\ \left(T^{0}\right):& \frac{\partial \bar{\gamma}_{\mathrm{p}0}}{\partial t_M} + \frac{\partial \bar{\gamma}_{\mathrm{p}1}}{\partial t_\mu} = C_0 \end{aligned} \tag{5.33}$$

It follows from the (T^{-1}) problem that the zero-order equivalent plastic strain does not evolve with the micro time coordinate, i.e., $\bar{\gamma}_{\mathrm{p}0} = \bar{\gamma}_{\mathrm{p}0}(t_M)$. Further, $\partial \bar{\gamma}_{\mathrm{p}1}/\partial t_\mu \approx 0$ in Eq. (5.33), since $\bar{\gamma}_{\mathrm{p}1}$ is almost periodic in t_μ and the equivalent plastic strain is a non-decreasing function. Therefore, by solving the zero-order problem we update the material state elastically at t_μ, and account for viscoplastic deformation at t_M, i.e., at macro time steps. Because the analysis is geometrically nonlinear, it is still necessary to utilize an iterative Newton-Raphson solver at micro time steps.

EFFECTIVE TIME INCREMENT

At the micro timescale, the cyclic variation of the load is accounted for, but the constitutive response is simplified. At the macro timescale, a constant load is applied and the complete constitutive model is used, but information from the micro time steps is used to perform the update. The stress-dependent plastic flow is averaged over the load cycle by replacing Δt in Eq. (5.27) with an effective time increment Δt_{eff}.

One load cycle with the proposed time stepping scheme is illustrated in Fig. 5.4, where the load period coincides with the time increment Δt. The loading cycle is divided into micro time steps at which the information necessary to compute Δt_{eff} for the macro time step is collected. The material update at micro time steps is elastic, without evolution in viscoplastic deformation, which means that $\lambda^n_{x,j} = 1$, see Eq. (5.25). However, in order to compute the effective time increment at an integration point, $\dot{\bar{\gamma}}_{\mathrm{p}}$ is computed from Eq. (5.21) in the elastic micro time steps. Also, symmetry is used at t_μ, such that $\dot{\bar{\gamma}}_{\mathrm{p}}$ is mirrored to the corresponding micro time step, see Fig. 5.4.

When all micro time steps for a single cycle are completed, a macro time step is made, with a jump from the previous converged macro time step to the current one. Macro time steps $n-1$ and n correspond to the same load level, that is $\sigma^{\max}_{yy}$ in this case. If no information is conveyed from micro time steps, the standard update of the EGP model would lead to a creep response, with the actual time increment Δt. In order to include the effect of cyclic loading, an effective time increment is introduced to correct for the variation in equivalent plastic strain rate over the cycle:

$$\dot{\bar{\gamma}}^{n}_{\mathrm{p}} \Delta t_{\mathrm{eff}} = \int_{t^{n-1}}^{t^{n}} \dot{\bar{\gamma}}_{\mathrm{p}}\, dt \tag{5.34}$$

where the integral on the right hand side is evaluated with a trapezoidal integration rule using $\dot{\bar{\gamma}}_{\mathrm{p}}$ from the micro time steps of the last cycle, as well as from the previous and current macro time

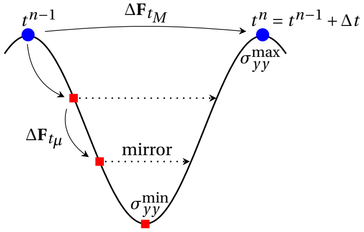

Figure 5.4: One load cycle divided in micro time steps (squares) and macro time steps (circles); increment in deformation gradient $\Delta\mathbf{F}_{t_\mu}$ computed with respect to previous converged macro time step for the first micro time step, and with respect to previous micro time step for other micro time steps; $\Delta\mathbf{F}_{t_M}$ computed with respect to previous converged macro time step

steps, $\dot{\gamma}_{\mathrm{p}}^{n-1}$ and $\dot{\gamma}_{\mathrm{p}}^{n}$, respectively. From Eq. (5.34) the expression for Δt_{eff} emerges as:

$$\Delta t_{\mathrm{eff}} = \frac{\int_{t^{n-1}}^{t^n} \dot{\gamma}_{\mathrm{p}} dt}{\dot{\gamma}_{\mathrm{p}}^{n}} \tag{5.35}$$

The concept of effective time in the EGP model was used by Janssen et al. [35] to capture the endurance limit in polymers at cyclic loading. It was computed employing stress- and temperature-based shift functions on the actual time, and used to evolve the ageing parameter in a phenomenological way. Despite the similar terminology in [35], our approach shows more resemblance to another paper by Janssen et al. [36], in which the so-called acceleration factor was computed as the ratio of the incremental equivalent plastic strain in cyclic loading to that in static loading, for one typical load cycle. The acceleration factor eventually multiplies the plastic strain rate due to static stress, in an analytical framework (not used in the EGP model) determining the time to failure in static as well as in cyclic loading. In our case, the product of the effective time increment and the equivalent plastic strain rate in static loading equals an increment in the equivalent plastic strain due to cyclic loading, Eq. (5.34).

5.3.3. TRANSVERSELY ISOTROPIC CONSTITUTIVE MODEL FOR CARBON FIBERS

Assuming absence of failure in the reinforcement, we use a hyperelastic transversely isotropic constitutive model for carbon fibers formulated by Bonet and Burton [19], with a minor modification reported in [24]. Since no additional changes are made to the model, only the elastic constants used to run simulations are listed here, see Table 5.3. The adopted values are the same as in [17]. E_1 is the Young's modulus in the preferential stiffness direction of the material, that is the fiber direction in this case; E_2 and ν_{23} are the Young's modulus and the Poisson's ratio defining the material behavior in the plane of isotropy; G_{12} and ν_{12} are the shear modulus and the Poisson's ratio for the planes perpendicular to the isotropic plane.

5.3.4. FATIGUE COHESIVE ZONE MODEL

To model microcrack propagation through the polymer matrix under the high- and low-cycle fatigue loading we utilize the cohesive zone model formulated by Dávila [2], in its implicit formulation with consistent linearization by Hofman et al. [22]. Dávila's model, originally developed for problems of delamination in composites, assumes a damage variable which grows with either quasi-static or fatigue loading. It is meant to represent creation of microcracks at a lower scale of observation. We apply the same CZM in the RVE, also assuming that the damage variable represents corresponding cracking processes in the polymer matrix at a yet lower scale.

The cohesive model is formulated in local orthonormal coordinate frame $(\mathbf{n}, \mathbf{s}, \mathbf{t})$, which defines the orientation of the cohesive surface at the integration point: $\mathbf{n}$ is the unit vector in the normal direction associated with the normal dummy stiffness K_n; $\mathbf{s}$ and $\mathbf{t}$ are the unit vectors tangent to the surface, associated with the shear dummy stiffness K_{sh}. Cohesive segments are inserted on the fly [21] when a suitable initiation criterion is satisfied, meaning that zero displacement jump corresponds with a nonzero traction vector. Because this combination may lead to the singularity problem in mixed-mode loading [37], the cohesive model is evaluated with the shifted displacement jump $[\![\mathbf{u}]\!]$ [38]:

$$[\![\mathbf{u}]\!] = [\![\mathbf{u}]\!]^{\mathrm{fe}} + [\![\mathbf{u}]\!]^{0} \tag{5.36}$$

where $[\![\mathbf{u}]\!]^{\mathrm{fe}}$ is the displacement jump obtained from the finite element space, and $[\![\mathbf{u}]\!]^{0}$ is the dis-

Table 5.3: Elastic constants of the transversely isotropic constitutive model

E_1 [GPa]	E_2 [GPa]	G_{12} [GPa]	ν_{12}	ν_{23}
125	15	5	0.05	0.3

placement shift:

$$[\![\mathbf{u}]\!]^0 = \left(\frac{t_n^0}{K_n}, \frac{t_s^0}{K_{\text{sh}}}, \frac{t_t^0}{K_{\text{sh}}}\right)^{\text{T}} \tag{5.37}$$

with t_n^0, t_s^0, t_t^0 the traction vector components at initiation.

QUASI-STATIC DAMAGE

The evolution of damage under quasi-static loading is described with Turon's cohesive model [39], which can be written in the following form:

$$\mathbf{t} = (\mathbf{I} - \Omega)\mathbf{K}[\![\mathbf{u}]\!] = (\mathbf{I} - \Omega)\mathbf{t}^{\text{eff}} \tag{5.38}$$

where $\mathbf{t}^{\text{eff}}$ is the effective traction on the cohesive surface; $\mathbf{I}$ is the identity matrix and $\mathbf{K}$ is the dummy stiffness matrix:

$$\mathbf{K} = \begin{bmatrix} K_n & 0 & 0 \\ 0 & K_{sh} & 0 \\ 0 & 0 & K_{sh} \end{bmatrix} \tag{5.39}$$

In Eq. (5.38), Ω is the damage tensor defined as:

$$\Omega_{ij} = d\delta_{ij}\left(1 + \delta_{i1}\frac{\langle -t_n^{\text{eff}}\rangle}{t_n^{\text{eff}}}\right) \tag{5.40}$$

The Kronecker delta δ_{ij} ensures nonzero components only on the main diagonal of Ω, while the Macaulay brackets restore the dummy stiffness in the normal direction, in the case of compression. The damage variable d measures the stiffness loss in a mixed-mode loading scenario, and its thermodynamically consistent evolution is ensured by relating the dummy stiffnesses:

$$K_{sh} = K_n \frac{G_{Ic}}{G_{IIc}}\left(\frac{f_{sh}}{f_n}\right)^2 \tag{5.41}$$

Here, G_{Ic} and G_{IIc} are the fracture energies for the mode I and mode II loading, while f_n and f_{sh} are the quasi-static strength parameters in the normal and shear direction, respectively. To compute the stiffness loss d, the cohesive model can be represented with an equivalent 1D traction-separation relation:

$$\sigma = (1-d)K_{\mathscr{B}}\Delta \tag{5.42}$$

where σ is the equivalent stress, $K_{\mathscr{B}}$ the mixed-mode dummy stiffness, and Δ is the equivalent displacement jump. The mixed-mode dummy stiffness reads:

$$K_{\mathscr{B}} = (1-\mathscr{B})K_n + \mathscr{B}K_{sh} \tag{5.43}$$

where $\mathscr{B}$ is the mode-mixity variable defined as:

$$\mathscr{B} = \frac{K_{sh}[\![u]\!]_{sh}^2}{K_n\langle[\![u]\!]_n\rangle^2 + K_{sh}[\![u]\!]_{sh}^2} \tag{5.44}$$

In this expression $[\![u]\!]_{sh}$ is the Euclidean norm of the displacement jump sub-vector corresponding with the shear components:

$$[\![u]\!]_{sh}^2 = [\![u]\!]_s^2 + [\![u]\!]_t^2 \tag{5.45}$$

The equivalent stress σ is defined as:

$$\sigma = \left[\langle t_n\rangle^2 + t_s^2 + t_t^2\right]^{1/2} \tag{5.46}$$

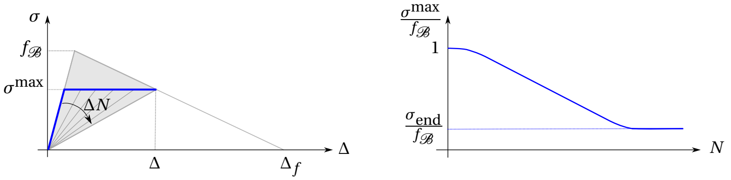

Figure 5.5: The quasi-static cohesive model [39] represents the failure envelope of the traction-separation response in fatigue loading (left). The evolution of fatigue damage is such that the CZM is able to reproduce an *S*-*N* curve, but does not account for actual loading frequency (right)

whereas the equivalent displacement jump emerges as:

$$\Delta = \frac{K_n\langle[\![u]\!]_n\rangle^2 + K_{sh}[\![u]\!]_{sh}^2}{\left[K_n^2\langle[\![u]\!]_n\rangle^2 + K_{sh}^2[\![u]\!]_{sh}^2\right]^{1/2}} \tag{5.47}$$

To track the damage process, the state variable $\mathscr{D}$ is introduced as an energy-based damage variable:

$$\mathscr{D} \equiv \frac{G_d}{G_c} = \frac{\Delta - \Delta_0}{\Delta_f - \Delta_0} \tag{5.48}$$

$\mathscr{D}$ represents the ratio between the dissipated energy G_d and the fracture energy G_c, and alternatively can be written as a function of the equivalent displacement jump. The state variable is evaluated by knowing the equivalent displacement jump at initiation Δ_0, and at the moment of fracture Δ_f:

$$\begin{aligned} \Delta_0 &= \left[\frac{K_n([\![u]\!]_n^0)^2 + \left(K_{sh}([\![u]\!]_{sh}^0)^2 - K_n([\![u]\!]_n^0)^2\right)\mathscr{B}^{\eta_{\text{BK}}}}{K_{\mathscr{B}}}\right]^{1/2} \\ \Delta_f &= \frac{K_n[\![u]\!]_n^0[\![u]\!]_n^f + \left(K_{sh}[\![u]\!]_{sh}^0[\![u]\!]_{sh}^f - K_n[\![u]\!]_n^0[\![u]\!]_n^f\right)\mathscr{B}^{\eta_{\text{BK}}}}{K_{\mathscr{B}}\Delta_0} \end{aligned} \tag{5.49}$$

In this equation η_{BK} is the Benzeggagh-Kenane (B-K) interaction parameter [40], while the pure mode I and the pure mode II displacement jump at initiation (superscript 0) and the moment of fracture (superscript f) are defined as:

$$\begin{aligned} [\![u]\!]_n^0 &= \frac{f_n}{K_n}, \qquad [\![u]\!]_n^f = \frac{2G_{Ic}}{f_n} \\ [\![u]\!]_{sh}^0 &= \frac{f_{sh}}{K_{sh}}, \qquad [\![u]\!]_{sh}^f = \frac{2G_{IIc}}{f_{sh}} \end{aligned} \tag{5.50}$$

Finally, the relation between the energy-based damage variable $\mathscr{D}$ and the damage variable d is:

$$d = 1 - \frac{(1-\mathscr{D})\Delta_0}{\mathscr{D}\Delta_f + (1-\mathscr{D})\Delta_0} \tag{5.51}$$

FATIGUE DAMAGE

Taking the quasi-static cohesive model as the failure envelope, Dávila formulated a fatigue cohesive zone model [2]. In the model, the state variable $\mathscr{D}$ may evolve before the quasi-static strength $f_{\mathscr{B}}$ is reached, given an increment in the number of load cycles ΔN. When the pair $(\sigma^{\max}, \Delta)$ reaches the softening line of the quasi-static CZM, failure of the material ensues, see Fig. 5.5 (left). The fatigue damage variable $\mathscr{D}_f$ is defined in such a way that the model reproduces the *S*-*N* curve of the material, but without considering effects of the actual loading frequency. The fatigue damage changes with the number of cycles N according to the evolution law:

$$\frac{\mathrm{d}\mathscr{D}_f}{\mathrm{d}N} = f_{\mathscr{D}}(\Delta, \Delta^*, \mathscr{D}) \tag{5.52}$$

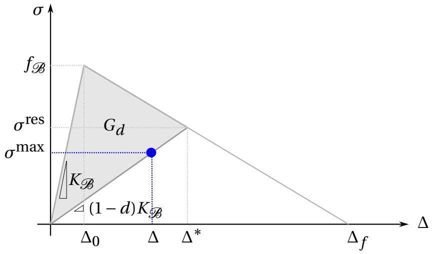

Figure 5.6: Graphical representation of the quantities used in formulation of fatigue cohesive zone model

where Δ^* is the equivalent displacement jump corresponding with the residual strength σ^{res}, see Fig. 5.6, defined as:

$$\Delta^* = \mathscr{D}(\Delta_f - \Delta_0) + \Delta_0 \tag{5.53}$$

To make sure that the traction-separation curve in fatigue scenarios remains inside the failure envelope, the quasi-static damage variable $\mathscr{D}_s$ is also computed:

$$\mathscr{D}_s = \frac{\Delta - \Delta_0}{\Delta_f - \Delta_0} \tag{5.54}$$

Finally, the state variable $\mathscr{D}$ is the maximum of $\mathscr{D}_s$ and $\mathscr{D}_f$:

$$\mathscr{D} = \max\left(\mathscr{D}_s, \mathscr{D}_f\right) \tag{5.55}$$

The fatigue damage function, Eq. (5.52), is integrated numerically using the trapezoidal rule [22]:

$$\mathscr{D}_f^n = \mathscr{D}_f^{n-1} + \frac{1}{2}\Delta N \left[f_{\mathscr{D}}^{n-1} + f_{\mathscr{D}}^n \right] \tag{5.56}$$

The evolution of fatigue damage, Eq. (5.52), is represented with the CF20 function [20]:

$$f_D^{\text{CF20}} = \frac{1}{\gamma} \frac{(1-\mathscr{D})^{\beta-p}}{E^{\beta}(p+1)} \left(\frac{\Delta}{\Delta^*}\right)^{\beta} \tag{5.57}$$

Here, $\gamma = 10^7$ is the number of cycles without failure at the relative endurance limit E, p is a fitting parameter adopted as: $p = \beta + 1$, and β is the parameter defining the slope of the S-N curve:

$$\beta = \frac{-7\eta}{\log E} \tag{5.58}$$

In this equation, η is the brittleness parameter which marks the kink in the S-N curve, that distinguishes between the low-cycle fatigue and the high-cycle fatigue regime. The relative endurance limit is defined as:

$$E = \frac{2C_l\epsilon}{C_l\epsilon + 1 + R(C_l\epsilon - 1)} \tag{5.59}$$

where ϵ is the relative endurance limit at $R = -1$ and mode I loading, while C_l is the correction factor that takes into account mixed-mode loading [41]:

$$C_l = 1 - 0.42\mathscr{B} \tag{5.60}$$

To evaluate Eq. (5.59) the load ratio R is computed locally for every cohesive surface, following the idea presented by Joosten et al. [20]. With a small adjustment that the Macaulay operation is not performed on t_n, the severity vector is defined as:

$$\bar{S} = \left(\frac{t_n}{f_n}, \frac{t_s}{f_{\text{sh}}}, \frac{t_t}{f_{\text{sh}}}\right)^{\text{T}} \tag{5.61}$$

In a loading scenario where the only nonzero traction component is t_n and the Macaulay brackets are included, it is not possible to distinguish between $R = 0$ and negative R. Eventually, R is computed as:

$$R = \frac{\bar{S}^{\min} \cdot \bar{S}^{\max}}{\|\bar{S}^{\max}\|^2} \tag{5.62}$$

where $\bar{S}^{\min}$ and $\bar{S}^{\max}$ are the minimum and the maximum severity vector encountered in one loading cycle, respectively. For this purpose, the severity vectors computed at t^{n-1} macro time step and at the micro time step with the minimum applied stress are utilized ($\bar{S}_M$ and $\bar{S}_\mu$, respectively). Of these two vectors, the one with larger Euclidean norm is assigned to $\bar{S}^{\max}$ in Eq. (5.62).

Parameters used to run simulations with the presented cohesive model are tabulated in Table 5.4, where the last three parameters are related to the fatigue damage part. The dummy stiffness acquires the high value in order to reduce the compliance effect introduced in the RVE by the presence of many cohesive segments. The fracture energies are adopted according to [26]. The relation for p follows the form presented in [42]. The B-K interaction parameter has a value according to [43]. The strength parameters f_n and f_{sh}, as well as the fatigue damage parameters ϵ and η, are calibrated on experimental S-t curves for $R = 0.1$, $f = 1$ Hz, $\chi = 90°$ and $\chi = 45°$, see Section 5.5.2.

5.3.5. COHESIVE MICROCRACK INITIATION

Inter-element cohesive segments are included in the RVE on the fly, when an initiation criterion is satisfied. Dealing with the low- and high-cycle fatigue, in this study we use the endurance limit-based initiation criterion introduced in [22]. In the criterion, the equivalent endurance limit (stress) is defined as:

$$\sigma_{\text{end}} = E f_{\mathscr{B}} \tag{5.63}$$

where E is computed with Eq. (5.59), and $f_{\mathscr{B}}$ is the mode-dependent quasi-static strength, $f_{\mathscr{B}} = K_{\mathscr{B}} \Delta_0$. It can be expressed in terms of the cohesive model input parameters and the mixed-mode variable $\mathscr{B}$:

$$f_{\mathscr{B}} = \left(\left[(1-\mathscr{B})K_n + \mathscr{B}K_{sh} \right] \left[f_n^2/K_n + \left(f_{sh}^2/K_{sh} - f_n^2/K_n \right) \mathscr{B}^{\eta_{\text{BK}}} \right] \right)^{1/2} \tag{5.64}$$

When the cohesive initiation criterion is checked, the corresponding cohesive segment is not present and the displacement jump is a zero vector. Therefore, the direct application of Eq. (5.44) to compute $\mathscr{B}$ is not possible, and $\mathscr{B}$ is expressed through the traction vector components on a potential cohesive surface:

$$\mathscr{B} = \frac{t_{sh}^2/K_{sh}}{\langle t_n \rangle^2/K_n + t_{sh}^2/K_{sh}} \tag{5.65}$$

where a potential cohesive surface is any surface between bulk finite elements in the matrix, or on the fiber/matrix interface, and the traction vector is obtained from the local stress as $\mathbf{t} = \boldsymbol{\sigma}\mathbf{n}$. Finally, a cohesive segment will initiate if the equivalent stress on the potential cohesive surface, Eq. (5.42), is larger than the relative endurance limit stress:

$$\frac{\sigma}{\sigma_{\text{end}}} > 1 \tag{5.66}$$

In this study we introduce a modification when checking for cohesive initiation by not letting the R used for computing E exceed a value of 0.1, i.e., for the initiation criterion $E(R)$ is replaced with $E(\min(R, 0.1))$. The reason for this constraint can be explained considering the creep rupture

Table 5.4: Values of cohesive zone model parameters; last three related to fatigue damage

K_n [N/mm^3]	G_{Ic} [N/mm]	G_{IIc} [N/mm]	f_n [N/mm^2]	f_{sh} [N/mm^2]
10^8	0.03	0.095	117.5	80
η_{BK}	ϵ	η	p	
2.284	0.5	0.39	$\beta + 1$	

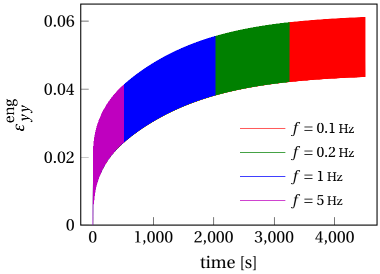

Figure 5.7: Strain response of single finite element with EGP model under uniaxial cyclic loading, where engineering stress $\sigma^{\max} = 90$ MPa and $R = 0.1$

problem. In that case $R = 1 \rightarrow E = 1$, and $\sigma_{\text{end}} = f_{\mathscr{B}}$ in Eq. (5.63). By setting the initiation threshold to quasi-static strength a large range of applied stresses is cut off from possible creep rupture. Therefore, we found this adaptation to be crucial for obtaining creep rupture at relevant stress levels. In this regard, the value of 0.1 was prescribed, but detailed sensitivity analysis on its value was not performed.

Given the endurance limit based initiation criterion, cohesive segments may initiate almost everywhere in the matrix and the fiber/matrix interface, see Section 5.5.2. To reduce computational complexity, cohesive initiation is allowed if the angle between a potential cohesive surface normal and the projection of maximum principal stress in the $\boldsymbol{e}_2$-$\boldsymbol{e}_3$ plane (plane perpendicular to the fiber direction, see Fig. 5.2) is less than 45°.

5.4. ADAPTIVE TIME STEPPING

The time stepping procedure outlined in the two-scale EGP formulation (Fig. 5.4) is part of a bigger, adaptive time stepping scheme. In this scheme, time increments between macro time steps vary depending on the convergence rate of the global Newton-Raphson scheme. If the number of iterations in a converged macro time step is less than a prescribed optimal number of iterations, the time increment of the next macro time step will increase, and vice versa. The change in time increment is according to Verhoosel et al. [44]:

$$\Delta t^n = \Delta t^{n-1} \left(\frac{1}{2}\right)^{\left(n_{\text{iter}}^{n-1} - n_{\text{iter}}^{\text{opt}}\right)/4} \tag{5.67}$$

where n_{iter}^{n-1} is the number of iterations in the last converged macro time step, and $n_{\text{iter}}^{\text{opt}}$ is the prescribed optimal number of iterations. The updated time increment is then used to evaluate the integral in Eq. (5.35), to obtain the effective time increment for the bulk material.

This computational procedure assumes that the time increment equals the loading period T, which is then changing throughout the analysis. This change in T is obviously in contrast with the experimental situation, where T (or the load frequency f) is constant. The assumption of changing T in the simulation can be introduced given the fact that the EGP response under cyclic loading is largely frequency independent. To support this statement, the full-field response of a single hexahedral finite element with the EGP model subject to different loading frequencies, with load ratio $R = 0.1$ and engineering stress $\sigma^{\max} = 90$ MPa, is shown in Fig. 5.7. As observed from the figure, there is practically no influence of f on the time-dependent response. A very minor influence is observed for the evolution of the strain at $\sigma^{\min}$, and even less for the evolution of the strain at $\sigma^{\max}$. This frequency independence allows for adaptive time stepping and taking that $\Delta t = T$, because the time homogenized response aims at capturing the maximum deformation in the matrix.

Given the elastic updates at micro time steps (t_μ), the time increment size is irrelevant for these computations, and the data collected at t_μ for computing the effective time increment is not altered if the macro time update is repeated due to the lack of convergence. Other implications of elastic updates at t_μ are that cohesive initiation is not allowed, and that the cycle increment to the

Table 5.5: Algorithm for adaptive time step n

```
1) update $\Delta t$, Eq. (5.67)
2) perform $n_\mu/2$ micro time steps
   - record $\dot{\bar{\gamma}}_\text{p}$, Eq. (5.21); elastic update of the matrix; no damage evolution in CZM
3) macro time update; matrix plasticity with $\Delta t_\text{eff}$ from Eq. (5.35); cohesive initiation with
   Eq. (5.66) and damage evolution with $\Delta N$ from Eq. (5.68)
   - if converged, go to 1)
   - if not converged, reduce $\Delta t$ and repeat 3)
```

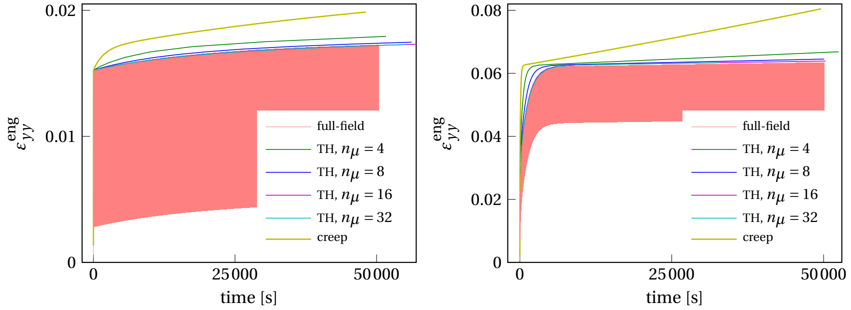

Figure 5.8: EGP response under uniaxial cyclic loading: $R = 0.1$, $\sigma^\text{max} = 70$ MPa (left) and $\sigma^\text{max} = 90$ MPa (right); full-field response compared with TH response for different number of micro time steps; the creep response corresponding to σ^max is also included

cohesive model is nonzero only at t_M. Given the actual time increment, the cycle increment at macro time steps is computed as:

$$\Delta N^n = \Delta t^n \cdot f \tag{5.68}$$

where f has a constant value equal to the actual frequency in the analysis. With $\Delta N \neq 0$ only at macro time steps, the fatigue cohesive model can also be regarded as *time-homogenized*. Although not derived from the TH formalism, see Section 5.3.4, by following the similar reasoning as in Section 5.3.2, it can be shown that in the zero-order approximation (T^0) the fatigue damage variable does not evolve with t_μ, i.e., $\mathscr{D}_f = \mathscr{D}_f(t_M)$.

An algorithm for update of material models in one time step is shown in Table 5.5. Other implementation details on setting the external force vector, checking for cohesive initiation, etc., can be found in [17], that is based on the algorithm presented in [45]. The model is implemented in Jive: a C++ library aimed for numerical simulations [46].

5.5. RESULTS AND DISCUSSION

5.5.1. TIME HOMOGENIZATION

The performance of the model is checked with several examples. In all reported cases cyclic engineering stress is applied. To begin with, the accuracy of the time homogenization procedure is examined on a single hexahedral finite element with the EGP material model. The time homogenized response for different number of micro time steps n_μ is compared with the fully-resolved response, which is evaluated with the constant time step of $T/40$ at a frequency of 0.1 Hz. The results are plotted in Fig. 5.8, for $R = 0.1$ and two maximum stress levels, where the creep response for the same stress level (at $R = 1$) is also included. As noticed from the figure, all time homogenized cases yield a lower strain compared to the creep response, which is in line with the observation that less plastic strain accumulates in cyclic loading. Furthermore, as the number of micro time steps increases, the TH response approaches the full-field response. For $\sigma^\text{max} = 70$ MPa already at $n_\mu = 16$ the TH response matches the reference result. For $\sigma^\text{max} = 90$ MPa, however, much more plastic deformation develops during cyclic loading and the TH response slightly deviates from the

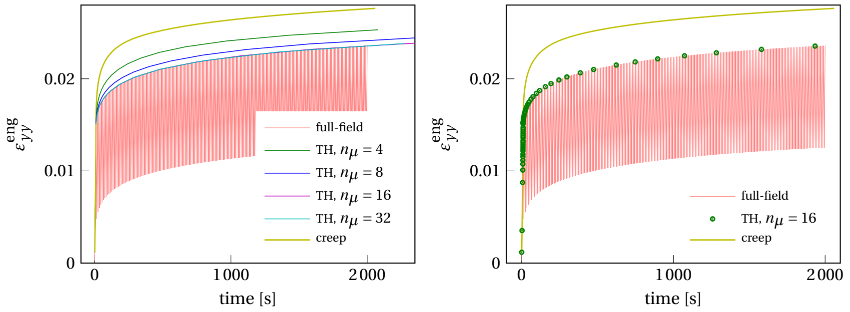

Figure 5.9: Unit cell RVE under cyclic loading: $R = 0.1$, $\sigma_{yy}^{\max} = 100$ MPa, $\chi = 45°$; creep and full-filed cyclic response ($f = 0.1$ Hz) compared with TH response for different number of micro time steps (left); TH response in scatter form illustrates adaptive stepping (right)

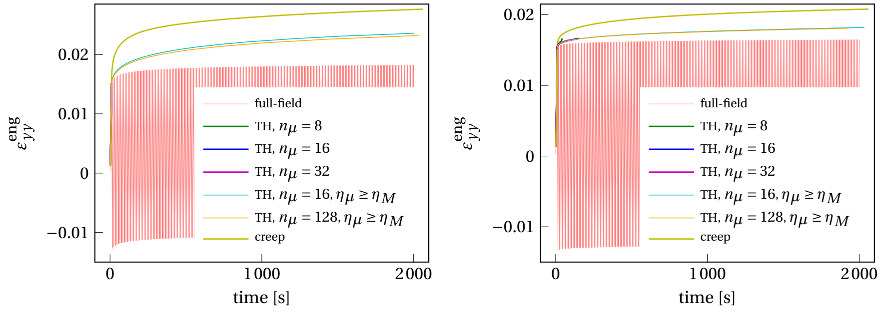

Figure 5.10: Unit cell RVE under cyclic loading: $R = -1$, $\sigma_{yy}^{\max} = 100$ MPa, $\chi = 45°$ (left), $\chi = 90°$ (right); TH response compared with creep and full-field cyclic results; η_μ is viscosity computed at micro time steps and η_M is viscosity from last macro time step

reference result: for $n_\mu = 16$ the relative error in the $\varepsilon_{yy}^{\text{eng}}$ at $t = 5 \cdot 10^4$ s is 0.74 %.

The accuracy of the TH procedure is also checked on a unit cell RVE. Finite elements representing bulk material are 12-node wedge-shaped elements, while, if present, cohesive zones are represented with 12-node cohesive elements [26]. The unit cell consisting of 274 finite elements with the minimum element length of 0.7 μm is loaded under 45°. The maximum engineering stress in the global loading direction is $\sigma_{yy}^{\max} = 100$ MPa, see Fig. 5.1, the load ratio is $R = 0.1$ and cohesive segments are not included. Comparison of the TH results with the full-field cyclic and creep response is shown in Fig. 5.9 (left). It is concluded again that increasing n_μ leads to more accurate TH results, with convergence around $n_\mu = 16$. In Fig. 5.9 (right), the TH response for $n_\mu = 16$ is plotted with markers to indicate the adaptive time stepping feature of the model. If significant plastic deformation develops in the model, the time step size is reduced to properly capture the equilibrium path, whereas in the absence of significant plastic deformation, or nonlinearity in general, the time step size is enlarged.

However, the TH procedure is not accurate in all loading situations. Let us consider the case where $R = -1$ and $\sigma_{yy}^{\max} = 100$ MPa, meaning that significant plastic deformation develops also at reversed loading. The creep and full-field cyclic response are compared with TH results for two loading angles, $\chi = 45°$ and $\chi = 90°$, see Fig. 5.10. It follows from the figure that the TH procedure is unstable: in the 45° case it fails to enter the cyclic loading phase, while in the 90° case the TH procedure fails quickly after the cyclic loading is started. The reason for this instability lies in the elastic updates at micro time steps, where the neglect of significant plastic deformation in the material leads to an overestimated equivalent stress and, correspondingly, to a lower viscosity, Eq. (5.18). Consequently, the equivalent plastic strain rate, Eq. (5.21), computed at micro time steps acquires high values, which reflects in an extremely large effective time increment at some integra-

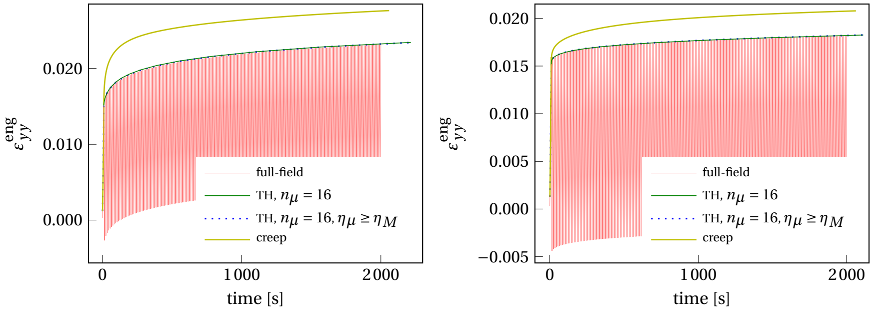

Figure 5.11: Unit cell RVE under cyclic loading: $R = -0.5$, $\sigma_{yy}^{\max} = 100$ MPa, $\chi = 45°$ (left), $\chi = 90°$ (right); TH response compared with creep and full-field cyclic response; η_μ is viscosity computed at micro time steps and η_M is viscosity from last macro time step

tion points, leading to the convergence problems. The computational instability may be circumvented by limiting the value of viscosity computed at micro time steps by setting, e.g., $\eta_\mu \geq \eta_M^{n-1}$. This condition says that the viscosity at t_μ cannot be less than the value obtained at the last macro time step. Note that the update of viscosity at micro time steps is only relevant for the computation of $\dot{\bar{\gamma}}_\text{p}$, since in the elastic update of the stress state there is no actual update of the state variables controlling viscoplasticity. With the added condition the computation becomes stable, although still inaccurate, because the equivalent plastic strain rate does not account for the direction of equivalent plastic strain, but only for the absolute value of its rate. Therefore, when computing Δt_eff, Eq. (5.35), $\dot{\bar{\gamma}}_\text{p}$ from the compression side is added to that from the tension side, leading to an overestimated effective time increment. It is possible to introduce information on the direction of plastic deformation by multiplying $\dot{\bar{\gamma}}_\text{p}$ with the normalized inner product ($\boldsymbol{\sigma}_M : \boldsymbol{\sigma}_\mu / |\boldsymbol{\sigma}_M : \boldsymbol{\sigma}_\mu|$) to define its sign, where $\boldsymbol{\sigma}_M$ is the Cauchy stress tensor computed at last converged macro time step, and $\boldsymbol{\sigma}_\mu$ is the Cauchy stress tensor computed at current micro time step. However, this action renders unstable computations and does not solve the problem, because $\dot{\bar{\gamma}}_\text{p}$ collected at elastic micro time steps corresponding with high compressive stress levels remains inaccurate.

The conclusion is that the introduced TH procedure is accurate as long as there is no significant reverse plasticity in the cycle. This claim is confirmed with another example on the unit cell, in which $R = -0.5$ and $\sigma_{yy}^{\max} = 100$ MPa. The TH response without limiting viscosity at micro time steps and the response with limited viscosity are compared with the creep and full-field cyclic response for two loading angles: $\chi = 45°$ and $\chi = 90°$, see Fig. 5.11. Although the load ratio is negative, the material behavior at reversed loading is predominantly elastic with diminishing $\dot{\bar{\gamma}}_\text{p}$, resulting in an accurate TH prediction.

5.5.2. FAILURE PREDICTION

Cohesive segments are now also included in the RVE, and a comparison is made with available experiments on fatigue of UD carbon/PEEK thermoplastic composites [23]. All examples assume room temperature conditions, such that $T = T_\text{ref}$ in Eq. (5.18). The fiber volume ratio is 0.4. The number of micro time steps between two macro time updates is $n_\mu = 16$, with actually running only half of them, see Section 5.3.2. Since the main intention here is to show the capabilities of the model, a micromodel that is too small to be entirely representative with 4 (2 × 2) fibers in total is considered, with a diameter of 5 μm. Similar conclusions on the mechanical behavior are expected from a bigger RVE size, especially because calibration of the cohesive model parameters was done particularly for this micromodel, improving its representativeness. Gmsh was used to generate the finite element mesh [47].

The model is calibrated on experimental S-t curves obtained for $R = 0.1$, $f = 1$ Hz, $\chi = 90°$ and $\chi = 45°$, see Fig. 5.12, where the experimental data are compared with the model results. Several things can be observed from the figure. First, the model is able to make a distinction between the

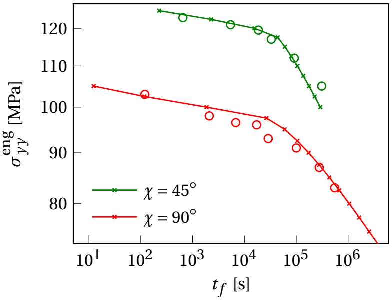

Figure 5.12: Maximum stress applied versus time to failure for two off-axis angles; solid lines represent model response, with x marking stress levels considered in simulations; empty markers represent experimental data used for calibration; $R = 0.1$, $f = 1$ Hz

plasticity controlled and crack growth controlled failure regimes. However, there is an offset in the model results from the experimental data in the transition zone between the two failure regimes for $\chi = 90°$. It should be noted that all the EGP parameters, including the relaxation spectrum, were adopted according to our previous work on creep rupture [17], and their calibration was not part of this work. Only the four parameters of the cohesive model were calibrated (f_n, f_{sh}, ϵ and η). While the strength parameters f_n and f_{sh} have an overall effect on the S-t (or S-N) curve, the two are also controlling the slope of the plasticity controlled part on which ϵ and η have no effect, with f_n being most dominant for the 90° loading case, while the influence of f_{sh} is stronger in the 45° case. The fatigue damage parameter ϵ largely controls the slope of the crack growth failure regime [20], and was adopted such that the slope in $\chi = 90°$ loading is properly reproduced, see Fig. 5.12, where the last two points of the 90° case are considered to define the slope of the crack growth regime. Given all the inputs, the fatigue damage parameter η determines the moment when the transition between the two failure mechanisms occur, horizontally shifting the onset of the crack growth controlled regime [20]. The value of η was adopted such that a good match was found for the last two points of the $\chi = 90°$ case, also checking for the proper transition between the failure mechanisms when $\chi = 45°$. Possibly, a further calibration of the constitutive models including the relaxation spectrum of the EGP and the cohesive model parameters could reduce the error in the results for $\chi = 90°$ and $f = 1$ Hz.

Another observation from Fig. 5.12 indicates a shortcoming of the model related to off-axis dependence of the crack growth controlled failure mechanism. For the carbon/PEEK composite system considered here, the same slope in S-t curves is reported for different loading angles [23], which is in contrast with the model results, where $\chi = 45°$ features a different slope in the crack growth regime than $\chi = 90°$. Although for some composite systems a change in the slope is reported when changing off-axis angles [48], the reported change is in the opposite direction: lowering the off-axis angle lowers the slope of the crack growth regime.

The following example considers the RVE loaded under 90° off-axis angle. Different stress levels and frequencies are considered at the load ratio of 0.1. In Fig. 5.13 (left) the model prediction of the time to failure is compared with the experimental data in a *loglog* plot. The model is able to properly capture the experimentally observed frequency dependency of the two mechanisms. While the plasticity controlled part is insensitive to the loading frequency, the crack growth controlled part is frequency dependent, leading to shorter lifetimes at higher frequencies. Overall, the accuracy of the model is good, with an already discussed offset from the experiment at $f = 1$ Hz in the transition zone between two failure regimes. In Fig. 5.13 (right), the number of cycles to failure is plotted for different stress levels, showing a different effect of the frequency on the failure regimes. In this representation, the plasticity controlled regime shows sensitivity to the loading frequency, while the crack growth controlled part is largely independent of the loading frequency.

The loading angle of 45° is considered next. The time to failure versus stress applied is plotted

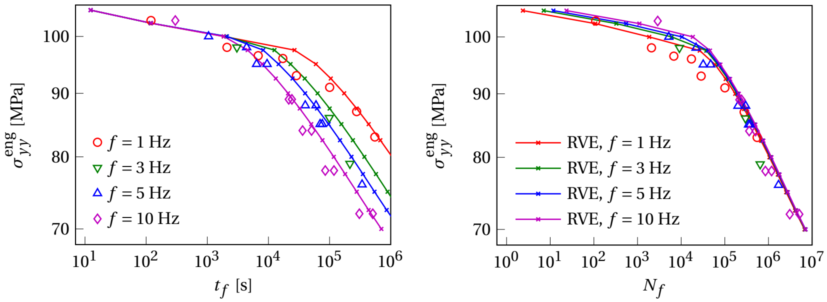

Figure 5.13: Maximum stress applied versus time to failure for $\chi = 90°$, $R = 0.1$ and different frequencies (left); corresponding number of cycles to failure (right); empty markers represent experimental data, solid lines represent RVE response with x marking stresses considered in simulations

in Fig. 5.14 (left) for the load ratio $R = 0.1$ and two different frequencies in a double logarithmic plot. The model response compares satisfactorily with the experiment results, and again captures two failure mechanisms. A moderate offset from the experimental data is observed in the crack growth regime. Fig. 5.14 (right) illustrates the corresponding number of cycles to failure, where the conclusion regarding the frequency dependency of each failure mechanism follows that observed for $\chi = 90°$.

Another aspect in which the model may be improved is the R-dependence of the crack growth failure mechanism. In Fig. 5.15 the model response for $R = -0.5$ and $R = 0.2$ is compared with experimental data for $\chi = 90°$. The loading frequency is 1 Hz and 10 Hz, respectively, and the response for $R = 0.1$ is included for reference. We conclude from the figure that the trend in the number of cycles to failure with different R is captured, but the quantitative prediction is wrong. In the model, the slope of the crack growth failure mechanism is controlled by the parameter β, Eq. (5.57), which in turn depends on the brittleness parameter η and the relative endurance limit E, Eq. (5.58). In the current formulation, the parameter η has a constant value, while E is locally changing with R. This change affects the slope of the crack growth regime and shifts the cycles to failure in the correct direction. Nevertheless, the experimental data does not show a change in the slope of the crack growth controlled part for different (global) R, indicating that for the specific material system the brittleness parameter η in Eq. (5.58) may also be a function of R.

It is reported in the literature, e.g. [4], that for a stress level in the crack growth regime, the number of cycles to failure changes with frequency for different R values. Considering a different composite system Kanters et al. [4] report an increase in the cycles to failure when increasing the frequency and the load ratio. How the model proposed here behaves in this regard is investigated

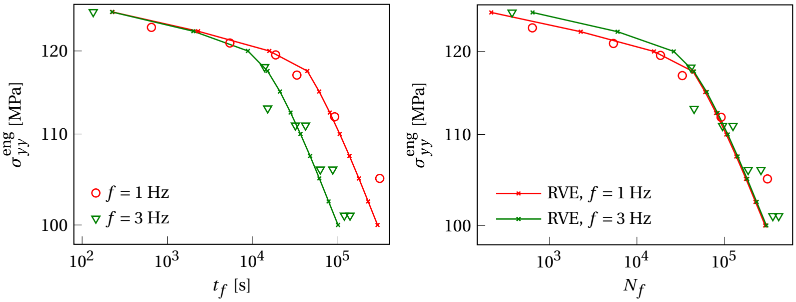

Figure 5.14: Maximum stress applied versus time to failure for $\chi = 45°$, $R = 0.1$ and two different frequencies (left); corresponding number of cycles to failure (right); empty markers represent experimental response, solid lines represent model response with x marking stress levels considered in analyses

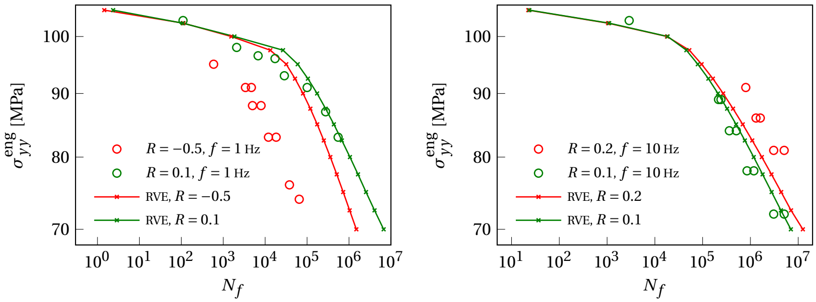

Figure 5.15: Comparison of model response with experiments for $\chi = 90°$ and different load ratios: $R = -0.5$ (left), $R = 0.2$ (right); response for $R = 0.1$ included for reference; empty markers stand for experimental data; in solid lines x marks stress levels considered in simulations

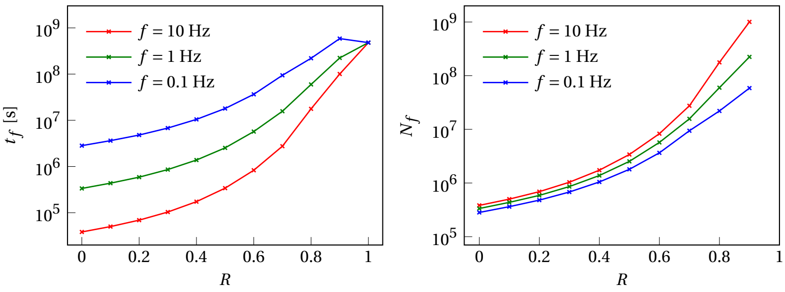

Figure 5.16: Dependence of time to failure on load ratio for $\sigma_{yy}^{\max} = 85$ MPa and different frequencies predicted by the model (left); corresponding number of cycles to failure versus load ratio (right); $\chi = 90°$

next. The stress level of 85 MPa is chosen, well within the crack growth-controlled regime (cf. Fig. 5.13). Load ratios ranging from 0 to 1 are considered, with three different frequencies: 0.1 Hz, 1 Hz and 10 Hz. Fig. 5.16 (left) shows the time to failure as a function of R and f. Like in [4], for a given load ratio the time to failure increases with a decrease in the frequency. As the load ratio increases, the logarithmic difference in time to failure for different f reduces, eventually converging to a unique value for $R = 1$. The case of $R = 0.9$ and $f = 0.1$ Hz actually shows longer time to failure than the $R = 1$ case, since the material here enters the plasticity-controlled regime where low amplitude cyclic loading only prolongs the lifetime. The corresponding number of cycles to failure is plotted in Fig. 5.16 (right), and follows the trend reported in [4]. For lower load ratios, N_f shows a small but nonzero dependence on f. For larger R values, the influence of f is much stronger as plasticity becomes more significant.

EFFECT OF VISCOPLASTICITY

The effect of viscoplastic deformation in the matrix, which introduces the timescale to the model and correspondingly the frequency dependency in the cycles to failure, is discussed next. For $f = 1$ Hz and $R = 0.1$, simulations are repeated for the same range of stress levels, but this time assuming an elastic behavior of the matrix ($\lambda^{n}_{x,j} = 1$ in Eq. (5.25)). The results are compared with the model response allowing for viscoplastic deformation in the matrix, see Fig. 5.17 (left) for $\chi = 90°$ and Fig. 5.17 (right) for $\chi = 45°$. As calibrated in this study, the cohesive model combined with an elastic matrix represents quite well the crack growth failure regime for both loading angles, but does not capture the transition to plasticity controlled failure at higher stresses. Although a dedicated calibration of the cohesive model with elastic matrix could improve corresponding results at higher stresses, the adequate frequency dependence of the S-N curve would still be absent, since the number of cycles would be the quantity governing the failure process. Including viscoplas-

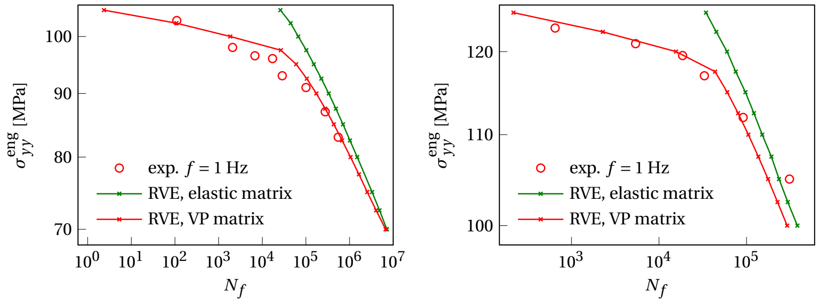

Figure 5.17: Influence of viscoplastic (VP) deformation in the matrix on failure of the RVE; $\chi = 90°$ (left), $\chi = 45°$ (right), $R = 0.1$; comparison made with simulation results with elastic matrix

tic deformation in the matrix drastically affects the model response at higher stresses for which significant yielding occurs inside the RVE and viscoplasticity practically dominates the response in this stress range. The mechanism at which the viscoplastic bulk deformation contributes to failure is the following: under the applied (creep or cyclic) stress the polymer matrix undergoes viscous deformation that increases in time. In the heterogeneous microstructure of the RVE with already initiated cohesive segments there may be a nonuniform plastic flow of the material from the two sides of the cohesive segment, leading to an opening of the cohesive zone and activating the quasi-static damage variable[1]. It is known in the polymer literature that crack propagation in cyclic loading features a static (creep) component and a cyclic component [49, 50]. As for physical interpretation, the cyclic component of crack propagation is due to bending, buckling or crushing fibrils [51], and is represented with the fatigue damage variable in the model. On the other hand, the creep component relates to failure of the fibrils in the fracture process zone (or craze zone) due to disentanglement or chain scission [52]. In the present model, it becomes dominant at higher stresses applied on the RVE, as opposed to the cyclic component that is dominant at lower applied stresses. Finally, the small but nonzero influence on the lifetime that is found from viscoplasticity in the crack growth regime mirrors the small frequency dependence that was found for the number of cycles to failure for low R-values in Fig. 5.16. Both observations point at a small but non-negligible influence of time-dependent plasticity on the lifetime in high-cycle fatigue.

CREEP RUPTURE

In order to elucidate the role of the loading amplitude on the time to failure in the plasticity controlled regime, the model response for $R = 1$ (creep) is compared with the model response for $R = 0.1$ and $f = 1$ Hz, see Fig. 5.18 (left), where the experimental results for creep rupture are also included [23]. Note that for $R = 1$, there is no micro time stepping in the simulations. As observed from the figure, the model predicts well the time to failure in creep, which shifts to shorter timescales as compared to the plasticity controlled regime in cyclic loading. This shift is due to the faster viscous deformation in the bulk material under a constant loading than that under cyclic loading. Despite this difference, both cases feature the same slope in the S-t curve, indicating the same failure kinetics. It is worth noting that the present model better predicts creep rupture than the model we introduced in [17]. There, a general cohesive initiation criterion based on the critical energy stored in the bulk material was considered, that further required the presence of another failure mechanism on the cohesive surface, to speed up the failure process for different loading angles. However, that approach led to a lower predictive accuracy compared to the current results. However, the described mechanism to activate the quasi-static damage in the current model is not possible in a homogeneous material like neat polymer, where the uniform viscous deformation of the surrounding bulk material will not change the cohesive zone opening, and the quasi-static

---

[1] Yet another mechanism at which the quasi-static damage variable can be activated in the present context is the application of the engineering stress, which means that in tension the actual stress on the RVE is increasing with deformation, Eq. (5.8).

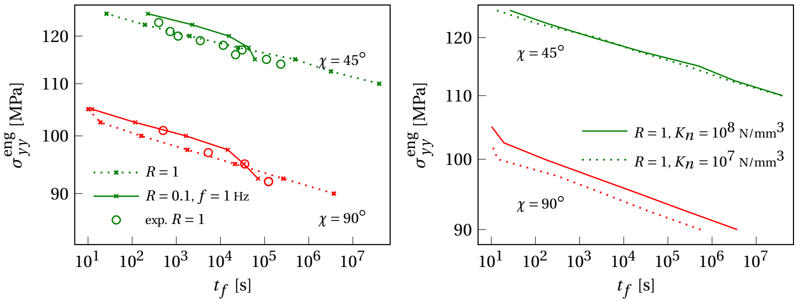

Figure 5.18: RVE prediction of time to failure for different load ratios and off-axis angles, where along dotted and solid lines x marks stress levels considered in simulations; empty markers represent experimental data on creep rupture (left); influence of dummy stiffness on time to failure in creep loading for two off-axis angles (right)

damage variable will not be activated for the stresses lower than the quasi-static strength. In such a scenario, the modeling of creep rupture or plasticity controlled failure in fatigue requires the existence of another failure mechanism if the cohesive zone approach is followed, e.g., viscous degradation on the cohesive surface [17].

Another important aspect about the model is that the cohesive model dummy stiffness K_n affects the model response. An indication for this is found in the observation that early initiation of cracks (using the endurance limit at $R = 0.1$) is essential to obtain failure in creep loading that is within the timescale of experimental data, even though the *fatigue damage* remains inactive for $R = 1$. To support this claim, the RVE is again exposed to a constant load, $R = 1$, with the dummy stiffness reduced from 10^8 N/mm^3 to 10^7 N/mm^3. The corresponding time to failure curves are shown in Fig. 5.18 (right), for two off-axis angles. It follows from the figure that for $\chi = 45°$ the response is almost unaltered by the change in stiffness. Nevertheless, the $\chi = 90°$ case shows a significant shift in the lifetime when changing the dummy stiffness. By lowering the value of K_n, it becomes easier for the two sides of the cohesive segment to detach, increasing the effect of viscoplastic flow in the surrounding matrix.

Although not every mechanism is fully captured, the proposed model shows a very good ability to reproduce highly-complex failure behavior.

FAILURE STATE OF THE RVE

A failure state of the RVE is reached by propagating microcracks through the matrix. The RVE is considered to have failed when the adaptive stepping algorithm cannot find a converging time increment anymore. It is checked from looking at the homogenized strain rates whether this non-convergence is preceded by increased deformation rates, as can be expected to happen just before the material cannot carry the applied load anymore. The homogenized strain rate is computed at macro time steps, when the applied stress is at its maximum. Fig. 5.19 illustrates the evolution of the strain rate for $\chi = 90°$ and $\chi = 45°$, $R = 0.1$, $f = 1$ Hz and different stress levels. After the initial loading phase is over ($t = 10$ s) and the cycling has started, the homogenized strain rate gradually decreases. Subsequently, the strain rate reaches a minimum value after which it transitions to an abruptly increasing phase. It is clear that the non-convergence of the model, that is taken as failure of the material, is caused by instability in the homogenized material response. A similar evolution of the strain rate is observed experimentally for creep loading, see e.g. [53].

For some loading cases, capturing the equilibrium path after the minimum strain rate is passed, may be computationally demanding. In Fig. 5.19 (left), points A and B are indicated for the stress level of 85 MPa, both of which belong to the phase of quickly increasing strain rate. The number of macro time steps needed to reach the point A ($t = 4.217 \cdot 10^5$ s, $runtime = 4.66 \cdot 10^4$ s) is 153, while the point B ($t = 4.357 \cdot 10^5$ s, $runtime = 9.776 \cdot 10^4$ s) was reached after 1008 macro time steps. Also, in some loading cases including the considered one, transition from point A to point B is not monotonic, i.e., the strain rate value oscillates, with the overall trend to increase. Furthermore, it

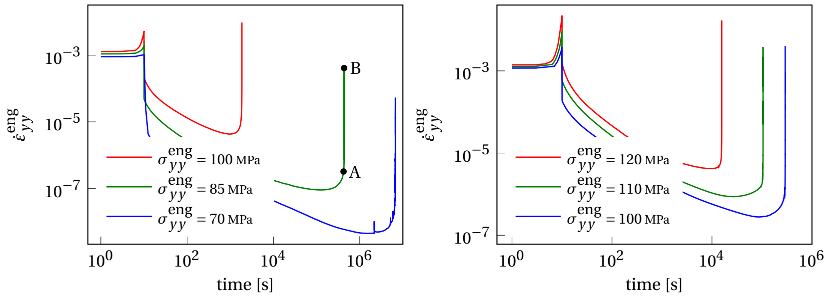

Figure 5.19: Homogenized strain rate versus time computed at macro time steps for different maximum stress levels, $f = 1$ Hz, $\chi = 90°$ (left) and $\chi = 45°$ (right); failure of RVE coincides with abrupt increase in strain rate; 153 macro time steps needed to reach point A ($t = 4.217 \cdot 10^5$ s) and 1008 macro time steps needed to reach point B ($t = 4.357 \cdot 10^5$ s)

is possible to lose convergence at micro time steps in this last phase of the simulation. In such a case, the data collected from the last successful micro time stepping are used to compute Δt_{eff} at macro time steps. This is the reason why the runtime between the points A and B differs by a factor of 2, while the number of macro time steps differs by a factor of 7, approximately. The clear increase in strain rate that is consistently found in the final phase of the simulation indicates that the non-convergence with which the simulation ends is indeed caused by the material losing the ability to carry the prescribed load.

Deformed RVEs at the moment of failure are shown in the contour plots of Fig. 5.20, where the distribution of the equivalent plastic strain is illustrated together with cohesive microcracks for two loading angles. Although it features much less equivalent plastic strain than the 45° example, the 90° case does not lack yielding in the matrix, which brings it to the plasticity controlled failure regime, see Fig 5.17. The difference in $\bar{\gamma}_{\text{p}}$ for two loading angles is due to the difference in shear deformation, which, by definition, promotes the accumulation of the equivalent plastic strain in the EGP model. In Fig. 5.20 (right) the discretization and the crack pattern are visualized, where the thicker lines indicate initiated cohesive segments in one typical simulation. In the depicted example, except for two cohesive segments (encircled green lines) in the elastic/unloading phase, all other cohesive segments (black lines) are in the loading phase, i.e., the damage increases at the moment of failure.

When changing the mode of failure, the density of developing cohesive microcracks in the domain changes as well. This fact is illustrated in Fig. 5.21, where the network of cohesive microcracks is shown for $\chi = 90°$ and three stress levels at the moment of failure. In the plasticity controlled regime, $\sigma_{yy}^{\text{max}} = 100$ MPa, two dominant cohesive cracks are running through the RVE. As the applied stress decreases and the failure mode transitions to the brittle mechanism, the density of developing cohesive microcracks increases.

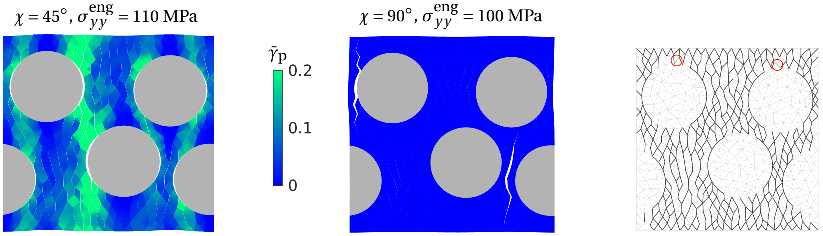

Figure 5.20: Front view of 3D thin slice RVE showing equivalent plastic strain and cohesive microcracks in the matrix at the moment of failure for two loading angles, $R = 0.1$ and $f = 1$ Hz; grey lines indicating finite element mesh, with thicker lines representing initiated cohesive segments for typical simulation (right); black lines indicate damaging cohesive segments, while (encircled) green lines represent cohesive segments in elastic/unloading phase

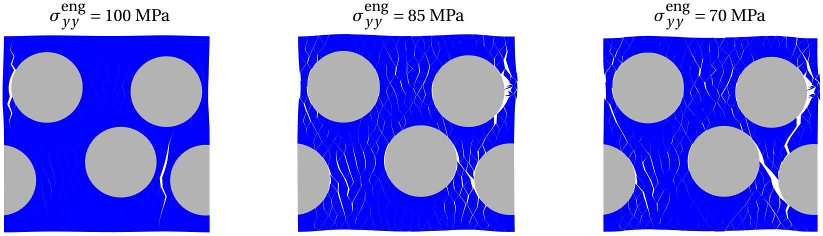

$\sigma_{yy}^{\text{eng}} = 100$ MPa

$\sigma_{yy}^{\text{eng}} = 85$ MPa

$\sigma_{yy}^{\text{eng}} = 70$ MPa

Figure 5.21: Density of developing cohesive microcracks at failure for $\chi = 90°$, $R = 0.1$, $f = 1$ Hz and three stress levels; 100 MPa belongs to plasticity controlled failure regime; the other two are in crack growth failure regime, see Fig. 5.13

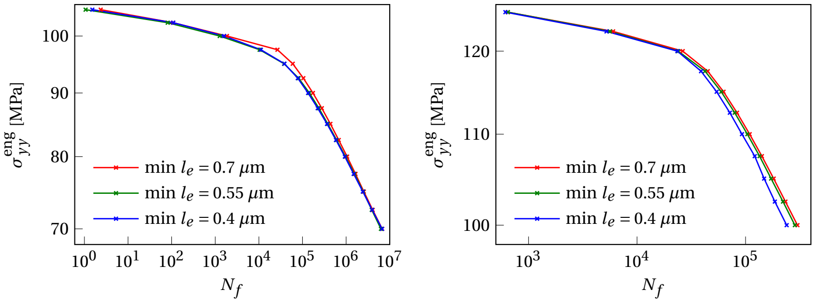

Figure 5.22: RVE prediction of S-N curves for different mesh sizes defined by minimum length of finite element; $\chi = 90°$, $f = 1$ Hz (left); $\chi = 45°$, $f = 3$ Hz (right); $R = 0.1$

MESH DEPENDENCY

Finally, S-N curves are generated with three different mesh sizes, see Fig. 5.22 (left) for $\chi = 90°$ and Fig. 5.22 (right) for $\chi = 45°$, where the mesh size is defined by the minimum finite element length. While for $\chi = 90°$ refinement of the mesh leads to a similar model response, for $\chi = 45°$ the results indicate a significant dependence on the mesh density. In this regard, careful studies on mesh dependency of the model are needed, particularly on the objectivity of viscosity evolution in the EGP model, and the influence of inter-element crack patterns on the model response.

5.6. CONCLUSION

In this work, a microscale spatial and two-scale temporal framework is introduced to capture the time- and cycle dependency of failure in unidirectional composites under cyclic loading. To efficiently pass through the loading signal, an adaptive stepping scheme is proposed. The scheme consists of macro time steps where viscoplasticity evolves in the polymer matrix, and micro time steps with an elastic update in the bulk material models, and blocked cohesive initiation and damage evolution in the cohesive zone model. The response of the matrix in cyclic loading is represented with the Eindhoven Glassy Polymer material model, for which a version based on two time scales is formulated. Following principles of the time homogenization procedure, an effective time increment is computed for integration points representing the matrix, and used in macro time step updates. The carbon fiber reinforcement is represented with a hyperelastic transversely isotropic material model. For considered examples, the time homogenization approach is shown to accurately capture the cyclic evolution of viscoplastic deformations for a range of stress ratios from $R = -0.5$ to $R = 1$. Only for lower negative R-values, when reverse plasticity becomes significant, the proposed approach loses accuracy.

Failure of the RVE is achieved by propagation of microcracks through the domain, whereby microcracking is represented with Dávila's cycle-dependent cohesive model, combined with an endurance limit-based cohesive initiation criterion. Eventually, the time-dependent failure process features two components. Firstly, there is cyclic failure due to the buckling and crushing of fibrils in the process zone, represented with the fatigue damage in the cohesive model. Secondly, there is nonuniform viscoplastic flow in the bulk material around cohesive segments, which may trigger quasi-static damage of the cohesive model. The static (creep) component is dominant at higher applied stresses, as opposed to the cyclic (fatigue) component, which dominates the response at lower stresses.

The model performance is compared with available experiments on fatigue of UD carbon/PEEK thermoplastic composites, tested under different off-axis angles, load ratios and frequencies. The model is able to capture the transition from plasticity controlled to crack growth controlled failure, and properly captures the frequency dependency of each mechanism. Despite showing very good performance for the aforementioned cases, the R-dependence and the off-axis angle dependence of the number of cycles to failure in the crack growth controlled regime is still not captured well. For the studied material system, modification of the cohesive zone model will be required to achieve a model that can make accurate predictions for a wider range of load cases.

As a limit case when $R = 1$, the model is able to capture the failure kinetics in creep loading, which are the same as in the plasticity controlled regime under cyclic loading. The difference is that the creep rupture state shifts toward shorter lifetimes due to the faster viscoplastic deformation under a constant loading. Regarding the accuracy of the predicted time to failure, the model proposed here outperforms our earlier model specifically developed for creep rupture [17]. A notable difference is that here we use a different initiation criterion that allows for early initiation of many cohesive segments. The heterogeneity of the microstructure allows for nonuniform viscoplastic flow of the matrix around cohesive segments, which triggers quasi-static damage and leads to creep rupture. However, this mechanism is not possible in neat polymer, where the matrix uniformly flows around cohesive segments and quasi-static damage does not evolve. In such a scenario, another failure mechanism is required to trigger the failure process, e.g., viscous degradation on the cohesive surface [17].

5.7. DATA AVAILABILITY

Data presented in this chapter are available at the 4TU.ResearchData repository through `https://doi.org/10.4121/c9592e56-9284-42ba-92b3-b6448e5beddb`

REFERENCES

[1] Kovačević D, Hofman P, Rocha IBCM, Van der Meer FP. Unifying creep and fatigue modeling of composites: A time-homogenized micromechanical framework with viscoplasticity and cohesive damage. *J Mech Phys Solids*, 193, 2024, p. 105904. DOI: 10.1016/j.jmps.2024.105904.

[2] Dávila CG. From S-N to the Paris law with a new mixed-mode cohesive fatigue model for delamination in composites. *Theor Appl Fract Mech*, 106, 2020, p. 102499. DOI: 10.1016/j.tafmec.2020.102499.

[3] Kanters MJW, Kurokawa T, Govaert LE. Competition between plasticity-controlled and crack-growth controlled failure in static and cyclic fatigue of thermoplastic polymer systems. *Polym Test*, 50, 2016, pp. 101–110. DOI: 10.1016/j.polymertesting.2016.01.008.

[4] Kanters MJW, Engels TAP, Van Erp TB, Govaert LE. Predicting long-term crack growth dominated static fatigue based on short-term cyclic testing. *Int J Fatigue*, 112, 2018, pp. 318–327. DOI: 10.1016/j.ijfatigue.2018.03.011.

[5] Melro AR, Camanho PP, Pinho ST. Influence of geometrical parameters on the elastic response of unidirectional composite materials. *Compos Struct*, 94 (11), 2012, pp. 3223–3231. DOI: 10.1016/j.compstruct.2012.05.004.

[6] Van der Meer FP. Micromechanical validation of a mesomodel for plasticity in composites. *Eur J Mech A Solids*, 60, 2016, pp. 58–69. DOI: 10.1016/j.euromechsol.2016.06.008.

[7] Totry E, González C, LLorca J. Failure locus of fiber-reinforced composites under transverse compression and out-of-plane shear. *Compos Sci Technol*, 68 (3), 2008, pp. 829–839. DOI: 10.1016/j.compscitech.2007.08.023.

[8] Rocha I et al. Combined experimental/numerical investigation of directional moisture diffusion in glass/epoxy composites. *Compos Sci Technol*, 151, 2017, pp. 16–24. DOI: 10.1016/j.compscitech.2017.08.002.

[9] Arteiro A et al. Micro-mechanical analysis of the in situ effect in polymer composite laminates. *Compos Struct*, 116, 2014, pp. 827–840. DOI: 10.1016/j.compstruct.2014.06.014.

[10] Reifsnider KL, Gao Z. A micromechanics model for composites under fatigue loading. *Int J Fatigue*, 13 (2), 1991, pp. 149–156. DOI: 10.1016/0142-1123(91)90007-L.

[11] Hessman PA, Welschinger F, Hornberger K, Böhlke T. A micromechanical cyclic damage model for high cycle fatigue failure of short fiber reinforced composites. *Composites B*, 264, 2023, p. 110855. DOI: 10.1016/j.compositesb.2023.110855.

[12] Mohammadi B et al. Damage-entropy model for fatigue life evaluation of off-axis unidirectional composites. *Compos Struct*, 270, 2021, p. 114100. DOI: 10.1016/j.compstruct.2021.114100.

[13] Fish J, Yu Q. Computational mechanics of fatigue and life predictions for composite materials and structures. *Comput Methods Appl Mech Eng*, 191 (43), 2002, pp. 4827–4849. DOI: 10.1016/S0045-7825(02)00401-2.

[14] Crouch R, Oskay C, Clay S. Multiple spatio-temporal scale modeling of composites subjected to cyclic loading. *Comput Mech*, 51 (1), 2013, pp. 93–107. DOI: 10.1007/s00466-012-0707-9.

[15] Ni T, Zaccariotto M, Galvanetto U. A peridynamic approach to simulating fatigue crack propagation in composite materials. *Proc R Soc A*, 381 (2240), 2023, p. 20210217. DOI: 10.1098/rsta.2021.0217.

[16] Rocha IBCM, Van der Meer FP, Sluys LJ. Efficient micromechanical analysis of fiber-reinforced composites subjected to cyclic loading through time homogenization and reduced-order modeling. *Comput Methods Appl Mech Eng*, 345, 2019, pp. 644–670. DOI: 10.1016/j.cma.2018.11.014.

[17] Kovačević D, Sundararajan BK, Van Der Meer FP. Micromechanical model for off-axis creep rupture in unidirectional composites undergoing finite strains. *Composites A*, 176, 2024, p. 107860. DOI: 10.1016/j.compositesa.2023.107860.

[18] Van Breemen LCA, Klompen ETJ, Govaert LE, Meijer HEH. Extending the EGP constitutive model for polymer glasses to multiple relaxation times. *J Mech Phys Solids*, 59 (10), 2011, pp. 2191–2207. DOI: 10.1016/j.jmps.2011.05.001.

[19] Bonet J, Burton AJ. A simple orthotropic, transversely isotropic hyperelastic constitutive equation for large strain computations. *Comput Methods Appl Mech Eng*, 162 (1), 1998, pp. 151–164. DOI: 10.1016/S0045-7825(97)00339-3.

[20] Joosten MW, Dávila CG, Yang Q. Predicting fatigue damage in composites subjected to general loading conditions. *Composites A*, 156, 2022, p. 106862. DOI: 10.1016/j.compositesa.2022.106862.

[21] Camacho GT, Ortiz M. Computational modelling of impact damage in brittle materials. *Int J Solids Struct*, 33 (20), 1996, pp. 2899–2938. DOI: 10.1016/0020-7683(95)00255-3.

[22] Hofman P, Van der Meer FP, Sluys LJ. A numerical framework for simulating progressive failure in composite laminates under high-cycle fatigue loading. *Eng Fract Mech*, 295, 2024, p. 109786. DOI: 10.1016/j.engfracmech.2023.109786.

[23] Sundararajan BK. Matrix dominated failure in continuous carbon fibre reinforced poly(ether ether ketone). PhD thesis. Enschede, The Netherlands: University of Twente, 2024. DOI: `10.3990/1.9789036560405`.

[24] Kovačević D, Van der Meer FP. Strain-rate based arclength model for nonlinear microscale analysis of unidirectional composites under off-axis loading. *Int J Solids Struct*, 250, 2022, p. 111697. DOI: `10.1016/j.ijsolstr.2022.111697`.

[25] Ke L, Van der Meer FP. A computational homogenization framework with enhanced localization criterion for macroscopic cohesive failure in heterogeneous materials. *J Theor Comp App Mech*, 2022. DOI: `10.46298/jtcam.7707`.

[26] Kovačević D, Sundararajan BK, Van der Meer FP. Microscale modeling of rate-dependent failure in thermoplastic composites under off-axis loading. *Eng Fract Mech*, 276, 2022, p. 108884. DOI: `10.1016/j.engfracmech.2022.108884`.

[27] Tervoort TA, Smit RJM, Brekelmans WAM, Govaert LE. A constitutive equation for the elasto-viscoplastic deformation of glassy polymers. *Mech Time Depend Mater*, 1 (3), 1997, pp. 269–291. DOI: `10.1023/A:1009720708029`.

[28] Klompen E, Govaert L. Nonlinear Viscoelastic Behaviour of Thermorheologically Complex Materials. *Mech Time Depend Mater*, 3 (1), 1999, pp. 49–69. DOI: `10.1023/A:1009853024441`.

[29] Khaleghi H, Amiri-Rad A, Mashayekhi M. A thermodynamically consistent continuum damage model for time-dependent failure of thermoplastic polymers. *Int J Plast*, 154, 2022, p. 103278. DOI: `10.1016/j.ijplas.2022.103278`.

[30] Eyring H. Viscosity, plasticity, and diffusion as examples of absolute reaction rates. *J Chem Phys*, 4 (4), 1936, pp. 283–291. DOI: `10.1063/1.1749836`.

[31] Klompen ETJ, Engels TAP, Govaert LE, Meijer HEH. Modeling of the postyield response of glassy polymers: Influence of thermomechanical history. *Macromolecules*, 38 (16), 2005, pp. 6997–7008. DOI: `10.1021/ma050498v`.

[32] Yu Q, Fish J. Temporal homogenization of viscoelastic and viscoplastic solids subjected to locally periodic loading. *Computational Mechanics*, 29 (3), 2002, pp. 199–211. DOI: `10.1007/s00466-002-0334-y`.

[33] Oskay C, Fish J. Fatigue life prediction using 2-scale temporal asymptotic homogenization. *Int J Numer Meth Engng*, 61 (3), 2004, pp. 329–359. DOI: `10.1002/nme.1069`.

[34] Haouala S, Doghri I. Modeling and algorithms for two-scale time homogenization of viscoelastic-viscoplastic solids under large numbers of cycles. *Int J Plast*, 70, 2015, pp. 98–125. DOI: `10.1016/j.ijplas.2015.03.005`.

[35] Janssen RPM, De Kanter D, Govaert LE, Meijer HEH. Fatigue Life Predictions for Glassy Polymers: A Constitutive Approach. *Macromolecules*, 41 (7), 2008, pp. 2520–2530. DOI: `10.1021/ma071273i`.

[36] Janssen RPM, Govaert LE, Meijer HEH. An Analytical Method To Predict Fatigue Life of Thermoplastics in Uniaxial Loading: Sensitivity to Wave Type, Frequency, and Stress Amplitude. *Macromolecules*, 41 (7), 2008, pp. 2531–2540. DOI: `10.1021/ma071274a`.

[37] Van der Meer FP, Sluys LJ. A phantom node formulation with mixed mode cohesive law for splitting in laminates. *Int J Fract*, 158 (2), 2009, p. 107. DOI: `10.1007/s10704-009-9344-5`.

[38] Hille TS, Suiker ASJ, Turteltaub S. Microcrack nucleation in thermal barrier coating systems. *Eng Fract Mech*, 76 (6), 2009, pp. 813–825. DOI: `10.1016/j.engfracmech.2008.12.010`.

[39] Turon A et al. Accurate simulation of delamination under mixed-mode loading using a cohesive model with a mode-dependent penalty stiffness. *Compos Struct*, 184, 2018, pp. 506–511. DOI: `10.1016/j.compstruct.2017.10.017`.

[40] Benzeggagh M, Kenane M. Measurement of mixed-mode delamination fracture toughness of unidirectional glass/epoxy composites with mixed-mode bending apparatus. *Compos Sci Technol*, 56 (4), 1996, pp. 439–449. DOI: `10.1016/0266-3538(96)00005-X`.

[41] Juvinall RC, Marshek KM. *Fundamentals of machine component design*. John Wiley & Sons, 2020.

[42] Raimondo A, Dávila CG, Bisagni C. Cohesive analysis of a 3D benchmark for delamination growth under quasi-static and fatigue loading conditions. *Fatigue Fract Eng Mater Struct*, 45 (7), 2022, pp. 1942–1952. DOI: `10.1111/ffe.13712`.

[43] Turon A, Camanho PP, Costa J, Dávila CG. A damage model for the simulation of delamination in advanced composites under variable-mode loading. *Mechanics of Materials*, 38 (11), 2006, pp. 1072–1089. DOI: `10.1016/j.mechmat.2005.10.003`.

[44] Verhoosel CV, Remmers JJC, Gutiérrez MA. A dissipation-based arc-length method for robust simulation of brittle and ductile failure. *Int J Numer Methods Eng*, 77 (9), 2009, pp. 1290–1321. DOI: `10.1002/nme.2447`.

[45] Van der Meer FP. Mesolevel Modeling of Failure in Composite Laminates: Constitutive, Kinematic and Algorithmic Aspects. *Arch Computat Methods Eng*, 19 (3), 2012, pp. 381–425. DOI: `10.1007/s11831-012-9076-y`.

[46] Nguyen-Thanh C et al. Jive: An open source, research-oriented C++ library for solving partial differential equations. *Adv Eng Software*, 150, 2020, p. 102925. DOI: `10.1016/j.advengsoft.2020.102925`.

[47] Geuzaine C, Remacle JF. Gmsh: A 3-D finite element mesh generator with built-in pre- and post-processing facilities. *Int J Numer Methods Eng*, 79 (11), 2009, pp. 1309–1331. DOI: `10.1002/nme.2579`.

[48] Pastukhov LV, Govaert LE. Crack-growth controlled failure of short fibre reinforced thermoplastics: Influence of fibre orientation. *Int J Fatigue*, 143, 2021, p. 105982. DOI: `10.1016/j.ijfatigue.2020.105982`.

[49] Dumpleton P, Bucknall C. Comparison of static and dynamic fatigue crack growth rates in high-density polyethylene. *Int J Fatigue*, 9 (3), 1987, pp. 151–155. DOI: `10.1016/0142-1123(87)90070-3`.

[50] Hu Y, Summers J, Hiltner A, Baer E. Correlation of fatigue and creep crack growth in poly(vinyl chloride). *J Mater Sci*, 38, 2003, pp. 633–642.

[51] Zhou YQ, Brown N. The mechanism of fatigue failure in a polyethylene copolymer. *J Polym Sci B: Polym Phys*, 30 (5), 1992, pp. 477–487. DOI: `10.1002/polb.1992.090300507`.

[52] Zhou Z, Hiltner A, Baer E. Predicting long-term creep failure of bimodal polyethylene pipe from short-term fatigue tests. *J Mater Sci*, 46 (1), 2011, pp. 174–182. DOI: `10.1007/s10853-010-4902-9`.

[53] Erartsin O, Amiri-Rad A, Van Drongelen M, Govaert LE. Time-dependent failure of off-axis loaded unidirectional glass/iPP composites. *J Appl Polym Sci*, 139 (23), 2022, p. 52293. DOI: `10.1002/app.52293`.

6
CONCLUSION

A microscale computational framework is introduced to simulate time- and cycle-dependent failure of unidirectional (UD) polymeric composites under off-axis loading. The micromodel is a 3D Representative Volume Element (RVE) defined in the local frame aligned with the fiber reinforcement. With the focus on matrix dominated failure, carbon fibers respond elastically in the simulations, according to [1]. Two nonlinear processes are included in the matrix: viscoplastic deformation and microcracking. Viscoplastic deformation is represented with the Eindhoven Glassy Polymer (EGP) material model [2], whereas microcracking is accounted for by means of cohesive zone modeling. Cohesive segments are added on the fly [3], when a suitable cohesive initiation criterion is satisfied. The model allows for finite deformations locally, at every integration point, but also globally for the RVE as a whole. Finite homogenized deformations of the RVE imply reorientation of the microstructure in a loading process. Failure of the material is studied for three different loading scenarios: constant strain rate, creep and cyclic loading, assuming that failure of the RVE corresponds with macroscopic crack formation in the matrix.

6.1. NEW DEVELOPMENTS

- A strain rate-based arclength model to impose a constant strain rate on the RVE under off-axis angle was introduced, with a dedicated constraint equation and expressions for the unit force vector. With small adjustments, the derived kinematical and stress relations can be used to impose a constant or a cyclic stress on the RVE, in a load control procedure.

- A cohesive model formulation was derived in 3D space, with detailed expressions for components of the internal force vector and the tangent stiffness matrix stemming from geometric nonlinearity.

- To model strain rate-dependent failure of the material, a power law cohesive initiation criterion based on the local stress and the local rate of deformation was proposed.

- A viscous degradation tensor was added to a quasi-static cohesive model, to simulate failure in the matrix under creep loading.

- In order to allow for representation of creep rupture for a large range of applied stresses, a cohesive initiation criterion based on a critical free energy in the matrix was proposed.

- Creep rupture was studied computationally for different temperature conditions and off-axis angles.

- A two-scale adaptive stepping scheme was introduced to efficiently go through a cyclic loading signal. The scheme consists of micro time steps where the response of the RVE constituents is elastic, and macro time steps where viscoplasticity evolves in the polymer matrix and damage grows in the cohesive zones. Depending on the global convergence rate of the analysis, the step size between macro time steps changes.

- Based on time homogenization and the effective time increment, a two-scale EGP model was formulated to represent the behavior of the matrix under cyclic loading.

- Failure state of the RVE under cyclic loading was defined as the moment when the homogenized strain rate in the global loading direction abruptly increases, after the point of minimum strain rate is passed.

- Viscoplastic deformation of the matrix was combined with Dávila's cycle-dependent cohesive model to address the behavior of (thermoplastic) composites under cyclic loading. With a single model it is possible to:

- capture the transition between plasticity controlled and crack growth controlled failure regimes and their frequency dependency

- represent the effect of the load amplitude on the time to failure in the two failure regimes
- represent creep rupture as a limit case when load is constant

6.2. CONCLUSIONS

- The change in orientation of the composite microstructure in a loading process has a significant effect on the material response under off-axis loading, especially for lower off-axis angles.

- To model rate-dependent failure of the material by relying on cohesive zone modeling, some aspect of the cohesive model (maximum traction, fracture energy) needs to be rate-dependent. Otherwise, the model will fail prematurely when increasing the strain rate with respect to the calibrated case. In the case of the carbon/PEEK composite system considered in the thesis, making the maximum traction rate-dependent led to more accurate results than making the fracture energy rate-dependent.

- Modeling creep rupture in a neat polymer by means of a quasi-static cohesive model is not possible, due to the uniform viscoplastic flow of the matrix around cohesive segments and the absence of change in the cohesive displacement jump. In the situation of a constant displacement jump in the cohesive zone, an additional failure mechanism is required to trigger the failure process, e.g., viscous degradation.

- The heterogeneity of the composite microstructure allows for a nonuniform viscoplastic flow of the matrix around cohesive segments in cyclic or constant stress loading, triggering quasi-static damage of a cohesive model. In this way, creep rupture or plasticity controlled failure in cyclic loading can be reproduced by the RVE model.

- Modeling of failure in polymeric materials (composites) under cyclic or constant stress loading by means of cohesive surface methodology, requires an initiation criterion that admits material failure for a large range of stresses. At present, an endurance limit-based cohesive initiation criterion, combined with a cohesive law enabling elastic loading until the quasi-static strength and featuring a finite dummy stiffness, is the most promising approach for cohesive modeling of creep rupture, as well as of cycle-dependent failure in polymeric (thermoplastic) composites.

- The EGP model for viscous deformation in the matrix and cohesive surface methodology for cracking is an effective combination for modeling matrix dominated failure in polymeric composites under different loading conditions, including constant strain rate, constant stress and cyclic loading.

6.3. FUTURE PERSPECTIVES

Before discussing the possible avenues to improve the micromodel and use it in new research, several *recommendations regarding experiments* are listed:

- To approach the uniform stress state as much as possible in a UD specimen under uniaxial off-axis loading, *oblique-end tabs* are recommended to use [4]. Furthermore, the uniformity of deformation across the specimen could be monitored using *Digital Image Correlation* (DIC) [5].

- Experiments on creep loading using an *extensometer* are recommended to increase the accuracy in recorded strain-time curves. These data combined with stress-strain curves obtained from the same setup and constant strain rate loading would provide a basis for obtaining a unique relaxation spectrum for the EGP model, to be used in different loading scenarios. A direct calibration of the EGP parameters on the composite material response is necessary due to a difference in the crystallinity of neat PEEK and the PEEK matrix in the presence of carbon fibers [6], rendering the relaxation spectrum from neat PEEK data inadequate in RVE simulations.

- It is stated in [6] that the crack growth controlled failure regime in cyclic loading features the same slope for different off-axis angles, namely for $\chi = 90°$ and $\chi = 45°$. Collecting more data in this failure regime and for more off-axis angles is desired to clearly establish the off-axis dependence of the crack growth controlled failure mechanism in the carbon/PEEK composite system.

- Cyclic off-axis loading is associated with *heating of the specimen* at higher frequencies and lower off-axis angles [6]. It would be relevant to record the change in the temperature field for different loading conditions and represent the observation in a computational framework. This effort would be compatible with a potential usage of the material in high strain rate loading conditions, where polymeric composites undergo an adiabatic heating process [7].

- Although notably time consuming, additional experiments on the crack growth controlled failure in cyclic loading for different frequencies and load ratios would help in establishing a proper relation between the cycles to failure, the frequency and the load ratio in the crack growth controlled failure regime for the carbon/PEEK composite material.

Several *aspects in which the micromodel can be improved*, and ideas for the future research are discussed next:

- As indicated in Chapter 5, some of the loading situations may result in a mesh-dependent response of the RVE. Preliminary results indicate that the evolution of the EGP viscosity function is not objective with respect to the mesh density. It is expected that an integral-type nonlocal computation of the viscosity would regularize the width of bands where deformation localizes [8, 9]. An alternative solution may be sought in gradient-enhanced plasticity, where recently a micromorphic plasticity formulation was used to regularize the inelastic behavior of polymeric composites at the microscale [10]. Furthermore, detailed investigation on mesh dependency is needed in the presence of many cohesive cracks whose degradation evolves inside the quasi-static cohesive envelope, whereby the cohesive segments dissipate energy as a function of the number of load cycles. Even if an increase in cohesive crack density has no significant effect on the total number of cycles to failure, it might have an effect on the homogenized deformation of the material. However, it is not clear to the author how to remedy the potential problem.

- Following discussion on the non-uniqueness of crystallinity in neat PEEK and in the PEEK matrix of a composite material, and the necessity to calibrate the EGP parameters directly on the composite material response, an efficient *calibration procedure* for the EGP model and the model representing the fiber reinforcement is necessary. The starting point for such a procedure may be the one introduced by Van Breemen et al. [2], where the EGP model represents a neat polymer.

- Although in Chapter 4 simulations on creep rupture consider different *temperature conditions*, other loading scenarios deserve the same attention in this regard.

- Regarding cyclic loading, R*-dependence* and *off-axis dependence* of the crack growth controlled failure mechanism need a correction for the carbon/PEEK material system, by modifying the cycle-dependent cohesive model. The study should provide a broader insight in how the mentioned dependencies can be controlled in the model, such that a different material system showing a different R- or off-axis dependence may be readily represented with the framework.

- As discussed in the previous sections, modeling of creep rupture in a neat polymer by means of a quasi-static cohesive zone model is not possible. Therefore, a *unified cohesive zone model* for time- and cycle-dependent failure of polymeric materials is yet to be formulated. A good starting point is Dávila's cohesive model [11, 12], already featuring a quasi-static and a cyclic component to failure. A time-dependent component is still necessary.

- The examples considered in the thesis indicate that the RVE model could be used to assess failure of the material under different loading scenarios. However, the examples rely on a small RVE size, due to a fairly high computational cost associated with the model. Beside the already mentioned improvements in constitutive modeling, a bigger size of the RVE is necessary to increase fidelity of the predicted results. In the current implementation, two computational bottlenecks can be identified: update of the EGP model and enforcement of the periodic boundary conditions. Emerging *data-driven surrogate modeling* offers an alternative for these two aspects of the model [13, 14], whereby the EGP model may be replaced with an efficient and reliable surrogate model, as well as the procedure to impose periodicity in boundary conditions accounting for microcracking in the RVE.

- Performing analysis on a single RVE and homogenizing the obtained results is sometimes termed numerical homogenization, and is used to obtain effective (or apparent) properties of a heterogeneous material [15]. Therefore, *failure envelopes* obtained from simulations on a single RVE can be used as a guidance in the design process of composite structures. An example is presented in Fig. 6.1, where the Hill anisotropic failure criterion [16, 17] is fitted through the RVE

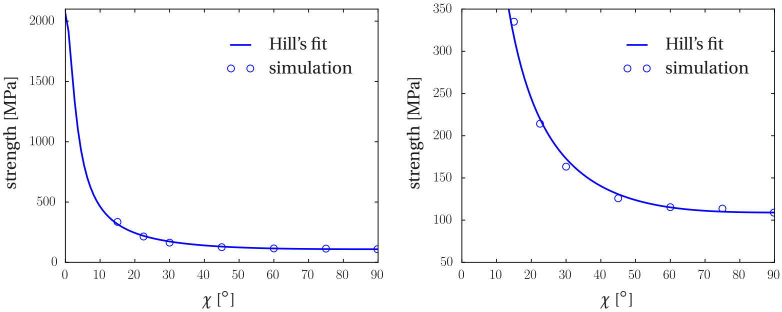

Figure 6.1: Hill's failure envelope fitted through simulation results (left); zoom in on the data range including the RVE model results [18]

data to obtain a failure envelope for the strain rate of 10^{-4}/s and the fiber volume ratio of 0.4 [18]. Furthermore, the obtained failure envelopes may be used as a failure criterion by meso- and macroscale models. The term *failure envelope* should be considered in a general sense, pertaining to S-N and S-t curves as well.

- The main idea behind *multiscale modeling* of heterogeneous materials is that an RVE represents a constitutive model of a macromodel. Therefore, the proposed RVE model may be employed in a multiscale computational framework to study different aspects of a macroscopic response given a detailed microstructure of the material. For example, the effect of the microstructure reorientation in a loading process on the global response of a laminate may be studied for different layups and boundary conditions. Furthermore, failure of laminates under different loading conditions, including fatigue, may be investigated. In this sense, the RVE model may be combined with an emerging model for simulating fatigue of multidirectional laminates [19, 20]. It would be necessary to ensure objectivity of such a multiscale framework with respect to the size of the RVE, as well as with respect to the mesh density of the macromodel [21].

- A long runtime hampers the straightforward application of the RVE in multiscale simulations. Again, data-driven surrogate modeling offers a possibility to substantially speed-up the simulations, while keeping the accuracy of the original RVE model. Based on the idea of embedding constitutive models in a data-driven surrogate [13, 22], a Physically Recurrent Neural Network (PRNN) has been trained to replace the RVE model without cohesive microcracks, resulting in a reliable rate-dependent orthotropic plasticity model [23]. Further developments require a *PRNN able to mimic the effect of evolving cohesive microcracks through the RVE*, eventually leading to softening (failure) of the RVE. Such a data-driven surrogate model can be integrated in an efficient multiscale framework for failure analysis of structural components, or even whole composite structures, under the time- and cycle-dependent loading conditions.

REFERENCES

[1] Bonet J, Burton AJ. A simple orthotropic, transversely isotropic hyperelastic constitutive equation for large strain computations. *Comput Methods Appl Mech Eng*, 162 (1), 1998, pp. 151–164. DOI: `10.1016/S0045-7825(97)00339-3`.

[2] Van Breemen LCA, Klompen ETJ, Govaert LE, Meijer HEH. Extending the EGP constitutive model for polymer glasses to multiple relaxation times. *J Mech Phys Solids*, 59 (10), 2011, pp. 2191–2207. DOI: `10.1016/j.jmps.2011.05.001`.

[3] Camacho GT, Ortiz M. Computational modelling of impact damage in brittle materials. *Int J Solids Struct*, 33 (20), 1996, pp. 2899–2938. DOI: `10.1016/0020-7683(95)00255-3`.

[4] Sun CT, Chung I. An oblique end-tab design for testing off-axis composite specimens. *Composites*, 24 (8), 1993, pp. 619–623. DOI: `10.1016/0010-4361(93)90124-Q`.

[5] Koerber H, Xavier J, Camanho PP. High strain rate characterisation of unidirectional carbon-epoxy IM7-8552 in transverse compression and in-plane shear using digital image correlation. *Mech Mater*, 42 (11), 2010, pp. 1004–1019. DOI: `10.1016/j.mechmat.2010.09.003`.

[6] Sundararajan BK. Matrix dominated failure in continuous carbon fibre reinforced poly(ether ether ketone). PhD thesis. Enschede, The Netherlands: University of Twente, 2024. DOI: `10.3990/1.9789036560405`.

[7] Sorini C, Chattopadhyay A, Goldberg RK. Micromechanical modeling of the effects of adiabatic heating on the high strain rate deformation of polymer matrix composites. *Compos Struct*, 215, 2019, pp. 377–384. DOI: `10.1016/j.compstruct.2019.02.016`.

[8] De Borst R, Sluys LJ, Muhlhaus HB, Pamin J. Fundamental issues in finite element analyses of localization of deformation. *Eng Comput*, 10, 1993, pp. 99–121.

[9] Jirásek M, Rolshoven S. Comparison of integral-type nonlocal plasticity models for strain-softening materials. *Int J Eng Sci*, 41 (13-14), 2003, pp. 1553–1602. DOI: `10.1016/S0020-7225(03)00027-2`.

[10] Klavzer N et al. Modelling of size-dependent plasticity in polymer-based composites based on nano- and macroscale experimental results. *Composites A*, 185, 2024, p. 108309. DOI: `10.1016/j.compositesa.2024.108309`.

[11] Dávila CG. From S-N to the Paris law with a new mixed-mode cohesive fatigue model for delamination in composites. *Theor Appl Fract Mech*, 106, 2020, p. 102499. DOI: `10.1016/j.tafmec.2020.102499`.

[12] Joosten MW, Dávila CG, Yang Q. Predicting fatigue damage in composites subjected to general loading conditions. *Composites A*, 156, 2022, p. 106862. DOI: `10.1016/j.compositesa.2022.106862`.

[13] Rocha IBCM, Kerfriden P, Van der Meer FP. Machine learning of evolving physics-based material models for multiscale solid mechanics. *Mech Mater*, 184, 2023, p. 104707. DOI: `10.1016/j.mechmat.2023.104707`.

[14] Berrone S, Canuto C, Pintore M, Sukumar N. Enforcing Dirichlet boundary conditions in physics-informed neural networks and variational physics-informed neural networks. *Heliyon*, 9 (8), 2023, e18820. DOI: `10.1016/j.heliyon.2023.e18820`.

[15] Andreassen E, Andreasen CS. How to determine composite material properties using numerical homogenization. *Comput Mater Sci*, 83, 2014, pp. 488–495. DOI: `10.1016/j.commatsci.2013.09.006`.

[16] Hill R. A theory of the yielding and plastic flow of anisotropic metals. *Proceedings of the Royal Society of London. Series A. Mathematical and Physical Sciences*, 193 (1033), 1997, pp. 281–297. DOI: `10.1098/rspa.1948.0045`.

[17] Erartsin O, Amiri-Rad A, Van Drongelen M, Govaert LE. Time-dependent failure of off-axis loaded unidirectional glass/iPP composites. *J Appl Polym Sci*, 139 (23), 2022, p. 52293. DOI: `10.1002/app.52293`.

[18] Kovačević D, Van Der Meer FP. Micromechanical modeling of rate-dependent off-axis failure in thermoplastic composites. Proceedings of the 20th European Conference on Composite Materials - Composites Meet Sustainability (Vol 1-6), 2022. DOI: `10.5075/EPFL-298799_978-2-9701614-0-0`.

[19] Hofman P, Van der Meer FP, Sluys LJ. A numerical framework for simulating progressive failure in composite laminates under high-cycle fatigue loading. *Eng Fract Mech*, 295, 2024, p. 109786. DOI: `10.1016/j.engfracmech.2023.109786`.

[20] Hofman P, Van der Meer FP, Sluys L. Modeling of progressive high-cycle fatigue in composite laminates accounting for local stress ratios. *Composites A*, 183, 2024, p. 108219. DOI: `10.1016/j.compositesa.2024.108219`.

[21] Ke L, Van der Meer FP. A computational homogenization framework with enhanced localization criterion for macroscopic cohesive failure in heterogeneous materials. *J Theor Comp App Mech*, 2022. DOI: `10.46298/jtcam.7707`.

[22] Maia MA, Rocha IBCM, Kerfriden P, Van der Meer FP. Physically recurrent neural networks for path-dependent heterogeneous materials: Embedding constitutive models in a data-driven surrogate. *Comput Methods Appl Mech Eng*, 407, 2023, p. 115934. DOI: `10.1016/j.cma.2023.115934`.

[23] Maia MA, Rocha IBCM, Kovačević D, Van der Meer FP. Physically recurrent neural network for rate and path-dependent heterogeneous materials in a finite strain framework. *Mech Mater*, 198, 2024, p. 105145. DOI: `10.1016/j.mechmat.2024.105145`.

CURRICULUM VITÆ

Dragan Kovačević

24-04-1990 Born in Knin, Croatia (Yugoslavia).

EDUCATION

2009–2013 BSc in Civil (Structural) Engineering
University of Belgrade, Serbia
Thesis: Simple model for predicting traffic-induced vibrations in buildings using dynamic stiffness method
Promotor: Prof. dr. Mira Petronijević

2013–2014 MSc in Civil (Structural) Engineering
University of Belgrade, Serbia
Thesis: Influence of soil-structure interaction on the seismic response of RC buildings
Promotor: Prof. dr. Mira Petronijević

2019–2024 PhD candidate in Computational Mechanics
Faculty of Civil Engineering and Geosciences
Delft University of Technology, the Netherlands
Supervisor and Promotor: Dr. ir. F. P. van der Meer
Promotor: Prof. dr. ir. L. J. Sluys

LIST OF PUBLICATIONS

JOURNAL ARTICLES

4. **D. Kovačević**, P. Hofman, I. B. C. M. Rocha, F. P. van der Meer, *Unifying creep and fatigue modeling of composites: A time-homogenized micromechanical framework with viscoplasticity and cohesive damage,* J Mech Phys Solids **193**, p. 105904 (2024).

3. **D. Kovačević**, B. K. Sundararajan, F. P. van der Meer, *Micromechanical model for off-axis creep rupture in unidirectional composites undergoing finite strains,* Composites A **176**, p. 107860 (2024).

2. **D. Kovačević**, B. K. Sundararajan, F. P. van der Meer, *Microscale modeling of rate-dependent failure in thermoplastic composites under off-axis loading,* Eng Fract Mech **276**, p. 108884 (2022).

1. **D. Kovačević**, F. P. van der Meer, *Strain-rate based arclength model for nonlinear microscale analysis of unidirectional composites under off-axis loading,* Int J Solids Struct **250**, p. 111697 (2022).

CO-AUTHORED JOURNAL ARTICLES

1. M. A. Maia, I. B. C. M. Rocha, **D. Kovačević**, F. P. van der Meer, *Physically recurrent neural network for rate and path-dependent heterogeneous materials in a finite strain framework,* Mech Mater **198**, p. 105145 (2024).

CONFERENCE ARTICLES

1. **D. Kovačević**, F. P. van der Meer, *Micromechanical modeling of rate-dependent off-axis failure in thermoplastic composites,* Proceedings of the 20th European Conference on Composite Materials – Composites Meet Sustainability, Vol IV (D).